Karlsruhe Institute of Technology

Institute of Meteorology and Climate Research

Atmospheric Aerosol Research

Spatial distribution of aerosol particles in and above the planetary boundary layer studied by scanning LIDAR measurements

Zur Erlangung des akademischen Grades einer

DOKTORIN DER NATURWISSENSCHAFTEN (Dr. rer. nat.)

von der KIT-Fakultät für Physik

des Karlsruher Instituts für Technologie (KIT)

genehmigte

DISSERTATION

von

M. Sc. Hengheng Zhang

aus

Henan, China

Tag der mündlichen Prüfung: 21.04.2023

Referent: Prof. Dr. Thomas Leisner

Korreferent: Prof. Dr. Jan Cermak

Erklärung

Hiermit erkläre ich, dass ich die vorliegende Dissertation, abgesehen von der Benutzung der angegebenen Hilfsmittel, selbständig verfasst habe.

Alle Stellen, die gemäß Wortlaut oder Inhalt aus anderen Arbeiten entnommen sind, wurden durch Angabe der Quelle als Entlehnungen kenntlich gemacht.

Diese Dissertation liegt in gleicher oder ähnlicher Form keiner anderen Prüfungsbehörde vor.

Karlsruhe, im April 2023

Hengheng Zhang

Acknowledgements

This dissertation couldn't have been be finished without the support of many people and many organizations! I sincerely want to thank all of them!

Firstly, I really want to say sorry to my parents as I did not take my time to be together with you in the last more than three years. In the meantime, I would like to thank you and my younger sister for supporting me even though they possibly cannot fully understand what I did. Your supports give me lots of confidence to tackle different difficulties in my life. More importantly, I would like to thank my beautiful and kind wife, Nan, for your love, trust, support, and especially your company in Germany. Your arrival in the last two years of my Ph.D. study gave me a new home in Germany and I had a happy and colorful life with your company in Karlsruhe. This two-year period also allowed us to travel to many places and enjoy different kinds of food. These experiences gave me sweet and impressive memories in Europe.

I also would like to thank my direct supervisor, Dr. Harald Saathoff, for his support and guidance. You are always patient to help me get through different kinds of scientific problems. I appreciated all your contribution in time, ideas, and findings to make my Ph.D. experience wonderful. Without your help, I would not finish my Ph.D. thesis as scheduled. In addition, I would also thank you for your help in my daily life in Germany. Grateful thanks to my official doctoral supervisor Prof. Thomas Leisner, for his valuable advice on my Ph.D. study and scientific career.

Many thanks to my colleague, Dr. Frank Wagner, for your advice and training in lidar data analysis. The lidar data analysis methods that I learned from you benefited me a lot for my further research. Many thanks also to my colleague at the University of Granada, Prof. Lucas Alados Arboledas, Dr. Juan Antonio Bravo-Aranda, and Jesús Abril Gago for their hosting and guidance while I visited the University of Granada. Special thanks to Dr. Juan Antonio Bravo-Aranda for teaching me lidar depolarization calibration and lidar data assurance.

Thanks to all modelers at IMK, Dr. Gholamali Hoshyaripour, Dr. Heike Vogel, and Dr. Christopher Claus Holst for providing model simulation data for my dissertation. Thanks to colleagues at Jülich Research Center (FZJ), Dr. Ralf Tillmann and Dr. Christian Rolf, for support in collecting UAV and radiosonde data during the Jülich MOSES campaign. Thanks to colleagues working at

KIT-cube for support during the Swabian MOSES campaign. Many thanks to my former colleague, Dr. Yuxuan Bian for help in data analysis and field campaign. During your one-year visit to our group, I learned a lot from you.

Furthermore, thanks to all colleagues at IMK-AAF for technical support, scientific support, and daily help. Georg and Steffen helped me a lot to solve many technical problems during the field campaigns (e.g. Swabian MOSES campaign and Karlsruhe Mülldeponie West field campaign). Frank Schwarz is really a nice person who helped me a lot with my computer and my bicycles. Susanne is really nice to help me with many office paper works. I also had a good time with other colleagues, Barbara, Lena, Tobias, Frankzika, Alexander, Jens, Naikannabasi, and Marco during these years. Special thanks to Junwei, Linyu, and Feng for staying together with me and helping me during the hardest time, the Covid-19 pandemic. Thanks to Yanxia and Yiwei for accompanying me and my wife on the wonderful trips to Spain and Italy. The Christmas parties, the cakes in the coffee room, the salmon, and Feuerzangenbowle et al., have given me good memories at our institute and I will keep all the good memories from you. I love Karlsruhe and enjoyed these years. I will miss you in the future!

I would also like to thank the MOSES project for funding me over my whole Ph.D. period and all my colleagues in the MOSES project for supporting me to finish my Ph.D. project.

To the end, thanks to all the people and everything we experienced together! Best wishes to you all!

Hengheng Zhang

Karlsruhe, 2023

Abstract

The spatial distribution of aerosol particles is of great relevance for air pollution caused by anthropogenic aerosol emissions but also for global climate by changing the radiative forcing either directly or via aerosol cloud interaction. Hence it is essential to study the spatial-temporal distribution of aerosol particles and the processes (e.g. sources, sinks, and transport) leading to these distributions. Currently, it is still difficult to obtain high-resolution and quantitative aerosol distributions due to instrumental limitations. However, scanning aerosol lidars have the capability to measure three dimensional aerosol distributions and to reduce retrieval uncertainties compared with traditional vertically pointing lidars. Hence, the scanning aerosol lidar used in this dissertation allowed me to determine high-resolution and quantitative aerosol distributions. These lidar data together with other measurements aid to better understand aerosol-boundary-layer interaction as well as aerosol-cloud interaction.

To investigate the spatial-temporal distribution and properties of aerosols as well as boundary layer dynamics, a comprehensive data set including remote sensing methods, *in-situ* measurements at ground level as well as on an Unmanned Aerial Vehicle (UAV) and on a balloon were collected and analyzed. Furthermore, these observational data can be used to validate results from the large eddy simulation (LES) model, PALM-4U, simulating the evolution of boundary layer and urban aerosol in the city of Stuttgart as well as the transport model ICON-ART simulating the regional transport of Saharan dust.

Firstly, I developed a new method to retrieve lidar ratios based on scanning elastic lidar measurements, which could significantly reduce the uncertainties compared to traditional elastic lidar retrievals. The newly proposed method was applied in one Saharan dust case and the retrieved lidar ratio is consistent with that retrieved by the Raman retrieval method. In addition, the scanning lidar retrievals were validated by comparison with *in-situ* measurements at ground level, on UAV flights in and above the boundary layer, and on a balloon flight up to the stratosphere. The good agreement between scanning lidar retrievals with the newly developed software and the single calculus chain reference software as well as the *in-situ* measurements is a clear indicator of the high quality of the measured data and the retrieval method.

Secondly, I characterized the dynamics of the urban boundary layer and the air quality in the urban

background of Stuttgart by comparison of scanning lidar results with those from a Doppler wind lidar, a radiometer, radiosonde measurements, and a collection of ground level *in-situ* methods including aerosol particle sizers, meteorological sensors, and an aerosol mass spectrometer (AMS). The boundary layer structure retrieved by the scanning aerosol lidar shows good agreement with radiosonde analysis with a slope and a Pearson correlation coefficient of 1.102 ± 0.135 and 0.860, respectively. The ground-level aerosol concentrations correlated with mixing layer heights but were anti-correlated with nocturnal boundary layer heights. Stagnating atmospheric conditions with temperature inversion, low wind speed, and a shallow boundary layer caused an accumulation of ground-level aerosols, which is one main reason for severe air pollution events in cities like Stuttgart especially in winter. In a case study I could show, that clouds during a previous night can accelerate growth of the boundary layer after sunrise by changing the thermal structure of the nocturnal boundary layer. In addition, I am going to use the observational data to validate the large eddy simulation model, PALM-4U, simulating the evolution of the boundary layer and the spatial-temporal distribution of aerosols in Stuttgart with a spatial resolution of 10 m.

Thirdly, I investigated the evolution and properties of Saharan dust plumes by combining remote sensing methods (aerosol lidar, sun photometer), *in-situ* measurements (aerosol sizer), and the transport model ICON-ART for four different Saharan dust cases in western Europe. Compared to the remote sensing measurements, the transport model predicts the plume arrival times ($\pm$ 20 min), layer heights ($\pm$ 50 m), and structures quite well. Only for one case significant differences in dust layer heights were observed. The modeled dust backscatter coefficients assuming non-spherical dust particles show a quantitative agreement with lidar retrievals for a wavelength of 355 nm. Furthermore, I found first indications that Saharan dust plumes can have an inhibiting effect on precipitation.

In summary, I investigated the boundary layer dynamics and spatial-temporal distributions of aerosol particles by employing mainly a scanning aerosol lidar in this dissertation. The additional information obtained from spatial aerosol lidar scans allowed me to investigate aerosol properties and the evolution of the atmospheric boundary layer in urban and rural locations in winter and summer, respectively. This work provides new insights in the application of a scanning aerosol lidar, its data quality, dynamics of the planetary boundary layer, the quality of the models ICON-ART and potentially PALM-4U, as well as aerosol distributions and their impact on air quality, weather, and climate.

Zusanmenfassung

Die räumliche Verteilung von Aerosolpartikeln hat großen Einfluss auf die Luftverschmutzung durch anthropogene Emissionen aber auch auf das globale Klima, indem der Strahlungsantrieb entweder direkt oder über Aerosol-Wolken-Wechselwirkung verändert wird. Daher ist es unerlässlich, die räumlich-zeitliche Verteilung von Aerosolpartikeln und die Prozesse, die zu diesen Verteilungen führen (z. B. Quellen, Senken und Transport), zu untersuchen. Derzeit ist es aufgrund instrumenteller Einschränkungen noch schwierig, hochauflösende und quantitative Aerosolverteilungen zu erhalten. Schwenkbare Aerosol-Lidare sind jedoch in der Lage, dreidimensionale Aerosolverteilungen zu messen und Auswerteunsicherheiten im Vergleich zu herkömmlichen, vertikal ausgerichteten Lidaren zu verringern. Das in dieser Dissertation verwendete schwenkbare Aerosol-Lidar ermöglichte es mir daher, hochaufgelöste und quantitative Aerosolverteilungen zu bestimmen. Diese Lidardaten helfen zusammen mit anderen Messungen, Aerosol-Grenzschicht-Wechselwirkungen sowie Aerosol-Wolken-Wechselwirkungen besser zu verstehen.

Zur Untersuchung der räumlich-zeitlichen Verteilung und Eigenschaften von Aerosolen sowie der Grenzschichtdynamik wurde ein umfangreicher Datensatz mit Fernerkundungsmethoden, in-situ-Messungen in Bodennähe sowie mit Drohnenflügen (UAV) und auf Ballons gesammelt und analysiert . Darüber hinaus habe ich diese Beobachtungsdaten verwendet um zwei Transportmodelle zu validieren. Das LES-Model PALM-4U, das die Entwicklung der Grenzschicht und des städtischen Aerosols in der Stadt Stuttgart simuliert und das Transportmodell ICON-ART, das den überregionalen Transport von Saharastaub beschreibt.

Zunächst habe ich eine neue Methode entwickelt, um Lidar-Verhältnisse auf der Grundlage von Lidar-Messungen unter mindestens zwei verschieden Winkel abzuleiten, was die Unsicherheiten gegenüber traditionellen Methoden erheblich verringern könnte. Die neu vorgeschlagene Methode wurde für eine Saharastaubwolke angewendet und das abgeleitete Lidar-Verhältnis stimmt mit dem überein, das durch die klassische Raman-Methode erhalten wurde. Darüber hinaus habe ich die Lidarauswertung durch Vergleich mit *in-situ*-Messungen auf Bodenhöhe, bei Drohnenflügen in und über der Grenzschicht, sowie auf einem Ballonflug in die Stratosphäre validiert. Die gute Übereinstimmung zwischen Auswertungen mit der neu entwickelten Software und der Single-Calculus-Chain-Referenzsoftware sowie den in-situ-Messungen ist ein klarer Indikator für die hohe Qualität

der Lidar-Messdaten und der verwendeten Methodik.

Zweitens wurde die Dynamik der städtischen Grenzschicht und die Luftqualität im städtischen Hintergrund von Stuttgart charakterisiert. Dazu habe ich Daten des schwenkbaren Lidars mit einem Doppler-Wind-Lidar, einem Radiometer, Radiosonden sowie einer Sammlung von bodennahen in-situ-Methoden (Größenverteilungen, Meteorologische Parameter, Aerosolzusammensetzung) verglichen. Die vom schwenkbaren Aerosol-Lidar gemessene Grenzschichtstruktur zeigt eine gute Übereinstimmung mit der Radiosondenanalyse mit einer Steigung der Korrelation von 1,102 $\pm$ 0,135 und einem Pearson-Korrelationskoeffizienten von 0,860. Die bodennahen Aerosolkonzentrationen korrelieren dabei mit den Mischungschichthöhen, aber sind antikorreliert mit den nächtlichen Grenzschichthöhen. Stagnierende atmosphärische Bedingungen mit Temperaturinversion, geringer Windgeschwindigkeit und einer flachen Grenzschicht führten zu einer Ansammlung von bodennahen Aerosolen insbesondere im Winter. Dies ist einer der Hauptgründe für die hohe Luftverschmutzung in Städten wie Stuttgart. In einer Fallstudie konnte ich zeigen, dass Wolken in einer vorangegangenen Nacht das Wachstum der Grenzschicht nach Sonnenaufgang beschleunigen können, indem sie die thermische Struktur der nächtlichen Grenzschicht verändern. Darüber hinaus verwende ich die Beobachtungsdaten zur Validierung des Large-Eddy-Simulationsmodells PALM-4U, dass die Entwicklung der Grenzschicht und die räumlich-zeitliche Verteilung von Aerosolen in diesem Stadtgebiet mit einer räumlichen Auflösung von 10 m simuliert.

Drittens habe ich die Entwicklung und die Eigenschaften einer Saharastaubwolke untersucht, wobei Fernerkundungsmethoden (Aerosol-Lidar, Sonnenphotometer), in-situ-Messungen (Aerosolgrößenverteilungen) und das Transportmodell ICON-ART für vier verschiedene Saharastaubfälle in Westeuropa kombiniert wurden. Im Vergleich zu den Fernerkundungsmessungen sagt das Transportmodell die Ankunftszeiten der Wolke ($\pm$ 20 min), ihre Schichthöhen ($\pm$ 50 m) und Strukturen für drei Fälle recht gut voraus, während für einen Fall signifikante Unterschiede in der Staubschichthöhe beobachtet wurden. Die modellierten Rückstreukoeffizienten des Staubs zeigen unter der Annahme von nicht kugelförmigen Staubpartikeln eine gute Übereinstimmung mit Lidardaten für eine Wellenlänge von 355 nm. Außerdem fand ich erste Hinweise darauf, dass Saharastaubfahnen niederschlagshemmend wirken können.

Ich habe in dieser Dissertation die Grenzschichtdynamik und die räumlich-zeitlichen Verteilungen von Aerosolpartikeln hauptsächlich unter Verwendung eines schwenkbaren Aerosol-Lidars untersucht. Die Informationen zu den räumlich-zeitlichen Aerosolverteilungen ermöglichten es mir,

Aerosoleigenschaften und die Entwicklung der atmosphärischen Grenzschicht in städtischen und ländlichen Gebieten im Winter bzw. Sommer zu untersuchen. Diese Arbeit liefert neue Einblicke in die Anwendung des schwenkbaren Aerosol-Lidars, in die Qualität seiner Daten, in die Dynamik der bodennahen Grenzschicht, in die Qualität der Modelle ICON-ART und zukünftig PALM-4U, sowie zu Aerosolverteilung und deren Auswirkungen auf Luftqualität, Wetter und Klima.

Contents

List of Figures

List of Tables

Abbreviations

DWD-DELiRA Deutscher Wetterdienst- Depolarizarion Raman lidar 85
EARLINET European Aerosol Research Lidar Network 9
ECWMF European Centre for Medium-Range Weather Forecasts 72
EMAC ECHAM/MESSy Atmospheric Chemistry 12
EMEP European Monitoring and Evaluation Programme 14
ERA5 ECMWF Reanalysis v5 36
FEP Fluorinated Ethylene Polypropylene copolymer 27
FMCW Frequency Modulated Continuous Wave 26
FOV Field Of View 29
FTIR Fourier-Transform Infrared Spectroscopy 11
FZJ Forschungszentrum Jülich 17
GAW Global Atmospheric Watch 10
GUI Graphical User Interface 43
WHO World Health Organization 5
HWT Haar Wavelet Transform 24
HSRL High Spectral Resolution Lidar 9
HYSPLIT HYbrid Single-Particle Lagrangian Integrated Trajectory 31
HATPRO Humidity And Temperature PROfilers 26
HTDMA Hygroscopicity Tandem Differential Mobility Analyzer 11
ICON ICOsahedral Nonhydrostatic model 12
INP Ice Nucleating Particles 1
IOPs Intensive Observation Periods 38
IWV Integrated Water Vapor 26
IPCC Intergovernmental Panel on Climate Change 1
KASCAL KArlsruhe SCanning Aerosol Lidar 17
LEDs Light-Emitting Diodes 29
LES Large Eddy Simulation 12
LV-OOA Low-Volatility Oxygenated Organic Aerosol 58
LPDR Linear Particle Depolarization Ratio 85
LUBW Landesanstalt für Umwelt Baden-Württemberg 34
LVDR Linear Volume Depolarization Ratio 26

LWP Liquid Water Path . . . 26
MODIS Moderate Resolution Imaging Spectroradiometer . . . 13
MOSES Modular Observation Solution for Earth System . . . 18
MLH Mixing Layer Height . . . 13
MPL Micro Pulse Lidar . . . 9
MPLNET Micro-Pulse Lidar Network . . . 10
MWR Microwave Radiometer . . . 17
NBL Nocturnal Boundary Layer . . . 2
NH_4 Ammonium . . . 28
NMTP Night and Morning Time Period . . . 60
NSP non-spherical . . . 85
NOAA National Oceanic and Atmospheric Administration . . . 31
NO_3 Nitrate . . . 28
OA Organic Aerosol . . . 28
OPC Optical Particle Counter . . . 11
PBL Planetary Boundary Layer . . . 13
PINE Portable Ice Nucleation Experiment . . . 40
PMF Positive Matrix Factorization . . . 58
PTR-MS Proton-Tranfer-Reaction Mass Spectrometer . . . 41
RCS Range Corrected lidar Signal . . . 24
RLH Residual Layer Height . . . 40
RPG Radiometer Physics GmbH . . . 26
SAMUM Saharan Mineral Dust Experiment . . . 13
SBL Stable Boundary Layer . . . 2
SCC Single Calculus Chain . . . 43
SDEs Saharan Dust Events . . . 8
SMPS Scanning Mobility Particle Sizer . . . 11
SO_4 Sulfate . . . 28
SPH spherical . . . 85
SSA Single Scattering Albedo . . . 14
TKE Turbulent Kinetic Energy . . . 65

1 Introduction

Aerosols are particles or liquid droplets suspended in the air (Lohmann & Feichter 2005) and comprise both, the gas and condensed phase components. The global and regional distributions of aerosols are of great concern as it affects visibility, air quality, cloud formation, atmospheric radiative transfer (Guo et al. 2009, Li et al. 2016, Chan & Yao 2008), and it also has discernible adverse effects on human health (Asadi et al. 2019, Leung 2021, Port et al. 2022).

The impact of aerosols on global radiative forcing and clouds are among the largest uncertainties in predicting climate change according to the Intergovernmental Panel on Climate Change (IPCC) report (Pörtner et al. 2022) as shown in Figure 1.1. This figure also shows that aerosol can affect climate in two ways: direct effect and indirect effect (Levy et al. 2013, Takemura et al. 2005, Stocker 2014, Ramanathan et al. 2001, Ackerman et al. 2004, Stocker 2014, Guo et al. 2017, Kiehl & Briegleb 1993). The direct effect refers the aerosol change of radiative forcing through scattering and absorption of sunlight and terrestrial emissions (Hatzianastassiou et al. 2007, Hong et al. 2020). Indirect effect means that aerosol particles can participate in cloud formation as Cloud Condensation Nuclei (CCN) and Ice Nucleating Particles (INP) and thus can influence cloud cover but also cloud properties to interact with solar or terrestrial radiation. (Ansmann et al. 2008, Su et al. 2008, DeMott et al. 2015, Möhler et al. 2021, Brunner et al. 2021*b*, Niemand et al. 2012, Min et al. 2009, Karydis et al. 2017).

There is a large uncertainty in aerosol radiative forcing due to the large variation of aerosol distributions and optical properties (Zhao et al. 2010, Alam et al. 2011). Aerosol particles can be distributed unevenly in both vertical and horizontal scales (Wei et al. 2019). In addition, the distinct value of optical parameters (e.g. scattering and absorption coefficient, albedo etc.) for different kinds of aerosol particles significantly affect the radiative forcing. Hence, collecting accurate data regarding aerosol particle distributions and optical properties as well as achieving a better understanding of the roles in which aerosols participate is thus crucial for understanding their effects on earth's climate.

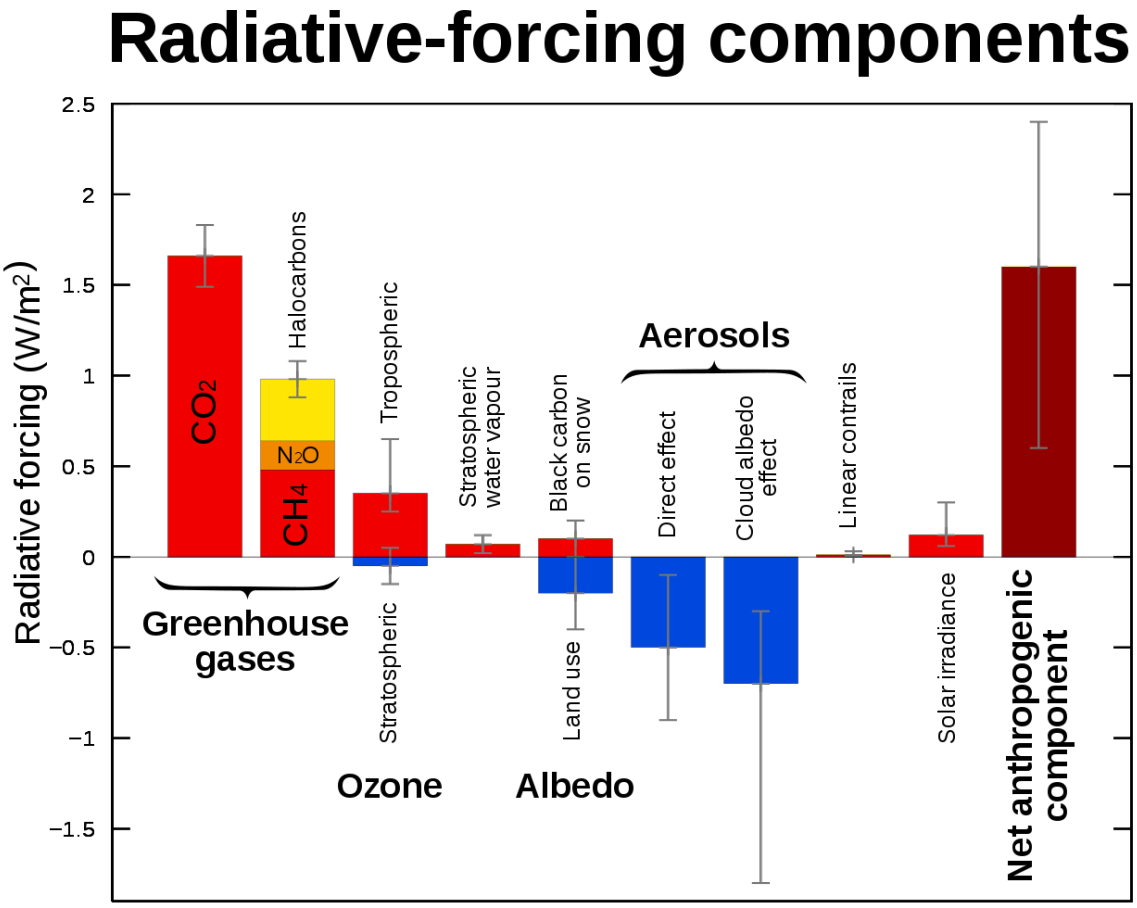

Figure 1.1: Global average radiative forcing estimates and ranges for aerosols and other important agents and mechanisms (Pörtner et al. 2022).

1.1 Planetary boundary layer and urban air quality

1.1.1 Planetary boundary layer and its interaction with aerosols

The Boundary Layer Height (BLH) is generally about 1 - 2 km (10% - 20% of the troposphere) from the surface, but can in extrem cases vary from 10 m to 4 km or more (Stull 1988). It is the main layer for human beings and the whole biosphere. The boundary layer greatly affects the entire atmospheric system, determining the exchange of heat, moisture, and momentum between the earth's surface and the free troposphere (Garratt 1994, Medeiros et al. 2005). The fundamental definition of boundary layer (normally refer to Nocturnal Boundary Layer (NBL), also called Stable Boundary Layer (SBL) specifically, has traditionally been turbulence based - the boundary layer is a turbulent layer adjacent to the earth's surface layer (Stull 1988). The top of the boundary layer is the boundary to the free troposphere where the mixing is comparatively less.

The boundary layer is not static but instead changes dramatically during the course of the day (Bianco et al. 2011). The structure of the boundary layer and its evolution is illustrated in Figure 1.2. The boundary layer consists of a mixed layer that is stirred by solar heating of the surface and convection of warm moist air that pops up sporadically from place to place and time-to-time, and, as a result, mixes the air within the boundary layer (Ferrero et al. 2012, Wiegner et al. 2006). This convective stirring takes about ten to twenty minutes to go from bottom to top. As the air bubbles up, it mixes with the air surrounding it and with the air from the free troposphere at the top, thus creating an entrainment zone, which is where also clouds can form (Liu et al. 2021, Vraciu 2021).

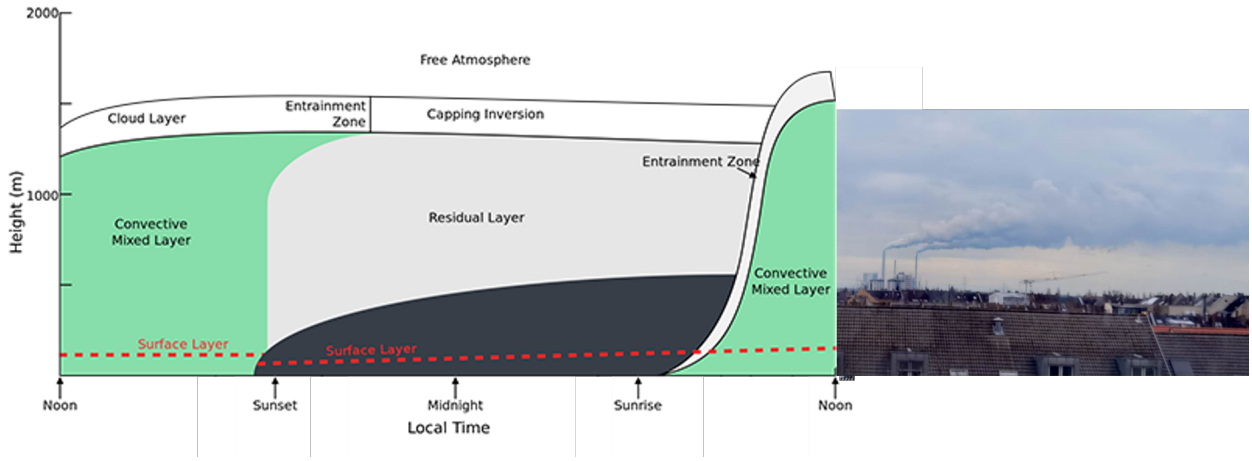

Figure 1.2: Left: Diurnal evolution of the atmospheric boundary layer and the related meteorological background. The black region is the stable (nocturnal) boundary layer (Stull 1988). Right: Industrial smoke from two coal fired power plants in Karlsruhe was dissipating in a cone-shape plume within the boundary layer (Photo by Hengheng Zhang).

After sunset, the solar heating of the surface and the convection and associated turbulent eddies cease (Pino et al. 2006, Tkachenko et al. 2021). Air from the surface no longer mixes with air throughout the Convective Boundary Layer (CBL), and the air that was mixed during daytime stays above the much lower nighttime SBL in a layer called the residual layer (Fochesatto et al. 2001, Blay-Carreras et al. 2014, Ma et al. 2022). Any gaseous or particle emissions from the surface are mixed within this SBL. Because convection ceases at night, the winds in the residual layer are no longer affected by the friction caused by convection and are accelerated in the presence of a horizontal pressure gradient. So, the residual layer winds are accelerated, blowing harder across the top of the more stagnant SBL and a shear develops (Tjernström et al. 2009). This shearing is unstable and creates turbulence that mixes the boundary layer air and the residual layer air near the interface, so the SBL grows a little during the night (Kim & Mahrt 1992).

In the morning, the sun reheats the surface and starts driving convection and mixing again. This convection bubbles up, bumping into and entraining air from the residual layer. As the solar heating increases, the convection has more energy and can rise higher and entrain more air from the residual layer. Eventually, the air driven by convection reaches its maximum energy level, and this maximum energy limits how high the boundary layer will grow into the stable free troposphere above it (Kaimal et al. 1976).

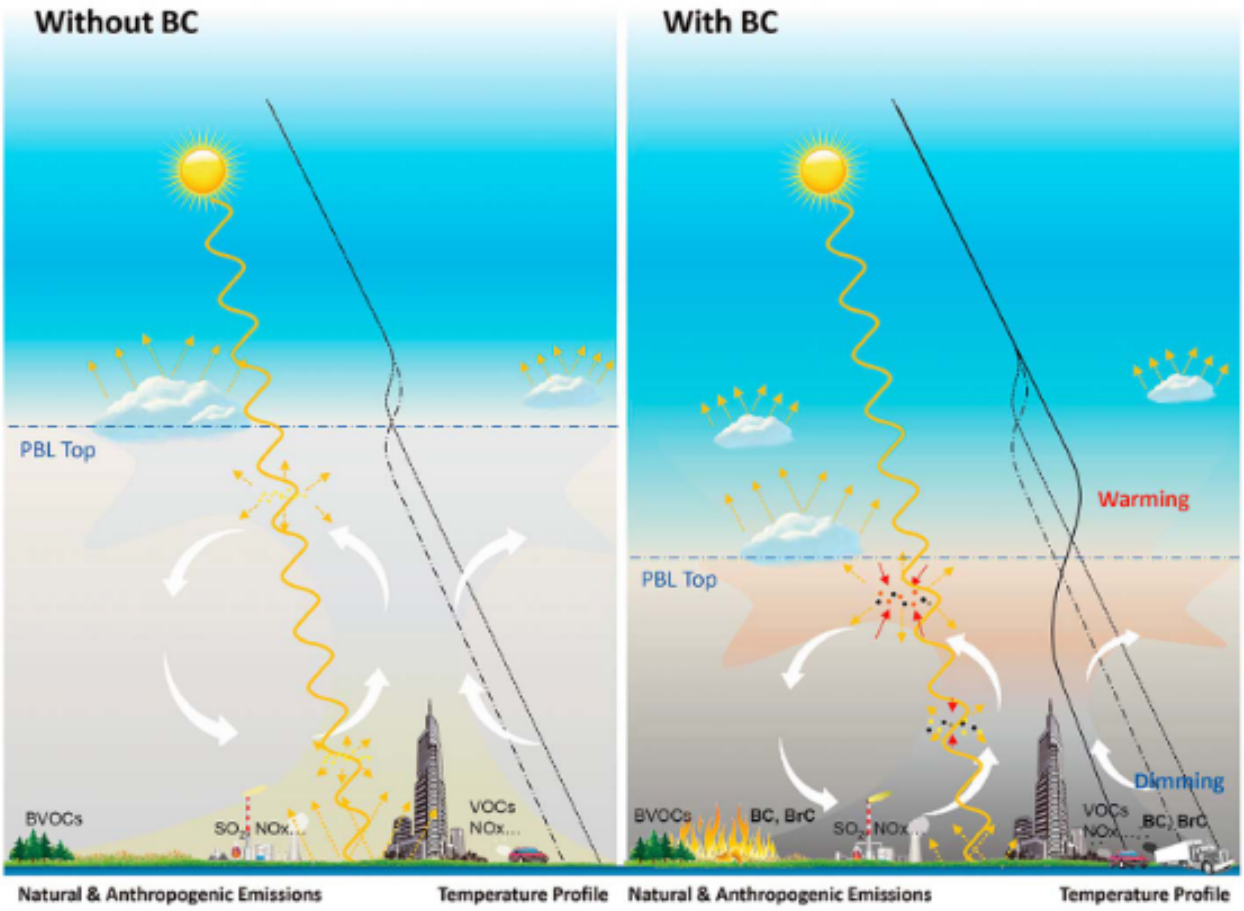

Figure 1.3: A schematic figure showing the aerosol-boundary-layer feedback loop for the scenarios without (left) and with (right) black carbon (BC) emissions in a megacity. The black lines give air temperature profiles (solid, dotted lines and dash-dotted for the scenarios with BC, without aerosols, and with aerosols except for BC, respectively). The yellow dashed lines with arrows denote the reflection of solar radiation by the ground surface, clouds, and aerosols. The red arrows show absorption of solar radiation by absorbing aerosols. The blue dash-dotted line indicates the top of the PBL. White arrows shows the vertical ventilation of urban plumes induced by circulations or large eddies induced by the urban heat island effect. (From Ding et al. (2016))

The boundary layer and aerosol particles can influence each other through aerosol-boundary-layer-interaction (Huang et al. 2020, Li et al. 2017*a*, Ding et al. 2021). The aerosol-boundary-layer-

interaction is depicted in Figure 1.3 and can be explained in two aspects: Firstly, the aerosol distribution and concentration within the boundary layer is affected by the BLH because of dilution for an expanding boundary layer but partally also a concentrating for a shrinking BLH (Pal et al. 2014, Miao et al. 2019, Lee et al. 2019). Secondly, absorbing aerosol particles like Black Carbon (BC) within the boundary layer can absorb sunlight and further enhance a temperature inversion. This enhancement of temperature inversion would cause a stable and shallow boundary layer and a lower BLH. This shallow boundary layer would induce the accumulation of aerosols at ground level again. This is a so-called positive feedback mechanism (Petäjä et al. 2016, Li et al. 2017*b*, Liu et al. 2018). To conclude, the boundary layer structure affects the aerosol concentration and distribution while the distribution and composition of these aerosols also has a feedback effect on the boundary layer by changing the thermodynamics of the boundary layer.

1.1.2 Urban air quality

Urban air quality has become a significant problem especially for certain megacities because of urban air pollution events which occurred in recent years (Shen et al. 2021, Li et al. 2018). According to the World Health Organization (WHO), each year air pollution is responsible for nearly seven million deaths around the globe. Nine out of ten human beings currently breathe air that exceeds the WHO's guideline limits for pollutants, with those living in low- and middle-income countries suffering the most (Fuller et al. 2022). Air pollution is a significant risk factor for a number of pollution-related diseases, including respiratory infections, heart disease, Chronic Obstructive Pulmonary Disease (COPD), stroke, and lung cancer (WHO 2014).

Air pollution results from a complex mixture of thousands of pollutants. This mixture may include solid and liquid particles suspended in the air (particulate matter (PM)), and various gases such as ozone (O_3), nitrogen oxides (NO_2 or NO_x), volatile organic compounds (VOCs), and carbon monoxide (CO) (Bell et al. 2009, Peng et al. 2009). Aerosol particle pollution in a city is commonly quantified by two parameters: $PM_{2.5}$ (particle matter less than 2.5 µm) and PM_{10} (particle matter less than 10 µm). The reason for choosing these two parameters is that aerosol size distributions are characterized by 3 modes: fine mode ($d < 2.5$ µm) and coarse mode ($d > 2.5$ µm); the fine mode is further divided in the nuclei mode (about 0.005 µm $< d <$ 0.1 µm) and accumulation mode (0.1 µm $< d <$ 2.5 µm).

The aerosol concentration in a city is determined by the sources, sinks and transport of aerosol in

this region (Salma & Maenhaut 2006, Guo et al. 2014). With respect to their emission sources, the aerosols can be grouped into biogenic and anthropogenic aerosols (KULMALA et al. 2001, Lei et al. 2011, Samset et al. 2018) with anthropogenic aerosols only accounting for 10% of total aerosols (Taylor et al. 2013). Though less abundant than natural forms, anthropogenic aerosols can dominate the air downwind of urban and industrial areas (Heald et al. 2006, Äijälä et al. 2017). In addition, the anthropogenic aerosols emitted from smokestacks, car exhausts, wildfires, and even clothes dryers have increased rapidly, largely in step with greenhouse gases responsible for climate change (Charlson et al. 1992, Fiedler et al. 2019). Their sinks are related to meteorological conditions like wind speed, BLH, and dry and wet deposition. Normally, a high wind speed provided a good opportunity for aerosol dilution while a low wind speed will favor accumulation of aerosols. The impact of the boundary layer on the urban aerosol concentrations is due to the changing volume of the boundary layer (Nilsson et al. 2001). The product of boundary layer and wind speed is the ventilation coefficient, which determines the aerosol dissipation ratio on the local scale (Lu et al. 2012, Genc et al. 2010). The photo on the right side of Figure 1.2 well illustrates the disipitation of the industrial plume, which shows that this plume had a cone shape within the boundary layer.

1.2 Saharan dust sources and transport

Saharan dust is an aeolian mineral dust from the Sahara desert, the largest hot desert in the world. The desert spans just over 9 million square kilometers, from the Atlantic Ocean to the Red Sea, from the Mediterranean sea to the Niger River valley, and the Sudan region in the south (Cook & Vizy 2015). The Saharan desert is the largest source of aeolian dust in the world, with annual production rates of about 400 - 700 x 10^6 tons/year, which is almost half of all aeolian dust inputs to the oceans (Middleton & Goudie 2001). Saharan dust is mainly produced by natural processes such as wind storms and doesn't appear to be heavily impacted by human activities (Kandler et al. 2007).

Saharan dust has been found to be transported in the free troposphere of long distances reaching e.g.the Amazon basin, middel and north america, Europe (Guerzoni & Chester 1996), Japan (Tanaka et al. 2005), and other regions. Figure 1.4 shows a massive Saharan dust storm engulfing western Europe observed by satellite on 16^{th}, March 2022, which illustrates that Storm Celia has carried dust from North Africa to Europe, affecting air quality in a number of countries including France, Spain, Portugal, and Germany. The dust supplied to the North Atlantic and the

Mediterranean (Guerzoni & Rampazzo 1993) brings limiting nutrients (e.g. iron) that help to boost primary biogenic production. For the Amazon basin, which is limited in phosphorus in much of the soil, Saharan dust is a main source of phosphorus. This dust has also impacted ecosystems in the southeastern United States and the Caribbean by supplying limiting nutrients, and in some cases promoting soil development on land (Guerzoni & Rampazzo 1993). Saharan dust has even been found on glaciers and studied to examine atmospheric circulation Aarons et al. (2013). Saharan dust can cause respiratory difficulties for humans Korenyi-Both et al. (1992), Garrison et al. (2006) and other adverse health conditions especially during dust storms (Goudie 2014).

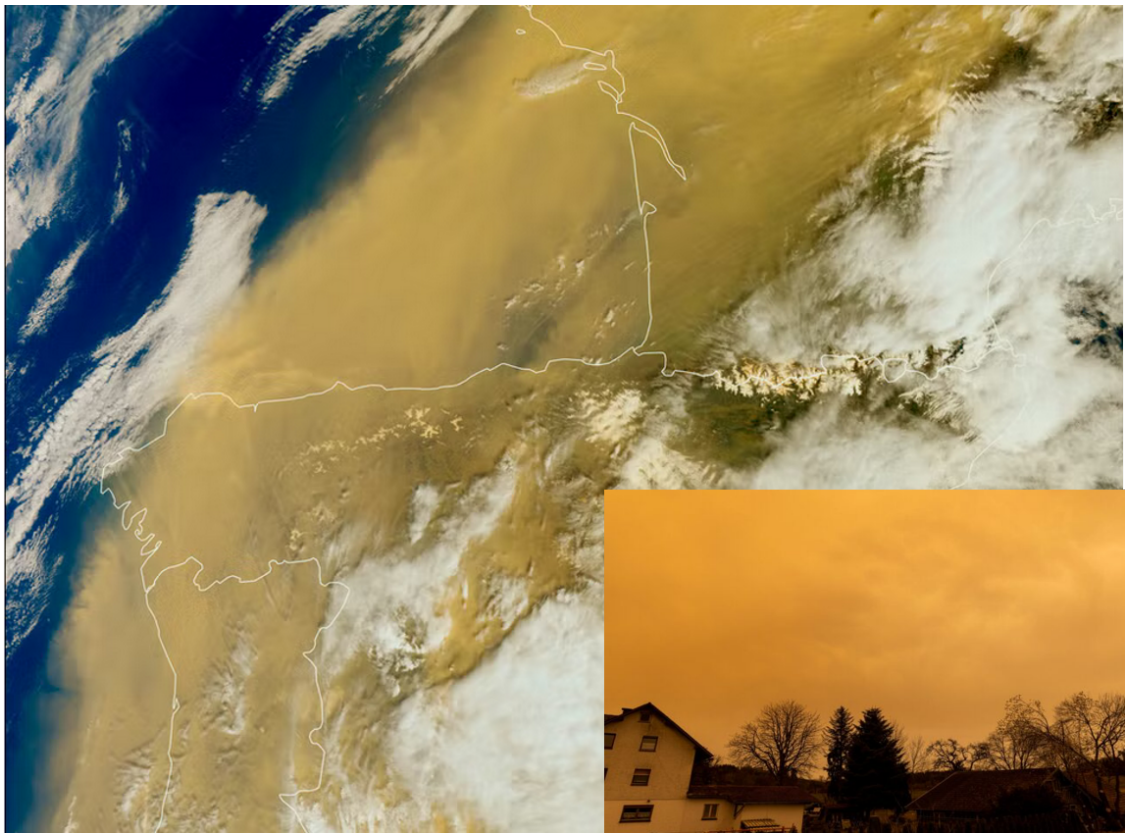

Figure 1.4: Massive Saharan dust storm engulfing western Europe observed by satellite (European Union, Copernicus Sentinel-3 imagery) on 16^{th}, March 2022. Insert: A photo of orange sky during this Saharan dust storm taken in Karlsruhe (Photo by Dr. Harald Saathoff).

The diameter of Saharan dust particles range from 100 nm to 50 µm and most of the particles obtain increasing coatings by sulfates or nitrates during their atmospheric transport (Kandler et al. 2007). Typically, Saharan dust particles in the size range of 1-5 µm dominate those transported over longer distances. In the atmosphere, these particles can deflect sunlight back into space, participate in cloud formation and redistribute solar energy over the globe. The albedo of all Saharan

samples varied between 0.945 and 0.955. Values close to 1 indicate that these particles are highly reflective (Kandler et al. 2007). The size of Saharan dust particles is largely determined by the distance from their source. The first particle to leave the atmosphere and return to the surface will be the largest. As the particles travel further, more of the smaller particles will then remain (Aarons et al. 2013).

Long range transport of Saharan dust occurs mainly in the free troposphere and has a great impact on the biosphere, weather, and climate change. Changes in circulation patterns associated with climate change have led to an increase in the frequency and intensity of Saharan Dust Events (SDEs) in the Carpathian Basin. The annual number of dust events was 4.2 on average between 1979 and 2010, while in the period of 2011–2018, it has increased to 10.3. And an average of about 33,000 tons of atmospheric dust was transported to Central Europe each year from 2002–2017 (Rostási et al. 2022). The increased frequency and amount of Saharan dust plumes have caused larger uncertainties in global radiative forcing (Saidou Chaibou et al. 2020, Zhao et al. 2011, Mallet et al. 2009).

1.3 Recent methods in boundary layer and aerosol measurement

1.3.1 Remote sensing methods

Various techniques have been used to characterize atmospheric boundary layer behaviors in recent years (Stellmach et al. 2014, Sullivan & Patton 2011). The characterization of the boundary layer usually refers to the measurement of atmospheric parameters (e.g. windspeed, potential temperature, turbulence etc.) affecting the boundary layer or atmospheric composition (e.g. aerosol, water vapor etc.) within the boundary layer (Lachmann 2014, Dang et al. 2019). And the BLH can be retrieved from the vertical distributions of these atmospheric parameters or atmospheric composition. Among these measurement techniques, remote sensing methods have become efficient ways because they can provide vertical profiles in high temporal and spatial resolution (Wang et al. 2012, de Arruda Moreira et al. 2020). For example, sodar can provide wind speed from tens of meters to hundreds of meters above ground level using the principle of Doppler shift (Prabha et al. 2002). Wind lidar has become an efficient tool for obtaining high-resolution wind profiles and further investigating the boundary layer structure (Zhang et al. 2018, Kiseleva et al. 2021).

Another very useful tool to investigate the boundary layer is the aerosol lidar (Barlow et al. 2011,

Korhonen et al. 2014, Pal et al. 2010*a*). The principle of determining BLH by an aerosol lidar is that the gradient of aerosol concentration reaches its maximum at the top of the boundary layer. In other words, most of the aerosols are within the boundary layer and the aerosol concentration above the boundary layer is much lower than that within the boundary layer. This typical distribution of aerosol concentrations will cause a negative gradient in lidar backscatter at the top of the boundary layer, from which the BLH can be determined. Different types of aerosol lidars have been used to study the boundary layer and Micro Pulse Lidar (MPL) is one type of them (Chu et al. 2019, Su et al. 2017). In addition, the boundary layer evolution was also studied by multiple wavelength lidar systems based on European Aerosol Research Lidar Network (EARLINET) multi-year observation (Boselli et al. 2009, Matthias et al. 2004, Amiridis et al. 2005). The disadvantage of this traditional vertically pointing lidar is that it cannot be used to detect very low boundary layers (e.g SBL) due to the overlap limit (Pal 2014). The field of view of the telescope collecting the backscattered photons of the lidar overlaps with the laser beam only after some hundred meters distance from the instrument. One way to solve this problem is to use a lidar with a complete or near complete transceiver overlap. Ceilometer is this kind of lidar with overlap normally being tens of meters (de Arruda Moreira et al. 2020, Lee et al. 2019, Kotthaus & Grimmond 2018). Another way is to use a scanning lidar allowing vertical to nearly horizontal measurements and hence to determine also very low BLHs (Strawbridge & Snyder 2004).

An aerosol lidar can be used not only to determine BLH but also to measure the vertical profiles of aerosols with high spatial and temporal resolution. However, retrieving backscatter coefficients from traditional elastic lidar data requires assumptions of lidar ratios and reference values (Fernald 1984, Klett 1985*a*). The lidar ratio is the ratio of extinction-to-backscatter coefficient and reference values are backscatter values without aerosol particles. The lidar ratio is an important parameter for lidar research as it can not only help to determine extinction coefficients but also be used in other aspects like aerosol typing (Haarig et al. 2018, 2022, Lei et al. 2021). However, determining lidar ratios is not easy. One of the most widely used technology is the Raman lidar (Wandinger 2005), which typically uses the backscatter by nitrogen Raman shift to determine the backscatter from the particle free atmosphere. However, this technology is mainly limited to nighttime measurements due to weak intensities of Raman scattering. Another widely used technology is the High Spectral Resolution Lidar (HSRL) (Liu et al. 1999) which used a narrow-band filter (e.g. atom or molecule filter) to separate signals from molecule and particle backscatter. But this kind of filter can only

work at specific wavelengths. For example, the most commonly used filter is the iodine cell, which only works at 532 nm (Piironen & Eloranta 1994). Recently, a HSRL that uses an interferometer as the filter has been deployed at other wavelengths. The recently launched Doppler wind lidar, ALADIN, uses this technology to measure tropospheric wind profiles on a global scale but can also obtain vertical aerosol profiles (Schillinger et al. 2003). However, this technology is still not widely used due to the complex configurations of this kind of system. The aerosol optical depth measured by a sun photometer (see below) can also be used to constrain the lidar retrieval, thus helping us get column average lidar ratios (Chen et al. 2009). Furthermore, a method using multiple angles e.g. based on scanning aerosol lidar measurements was proposed to retrieve extinction coefficients independently in horizontal homogeneous atmospheres (Adam 2012, Gutkowicz-Krusin 1993). The uncertainties of this method applied for inhomogeneous atmospheres and an improved method for poorly stratified atmospheres was also discussed (Kovalev et al. 2011, 2012, 2015). This method has the advantage of retrieving extinction from elastic lidar measurements without assumptions of lidar ratios for the elastic lidar. Another better way to obtain extinction coefficients from elastic scattering lidar measurements is via the Klett-Fernald method with a known lidar ratio. Recently, a method to retrieve lidar ratio based on multi-angle scanning elastic scatter lidar (at least two angles) was proposed to eliminate uncertainties in lidar retrievals (Zhang et al. 2022).

In the last decades, different lidar networks was established to measure the aerosol and cloud profiles as well as BLH. For example, the EARLINET was established in 2000 as a research project with the goal of creating a quantitative, comprehensive, and statistically significant database for the horizontal, vertical, and temporal distribution of aerosols on a continental scale. Since then EARLINET has continued to provide the most extensive collection of ground-based data for the aerosol vertical distribution over Europe (Pappalardo et al. 2014, Matthias et al. 2004, Bösenberg & Matthias 2003). The NASA Micro-Pulse Lidar Network (MPLNET) is a federated network of MPL systems designed to measure aerosol and cloud vertical structure, and BLHs. The data are collected continuously, day and night, over long time periods from sites around the world. Most MPLNET sites are co-located with sites in the NASA AErosol RObotic NETwork (AERONET). MPLNET is also a contributing network to the World Meteorological Organization (WMO) Global Atmospheric Watch (GAW) Aerosol Lidar Observation Network, GALION (Welton et al. 2006, 2018). Another network of researchers in East Asia (Japan, Korea, and China), Asian Dust and Aerosol Lidar Observation Network (AD-Net), for studying Asian dust was formed around (Sugimoto et al.

2014, Nishizawa et al. 2016).

In addition to these active remote sensing measurements, passive remote sensing methods also help us to understand the distribution and proprieties of aerosols. Most satellite carried passive remote sensing devices that provide column-integration aerosol products like Aerosol Optical Depth (AOD). Sun photometer is another passive remote sensing instrument that can be used to infer wavelength-dependent optical and microphysical properties of aerosols from observing direct and diffuse solar radiation (Holben et al. 1998, 2001). The ground-based sun photometers aerosol network AERONET has provided a long-term, continuous, and readily accessible public domain database for aerosol research (Holben et al. 1998).

1.3.2 *In-situ* methods

Also *in-situ* measurements can provide an accurate and reliable dataset to characterize aerosol proprieties and atmospheric conditions. The aerosol parameters measured by *in-situ* instruments can be grouped into physical properties and chemical composition. The physical proprieties include aerosol concentration, size distribution, hygroscopicity, and optical proprieties etc. The aerosol concentration and size distribution can be measured by different aerosol sizers like Condensation Particle Counte (CPC), Scanning Mobility Particle Sizer (SMPS), Optical Particle Counter (Optical Particle Counter (OPC)), and Aerodynamic Particle Sizer (APS). Also, aerosol mass concentration can be measured by different gravimetric methods or mass spectrometers. The aerosol hygroscopicity can be measured by a Hygroscopicity Tandem Differential Mobility Analyzer (HTDMA) (Zardini et al. 2008). The optical proprieties can be determined e.g. by nephelometer (Moallemi et al. 2022), aethalometer, Fourier-Transform Infrared Spectroscopy (FTIR), photoacoustics (Lindberg et al. 2022). The chemical composition can be measured by mass spectrometry like Aerosol Mass Spectrometry (AMS) (Nash et al. 2006, Aljawhary et al. 2013, Jordan et al. 2009). Last but not least, weather sensors deployed in meteorological stations can provide information on heat, moisture, and momentum in the boundary layer (Gentine et al. 2016, Stull & Eloranta 1984). Finally, these *in-situ* instruments can also be deployed aboad of balloons, aircraft, or Unmanned Aerial Vehicle (UAV) to get vertical profiles of aerosols and atmospheric parameters (Greenberg et al. 1999, Neff et al. 2008, Reineman et al. 2016, Kim & Kwon 2019, Zhang et al. 2020, Lenschow 1986).

1.4 Aerosol and boundary layer modeling

Large Eddy Simulation (LES) is a mathematical model for turbulence used in computational fluid dynamics. It was initially proposed in 1963 by Joseph Smagorinsky to simulate atmospheric air currents (Smagorinsky 1963) and first explored by Deardorff (1970) (Deardorff 1970). LES is currently applied in a wide variety of engineering applications, including combustion (Pitsch 2006), acoustics (Wagner et al. 2007), and simulations of the atmospheric boundary layer (Sullivan et al. 1994). Advantage of LES models is the potentially high spatial resolution e.g. allowing predictions for individual street canyons with a resolution of 10 m or even 1 m (Stoll et al. 2020, Moeng & Wyngaard 1988).

Transport models can simulate the distribution and evolution of aerosol over the globe. Recently, various global and regional transport models have been developed and many of them can simulate the transport, transformation, and properties of aerosol particles. Examples of such models are the general circulation model the ECHAM-HAMMOZ (Pozzoli et al. 2008*a*,*b*), the ECHAM/MESSy Atmospheric Chemistry (EMAC) (Roeckner et al. 2006, Jöckel et al. 2006, 2010), the Whole Atmosphere Community Climate Model (WACCM) (Kunz et al. 2011, Smith et al. 2011), the Weather Research and Forecasting (WRF) model coupled with Chemistry (WRF/Chem) (Chapman et al. 2008), COsortium for Small-scale MOdeling (COSMO) and its extension on Aerosol and Reactive Trace gases (ART) (Vogel et al. 2014), and its successor the ICOsahedral Nonhydrostatic model (ICON) and its extension on Aerosol and Reactive Trace gases (ART) (Rieger et al. 2017*a*, Weimer et al. 2017). A special focus has been on mineral dust due to its strong impact on atmospheric radiative forcing (Stocker 2014). A three dimensional mineral dust model has been developed to study its impact on the radiative balance of the atmosphere (Tegen & Fung 1994). Recently, various models like Copernicus Atmosphere Monitoring Service (CAMS) (O'Sullivan et al. 2020), WRF/Chem (Kang et al. 2011) , EMAC (Gläser et al. 2012), COSMO-ART (Deetz et al. 2016, Vogel et al. 2014) and ICON-ART (Rieger et al. 2017*a*, Gasch et al. 2017, Hoshyaripour et al. 2019) have been used to predict mineral dust plumes. A multi-model forecast comparison is available by the Sand and Dust Storm Warning Advisory and Assessment System (WHO 2021), a program of the WMO. High-resolution spatial aerosol distributions are ideal data to validate the prediction of LES but also of global or regional transport models.

1.5 Synergistic methods for characterising boundary layer and aerosols

Recently, synergistic methods by combining remote sensing and *in-situ* measurement have been widely used in characterizing the boundary layer behavior and the distribution of aerosols within and above the boundary layer. For example, Kong & Yi (2015) investigated the relationship between the CBL and surface aerosol concentration in Wuhan using lidar and OPC and suggested that the seasonal behavior of the surface fine particle concentration mainly depends on the seasonal variation in available volume (determined by the Mixing Layer Height (MLH)) for aerosol dispersion. Cooper & Eichinger (1994) used lidar and radiosonde measurements to study the structure of the atmosphere in an urban Planetary Boundary Layer (PBL). de Arruda Moreira et al. (2018) compared PBL measured by microwave radiometer, elastic lidar, and Doppler lidar estimations in the Southern Iberian Peninsula. Lenschow et al. (2012) compared higher-order vertical velocity moments in the CBL from lidar with *in-situ* measurements and large-eddy simulation. Panahifar et al. (2020) monitored atmospheric particulate matters by using lidar, *in-situ* measurement, and satellite data over Tehran, Iran. Combination of these different methods increases the accuracy of information about the boundary structures and aerosol distributions.

For the mineral dust investigation, synergistic methods including ground-based, airborne, remote sensing, and numerical modeling have become important ways to better understand dust plume evolutions (Haarig et al. 2019, Papayannis et al. 2012, Perrone et al. 2004) and to optimize the models. Various studies characterized Saharan dust in the last decades either near the sources or during long-range transport. Freudenthaler et al. (2009) reported pure Saharan dust depolarization ratio profilings at several wavelengths during the Saharan Mineral Dust Experiment (SAMUM) 2006. Kanitz et al. (2014) observed Saharan dust with shipborne lidar from 60° to 20°W along 14.5°N. Soupiona et al. (2020) studied dust properties and their impact on radiative forcing over the northern Mediterranean region based on EARLINET observations. The three-dimensional evolution of Saharan dust transport towards Europe was studied based on a 9-year EARLINET-optimized Cloud-Aerosol Lidar and Infrared Pathfinder Satellite Observations (CALIPSO) dataset (Marinou et al. 2017). The CAMS forecast systems simulated the aerosol transport events over Europe during the 2017 storm Ophelia and validated these results with passive (Moderate Resolution Imaging Spectroradiometer (MODIS) aboard Terra and Aqua) and active (Cloud-Aerosol LIdar with Orthogonal Polarization (CALIOP)/CALIPSO) satellite sensors as well as ground-based

measurements (European Monitoring and Evaluation Programme (EMEP)) (Akritidis et al. 2020). Osborne et al. (2019) compared model simulations with ground-based remote sensing measurements (lidar and sun photometer network). A comparison of dust observations by lidar and BSC-DREAM8b model results was studied by Mona et al. (2014). In addition, intensive field campaigns such as SAMUM investigated the relationship between chemical composition, shape, morphology, size distribution, and optical properties of dust particles with an emphasis on vertical profiling of dust optical properties. The SAMUM experiment consists of two campaigns – SAMUM-1 and SAMUM-2. SAMUM-1 was mostly conducted at Ouarzazate (30.9° N, 6.9° W, 1133 m asl) and Tinfou near Zagora (30.24°N and 5.61°W about 730 m asl) in 2006 and SAMUM-2 was conducted at Praia (Sao Vicente island, Cape Verde, 14.9°N, 23.5°W, 75 m asl) in 2008 (Freudenthaler et al. 2009, Müller et al. 2010, Groß et al. 2011, Heintzenberg 2009, Petzold et al. 2009, Kandler et al. 2009). By these field campaigns, the chemical/mineralogical composition, microphysical characteristics, and optical properties of Saharan dust were studied. The chemical composition is beyond the scope of this thesis. Here we briefly summarize the latter two characteristics. On the African continent, particles with diameters significantly larger than 10 µm were observed e.g. during the SAMUM-1 study. However, in 80% of the cases, the measured particle diameters were below 40 µm. During SAMUM-2, the mean dust particle diameter was significantly smaller than during SAMUM-1 (Kandler et al. 2009, Weinzierl et al. 2009, Kandler et al. 2011). This phenomenon is related to that large particles were falling out of the plume during long-range transport and the observation station of SAMUM-2 is further away from the dust source region(Ansmann et al. 2011). The authors also found that Saharan dust particles observed during SAMUM–1 and SAMUM–2 were almost non-hygroscopic (Schladitz et al. 2011). In addition, the complex refractive index of pure dust (from 1.55 to 1.56 for real part but showing strong variations for imaginary part), the Single Scattering Albedo (SSA) at different wavelengths (0.91 at 450nm, 0.96 at 550 nm, and 0.98 at 950 nm), and the Ångström Exponent (AE) (around 0 for large dust particles) were obtained with remote sensing and airborne measurements (Petzold et al. 2009, Müller et al. 2010, Weinzierl et al. 2011).

1.6 Research objectives

As outlined above, the spatial-temporal distribution and the optical properties of aerosols are of great importance and reward dedicated research using advanced methods. Figure 1.5 shows the

research objectives and methods used in this thesis. For the urban background aerosol, most of the aerosol is accumulated within the boundary layer and their distribution is largely affected by meteorological parameters like wind and boundary layer evolution. The boundary layer structure and evolution have become key factors in understanding or explaining urban air pollution. Despite the large number of studies that have been done on the aerosol-boundary-layer interaction to date, at least three major questions are still unclear and remain to be addressed. One question is how the boundary layer influences the distribution of aerosol in complex topography areas. As the movement of airborne particles near the ground level is different from that in the free troposphere which is only influenced by pressure gradients and Coriolis force but also is affected by the friction force which is greatly influenced by surface topography. Furthermore, only few experimental studies characterized the evolution of the SBL. The stable boundary layer height is usually so shallow (tens of meters to hundreds of meters) that the traditional vertically pointed lidar can not get reliable measurements due to the overlap limits of lidars. Benefiting from the unique capabilities of a scanning aerosol lidar, I want to determine the stable boundary layer height evolutions and aerosol profiles close to ground level. Another important question is what is the role of clouds in the aerosol-boundary-layer interaction? In most previous research, the evolution of the boundary layer and its interaction with aerosol were studied under the clear sky without considering clouds. Hence, the effect of clouds on aerosol-boundary-layer interaction is still unclear until now.
For the long-distance transport of Saharan dust plumes, the optical proprieties and distributions determine their impact on radiative forcing. Employing a scanning aerosol lidar and new innovative methods, I want to reduce the uncertainties in corresponding lidar retrievals significantly. In addition, the comparison between observations and model simulations allows evaluation of the model performance e.g. based on observations of different characteristic Saharan dust plumes. These existing knowledge gaps in atmospheric aerosol and boundary layer research lead to my following main research questions:

1. What kind of additional information can we get from scanning aerosol lidar compared with vertically pointed lidar? How can this additional information help us better understand aerosol proprieties and boundary layer dynamics?

2. What is the structure of the boundary layer and how does the boundary layer influence the surface aerosol concentration in complex terrain regions and during the nocturnal period?

What is the role of clouds in aerosol-boundary-layer interaction?

3. How do the ICON-ART transport model and the PALM-4U LES model perform when compared with observational data? Can the observational data help to validate and improve model predictions?

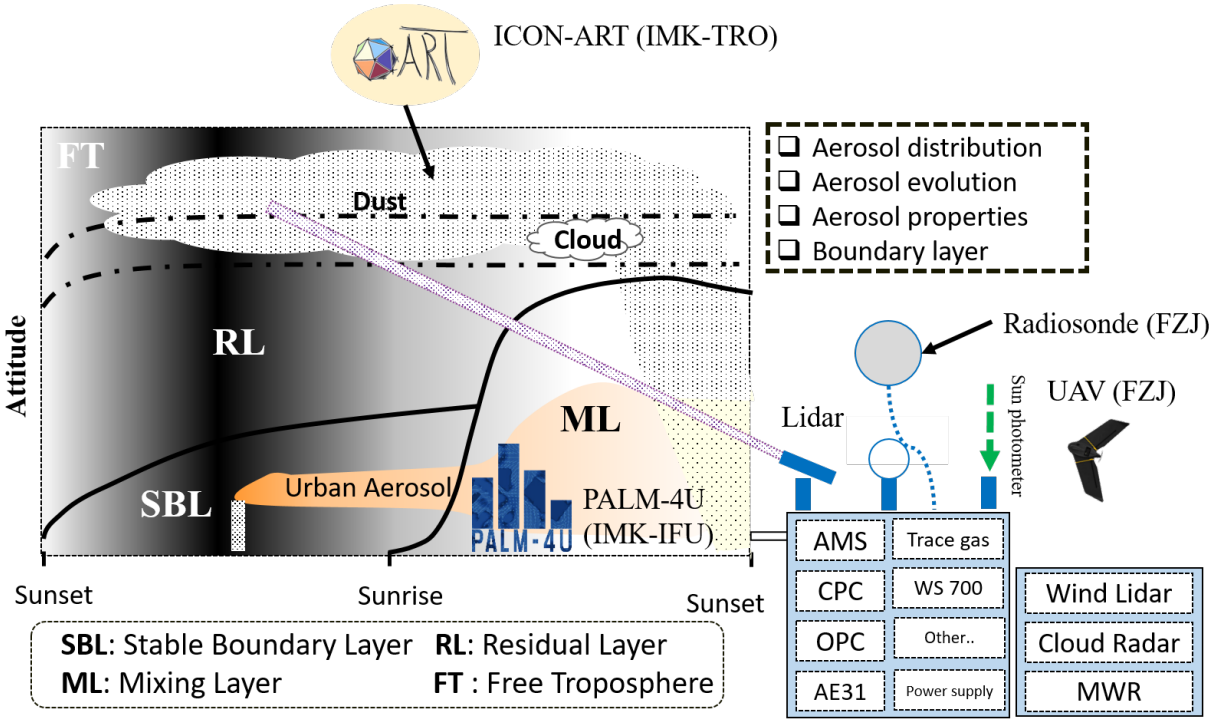

Figure 1.5: Schematic diagram of my research objectives, and methods (cf. chapter 2) modified based on Stull (1988). (Abbreviations: **SBL** - Stable Boundary Layer, **RL** - Residual Layer, **ML** - Mixing Layer, **FT** - Free Troposphere, **AMS** - Aerosol Mass Spectrometer, **CPC** - Condensation Particle Counter, **OPC** - Optical Particle Counter, **MWR** - Microwave Radiometer)

This thesis is organized as follows. Chapter 2 describes the methods used in this thesis including remote sensing, *in-situ* measurement, and model simulations. In section 3.1, the comparison of different retrieval software and the validation of lidar retrievals using *in-situ* measurement will be discussed. In section 3.2, I will discuss the boundary layer dynamics and related air quality during winter time in downtown Stuttgart by using a comprehensive dataset from scanning aerosol lidar and ground-level *in-situ* measurements. The boundary layer dynamics during summer will be discussed in section 3.3. The properties of Saharan dust plumes are discussed in section 3.4 employing observational data and ICON-ART modelling results. In the final chapter, I provide some conclusions and an outlook for my thesis.

2 Methodology

To achieve my research goals, I used the methods illustrated in Figure 1.5 to investigate the aerosol particle distributions and optical properties within and above the boundary layer. The scanning aerosol lidar called KArlsruhe SCanning Aerosol Lidar (KASCAL) that is usually deployed on the roof of a mobile container for the field campaigns but is also deployed at KIT campus-north which can measure spatial and temporal distributions of aerosol particles, cloud base heights, boundary layer heights, and aerosol particle optical properties. A mobile 16-feet container containing aerosol characterization instruments allows determination of aerosol chemical and physical properties including aerosol particle size distributions, aerosol chemical compositions, aerosol particle absorption coefficients, and different meteorological parameters (e.g. air temperature, air relative humidity, wind, solar radiation, and precipitation etc.). I could also make use of data from several instruments belonging to the KITcube of IMK-TRO. A wind lidar can provide vertical profiles of 3 dimension wind speed and the Microwave Radiometer (MWR) can provide vertical profiles of temperature and humidity. The cloud radar can measure cloud parameters including reflectivity factor, velocity, spectral width, and linear depolarization ratio. The sun photometer can measure column-integrated aerosol optical proprieties. In addition, the radiosonde balloon and UAV (both Forschungszentrum Jülich, FZJ) provide vertical profiles of aerosol and meteorological parameters. Finally, the transport model ICON-ART (IMK-TRO) can predict aerosol particle and trace gases as well as the structure and optical parameters of Saharan dust plumes. The LES model, PALM-4U, can simulate the wind flow, BLH, and aerosol distribution in the boundary layer with spatial resolution down to 1 m.

The scanning aerosol lidar is the main instrument I used for this thesis. I operated this lidar system, developed and validated retrieval software and analysed data from multiple field measurements. Other remote sensing dataset including wind lidar, cloud radar, and MWR was provided by KITcube (Dr. Jan Handwerker, IMK-TRO). The sun photometer dataset is from the AERONET website. The *in-situ* aerosol characterization instruments employed in a mobile container are operated by our research group (Dr. Harald Saathoff, IMK-AAF) and analysed for several cases by myself. The vertical profiles of *in-situ* measurements based on a radiosonde balloon and an UAV were provided by Dr. Christian Rolf and Dr. Ralf Tillman (both Forschungszentrum Jülich (FZJ)) , respectively.

The output simulated by the LES model (PALM-4U, developed by the Leibniz Universität Hannover) is provided by Dr. Christopher Claus Holst (IMK - IFU) and the Saharan dust predictions based on ICON-ART calculations were provided by the German Weather Service (DWD) and Dr. Heike Vogel and Dr. Gholamali Hoshyaripour (both IMK-TRO).

2.1 Remote sensing

2.1.1 3-D scanning aerosol LIDAR

All the experiments for this work were mainly carried out using the KASCAL (LR111-ESS-D200, Raymetrics Inc.). Figure 2.1 shows a picture of this lidar system and a photo taken during the Modular Observation Solution for Earth System (MOSES) campaign. The laser head, a 200 mm telescope, and the control unit are shown in this figure. The control unit includes a rotating platform that allows lidar scanning from $-7°$ to $90°$ for the zenith angle and from $0°$ to $360°$ for the azimuth angle. The photo on the right side of Figure 2.1 shows that the KASCAL was deployed on the roof of the aerosol container of IMK-AAF. The Wavelength Separation Unit (WSU) of KASCAL installed in the lidar head is shown in Figure 2.2, which indicates that KASCAL has an emission wavelength of 355 nm and is equipped with elastic, depolarization, and Raman channels, potentially providing profiles of extinction coefficients, backscatter coefficients, and depolarization ratios. The

Figure 2.1: The picture of KASCAL (left, provided by Raymetrics Inc.) and the photo of the lidar on the roof of a mobile container taken during the Swabian MOSES campaign in July 2021 (right, photo by Hengheng Zhang).

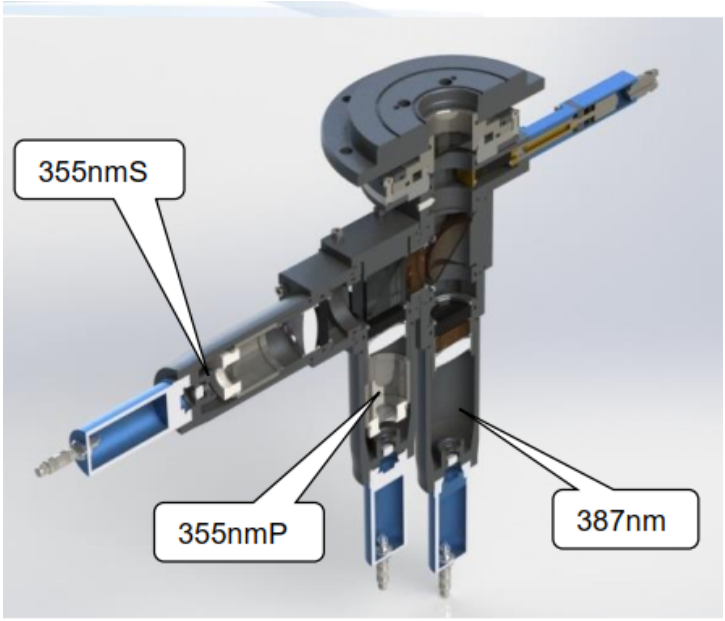

Figure 2.2: The Wavelength Separation Unit (WSU) of KASCAL. (Provided by Raymetrics Inc.)

laser pulse energy and repetition frequency are 32 mJ and 20 Hz, respectively. This KASCAL works automatically, time-controlled, and continuously via a software developed by Raymetrics. Detailed information can be found at the Raymetrics homepage (Raymatrics 2021) and reference literature (Avdikos 2015). For the data analysis and calibration of the system, I followed the quality standards of the EARLINET (Freudenthaler 2016). Extinction and backscatter coefficients at 355 nm were both calculated from the elastic channel using the Klett-Fernald method (Klett 1985*a*, Fernald 1984) and are also calculated from the elastic and Raman channels (Ansmann et al. 1992). The extinction coefficients and lidar ratios were also retrieved using a multi-angle method which is also called the ratio method in this thesis (Adam 2012, Gutkowicz-Krusin 1993).

The return signal recorded by a lidar system can be described by the lidar equation as follow:

$$P(r) = C_0 \frac{\beta_{aer}(r) + \beta_{mol}(r)}{r^2} \exp\left(-2 \int_0^r [\alpha_{aer}(r) + \alpha_{mol}(r)]\, dr\right) \tag{2.1}$$

Where P(r) is range-dependent lidar received power; C_0 is lidar constant; r is the distance from lidar; $\beta_{mol}(r)$ and $\alpha_{mol}(r)$ are the backscatter coefficient and extinction coefficient of the molecule, respectively; $\beta_{aer}(r)$ and $\alpha_{aer}(r)$ are the backscatter coefficient and extinction coefficient of aerosol, respectively. In any form of the equation 2.1 has two unknown quantities ($\beta_{aer}(r)$ and $\alpha_{aer}(r)$). This is an intrinsic problem of an elastic backscatter lidar. Several solutions (depending on different assumptions) have been proposed in previous literature in order to solve the lidar equation.

There are two commonly used methods to solve this problem. The first retrieval method was proposed by Klett (1981). In this method, the contribution of molecule backscatter and extinction were ignored and this method can be applied in very polluted environments. By using this assumption, we can get $\beta_{aer}(r) >> \beta_{mol}(r))$ and $\alpha_{aer}(r) >> \alpha_{mol}(r))$, so $\beta(r) \approx \beta_{aer}(r)$ and $\alpha(r) \approx \alpha_{aer}(r)$. Let $\alpha(r) = K\beta(r)$. The lidar equation can be written as follow.

$$P(r) * r^2 = C_0 * \frac{\alpha(r)}{K} \exp(-2 \int_0^r \alpha(r)dr) \tag{2.2}$$

After some mathematical operations, we can arrive the final solution as follow:

$$\alpha(r) = \frac{RCS(r)}{\frac{RCS(r_c)}{\alpha(r_c)} + 2\int_r^{r_c} RCS(r)dz} \tag{2.3}$$

Where $RCS(r) = P(r) * r^2$.

Another method which was proposed by Fernald (1984) considered separating the total backscatter and extinction into a molecular part and an aerosol particle part. In this method, two new variables ($S_a(r)$ and $S_m(r)$) are introduced. And let $\alpha_{aer}(r) = S_a(r) * \beta_{aer}(r)$ and $\alpha_{mol}(r) = S_m * \beta_{mol}$. By using these conditions, the lidar equation can be written as follow:

$$\frac{dS(r)}{dr} = \frac{1}{\beta(r)}\frac{\beta(r)}{dr} - 2 * [S_a(r) * \beta_{aer}(r) + S_m\beta_{mol}(r)] \tag{2.4}$$

where $S(r) = ln(P(r) * r^2)$, $\beta(r) = \beta_{aer}(r) + \beta_{mol}(r))$, After some mathematical operations, we can arrive the final solution as follow:

$$\beta(r) = \frac{RCS(r)e^{\int_0^r -2(S_a(r)-S_m)*\beta_{mol}(r')dr'}}{\frac{RCS(r_0)}{\beta(r_0)} - \int_0^r 2S_a(r) * RCS(r)e^{\int_0^r -2(S_a(r)-S_m)*\beta_{mol}(r'')dr''}dr'} \tag{2.5}$$

By comparing these two methods, we can conclude that the former method is an approximate solution that can be only applied in very polluted environments. Figure 2.3 shows a simulation result for both two methods. The three panels in this figure represent different air pollution levels with extinction coefficient increasing from left to right. From this figure, we can see that only in the very polluted environment (the right side of this figure), the former method can achieve a correct solution.

For a well-calibrated lidar system, the reference value $\frac{RCS(r_0)}{\beta(r_0)}$ can be replaced by the lidar constant.

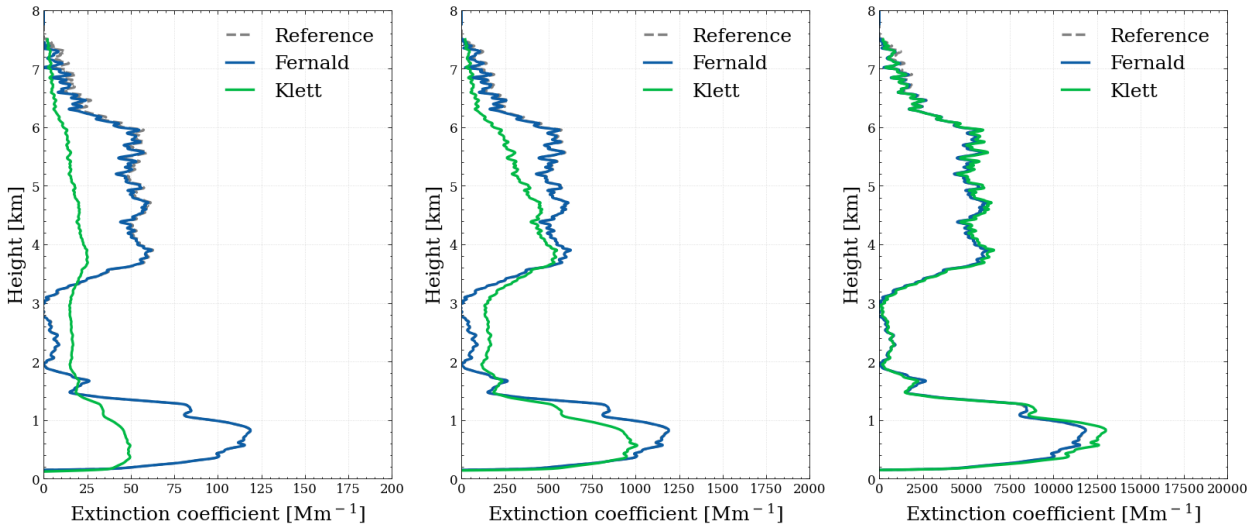

Figure 2.3: Simulation of backscatter coefficient for two elastic lidar retrieval methods proposed by Klett (1981) and Fernald (1984) for three different air pollution levels. (The legend is named after the first contributor. The Klett is the former method and Fernald is the later method.)

And the solution of the lidar equation can be written as:

$$\beta(r) = \frac{RCS(z)e^{\int_0^r -2(S_a(r)-S_m)*\beta_{mol}(r')dr'}}{C_0 - \int_0^r 2S_a(r) * RCS(z)e^{\int_0^r -2(S_a(r)-S_m)*\beta_{mol}(r'')dr''}dr'} \tag{2.6}$$

Where C_0 is the lidar constant. Equation 2.6 is also called the forward integration method in some literature. Compared with equation 2.5, equation 2.6 does not need any reference value if the lidar is well calibrated. However, equation 2.6 will cause unstable results sometime. Figure 2.4 shows the simulation result of the Fernald method using equation 2.6. This figure shows that equation 2.6 will cause unstable results at high altitudes, especially at short wavelengths. Since this unstable solution is wavelength-dependent, equation 2.6 is mainly used in ceilometer retrievals which have longer emission wavelengths in the infrared region. The full mathematical derivation of the lidar retrieval method is presented in Appendix B.1

Particle depolarization ratio, which represents sphericity of detected particles, is calculated based on lidar measurement as suggested by (Freudenthaler et al. 2009)

$$\delta^p = \frac{(1+\delta^m)\delta^v R - (1+\delta^v)\delta^m}{(1+\delta^m)R - (1+\delta^v)} \tag{2.7}$$

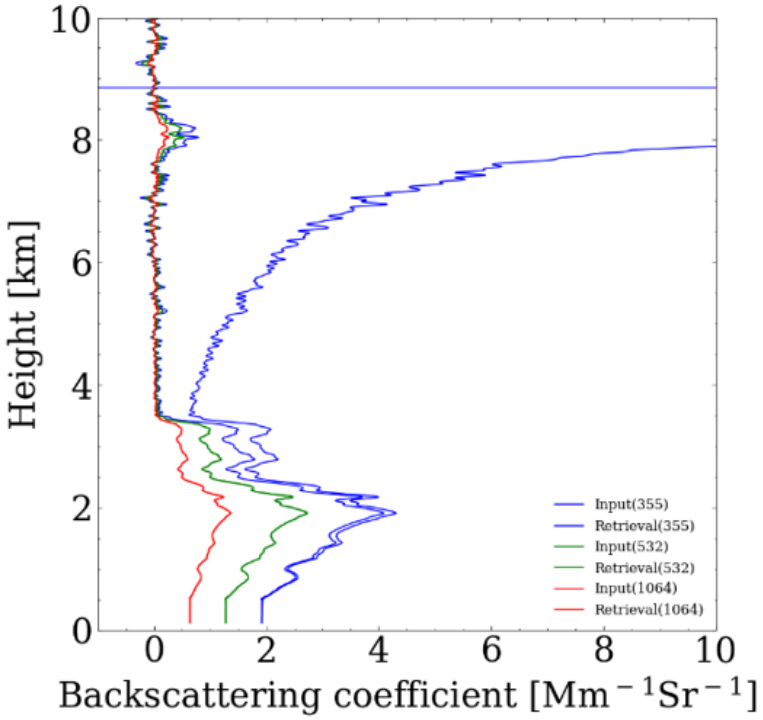

Figure 2.4: Backscatter coefficient retrieved from forward retrieval method (Equation 2.6) at three different wavelengths.

Here δ^m is the depolarization ratio of gas molecules, δ^v is the volume depolarization ratio and R is the backscatter ratio:

$$R = \frac{\beta^p + \beta^m}{\beta^m} \tag{2.8}$$

Here β^p is the backscatter coefficient of particles and β^m is the backscatter coefficient of molecules. δ^m can be calculated from the Rayleigh spectrum (Murphy 1977) and δ^v can be calculated from two cross polarization lidar signals for a well calibrated depolarization lidar system. The depolarization calibration includes two aspects: Polarization channel gain factor calibration and polarization cross-talk calibration for transmitted and reflected channels. Several depolarization methods have been proposed in recent years. For this thesis, I used the so-called "GHK" parameters depolarization calibration which were proposed by Freudenthaler (2016). In this method, the polarization channel gain factor is derived from $\pm 45°$ measurements. The cross-talk correction parameters are calculated from the optical parameters of the optical lens and their relative rotation by using the stoke vector and Mueller matrix. In this method, the δ^v can be expressed as follow:

$$\delta^v = \frac{\delta^*(G_T + H_T) - (G_R + H_R)}{(G_R - H_R) - \delta^*(G_T - H_T)} \tag{2.9}$$

Where the calibrated parameters, G_T, H_T, G_R, and H_R, are expressed as equation (59) of Freudenthaler (2016). And δ^* is the gain factor calibrated depolarization ratio which can be written as:

$$\delta^* = \frac{K}{\eta^*}\frac{I_R}{I_T}(0°, 90°) \tag{2.10}$$

Where K is the polarization calibration correction parameter and η^* is the gain factor.

$$\eta^* = \frac{I_R}{I_T}(\pm 45°) \tag{2.11}$$

The calibration process and the volume depolarization ratio for a Saharan case are shown in Figure 2.5. This Figure shows that the volume depolarization ratio equals to the molecule volume depolarization at the altitudes free of aerosol (the vertical orange line is the molecule volume depolarization), which reflects the good data quality of our lidar system in depolarization measurement.

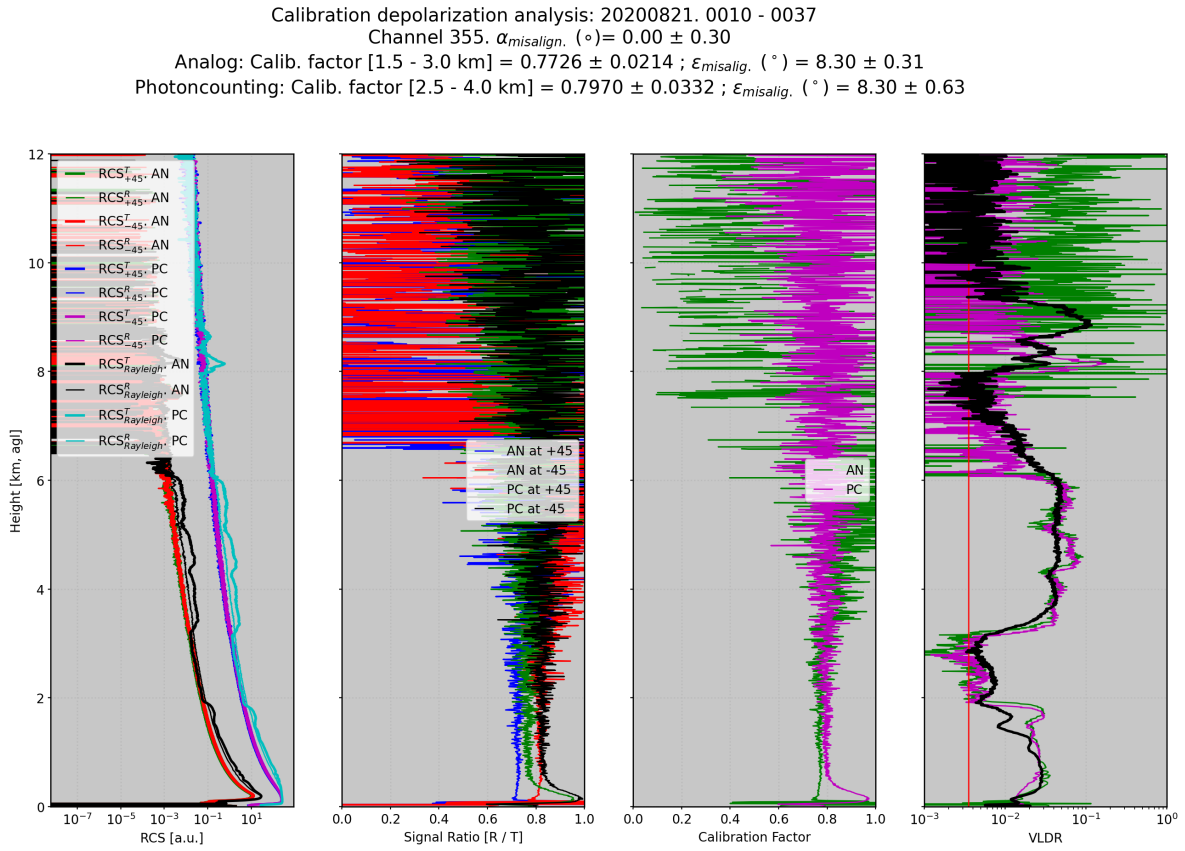

Figure 2.5: Depolarization calibration according to Freudenthaler (2016) based on data collected on 21^{st}, August 2020 and volume depolarization ratio for a Saharan dust case based on data collected on 8^{th}, April 2018.

The telescope cover test was performed with Raymetrics software to check the alignment between the laser beam and the telescope before each measurement. Rayleigh fitting was performed to check the lidar data quality. Figure 2.6 shows the Rayleigh fitting result. The profiles of molecular backscatter profiles as shown in the grey line are calculated from air temperature and air pressure measured by radiosonde. This figure shows that the measured backscatter is well consistent with molecular backscatter at altitudes above 10.0 km, which also reflects the good data quality of our lidar system.

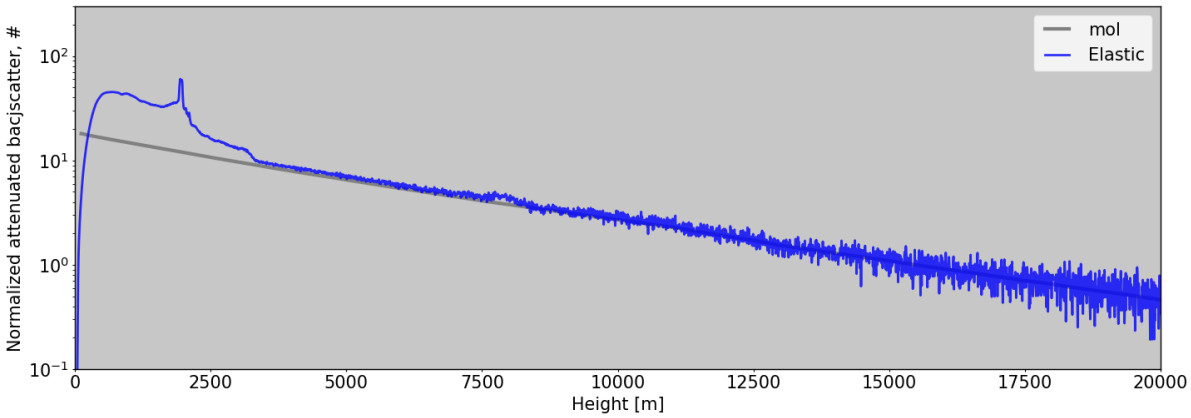

Figure 2.6: Rayleigh fitting of KASCAL elastic channel on July 12^{th}, 2018. The blue line is the range corrected lidar signal and the green line is the molecular backscattter coefficient calculated from air temperature and pressure measured by radiosonde sensors.

The atmospheric BLH was determined from lidar data by using the Haar Wavelet Transform (HWT) method (Pal et al. 2010*b*). The method is defined as

$$z_{HWT} = \max[w_f(a,b)] = \max \frac{1}{a} \int_{z_{min}}^{z^{max}} X(z) H(\frac{z-b}{a})\, dz \tag{2.12}$$

In which W_f is the covariance transformation value, $X(z)$ is the Range Corrected lidar Signal (RCS) defined as $X(z) = P(z) * z^2$, and $H(\frac{z-b}{a})$ is the Harr Wavelet function which is defined as followed:

$$H(\frac{z-b}{a}) = \begin{cases} 1 & b - \frac{a}{2} \leq z \leq b \\ -1 & b \leq z \leq b + \frac{a}{2} \\ 0 & \text{elsewhere} \end{cases} \tag{2.13}$$

The dilation a is tested and set to be 75 m for this work. Z_{min} and z_{max} are the lower and upper heights for the lidar signal profile, respectively.

2.1.2 Sun photometer

The sun photometer (CE-318, CIMEL) (Holben et al. 1998) measures solar radiance at 339, 379, 441, 501, 675, 869, 940, 1021, and 1638 nm. It was operated by different colleagues of the IMK-TRO. It allows the calculation of wavelength-dependent Aerosol Optical Depth (AOD). The sun photometer data can also be used to infer calculate other aerosol parameters (e.g. SSA, AE, Aerosol Size Distribution (ASD), and Complex Refractive Index (CRI) (Vermeulen et al. 2000, Sinyuk et al. 2020). The SSA is the ratio of the scattering coefficient to the extinction coefficient, which has a negative correlation with the absorption ability of the aerosol particles. Hence, this parameter can be used to characterize the scattering and absorption capability of the particles. The AE is a parameter that describes how optical depth typically depends on the wavelength of light. Typically, stronger wavelength dependence occurs when the sizes of particles are smaller than or equivalent to the incident wavelength. Hence, AE has a negative correlation with particle size. From clear sky measurements with the sun photometer, ASD between $0.05\,\mu m$ to $15\,\mu m$, the complex refractive index in the range 1.33 – 1.6 and 0.0005i – 0.5i (Dubovik & King 2000, Müller et al. 2010) can be derived. The sun photometer data I used in my work is available on the AERONET Homepage (NASA 2022) and I used typically level 2.0 data.

2.1.3 Satellite aerosol particle data

To investigate Saharan dust transport and optical properties, I used data from two satellites (Terra & Aqua). The MODIS instrument on these two satellites monitors the atmospheric aerosol optical thickness over the oceans with global coverage and also over a part of the continents. Furthermore, aerosol size distributions are derived over the oceans, and the aerosol types are derived over the continents. Daily Level 2 data are produced at the spatial resolution of a 10x10 km (at nadir)-pixel array. I used the MODIS data available on the corresponding NASA webpage (`https://modis.gsfc.nasa.gov/data/`).

2.1.4 Wind lidar

The measurement principle of a wind lidar relies on the Doppler shift of the laser when the laser interacts with the aerosol particles in the air. The WindCube v2 (Leoshpere a VAISALA company) measures wind speed with a Doppler Beam Swinging (DBS) technique (Rao et al. 2008), where an

optical switch is used to point the lidar beam in the four cardinal directions (north, east, south, and west) at an elevation angle of 62° from the ground. This allows to deduce vertical wind profiles of wind speed and direction, turbulence, and wind shear. Detailed information about the WindCube is available on the Vaisala homepage (Vaisal 2021). The wind lidar data like wind speeds and turbulence used in this thesis were provided by Dr. Jan Handwerker (IMK-TRO).

2.1.5 Microwave radiometer

The MWR, Humidity And Temperature PROfilers (HATPRO), was manufactured by Radiometer Physics GmbH (RPG), Germany as a network-suitable MWR with very accurate retrievals of Liquid Water Path (LWP) and Integrated Water Vapor (IWV) at high temporal resolution (1 s). The spectral characteristics of the instrument also make it possible to observe the temperature profile and to a limited extent also the humidity profile (Löhnert & Maier 2012). I used vertical profiles of humidity and temperature in this thesis. These data were provided by different colleagues from IMK-TRO who also operated the instrument.

2.1.6 Cloud radar

The cloud radar data used in this thesis is from a dual-frequency Frequency Modulated Continuous Wave (FMCW) dual-pol cloud radar with the operating frequency of 35 and 94 GHz (Görsdorf et al. 2015). Operation and data analysis for this cloud radar was done by the group of Dr. Jan Handwerker (IMK-TRO) for the Swabian MOSES campaign. This cloud radar can measure cloud reflectivity factor, cloud droplet speed, droplet spectrum width as well as cloud Linear Volume Depolarization Ratio (LVDR). The cloud radar used in this thesis is to investigate the aerosol-cloud interaction in combination with data from the aerosol lidar (KASCAL).

2.2 *In-situ* measurements

For the field campaign in Stuttgart (February 2018), Rottenburg (Swabian MOSES, June - August 2021), and Karlsruhe Mülldeponie West (July - August 2022), a mobile 16-feet container with different aerosol characterization instruments was deployed. These instruments allow determination of aerosol particle number, size, mass, absorption, and chemical composition. In addition as all major meteorological parameters were measured. For the winter campaign from February to March 2021 at the KIT campus north, these *in-situ* measurements were also deployed in the IMK-AAF

laboratory. These *in-situ* instruments were operated by colleagues in our research group.
These *in-situ* measurements can provide properties of aerosol particles (e.g. number & mass concentration, size distribution, chemical composition) that can be used for comparison with remote sensing measurements. Besides ground level *in-situ* measruements also *in-situ* measurements on a balloon and an UAV (drone) were used for this purpose.

2.2.1 Ground-based *in-situ* measurements

The ground *in-situ* measurements were mainly conducted in a mobile container. Ambient air temperature, air relative humidity, wind direction, wind speed, global radiation, pressure, and precipitation data were measured by a meteorological sensor (WS700, Lufft GmbH;). Trace gases (O_3, CO_2, NO_2, SO_2) were measured with commercial gas monitors. Particle number concentrations were recorded with two CPCs. Particle size distributions were measured with a SMPS, an OPC, and an APS. BC concentrations and absorption were measured with aethalometers. A high-resolution time-of-flight aerosol mass spectrometer equipped with an aerodynamic high-pressure lens (Williams et al. 2014) was deployed to continuously measure total non-refractory particle mass as a function of size (up to 2.5 µm particle aerodynamic diameter) at a time resolution of 0.5 min. A brief introduction to these *in-situ* measurements is given below:

Gas monitors: Trace gas were regularly measured via a Fluorinated Ethylene Polypropylene copolymer (FEP) sampling tube with different gas monitors including carbon dioxide (CO_2, NGA200, Rosemount Inc), ozone(O_3, O341M, Environment SA), nitrogen dioxide (NO_2, AS32M, Environment SA), and sulfur dioxide (SO_2, AF22M, Environment SA). Operation and data analysis of these gas monitors were performed by Dr. Harald Saathoff (IMK-AAF) proving the time series of their concentrations.

Condensation particle counter (CPC): Particle number concentration were measured regularly by two CPCs (CPC 3022A and CPC 3776, TSI Inc.) with 1-butanol as a working fluid. The CPC3776 and CPC3022A measured the total number concentration of particle diameter $\geq$ 2.5 nm and $\geq$ 7 nm, respectively. Both CPCs collected the data every second. This data was averaged over 10 minutes for further analysis. Operation and data analysis of these CPCs was performed by Dr. Harald Saathoff (IMK-AAF).

Scanning Mobility Particle Sizer(SMPS): The SMPS was used to measure the particle size distributions, which consists of a Different Mobility Analyzer (DMA) (TSI 3080, TSI Inc.) and a

CPC (CPC3010). The SMPS collected a size distribution every 7 minutes covering the size range of 13.6-700 nm. I used the SMPS data measured in the Swabian MOSES campaign, which was performed by Dr. Franziska Vogel and Alexander Böhmländer (IMK-AAF).

Optical particle counter (OPC): The OPC (Fidas 200, Palas Inc.) used in this thesis continuously measures particles in the size range of 0.18 - 18 µm. The OPC used Lorenz-Mie scattering theory to determine the particle number size distributions. From this it calculates the total particle mass concentrations and also the mass concentration of PM_1, $PM_{2.5}$, and PM_{10}. Fidas200 was operated with a flow rate of 5 L/min and with a time resolution of 1 s. Operation and data analysis of this Fidas200 OPC was performed by Dr. Harald Saathoff (IMK-AAF).

Aerodynamic particle sizer (APS): The APS (TSI3321, TSI Inc.) measured aerodynamic particle size distribution in the size range 0.5 µm-20µm. The APS spectrometer uses a patented, double-crest optical system. It also includes a redesigned nozzle configuration and improved signal processing. Operation and data analysis of this APS was performed by Dr. Franziska Vogel and Alexander Böhmländer (both IMK-AAF).

Aethalometers: BC was measured by aethalometers (Alas et al. 2020) including an AE51, a MA200 (AethLabs Inc.), and an AE33 (Magee Scientific Inc.). The AE51 draws ambient air on a quartz filter-based strip which then measures BC using a single 880 nm LED. The flow rate of AE51 was set at 100 mL/min to collect data every 5 minutes. MA200 can continuously collect aerosol particles on a filter tape and measures the Aerosol Optical Attenuation (ATN) at five wavelengths (375, 470, 528, 625, and 880 nm). MA200 was operated with a flow rate of 150 mL/min and a time resolution of 5 minutes. AE33 is a dual-spot aethalometer and measured the aerosol light absorption at seven wavelengths (370,480,520,590,660, 880, and 950 nm). AE33 was operated with a flow rate of 5 L/min and a time resolution of 1 minute. The mass of particles that absorb light at 880 nm for MA200 and AE33 is considered to represent BC. Operations and data analysis of these aethalometers were performed by Feng Jiang and Dr. Harald Saathoff (both IMK-AAF).

Aerosol mass spectrometry (AMS): The AMS (Aerodyne Inc.) is a powerful instrument for online measurement of the size-resolved (0.07-2.5µm) chemical composition of non-refractory aerosol particles including total Organic Aerosol (OA) and inorganic species Sulfate (SO_4), Nitrate (NO_3), and Ammonium (NH_4). The AMS inlet was connected to a $PM_{2.5}$ head (flow rate 1 m^3 h^{-1}; Comde-Derenda GmbH) and a stainless-steel tube of 3.45 m length (flow rate 0.1 L min^{-1} residence time 0.9 s.). AMS data were analyzed with the AMS data analysis software packages SQUIRREL (ver-

sion 1.60C) and PIKA (version 1.20C)(Huang et al. 2019). Operation and data analysis of the AMS during the Stuttgart campaign was performed by Dr. Wei Huang and Dr. Harald Saathoff (IMK-AAF).

2.2.2 UAV and balloon-borne *in-situ* measurements

The UAV data used in this thesis is from an eBee plus drone (SenseFly Inc.) which is operated by Dr. Ralf Tillmann of the Institute of Energy and Climate Research - Troposphere (IEK-8), FZJ. The particle sizer and meteorological sensors were mounted inside the UAV. The size-dependent particulate matter was measured in real-time with a time resolution of 1 s by OPC-N3 (Alphasense, Inc). Additionally, atmospheric parameters such as air temperature (T), air pressure (P), relative humidity (RH), wind speed (WS), and wind direction (WD) was measured with the same temporal resolution as particle matter up to the altitudes of about 1400 m. The UAV was launched from early morning to late afternoon for 3 days (9^{th}, 10^{th}, and 12^{th}, July 2018) in this experiment to study the boundary layer behavior and to determine vertical profiles of atmospheric aerosol particles in and above the boundary layer.

The radiosonde balloon was operated by Dr. Christian Rolf of the Institute of Energy and Climate Research - Stratosphere (IEK-7), FZJ. A Compact Optical Backscatter Aerosol Detector (COBALD) backscatter sensor and weather sensors were mounted on this balloon that measured the backscatter ratio and atmospheric parameters with the temporal and spatial resolution of 1 s and around 5 m/s, respectively. The COBALD is a lightweight (500 g) aerosol backscatter detector for balloon-borne measurements developed at ETH Zürich, based on the original prototype by Rosen & Kjome (1991). Using two Light-Emitting Diodes (LEDs) as light sources and a photodiode detector with Field Of View (FOV) of 6°, COBALD provides high-precision *in-situ* measurements of aerosol backscatter at wavelengths of 455 nm (blue visible) and 940 nm (infrared). COBALD was originally developed for the observation of high-altitude clouds, such as cirrus (Brabec et al. 2012, Cirisan et al. 2014) and polar stratospheric clouds (Engel et al. 2014), while recently it was proven able to detect and characterize aerosol layers in the upper troposphere–lower stratosphere (Vernier et al. 2015, 2018, Brunamonti et al. 2018). In this work, we compared COBALD measurements with scanning aerosol lidar measurements for the analysis of boundary layer and lower-tropospheric aerosols. For the comparison between COBALD and lidar measurement, the FOV correction is conducted according to Brunamonti et al. (2021*a*) due to different FOVs between li-

dar and COBALD.

In addition, I also used the radiosondes data at Schnarrenberg meteorological station (9.2008° E, 48.8292° N, 314 m above sea level) during the Stuttgart field campaign as provided by DWD. These data were used to determine BLHs for comparison with those values retrieved from lidar measurements. These radiosonde data were analysed for boundary layer heights by Dr. Olga Kiseleva (IMK-TRO).

2.3 Modelling

2.3.1 Large eddy simulation (PALM-4U)

The model PALM-4U is a large eddy simulation model developed by the Leibniz Universität Hannover based on the non-hydrostatic, filtered, incompressible Navier-Stokes equations in Boussinesq-approximated form (an anelastic approximation is available as an option for simulating deep convection). PALM-4U is frequently referred to as a separate model for the simulation of urban atmospheric boundary layers. However, from a technical point of view, PALM-4U are special components that have been developed to suit the needs of modern academic urban boundary layer research and practical city planning related to the urban microclimate and climate change. PALM-4U components are shipped with PALM and are available after installation of PALM. PALM-4U components are thus also available in PALM and might be used without being limited to urban area applications (Pfafferott et al. 2021, Steuri et al. 2020). The PALM-4U model used in this thesis is to simulate the wind flow and aerosol distribution within the boundary layer to compare with observations in the city of Stuttgart. The PALM-4U results used for comparison with my observations were provided by Dr. Christopher Holst (IMK-IFU).

2.3.2 Dust transport modeling (ICON-ART)

For predicting Saharan dust transport and distribution the online-coupled model system ICON-ART (Rieger et al. 2015, 2017*b*) was used. ICON is a weather and climate model that solves the full three-dimensional non-hydrostatic and compressible Navier–Stokes equations on an icosahedral grid (Zängl et al. 2015). The ART module is an extension of ICON to include the life cycle and cloud/radiation feedback of aerosols and trace gases. Mineral dust in ART is represented by three lognormal modes with mass median diameters of 1.5, 6.7, and 14.2 µm, and standard deviations

of 1.7, 1.6, and 1.5, respectively. The dust emission scheme is based on (Vogel et al. 2006) and (Rieger et al. 2017*b*) that considers the soil properties (size distribution, residual soil moisture), the soil dispersion state and soil type heterogeneity. The dust removal processes include sedimentation, dry, and wet deposition. The simulations are performed on a global domain including a regional nest (over north Africa and Europe) with horizontal resolutions of 40 and 20 km, respectively.ICON-ART model calculations were provided for my work by Dr. Gholamali Hoshyaripour and Dr. Heike Vogel (both IMK-TRO, KIT). In addition to the ICON-ART transport model, the HYbrid Single-Particle Lagrangian Integrated Trajectory (HYSPLIT) model developed by National Oceanic and Atmospheric Administration (NOAA) Air Resources Laboratory (Stein et al. 2015) was used to generate seven-day back-trajectories with an arrival altitude from 500 m to 7500 m with an interval of 1000 m to investigate the sources and transport of Saharan dust plumes. I calculated the back-trajectories using the HYSPLIT python package - Pyhsplit (Cross 2015) developed by the NOAA Air Resources Laboratory.

2.4 Field campaigns

During my Ph.D. study, I analyzed data of seven field campaigns. I did lidar measurements in four of these campaigns and for three of them the measurement were conducted by Dr. Harald Saathoff (IMK-AAF). Based on my research proposal, I classified these fieldcampaigns into 2 groups: Urban and rural aerosol observations, and Saharan dust studies. The observation sites of these field campaigns are shown in Figure 2.7 and photos taken during these field campaigns are shown in Figure 2.8. Detailed information on each field campaign with the research topics and my contributions are summarized in Table 2.1.

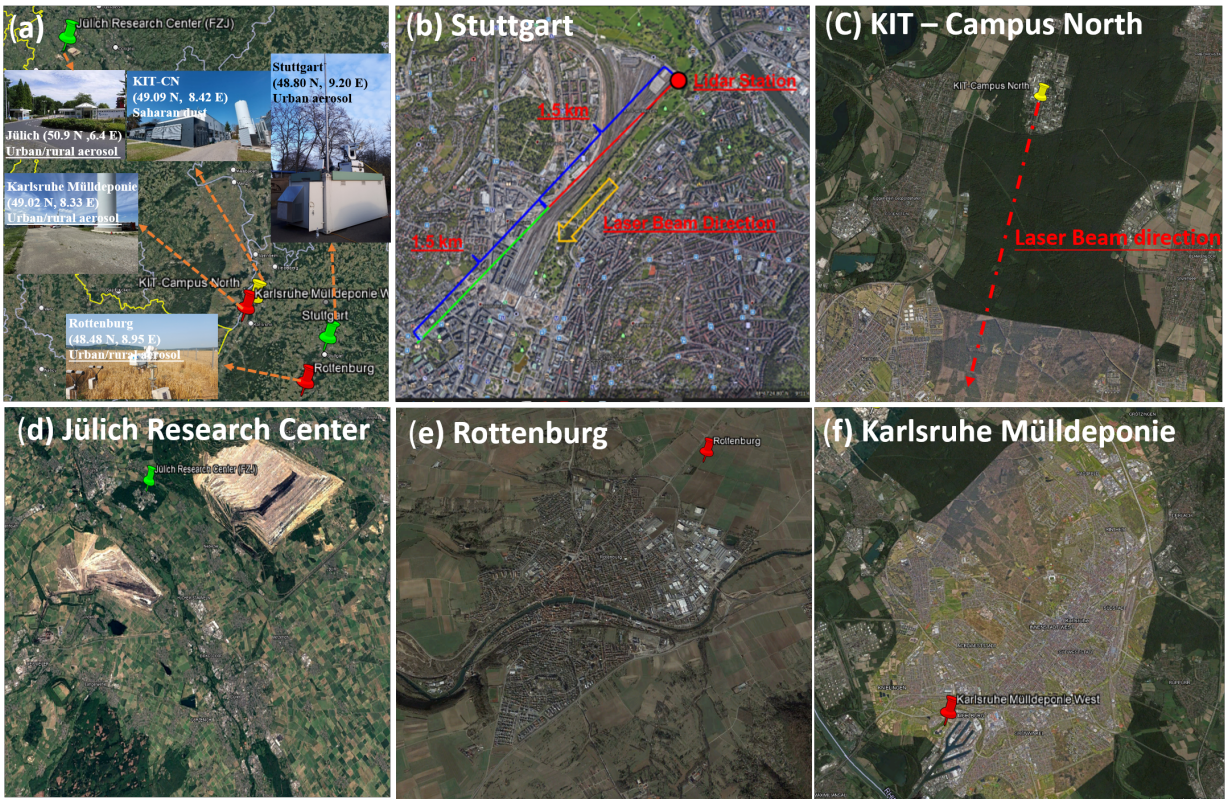

Figure 2.7: (a) Map of observation sites for all field campaigns, Map of Stuttgart (b), KIT-Campus North (c), Jülich Research Center (d), Rottenburg (e), and Karlsruhe Mülldeponie West (f). (The red markers in panel(a) represent the field campaigns that I participated in and the green markers represent the campaigns that I did not participate in. The yellow marker represents that there were 3 campaigns but I only participated in 2 of them in February, 2021 and March, 2022.)

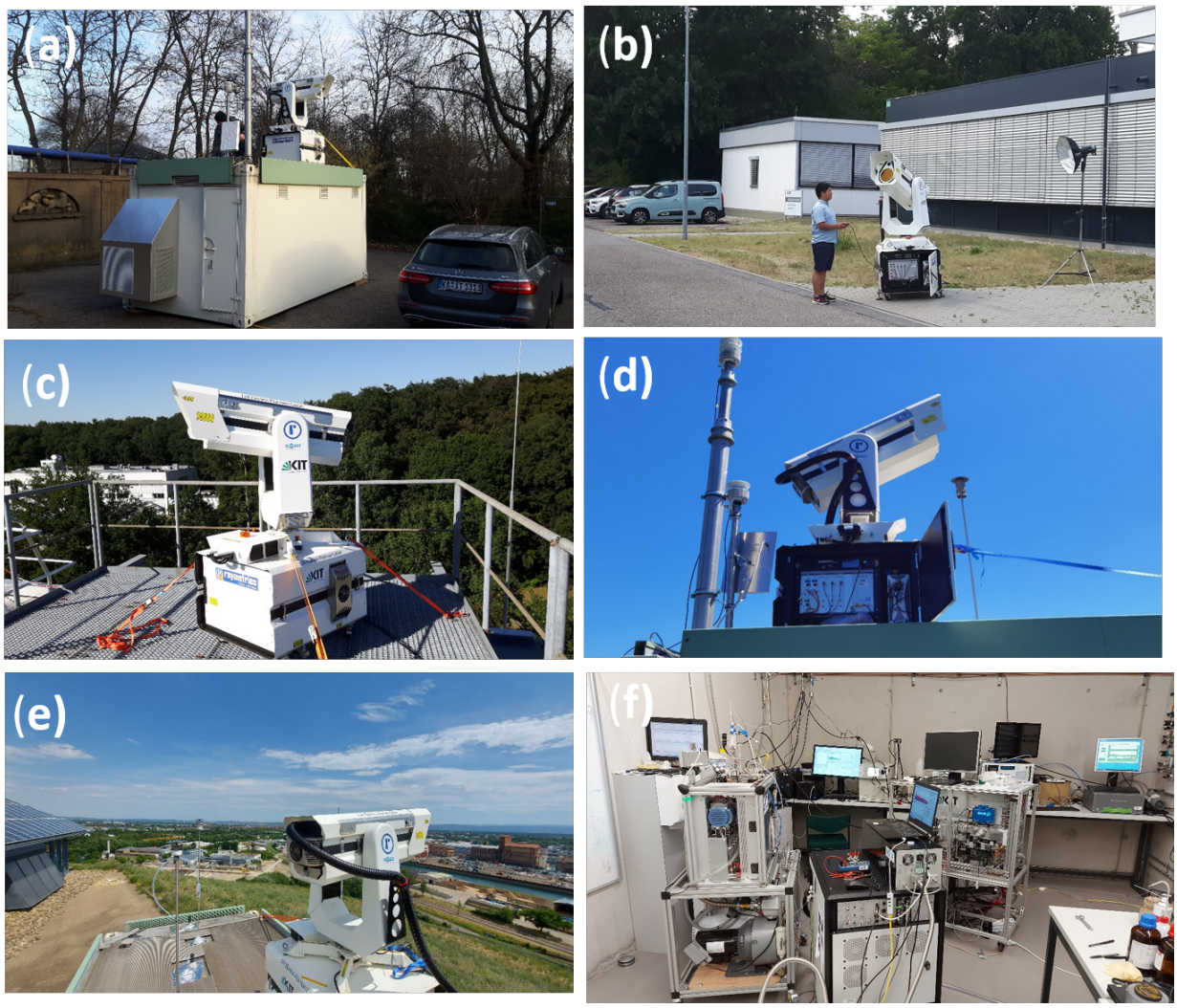

Figure 2.8: Photos of the lidar during the field campaigns in Stuttgart (a, Photo: H. Saathoff, 02.2018), KIT-Campus North (b, Photo: KIT photographer, 08.2020), Jülich Research Center (c, Photo: H. Saathoff, 07.2018), Rottenburg (d, Photo: H. Zhang, 06.2021), and Karlsruhe Müllde-ponie West (e, Photo: H. Zhang, 07.2022) as well as the main *in-situ* instruments used in this thesis.(f, Photo: H. Saathoff, 02.2021).

.

2.4.1 Urban and rural aerosol observations

Stuttgart urban: The aerosol composition, boundary layer dynamics, and air quality were investigated in Stuttgart by two field campaigns which were conducted in the summer of 2017 (Stuttgart 01) and winter of 2018 (Stuttgart urban) but only for Stuttgart urban the KASCAL was available. The observation site was in the urban background, the Rosenstein park in downtown Stuttgart (9.2024° E 48.7986° N, 247 m above sea level). The city of Stuttgart is a big industrialized city located in southwest Germany with a population of more than 630000 in a metropolitan area of 2.6

Table 2.1: Field Campaign with the research topics, my contributions, and tentative publications.

Name	Time	Research topic	Contribution	Results
Stuttgart urban	Feb.-Mar. 2018	Characterize boundary layer dynamic and aerosol evolution in the downtown of Stuttgart	Data analysis	First-author paper (in preparation)
Jülich MOSES	Jul. 2018	Characterize vertical aerosol profiles with remote sensing and *in-situ* methods	Data analysis	First-author paper (in preparation)
Swabian MOSES	Jun.-Aug. 2021	Investigate aerosol-cloud interaction and Saharan dust plumes	Operated KASCAL and data analysis	Co-author papers (Kunz et.al., 2022, others in preparation)
Karlsruhe	Jul.- Aug. 2022	Characterize industrial emission and urban boundary layer dynamics.	Operated KASCAL and data analysis	Analysis ongoing
Saharan Dust18	Apr. 2018	Characterize Saharan dust plume and validate the dust transport model	Data analysis	First-author paper (Zhang et.al., 2022)
Saharan Dust21	Feb.-Mar. 2021	Characterize Saharan dust plume and validate the dust transport model	Operated KASCAL and data analysis	
Saharan Dust22	Mar. 2022	Characterize Saharan dust plume and validate the dust transport model	Operated KASCAL and data analysis	First-author paper (All Saharan Dust cases, In preparation)

million inhabitants. Stuttgart is located in the valley of the Neckar river, in a "bowl" surrounded by a variety of hills, small mountains, and valleys. The complex topography can prevent the dispersion of air pollutants, and the location is characterized by low wind speeds and weak air circulation (Schwartz et al. 1991, Hebbert et al. 2012). Air quality has been a long-standing concern in Stuttgart, as it is one of the most polluted cities in Germany (Schwartz et al. 1991, Zeitung 2016, for Environmental Protection 2016); however, few detailed studies are available. For the year 2017, the state environmental protection agency, Landesanstalt für Umwelt Baden-Württemberg (LUBW), attributed 58 % of the annual mean PM_{10} at their monitoring station "Am Neckartor" in downtown Stuttgart to road traffic (45% abrasion, 7% exhaust, 6% secondary formation), 8% to small and medium-sized combustion sources, and 27 % to regional background (LUBW 2019). Mayer

(1999) showed the temporal variability of urban air pollutants (NO, NO_2, O_3, and O_x (sum of NO_2 and O_3)) caused by motor traffic in Stuttgart based on more than 10 years of observations, with higher NO concentrations in winter and higher O_x concentrations in summer. Figure 2.9 shows the seasonal average of PM_{10} in four LUBW monitoring stations and the average values of these four stations in Stuttgart from 2011 to 2021. This figure shows that the concentration of PM_{10} is highest in winter (December, January, and February) and the monitoring station "Am Neckartor" in downtown Stuttgart shows the highest concentrations compared with other monitoring stations. Hence, a detailed study on aerosol evolution and its related boundary dynamics in downtown Stuttgart during winter can help to better understand the air quality in Stuttgart and potentially help to improve air quality in this area. This field campaign was conducted from February 5^{th} to March 5^{th},

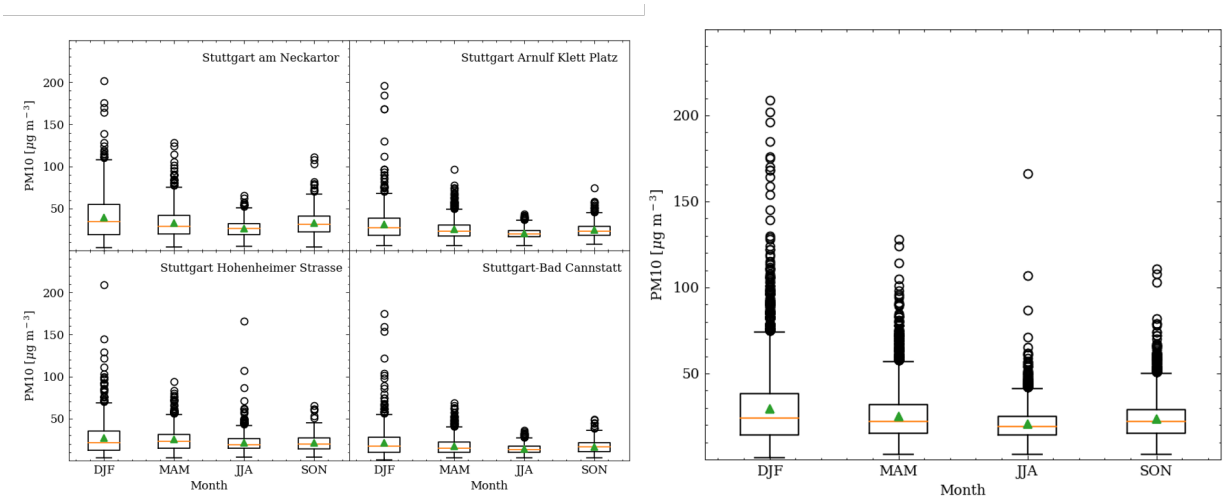

Figure 2.9: Seasonal average of PM_{10} measured in four Landesanstalt für Umwelt Baden-Württemberg (LUBW) monitoring stations in Stuttgart (left) and the average of those four stations (right) for ten years data from 2011 to 2021.

2018, with the KASCAL on the roof of a mobile 16-feet container. The measurement container carried different aerosol characterization instruments including AMS, Fidas200, and meteorological sensors to measure the aerosol chemical composition, aerosol size distribution, and atmospheric parameter. The container was installed on a railway bridge in the Rosensteinpark (RSP, 247 m asl). In addition, radiosondes launched at Schnarrenberg (SB, 321 m asl) by DWD provided vertically resolved meteorological parameters. A wind lidar and a microwave radiometer at the Town hall (TH, 275m asl) measured vertically resolved wind and temperature, respectively. Besides, a LES model, PLAM-4U, was used to simulate the vertical and horizontal airflow as well as the aerosol concentrations in this area (Pfafferott et al. 2021, Steuri et al. 2020). The location of Rosenstein-

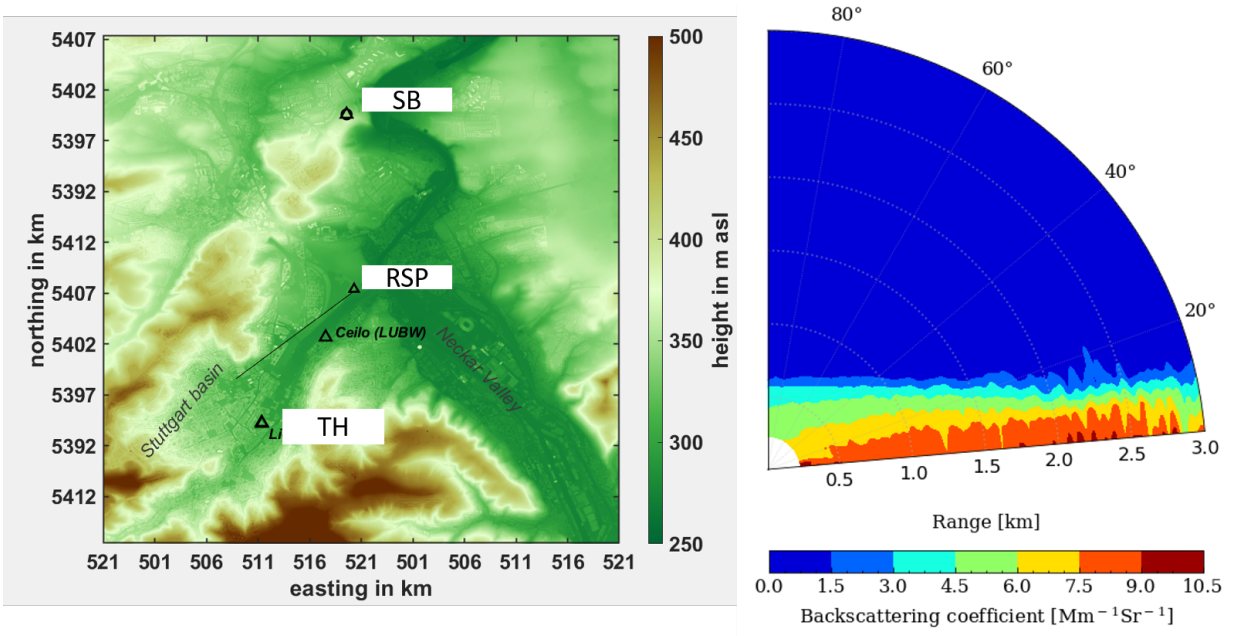

Figure 2.10: Left: The terrain of the research area surrounding Stuttgart and the observation sites during the winter campaign of 2018 in Stuttgart. Right: Example of zenith scanning measurement during Stuttgart urban field campaign in the downtown Stuttgart on 14^{th} February 2018.

park (RSP), Schnarrenberg (SB), and Town hall (TH) is indicated in the left side of Figure 2.10. In addition, the KASCAL did zenith scanning measurement with elevation angle from 90° to 5° with the step of 5°. The lidar beam direction is shown in Figure 2.7b. There are 19 profiles for each scanning plane and 1000 laser shoots (50 s) for each profile. The example of zenith scanning measurement is shown in the right side of Figure 2.10, which illustrates the spatial distribution and the concentration of aerosol within the boundary layer. The methods used in this field campaign are summarized in Table 2.2. Finally, the boundary layer heights were both retrieved from lidar and radiosonde measurements and compared with those from ECMWF Reanalysis v5 (ERA5). During my Ph.D. study, I analyzed the dataset collected by the above methods in this campaign and investigated the urban boundary layer and aerosol evolution in Stuttgart. Detailed results of this campaign are presented in section 3.2.

Table 2.2: List of methods used in Stuttgart urban field campaign.

Method	Main parameter
KASCAL	Aerosol backscatter, N_2 Raman, depolarization at 355 nm
AMS	Particle composition, Non-refractory species, e.g. organics, inorganics, 70 nm - 2.5 µm
Particle sizer and counter	Aerosol particle number, size
Gas monitors	Trace gases: O_3, NO, NO_2, CO_2, SO_2, NH_3
Lufft WS800	Meteorological parameters
radiosonde	Vertical profiles of meteorological parameters
MWR	Vertical profiles of temperature and humidity
Wind lidar (Wind cube WLS8)	3D wind vectors
PALM-4U	Simulation of wind flow and PM2.5

Jülich MOSES: The Jülich MOSES campaign was conducted in the Forschungszentrum Jülich, FZJ (6.4131 °E, 50.9084 °N, 110 m above sea level) near the city of Jülich from July 5^{th} to July 12^{th}, 2018 in frame of the MOSES project. In this field campaign, a comprehensive dataset was collected including remote sensing by a a scanning lidar and vertical *in-situ* measurements. An optical particle counter OPC (OPC-N3, Alphasensor Inc.) on an UAV flying up to 1400 m a.s.l. altitude, and a COBALD backscatter sonde aboard a balloon flying up to the stratosphere were used to investigate the vertical distribution of aerosol particles within and above the boundary layer. The UAV borne OPC measurements provides vertical profiles of atmospheric parameters from ground to about 1400 m a.s.l., which can be used to determine the vertical profiles of aerosol particles within the boundary layer as well as the boundary layer evolution in the morning hours. The COBALD aboard the balloon measured particle backscatter during one flight at wavelengths of 455 nm and 940 nm as well as atmospheric parameters, which can be used to validate lidar retrieval. The balloon was launched in the middle of the night. In addition, KASCAL did zenith and horizontal scans to determine temporal and spatial distributions of aerosol particles. For zenith scans, the elevation angle varied from 90° to 5° with step of 5° at two azimuth angle at 110° and 290°, respectively. The zenith scanning plane is similar to the measurements in Stuttgart as shown in the right side of Figure 2.10. For Azimuth scans, the azimuth angle varied from 110° to 290° with the elevation angle being 5°. The zero-degree azimuth angle is indicated as a red arrow dash line as shown in 2.11. This picture also shows a case of horizontal aerosol distributions around the

observation site. The methods used in this field campaign are summarized in Table 2.3. During my Ph.D. study, I analyzed the dataset collected by the above methods during this campaign and investigated boundary layer evolution and vertical aerosol distributions during a heat wave period. Detailed results of this campaign are presented in section 3.1.

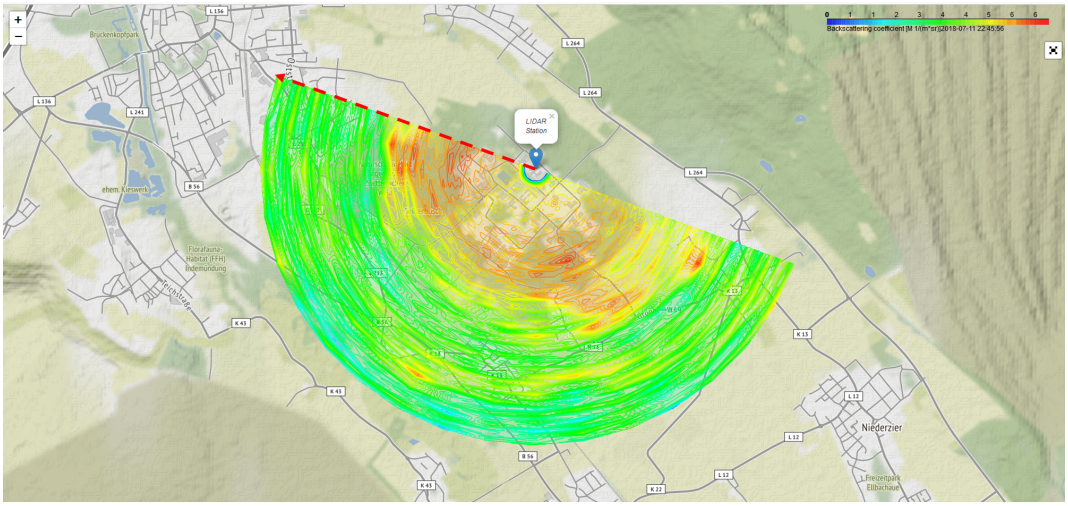

Figure 2.11: Polar map of horizontal backscatter coefficients measured by KASCAL on 11^{th}, July 2018 as well as the location of the observation site on the roof of the IEK7 building at FZJ.

Table 2.3: List of methods used in Jülich MOSES field campaign.

Platform	Instruments	Main parameter
Ground-based	KASCAL	Aerosol backscatter, N_2 Raman, depolarization at 355 nm
UAV	OPC-N3	vertical profiles of Aerosol particle size
	Meteorological sensor	Vertical profiles of meteorological parameters
Balloon radionsonde	COBALD	Vertical profiles aerosol backscatter at 2 wavelengths (455 & 940 nm)
	Meteorological sensor	Vertical profiles of meteorological parameters

Swabian MOSES: The Swabian MOSES field campaign was condicuted in Rottenburg (48.4892° N, 8.95452° E 339 m a.s.l.). This field campaign is an interdisciplinary field campaign to investigate thunderstorms and the associated event chains (Kunz et al. 2022) in the Neckar Valley and the Swabian Jura, southwest Germany. Seven intensive operation eriods Intensive Observation Periods (IOPs) were conducted with a total of 21 operating days as shown in Table 2.4 and the light

Table 2.4: Overview of all Swabian MOSES IOPs and each IOP started at 00:00 and ended at 23:59 UTC. Radiosondes (RS), payloads (PL), swarmsondes (Sw), the cosmic ray rover (CRR), water samplers (WS), aircrafts (Air), and aerosol filter probes (AFP) were used for additional observations. (The light green shaded rows indicate the Intensive Observation Periods (IOPs) that KASCAL participated in.)

	Dates	**Weather regime**	**Precipitation**	**Convection**	**Characteristics**	**Additional observations**
IOP1	10 May	Atlantic Trough	Mostly dry	Stratiform large scale lifting	Test IOP	RS, CRR
IOP2	2-5 June	European Blocking	Heavy rain	Isolated, unorganized, 6 km to 9 km high	Flooding near Stuttgart	RS, CRR
IOP3	9-10 June	Zonal regime	Heavy rain	Isolated, unorganized, >10 km high	Small local floodings, overshooting top event	RS, PL, WS
IOP4	17-24 June	European Blocking	Heavy rain, hail	Organized, >10 km high	Super cell passes Rottenburg, Saharan dust	RS, Sw, PL, CRR, WS, Air, AFP
IOP5	28-30 June	European Blocking	Heavy rain, hail	Unorganized and line organized, >10 km high	Heavy run-offs Ammer/ Steinlach, Cell initiation	RS, Sw, PL, CRR, WS, Air, AFP
IOP6	12-13 July	Scandinavian, European Blocking	Some rain west of observation area	7 km to 8 km high, mostly east of observation area	Non case	RS, Sw, PL, AFP
IOP7	24-25 July	European, Scandinavian Blocking	Showers	Isolated, outside study area	Saharan dust, hailstorm on 26 July (no IOP)	RS, Sw, AFP

green shaded rows indicate the IOPs that KASCAL was measuring. My aim during this campaign was to investigate aerosol-cloud interaction and aerosol distributions by combining remote sensing and *in-situ* measurements. One mobile 16 feet container with KASCAL on the roof of the container was installed together with KITcube in Rottenburg (8.95° E, 48.48° N, 339 m above sea level) from June 1^{st} to August 1^{st}, 2021. The measurement container contained different aerosol characteri-

zation instruments including aerosol particle sizers (SMPS, APS, OPC) and counters (CPC), a Portable Ice Nucleation Experiment (PINE) (Möhler et al. 2021) to determine the ice nucleating particles INP and a meteorological sensor. The KASCAL employed on the roof of the container did zenith scanning measurement from 90° to 5° with the step of 5° at two azimuth angle at 230° and 320° relative to the north direction (0°). The schedule of the scanning lidar had two modes - IOP and Non-IOP. The KASCAL did 4 zenith scan planes each hour (2 scans for each direction) during IOPs and 2 zenith scan planes each hour (1 scan for each direction) during non-IOPs. In addition, 15 minutes vertical measurement was conducted during noon time and midnight to measure the MLH and Residual Layer Height (RLH). In addition, cloud radar, MWR, radiosonde, ceilometer, and sun photometer data provided by KITcube was used. Finally, the ICON-ART model was used to simulate the aerosol-cloud interaction. The methods used in this field campaign are summarized in Table 2.5. During my Ph.D. study, I participated in this field campaign and also analyzed this dataset together with Dr. Yuxuan Bian (IMK-AAF, now at Chinese Academy of Meteorological Sciences).

Table 2.5: List of methods used in the Swabian MOSES campaign.

Method	Main parameter
KASCAL	Aerosol backscatter, N_2 Raman, depolarization at 355 nm
SMPS, APS, OPC, CPC	Aerosol particle number, size
PINE	INP number
Lufft WS800	Meteorological parameters
cloud radar	cloud reflectivity factor, cloud droplet speed and spectrum width, and LVDR
MWR	Vertical profiles of temperature and humidity
Wind lidar (Wind cube WLS8)	3D wind vectors
Radiosonde	Vertical profiles of meteorological parameters
Ceilometer	Aerosol backscatter at 1064 nm
Sun photomter	Column integrated aerosol optical parameters
ICON-ART	Simulation of aerosol-cloud-interaction and dust

Karlsruhe Mülldeponie West: This field campaign was conducted at Karlsruhe Mülldeponie West (8.33° E, 49.02° N, 159 m above sea level) from July 14^{th} to August 4^{th}, 2022 with a similar in-

strumentation as during the Stuttgart urban campaign with one additional Proton-Tranfer-Reaction Mass Spectrometer (PTR-MS) which was operated by Yanxia Li (IMK-AAF). The observation site is on the top of a small hill (old landfill about 50 m above ground) overlooking the west of Karlsruhe, which allows KASCAL to make horizontal measurements (0°). During this campaign, the KASCAL did zenith scanning measurements in 4 directions (north (0°), east (90°), south (180°), and west (270°)) and also made horizontal scans (from 90° to 243° in steps of 17°) from the east direction to the west direction. The aim of this campaign was to study the industrial and urban aerosol distribution as well as boundary layer evolution during a summer heat wave. I participated in this field campaign together with Dr. Yuxuan Bian and data analysis is still ongoing.

2.4.2 Saharan dust observations

Five Saharan dust cases reaching Germany were measured by remote sensing, *in-situ* measurements, and compared to preditions by the ICON-ART model. The remote sensing methods included the KASCAL which did two-angle fixed point measurements for most of the time and sun photometers which were operated by IMK-TRO as AERONET observation stations. The *in-situ* measurements including OPC and APS measured the size distributions of the Saharan dust particles if these particles reached ground level. The ICON-ART model predicted the dust layer height, structure, and proprieties that were compared to observational data for each case. The main characteristics of the five cases are given in the following.

Case 1 lasted from April 7 th to April 9th, 2018. The Saharan dust plume was characterized by remote sensing methods including two lidars (one scanning lidar (KASCAL), one vertically pointing lidar, both from Raymetrics Inc.) and one sun photometer (AERONET, Karlsruhe) at KIT campus north (8.4298° E 49.0953° N, 110 m a.s.l.). These three days were almost free of clouds except for certain periods with clouds existing above 6.0 km altitude.

Case 2 included three Saharan dust periods - the first period was from February 19th to February 20th, 2021 and the second period was from February 23rd to February 26th, 2021 and the last period was from March 2rd to march 4th, 2021. The days for period 1 and period 2 are free of clouds while period 3 was cloudy. This Saharan dust case was not only characterized by the remote sensing methods mentioned for case 1 but in addition by ground level *in-situ* measurements (e.g. SMPS, OPC, CPC, and APS) since the dust plume reached ground level at KIT campus north.

Case 3 lasted from June 19 th to June 20th, 2021 with some clouds and was measured at Rot-

tenburg (48.4892° N, 8.95452° E 339 m a.s.l.). The same characterization methods were used as for case 2.

The Saharan dust case 4 occurred from March 16^{th} to March 21^{th} , 2022 with days partly cloudy, which was also characterized by the same methods as mentioned for case 1 at KIT campus north.

Case 5 occured on 18^{th}, July 2022 without clouds and was characterized by the same methods as mentioned for case 2 but without APS in Karlsruhe Mülldeponie West (8.33° E, 49.02° N, 159 m above sea level). The main methods used in these campaigns are summarized in table 2.6. The dataset collected during periods free of clouds allowed me to study the individual Saharan dust plume properties without considering the influence of clouds while the dataset collected during cloudy periods allowed me to investigate the aerosol-cloud interactions. For case 4 in March 2022, I participated in Saharan dust observations in Granada as I was visiting the University of Granada during that time and the measurements in Karlsruhe were done with remote control with the help of Dr. Yuxuan Bian and Dr. Harald Saathoff (IMK-AAF).

Table 2.6: List of main methods used for 5 Saharan dust cases.

ID	Date	Observation site	KASCAL	OPC	APS	SPH[a]	ICON-ART
1	Apr. 2018	KIT-CN[b]	X			X	X
2	Feb. & Mar. 2021	KIT-CN	X	X	X	X	X
3	Jun. 2021	Rottenburg	X	X	X	X	X
4	Mar. 2022	KIT-CN	X			X	X
5	Jul. 2022	Karlsruhe	X	X		X	X

*SPH[a]: Sun photometer; KIT-CN[b]: KIT campus north;

3 Results and discussion

3.1 Development and validation of lidar retrieval methods

3.1.1 New retrieval method for scanning aerosol lidar and comparison of different retrieval software

During my Ph.D. study, I have used different lidar retrieval software including a LabVIEW code from the instrument manufacturer Raymetrics Inc., the Single Calculus Chain (SCC) as European standard retrieval code in the lidar network EARLINET, a lidar data analysis tool from the University of Granada, and a retrieval software especially suitable for scanning lidar data developed by myself. The EARLINET SCC is a tool for the automatic analysis of aerosol lidar measurements. The SCC is a major component of the Aerosol, Clouds and Trace Gases Research Infrastructure (ACTRIS) Aeorosol Remote Sensing Node (ARSN) responsible for the curation and processing of the ACTRIS aerosol remote sensing data. In this thesis, I compared my own retrieval software with the SCC retrieval code. The result of this comparison is shown in Figure S1, which shows that my own algorithm agrees well with the SCC retrieval. The agreement between my own algorithm and the SCC code allowed me to develop a lidar software that is more suitable for scanning lidar data analysis. During my Ph.D. study, I have developed two lidar data analysis software based on the program language Python. The first one is a software with Graphical User Interface (GUI) as shown in figure S2 and another one is an auto-analysis software which can analyze datasets at a fixed time autonomous according to a fixed schedule. The parameters retrieved for each lidar data set can be changed by the GUI or configuration text files. Both software tools allowed me to analyze especially scanning lidar data partially automatic and more conveniently than by existing software.

Furthermore, I found that scanning elastic lidar observations are not only useful to determine extinction coefficients as mentioned in section 2.1.1 but can also be used to get information on lidar ratios from elastic lidar signals. I found that the backscatter coefficients retrieved using the Klett-Fernald method for different lidar viewing angles showed discrepancies even in a horizontally homogeneous atmosphere. These discrepancies varied with lidar ratios assumed. Hence, I can use the backscatter coefficients measured at different lidar viewing angles to determine lidar ratios.

Consequently, I developed a method to retrieve lidar ratios from elastic lidar signals independently. Although retrieval of lidar ratios is straightforward with known extinction coefficients based on the lidar equation, to my best knowledge, there is no report about retrieving lidar ratios from single elastic lidar measurements. Hence, finding a stable method to determine lidar ratios is important for the further application of elastic lidar. This method was tested by simulations, proven mathematically, and validated using a Saharan dust plume. Firstly, I constructed lidar signals based on the lidar equation at two elevation angles with the same aerosol backscatter coefficient profile. Then I retrieved backscatter coefficients at these two angles with different values of the lidar ratio using the Klett-Fernald method. Figure 3.1 shows the input (dashed line) and retrieved (red and green line) backscatter coefficient profiles for different values of lidar ratios. The input lidar ratio used in the lidar equation for this simulation is 55 sr. The differences between input and retrieved profiles increase with lidar ratios deviating from the input lidar ratio (55 sr). More importantly, I found increasing differences between the profiles retrieved for different viewing angles for lidar ratios deviating from the input lidar ratio (55 sr). This implies that I can use the difference between two retrieved profiles at different view angles to determine lidar ratios.

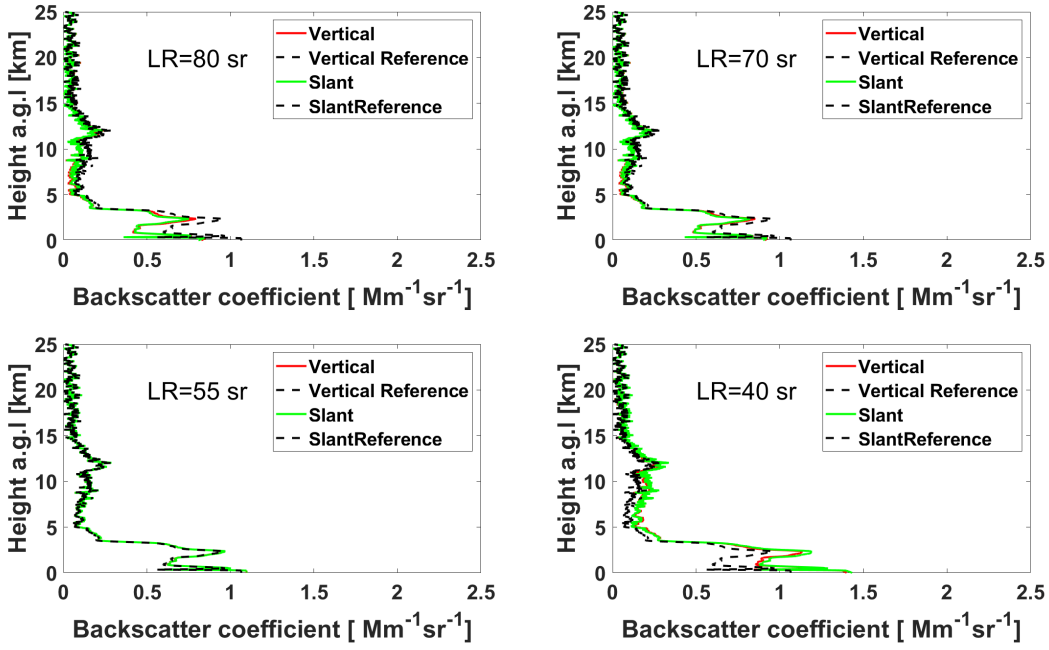

Figure 3.1: The input (dash line) and retrieved (red and green line) backscatter coefficient profiles for different values of the lidar ratio with an input lidar ratio of 55 sr for the simulation result.

In conclusion, this method allows for retrieving the lidar ratio if assuming a horizontal homogeneous atmosphere based on elastic lidar measurements at two different observation angles. A mathematical derivation for this method is given in Appendix B.2. To test how sensitive this difference in backscatter coefficients of different viewing angles depends on the lidar ratio, I performed a series of simulations. Figure 3.2 shows the ratio between vertical and slant backscatter coefficients for different lidar ratios with input lidar ratios being 55 sr and 30 sr, respectively. From this figure, we can identify the ratio equal to unity when the retrieved lidar ratio is equal to the correct lidar ratio. Besides, a smaller value of a chosen lidar ratio caused the backscatter coefficient from the vertical retrieval to be smaller than that from the slant retrieval, and vice versa. Hence, I proposed that the lidar ratio can be retrieved from a new method based on scanning aerosol lidar, which can help us determine the backscatter coefficient and extinction coefficient from Klett-Fernald method without the assumption of a lidar ratio.

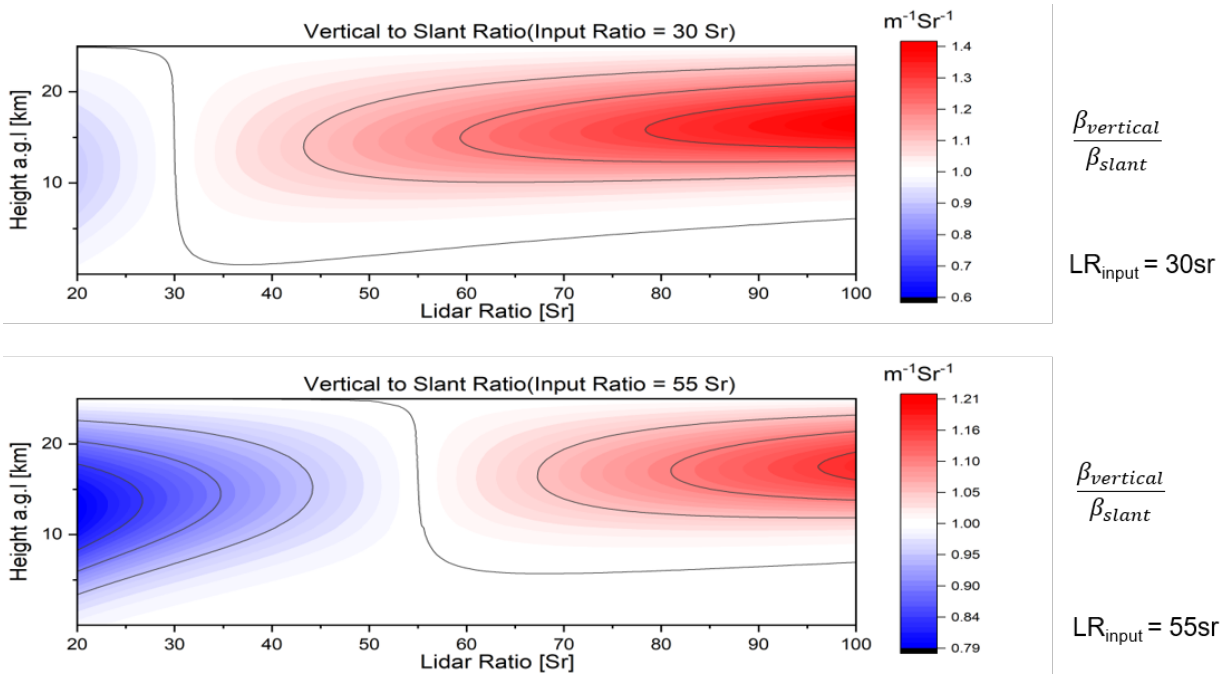

Figure 3.2: The ratio between vertical and slant backscatter coefficient for different values of the lidar ratio with input lidar ratios being 30 sr (upper panel) and 55 sr (bottom panel), respectively.

3.1.2 Validation by ground-based aerosol particle sizers

The comparison of lidar data with ground-based aerosol particle sizers was conducted during the field campaign in the urban background of the city of Stuttgart. In this campaign, the aerosol

lidar did zenith scanning measurement with elevation angles from 90 ° to 5°. The nearly horizontal measurements (5°) allows to retrieve extinction coefficients from lidar data near ground level (around 10 m above ground level) that can be compared with ground level *in-situ* measurement. The ground level *in-situ* instrument, OPC (Fidas-200, Palas, inc) measured the size distribution of aerosol based on side scattered white light. The aerosol size distribution was used to calculate the aerosol extinction coefficient via Mie calculation and this extinction coefficient can be compared with lidar retrieved extinction coefficients. The extinction coefficients retrieved from lidar and calculated based on measured aerosol size distributions (legended as "Raw size distribution") are shown in Figure 3.3. The extinction coefficients obtained from lidar were retrieved by a slope retrieval method. Figure 3.3 shows that the extinction coefficients calculated by Mie theory are systematically lower than from lidar retrieval by a factor of 4.70 ± 1.49. The main reason for this phenomenon is that this OPC (Fidas 200) underestimates the particle number by a factor of 2-10 at a diameter between 250 nm and 500 nm when comparing with SMPS data as shown in Figure S3. The left side of Figure S3 shows number size distribution from OPC and merged size distributions from SMPS and APS measurements. From this figure, we can see that the OPC underestimated particle number size distribution at the diameters between 250 nm and 500 nm when compared with the merged size distribution (called "loss effect"). Please note that the SMPS can measure the particle size distribution from several nanometers up to around 800 nm. The right plot of Figure S3 shows the accumulated extinction coefficients calculated by Mie theory based on those two size distributions shown in the left of this figure. The underestimation of particle numbers from 250 to 500 nm leads to lower extinction coefficients by a factor of 4. Hence, I conclude that the underestimation of particle number from 250 to 500 nm is the main reason for this underestimation of extinction coefficients.

The underestimation of particle number for the lowermost channels of the OPC in the size range 250 - 500 nm is systematical, which can be seen by comparison with observational data (Figure S4). So I calculated the counting efficiency curve by dividing the merged size distribution by the OPC size distribution. Then I applied this counting efficiency correction to the OPC size distributions measured in Stuttgart urban field campaign and this corrected size distribution is used to calculate the extinction coefficient via Mie calculation. The time series of the corrected extinction coefficients calculated from the corrected size distribution is shown in Figure 3.3 and the orange areas refer to the extinction coefficients corrected for the underestimation of aerosol particle num-

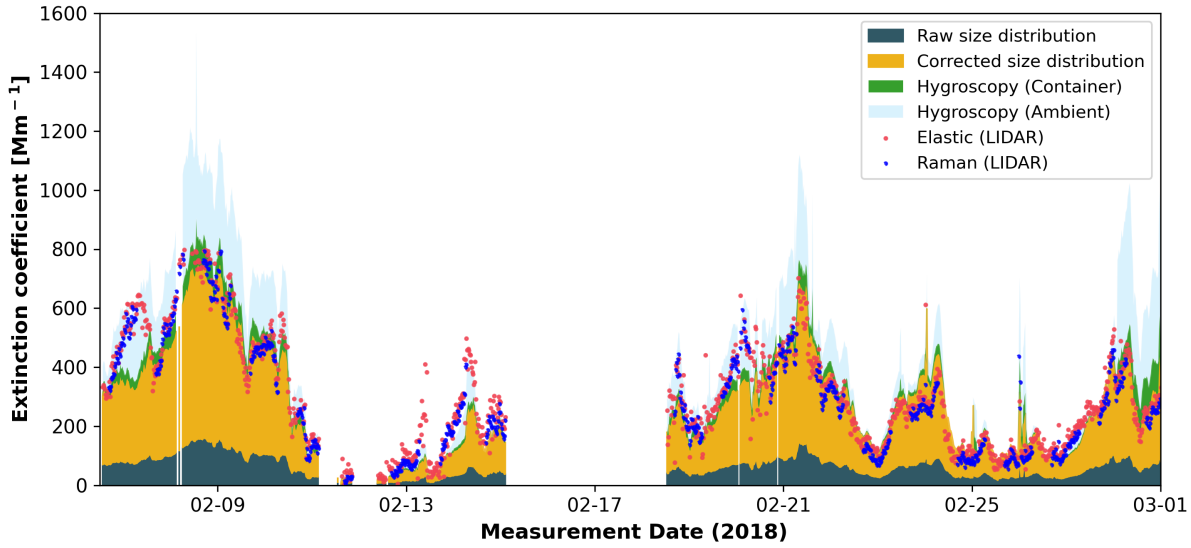

Figure 3.3: Time series of ground-level extinction coefficients retrieved by the multi-angle retrieval method, Raman retrieval method, Mie calculations based on Fidas200 raw size distributions as well as size distribution corrected for counting efficiency and hygroscopicity effects from February 5^{th} to March 5^{th}, 2018, in downtown Stuttgart.

bers from 250 to 500 nm. After taking into account particle number underestimation, the modelled extinction coefficients show good agreement with lidar retrievals. Although good agreement between *in-situ* and lidar measurements, the aerosol hygroscopic growth effect is still not considered. The modelled extinction coefficient contributed by aerosol hygroscopic growth is legended as "hygroscopy (container)" and "hygroscopy (Ambient)" in Figure 3.3, representing the humidity used in the model are container indoor humidity and ambient humidity, respectively. As shown in this figure, the extinction coefficient retrieved from lidar measurement shows a similar trend with both two hygroscopic extinction coefficients but shows better agreement with the one used container indoor humidity, which implies that the aerosol particles were not thermodynamical equilibrated and particles lost water partly but not completely when they were sampled by the instruments. The fraction of water to be lost depends on the humidity, the temperature difference between the ambient and container indoor environment, and the flow rate. It is hard to quantify in this experiment. However, for most of the time the hygroscopic growths seems to have only limited influence on our measurements or the particle drying inside the container before the OPC detector is relatively small. The correlation plot between the hygroscopic extinction coefficient by container indoor humidity and the lidar-derived extinction coefficient is shown in Figure 3.4, which shows that a slope and a Pearson correlation coefficient are 1.037 ± 0.015 and 0.878, respectively. The dash-dot line in this figure is the regression fitting curve between the lidar-derived extinction coefficient and

Mie calculation by using ambient humidity. From the fraction of extinction coefficient shown in Figure 3.3, we can determine that the main reason for causing extinction coefficient inconsistency between *in-situ* measurement and lidar retrieval is the ”loss effect” of the OPC. In addition, the comparison between remote sensing with raw *in-situ* measurements implicates a good agreement between lidar-derived extinction coefficients and *in-situ* ground measurements and also reflects the good quality of lidar retrievals.

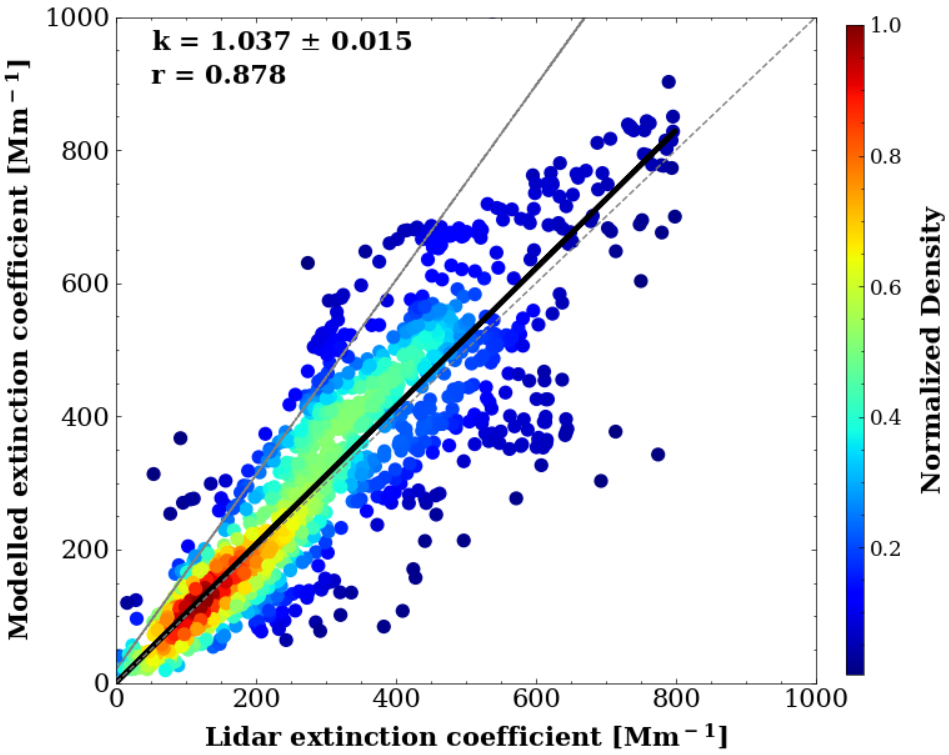

Figure 3.4: Correlation of extinction coefficients from multi-angle lidar retrievals and Mie calculations based on counting efficiency corrected particle size distributions (left). The right plot shows the same correlation considering also a potential hygroscopic growth effect from February 5^{th} to March 5^{th}, 2018, in Stuttgart.

3.1.3 Validation by UAV borne aerosol sizers

The comparison of lidar with UAV and balloon *in-situ* measurements was conducted based on the dataset collected during the MOSES summer field campaign at the FZJ (see section 2.4). In this section, I will discuss the comparison between lidar and UAV borne aerosol measurements. The validation of lidar retrievals by balloon-borne COBALD measurements is discussed in section 3.1.4.

The comparison of lidar and UAV borne *in-situ* measurements was conducted at two days, on July 9^{th} and July 12^{th}, 2018, to study the vertical distribution of aerosol particles and the boundary layer structure. The UAV was launched 5 times during the morning from 07:00 to 10:00 on July 9^{th}, 2018 and was launched 7 times from 03:50 to 16:30 on July 12^{th}, 2018 to measure the boundary layer evolution during these times. Details on these UAV flights are gven in table 3.1. The sky was almost free of clouds during UAV flights on July 9^{th}, 2018 while it was affected by clouds within the boundary layer on July 12^{th}, 2018.

Table 3.1: The start time, altitude range, and duration of UAV flights for the experiments on July 9^{th} and July 12^{th}, 2018.

ID	Date & Start time	Min. altitude (masl)	Max. altitude (masl)	Duration (s)
2018070901	07.09 07:39	90.9	1246.5	709.5
2018070902	07.09 07:48	92.4	1244.8	705.1
2018070903	07.09 08:10	90.9	1243.8	711.7
2018070904	07.09 08:29	89.5	1235.5	691.6
2018070905	07.09 09:34	93.1	1752	1105.5
2018071201	07.12 04:16	91.4	1247.1	701.3
2018071202	07.12 04:31	94.8	1246.1	721.7
2018071203	07.12 07:09	92.7	1246.5	719.6
2018071204	07.12 07:33	93.2	1240.9	717.8
2018071205	07.12 09:44	98.6	1253.7	722.3
2018071206	07.12 14:30	92.8	1248.9	721.3
2018071207	07.12 16:30	92.9	1240.2	716.5

The comparison of the vertical aerosol particle profiles from lidar and UAV borne measurements was conducted in the following steps. First, I used the temperature and pressure measured by the UAV instead of the standard atmospheric model to calculate the profiles of molecular backscatter coefficients for lidar retrieval. Second, the backscatter coefficients at all observation angles were calculated using the Klett-Fernald method with reference values obtained from vertical profiles of the backscatter coefficient. Finally, Mie scattering theory was used to calculate the aerosol backscatter coefficients based on size distributions measured by the UAV borne OPC. Figure 3.5 shows the backscatter coefficients retrieved from KASCAL measurements and those calculated

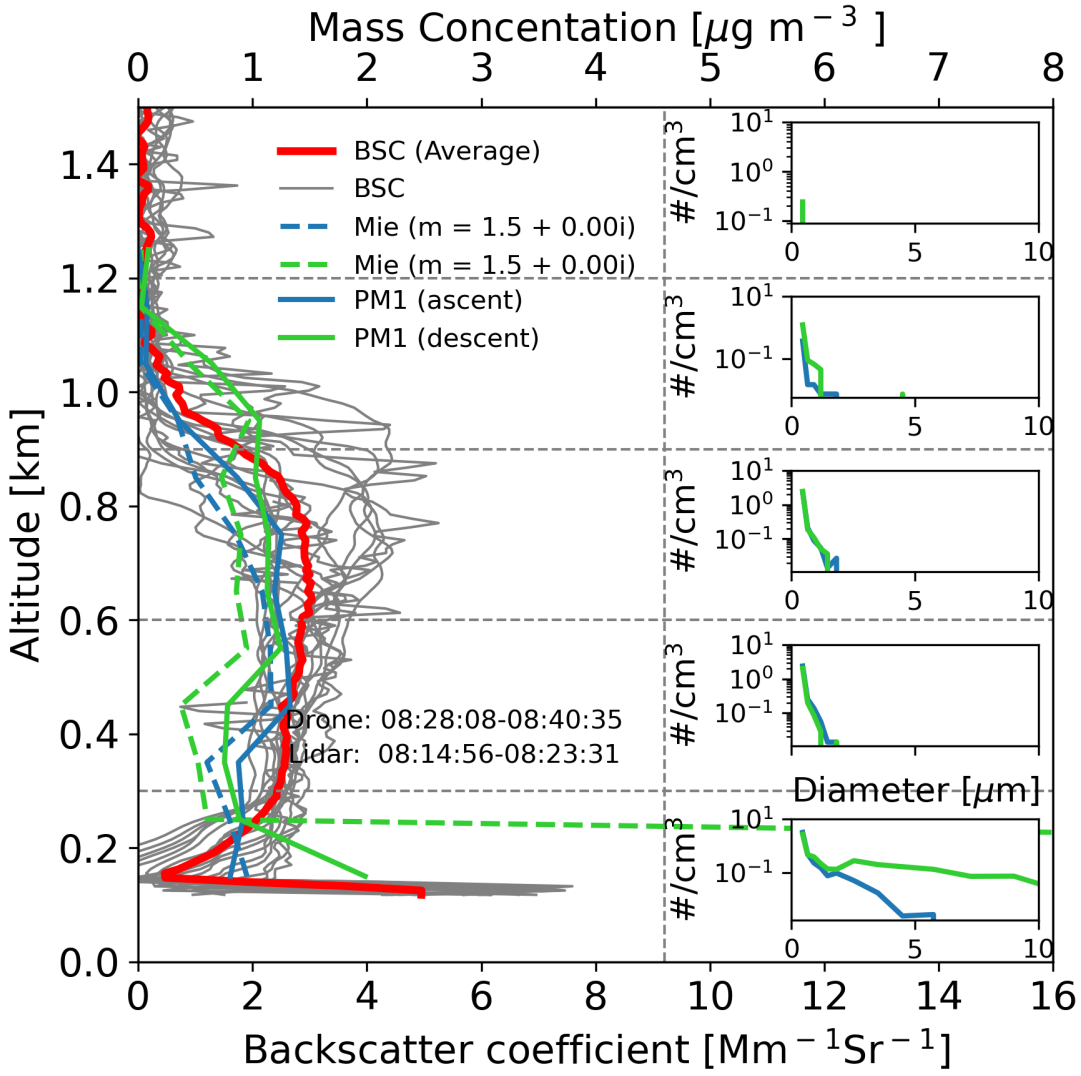

Figure 3.5: Backscatter coefficients from lidar measurements at different angles (grey lines) and the average of these profiles (thick red line), as well as backscatter coefficients (dashed lines) calculated from particle size distributions measured by the UAV borne OPC-N3 (blue ascent). OPC based PM1 mass concentrations (solid line, blue ascent; green descent), and particle size distributions for different average altitudes (inserts on the right side) on July 9^{th}, 2018. Note: The blue and green colors indicate UAV ascent and descent measurements respectively.

based on measured size distributions as well as vertical profiles of PM_1 (particulate matter with diameter less than 1 µm) concentrations. In this experiment, the lidar performed zenith scans using elevation angles from 90° to 5° with steps of 5°. The backscatter coefficients for each observation angle are indicated as thin gray lines in Figure 3.5 and the average of these backscatter coefficients is shown as thick red line. The comparison shows that the vertical distribution of the aerosol particles in the well-mixed boundary layer is reflected well in both lidar and OPC measurements. Furthermore, the backscatter coefficients from OPC retrieval show a similar vertical trend as those

retrieved from lidar measurements but are significantly smaller. In addition, the aerosol size distribution measured by UAV borne OPC is shown in the right part of this figure. Please note that the particle size was averaged over 300 m of altitude and the horizontal dashed lines represent these average altitude zones. These size distributions show that large particles were detected only below 300 m altitude above sea level.

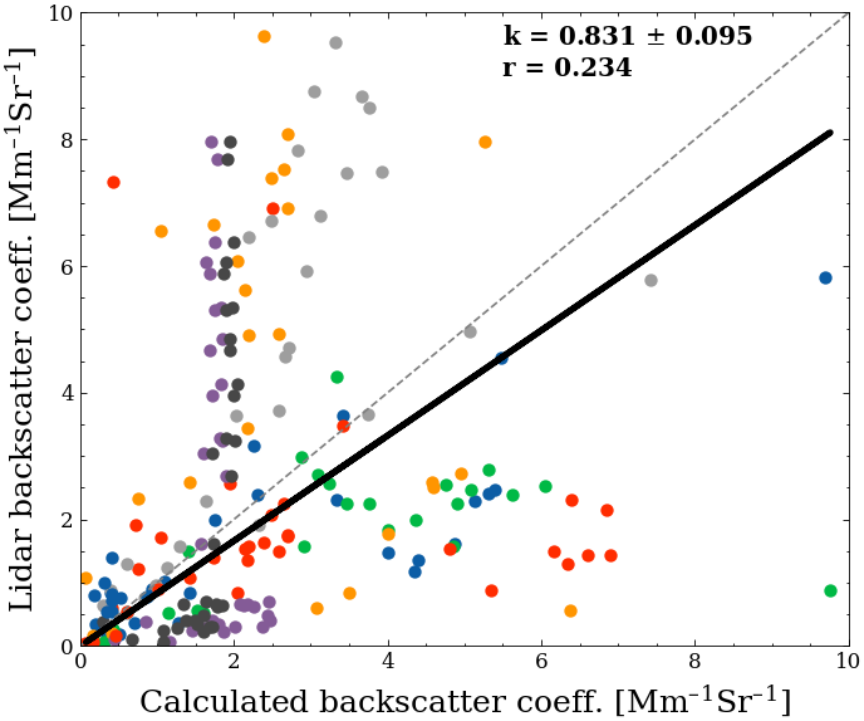

Figure 3.6: Correlation of backscatter coefficients retrieved from lidar measurement and calculated by Mie theory based on aerosol size distributions measured by OPC-N3 on the UAV for all UAV flights on July 9^{th} and July 12^{th}, 2018. The different scatter point colours indicate the different UAV flights.

12 UAV flights were conducted on July 9^{th} and July 12^{th} as shown in table 3.1 for comparison with lidar retrievals. Figure 3.6 shows correlation of backscatter coefficients retrieved from lidar measurement and calculated from Mie theory based on aerosol size distributions measured by OPC-N3 on the UAV. The data from lidar and UAV was averaged over 60 m in vertical direction to reduce noise the of OPC-N3 measurements. The colours of scatter points indicated different UAV flights. This figure shows that the backscatter coefficients retrieved from lidar correlate with those calculated from size distributions with a slope of 0.831 $\pm$ 0.095 and a Pearson correlation coefficient of 0.234. This means that the UAV measurements show a similar trend and magnitude

as the lidar measurement but also show large deviations varying with from flight to flight. All these results of UAV borne measurements show that the OPC-N3 on UAV could be comparable with lidar measurements but cannot provide stable observational data due to very large flight to flight fluctuations. Potential reasons for this are changing particle size distributions from flight to flight of which especially the small particles are not detected well by the OPC. Furthermore, also a changing relative humidity may change the particle size due to hygroscopic growths which may be captured differently by the two instruments. In addition, the airflow into the OPC on the UAV was not isokinetic and may lead to certain particle losses especially of larger particles.

3.1.4 Validation by a backscatter sensor on a balloon

A radiosonde balloon that carried a COBALD instrument to measure *in-situ* backscatter coefficients was launched to an altitude of around 30 km at the night of July 12^{th} to validate lidar retrievals. The lidar (KASCAL) did only vertical measurements with an integration time of 60 s for each profile during the balloon flight. Figure S5 shows the range-corrected lidar signal for two hours of continuous measurement and the vertical trajectory of the balloon. As shown in this figure, the lidar signal almost did not vary too much in the first hour (the period was highlighted in this figure) while shows changes in the second half of the experiment. Hence, I select lidar data during the first hour to compare with the radiosonde measurement. Figure S6 shows the horizontal trajectory of the radiosonde with the color of the plot indicating the radiosonde altitude and the circle indicating the distance from the lidar observation station. This figure shows that the horizontal displacement of the radiosonde is about 10 km when the radiosonde reached an altitude of 10 km and this horizontal displacement is a main reason for the difference in backscatter coefficients between lidar and COBALD. For the lidar analysis in this experiment, the backscatter coefficients were retrieved from elastic and Raman data with the vertical profiles of molecular backscatter coefficients being calculated from temperature and pressure measured by the balloon. The COBALD data analysis follows the procedure proposed by Brunamonti et al. (2021*b*). First, a wavelength conversion was conducted to get the backscatter coefficients at a wavelength of 355 nm from the COBALD measurements. The AE used for this wavelength conversion is measured by COBALD at two wavelengths (455 nm/940 nm) and extrapolated to the wavelength of 355 nm. Second, as the FOV of the lidar and the COBALD are different (the FOV of COBALD is 6° whereas the FOV of lidar is 2.3 mrad), also a FOV correction is necessary. The correction factors are calculated based

on Mie scattering theory and these values are shown in figure 2 in Brunamonti et al. (2021*b*).

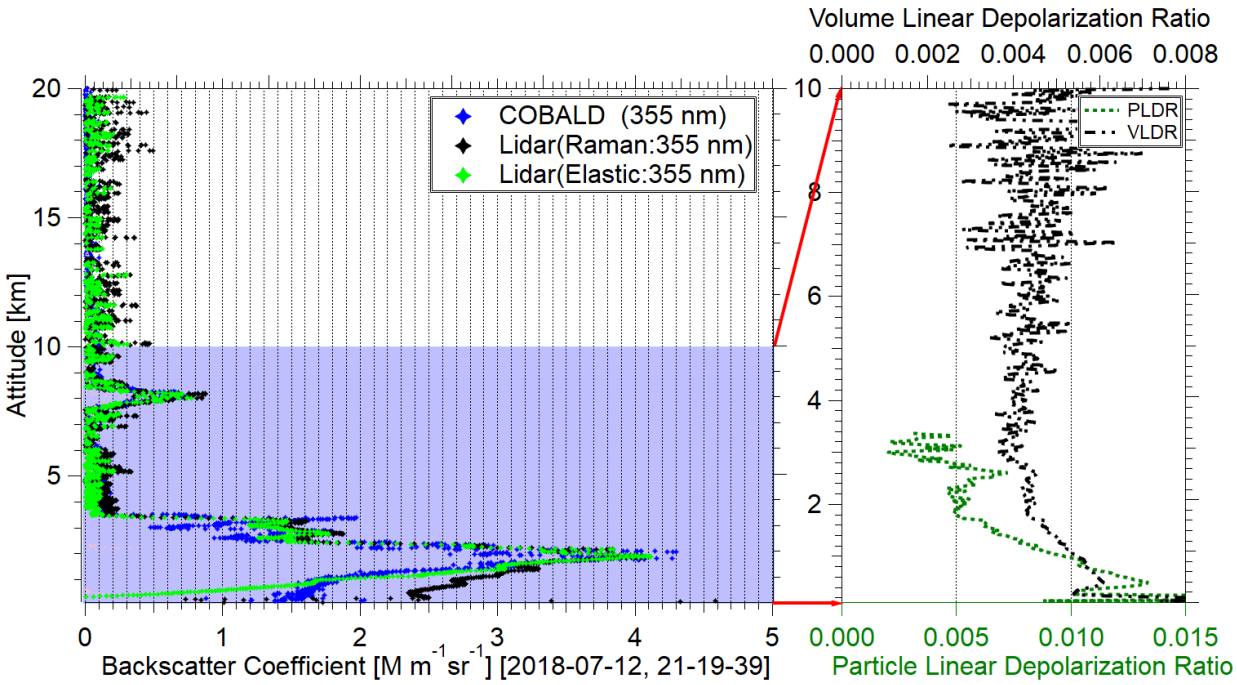

Figure 3.7: Backscatter coefficients measured by balloon-borne COBALD and lidar (left) as well as aerosol volume and particle depolarization ratio measured by lidar (right) on the night time of July 12^{th} of 2018. (The integration time of lidar is 1 hour from 21:19 to 22:19 UTC.)

Figure 3.7 shows the backscatter coefficients from COBALD and lidar measurement for a lidar integration time of 1 hour. These two profiles of backscatter coefficients from lidar are retrieved from the elastic and Raman channel dat, respectively. The retrieval of backscatter coefficients from the elastic channel remained uncertain due to the assumption of a lidar ratio in the Klett-Fernald method. Hence, it is meaningful to compare backscatter coefficients from the Raman data with those from COBALD measurements. This figure shows a good agreement in backscatter coefficients between lidar Raman data retrieval and the COBALD measurement at an altitude above 2 km. However, there is still a discrepancy at altitudes below 2 km. In addition, the volume and particle depolarization ratios measured by lidar are shown on the right side of Figure 3.7. The low depolarization ratios support our assumption that the particles are spherical and that I can use Mie calculations for the FOV correction.

The discrepancy of backscatter coefficients between lidar retrievals and COBALD measurements at low altitudes is due to the temporal/vertical variability of aerosol particles in the boundary layer as can be seen from vertical profiles of backscatter coefficients with high temporal resolution as

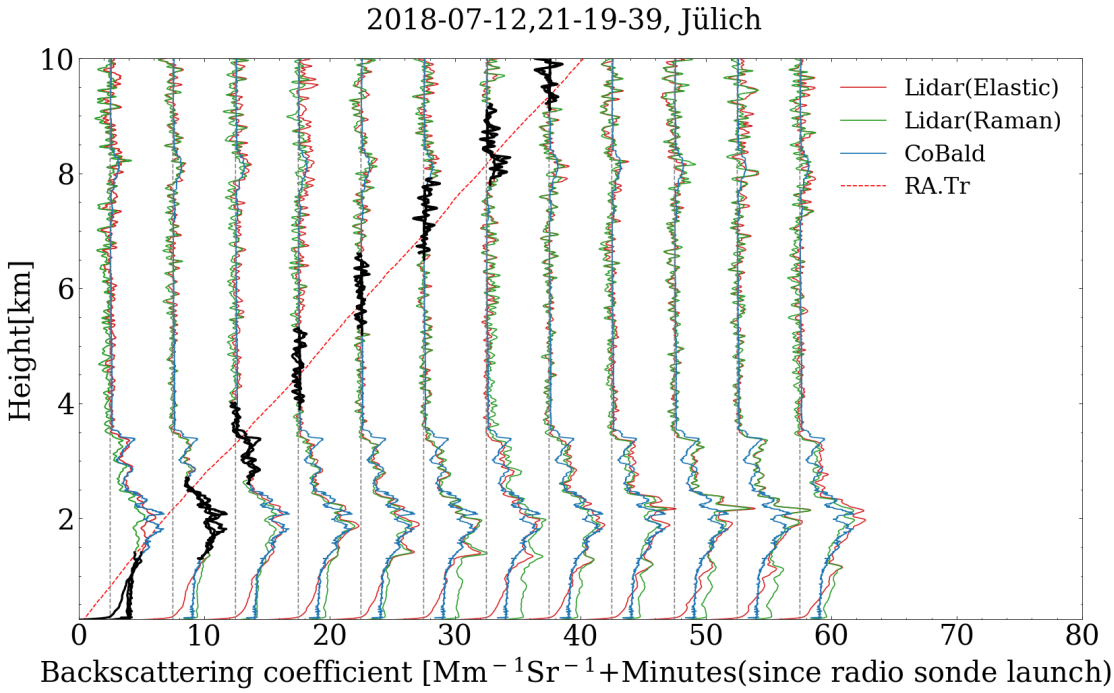

Figure 3.8: Profiles of backscatter coefficients from lidar for integration times of 5 minutes and vertical profile of *in-situ* backscatter coefficients measured by balloon-borne COBALD on July 12^{th} of 2018. The black line segments indicate the altitude ranges selected to get the merged profile of the backscatter coefficients from lidar.

Figure 3.8. This figure shows profiles of backscatter coefficients retrieved from lidar Raman data with 5 - minute temporal resolution and backscatter coefficients measured by COBALD as well as the vertical balloon trajectory. This figure shows a good agreement in backscatter coefficients between COBALD measurement and lidar Raman data retrievals if compared for the actual flight altitude of the balloon. The backscatter values at the altitude of the balloon passing by are selected as shown by the back line in this figure to get merged Raman backscatter coefficients. The merged Raman backscatter coefficients and backscatter coefficients from COBALD measurements are shown on the left side of Figure 3.9. This shows very good agreement of backscatter coefficients between lidar and COBALD measurements at all altitudes. The correlation between lidar merged Raman backscatter coefficients and COBALD backscatter coefficients is shown in the right side of Figure 3.9. The backscatter coefficients are well correlated with a slope of 1.063 ± 0.016 and a Person correlation coefficient of 0.925. The good agreement in backscatter coefficients between lidar retrievals and COBALD *in-situ* measurements validates vertical profiles of lidar retrievals but also the good quality of the COBALD data.

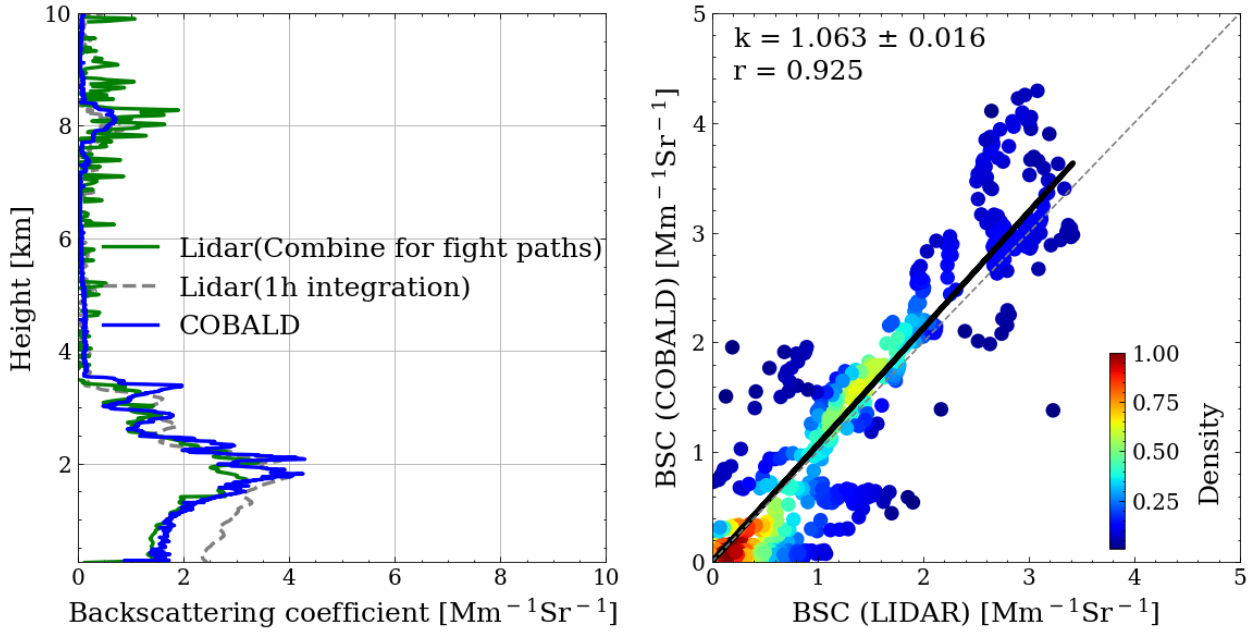

Figure 3.9: Left: Profiles of backscatter coefficients from lidar for an integration time of 1 hour (grey dash line) and merged backscatter coefficients (green line) from 5-minute integration profiles as shown in Figure 3.8 as well as the vertical profile of in-suit backscatter coefficients measured by balloon-borne COBALD (blue line) on July 12^{th} of 2018. Right: Correlation between lidar merged backscatter coefficients (the green line in the left) and balloon-borne COBALD backscatter coefficients (the blue line in the left).

3.1.5 Summary

I have developed a new retrieval software for a scanning aerosol lidar and validated it by comparison with software from the instrument manufactorer (Raymetrics Inc.) and the European reference lidar retrieval software SCC. The new software is more suitable for scanning lidar data analysis. Furthermore, I developed and validated a method which can retrieve lidar ratios from scanning elastic lidar data with at least two different observation angles. Under the assumption of a horizontally homogeneous atmosphere it can help to reduce uncertainties of the Klett-Fernald method. Scanning lidar measurements with low elevation angles allows retrieval of extinction coefficients near ground level. I validated this approach by comparsion with ground level based *in-situ* size distribution measurements. The comparison shows that OPC measurements, e.g. by Fidas200, can underestimate particle number concentrations by a factor of 2-10 at the diameters between 250 nm and 500 nm, thus causing the total extinction calculated from size distributions to be systematically lower than that from lidar retrievals by a factor of 4.70 $\pm$ 1.49. Correcting the aerosol particle size distributions including SMPS size distribution measurements (14-760 nm) leads to a good

correlation with lidar-derived extinction coefficients with a slope of 0.916 ± 0.012 and a Pearson correlation coefficient of 0.895. The comparison also shows that the underestimation of aerosol particles between 250 nm and 500 nm contributes the largest discrepancy between lidar retrieval and these *in-situ* measurements. In addition, comparison of lidar and UAV based measurements shows good agreement for boundary layer heights with similar trends as the ERA5 boundary layer evolution. The OPC-N3 abroad the UAV shows the similar aerosol vertical distributions and comparable backscatter coefficients as the lidar measurement. However, the backscatter coefficients calculated from these OPC data were unstable and with large uncertainties for different flights mainly due to the uncertainties of the OPC-N3 sensor. Finally, the backscatter from balloon-borne COBALD measurements is well correlated with the backscatter retrieved from lidar measurements from near ground level up to the stratosphere with a slope of 1.063 ± 0.016 and a correlation coefficient of 0.925. This consistency between lidar and COBALD sensor validated both methods and proved that both can provide reliable and high-resolution vertical profiles of aerosols. In conclusion, these comparisons validated the lidar retrieval and assessed uncertainties of different methods, thus providing a good base for further investigations related to my Ph.D. topic.

3.2 Urban aerosol and boundary layer dynamics in Stuttgart in winter

This section presents the results of boundary layer dynamics, aerosol composition, and air quality in downtown Stuttgart in winter 2018 based on data collected during the "Stuttgart urban" field campaign. One main objective of this work is to study the evolution of the boundary layer, especially during nighttime, and its relationship with aerosol concentrations at ground level combining different remote sensing and *in-situ* measurements. In addition, a LES model, PLAM-4U, was used to simulate the boundary layer dynamics and aerosol spatial-temporal distribution and these simulations can be validated by the observational data. This study should help to get a better understanding of air pollution in Stuttgart and especially on the interplay of boundary layer dynamics and emissions as well as transport of pollutants. My study, therefore, adds an important piece of information on air quality in cities like Stuttgart.

The "Stuttgart urban" field campaign employed remote sensing, *in-situ*, and radiosonde methods. It was conducted from February 5^{th} to March 5^{th}, 2018. One mobile container containing different aerosol characterization instruments and one scanning aerosol lidar on the roof of this container were installed in downtown Stuttgart, in southwest Germany. A detailed description of instruments

and measurement modes for this field campaign is given in section 2.4.

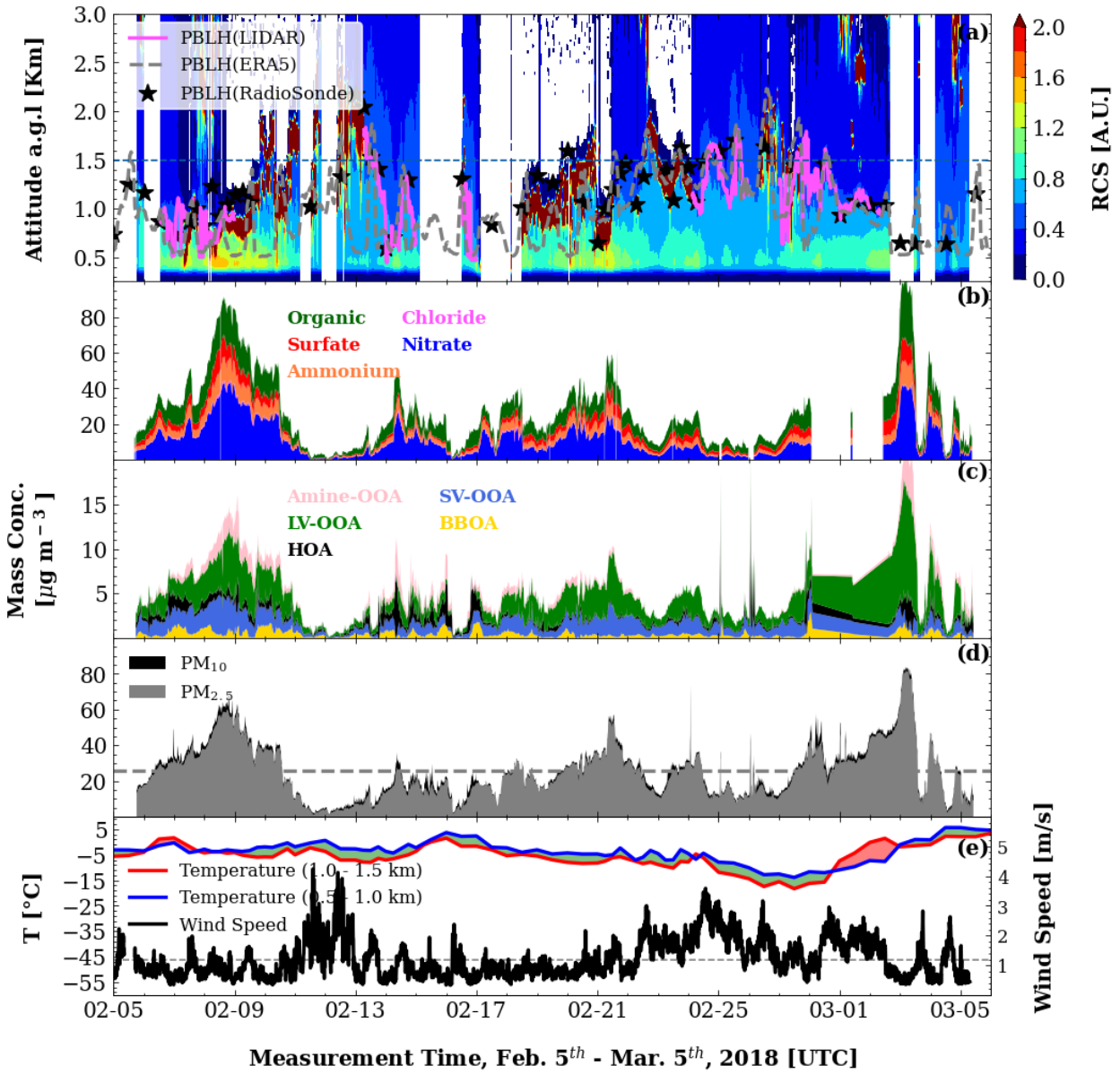

Figure 3.10: Time series of range corrected lidar signal and boundary layer heights derived from scanning aerosol lidar (pink line), radiosonde data at Schnarrenberg station (black stars), and an ERA5 dataset (grey dash line) (upper panel) (a), the aerosol mass concentrations measured by AMS (b), five-factor PMF solution of organic aerosol (c), the particulate matter measured by Fidas200 (d), and the temperature at two different altitude levels measured by radiosonde as well as wind speed measured by a meteorological sensor at ground level (e).

Figure 3.10 shows the time series of the RCS for one-month of measurements as well as the BLH retrieved from lidar data during periods that were free of clouds within 3 km above the ground level. In addition, BLH derived from radiosonde data and obtained from the ERA5 dataset are also shown in this figure as indicated by black stars and the grey dashed line, respectively. This comparison

shows a quite good agreement in BLH among lidar and radiosonde measurement as well as the ERA5 dataset. The correlation of BLH between lidar and radiosonde measurements is shown on the left side of Figure 3.11. The BLH retrieved from lidar and radiosonde correlate well with each other with a slope of 1.102 ± 0.135 and a Pearson correlation coefficient of 0.86. The correlation of BLH between lidar and the ERA5 dataset is shown on the right side of Figure 3.11. They correlate with a slope of 0.698 ± 0.067 and a Pearson correlation coefficient of 0.607. The BLH from the ERA5 dataset is systematically lower than that retrieved from lidar and radiosonde data but still shows a similar trend. A similar underestimation of BLH by the ERA5 dataset due to surface heterogeneity as well as land use and land cover was also reported by Dias-Júnior et al. (2022). The evolution of aerosol composition measured by HR-TOF-AMS as shown in Figure 3.10b indicates that nitrate dominates the aerosol chemical composition due to low air temperatures, shallow mixing layer, and high NOx emissions in winter. The Positive Matrix Factorization (PMF) analysis of OA results in five main source factors as shown in Figure 3.10c. It illustrates that Low-Volatility Oxygenated Organic Aerosol (LV-OOA) are dominant during this time periode in winter. They are manly related to regional transport of aerosol. Detailed analysis of the chemical composition of aerosol in Stuttgart can be found in Huang et al. (2019). The average temperatures at two altitude ranges (0.5-1.0 km and 1.0-1.5 km) measured by radiosonde as well as surface level wind speed measured by a meteorological sensor (WS700) on a 10 m mast at the container is shown in

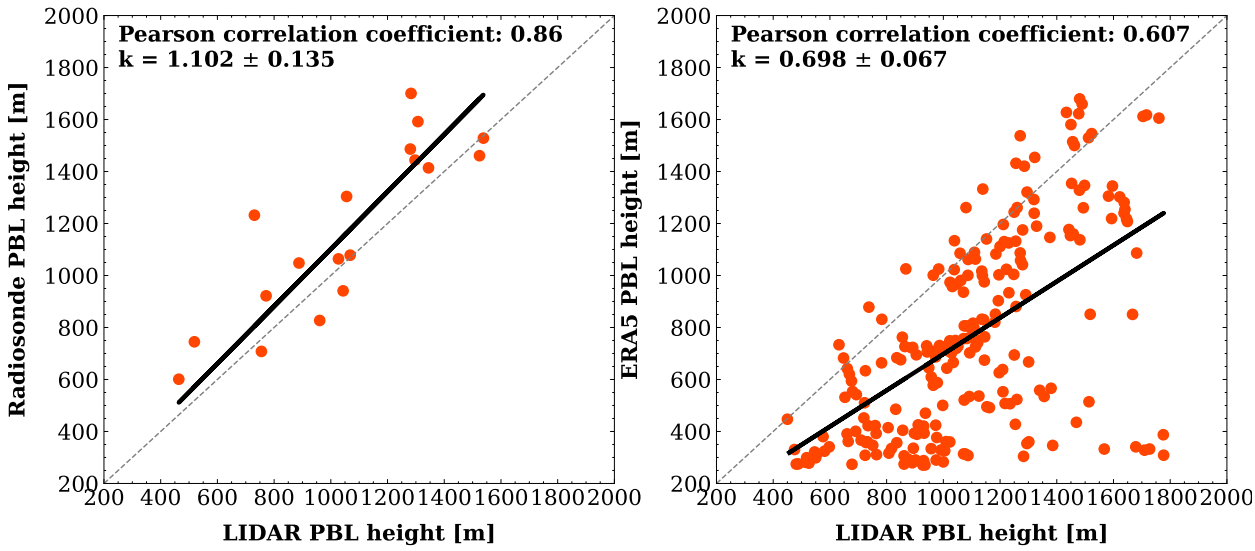

Figure 3.11: Correlation of boundary layer height (BLH) retrieved from lidar data and radiosonde measurement (left) as well as the correlation between lidar measurement and the ERA5 dataset.

Figure 3.10e. It shows that a temperature inversion and low wind speeds cause an accumulation of aerosols (e.g. time periods from February 6^{th} to February 8^{th} and from February 28^{th} to March 2^{th}). The obvious temperature inversion and low wind speeds during the above two periods are classified as stagnant weather conditions. The low wind speed and strong temperature inversion during stagnant weather conditions suppressed the convection in the troposphere, hence causing a shallow and stable boundary layer associated with accumulation of aerosols at ground level. These stagnate weather conditions are a typical reason of elevated air pollution in larger cities (Huang et al. 2018, Katsoulis 1988, Ji et al. 2014).

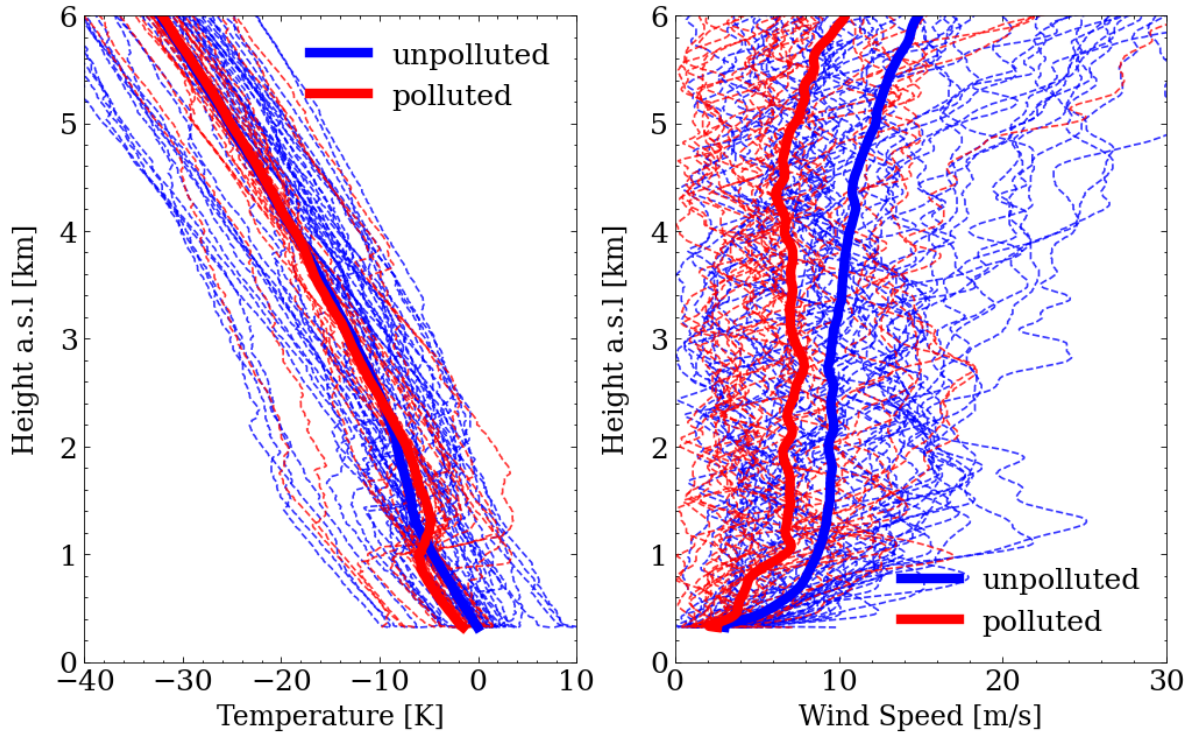

Figure 3.12: Vertical profiles of temperature and wind speed measured by radiosonde for polluted and unpolluted periods. (The time when the concentration of PM_{10} is larger than the average value is defined as the polluted period.)

Figure 3.12 shows the vertical profile of temperature (left) and wind speed (right) during polluted and unpolluted periods. The polluted period have concentrations of PM_{10} of larger than the average value of 25.8 µg/m^3 indicated as the grey dashed line in Figure 3.10d. These average vertical profiles of temperature and wind speed were calculated after weekend data were excluded to avoid the influence of local emissions. This figure shows obvious temperature inversion and low wind speed during the polluted period as expected.

In order to further investigate the evolution of the boundary layer and the impact of BLH on ground-

level aerosol dispersion, the correlation between BLH and surface aerosol concentration will be discussed in section 3.2.1. In addition, two cases were selected to better demonstrate the boundary layer behavior and surface aerosol concentration as well as the related meteorological background (see section 3.2.2).

3.2.1 Correlation between boundary layer height and ground-level aerosol concentrations

The correlation between ground-level aerosol concentrations and BLH is discussed in this section. Here I calculated the BLH from lidar measurement when free of clouds within 3 km above the ground. Figure 3.13 shows the correlations between boundary layer heights and PM_{10} as well as back carbon concentrations for three different periods (All data (a), afternoon 12:00-18:00 UTC (b), and night time and morning 00:00-12:00 & 18:00 - 24:00 UTC (c)). The color of the scatter points indicates the relative humidity. The correlation for all data is shown in figure 3.13a, which shows that PM_{10} values are anti-correlated with boundary layer heights as expected. This anti-correlation means that a higher boundary layer would dilute the aerosol while a shallow boundary layer would accumulate aerosol near the ground. However, I also found a positive correlation between PM_{10} and boundary layer heights for boundary layer heights below 800 m (a.s.l). This positive correlation is also reported in Yuval et al. (2020). This positive correlation corresponds to a low wind speed, and a high relative humidity, indicating the typical proprieties of a SBL.

Then I divided the data into two groups for two different time periods - Afternoon Time Period (ATP) as well as Night and Morning Time Period (NMTP). And the correlations between the boundary layer and surface aerosol concentrations (PM_{10}) for ATP and NMTP are shown in Figure 3.13b and Figure 3.13c, respectively. From these two subplots, we can see that the positive correlation only appeared in NMTP and the MLH during ATP only shows an anti-correlation with ground-level aerosol concentrations. The correlation between BC concentrations and BLH are shown in Figures 3.13d-f. These figures revealed that the BC concentrations are always anti-correlated with the BLH. The potential reasons for the positive correlation between PM_{10} and the BLH are accumulation of local emission or new particle formation while the SBL slowly increases during NMTP. The corresponding growths ofparticle mass can be seen from the time series of chemical composition measured by the AMS as shown in Figure 3.10b. And the reason for only anti-correlation between the BC concentrations and the BLH is that the only sources of BC are car emissions and biomass burning and the generation of the BC particles could be diluted in the

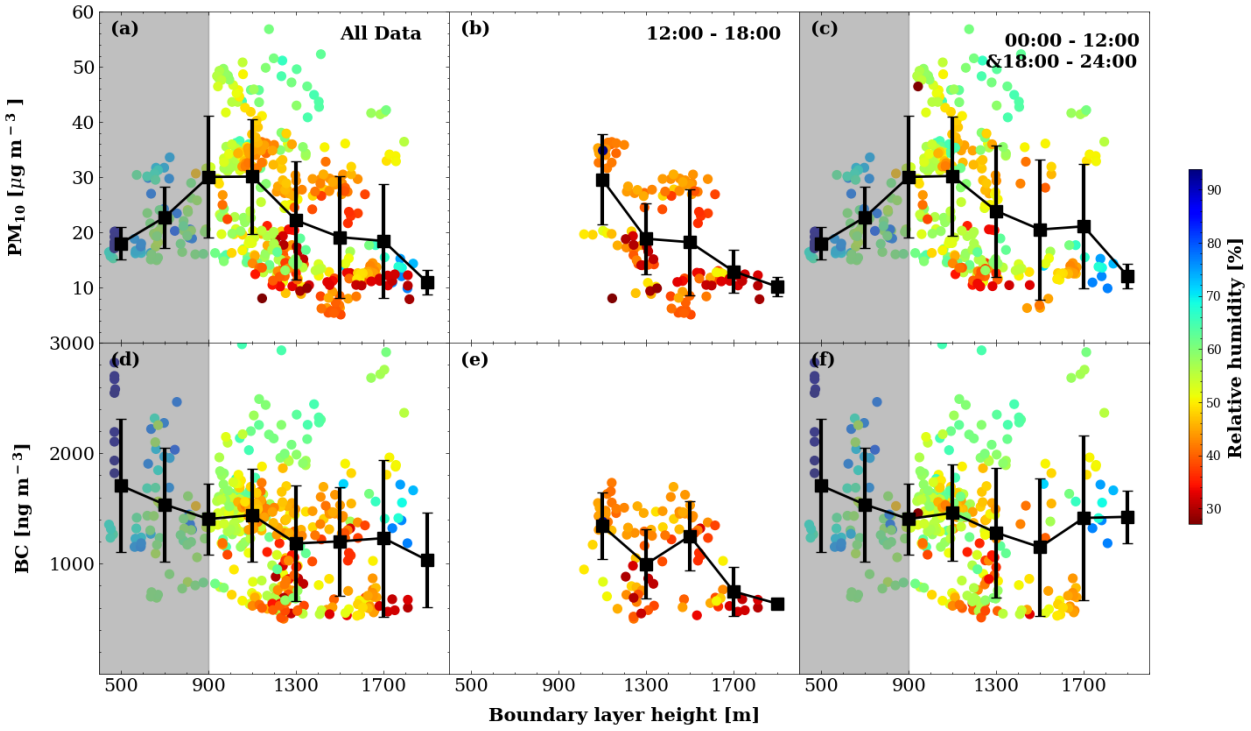

Figure 3.13: Correlation between boundary layer height and PM_{10} (upper panel) as well as black carbon (bottom panel) concentration for three different time periods (All data (a), afternoon 12:00-18:00 UTC (b), and night time and morning 00:00-12:00 & 18:00 - 24:00 UTC (c)) from February 5^{th} to March 5^{th}, 2018 in Stuttgart. (The color of the scatter points indicates different relative humidity.)

increasing of boundary layer during NMTP. A good case to illustrate this phenomenon is shown in Figure 3.16, which shows the chemical composition measured by the AMS shown in Figure 3.16b, From this figure, I found that the mass concentrations of ammonium sulfate and ammonium nitrate increased from February 13^{th}, 18:00 to February 14^{th}, 05:00 while the boundary layer heights also increased slowly during this time period, which cause a positive correlation between the boundary layer and PM_{10} concentrations. However, the BC concentration shown in Figure 3.16d is also constant during the nighttime. Hence the PM_{10} concentration can be correlated with the BLH while the BC concentration is always anti-correlated with the BLH. Figure S7 also shows the relationship between boundary layer and ground level extinction coefficients as well as CO_2 concentration. These two figures show that the extinction coefficient was also correlated with the BLH for heights below 800 m (a.s.l). Although the PM_{10} and extinction coefficients both show the same positive correlation with the boundary layer for low boundary layer heights, the PM_{10} decreased more than the extinction coefficient as BLH decrease. In addition, there is no obvious correlation between CO_2 and boundary layer heights, suggesting that the boundary layer has less impact on gas than

particle concentrations.

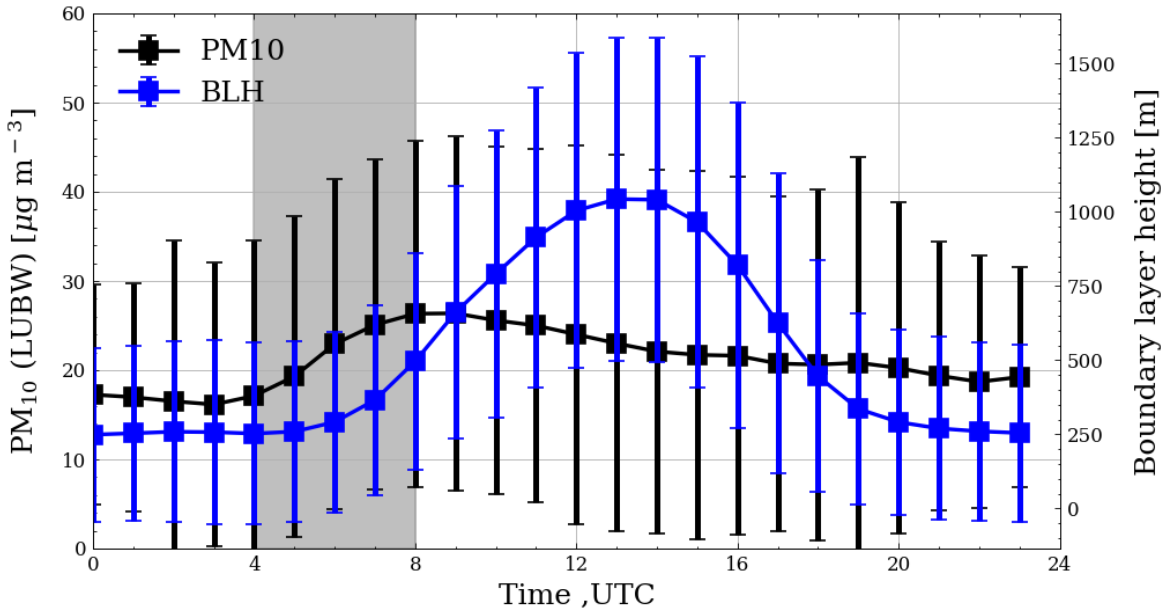

Figure 3.14: Diurnal variations of PM_{10} and boundary layer height (BLH) based on two years data from January 1^{st}, 2020 to January 1^{st}, 2022 in Stuttgart. (PM_{10} concentrations are hourly reported by Landesanstalt für Umwelt Baden-Württemberg (LUBW) and the BLH are from an ERA5 dataset).

The above statistical data analysis of the correlation between ground-level aerosol concentrations and BLH is based on data collected during one month. The correlation would be more reliable if more data was used. Figure 3.14 shows the diurnal variations of PM_{10} and BLH based on two-year data from January 1^{st}, 2020 to January 1^{st}, 2022 in Stuttgart. The PM_{10} concentration is the hourly reported dataset by LUBW and the BLH is from an ERA5 dataset. From this figure, a positive correlation between BLH and PM_{10} can be found between 04:00 - 08:00, UTC as shaded in Figure 3.14, and this positive correlation is possibly related to the morning local emissions during rush hours. In addition, the increased boundary layer after sunset (08:00 - 12:00) dilutes the aerosol in the boundary layer, thus causing a decrease of PM_{10} concentration.

The diurnal variations of PM_{10} and BLH for different seasons based on LUBW and ERA5 data are shown in Figure 3.15, which also shows that the ground-level PM_{10} concentration is correlated with BLH from 04:00 to 08:00 for all seasons. However, the strength of the correlation is different for different seasons. The spring (MAM) shows the strongest correlation while the winter (DJF) shows the weakest correlation. In addition, the summer has the highest MLH while the winter has

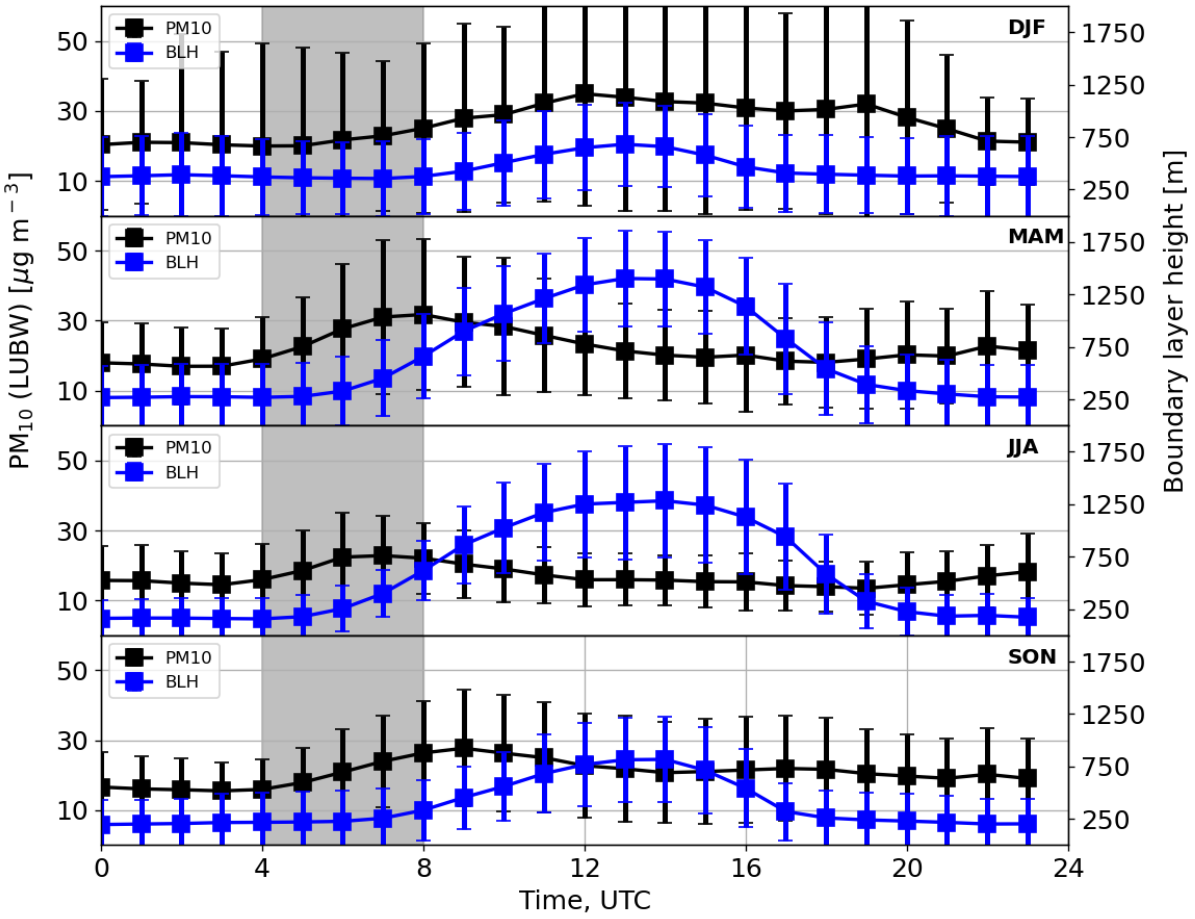

Figure 3.15: Diurnal variations of PM_{10} and boundary layer height (BLH) for different seasons (Winter: DJF, Spring: MAM, Summer: JJA, Spring: SON) based on two years data from January 1^{st}, 2020 to January 1^{st}, 2022 in Stuttgart. (PM_{10} concentrations are hourly reported by Landesanstalt für Umwelt Baden-Württemberg (LUBW) and the BLH are from an ERA5 dataset).

the lowest MLH as expected due to the solar radiation being strongest in summer while weakest during winter. The ground aerosol concentration is anti-correlated with the mixing layer heights and shows the highest concentrations during winter and the lowest concentrations during summer. From the correlation between PM_{10} concentration and boundary layer heights, I concluded that the ground-level aerosol concentration was anti-correlated with the MLH but correlated with the stable boundary layer height.

3.2.2 Boundary layer dynamic and surface level aerosol - a case study

In Figure 3.10, the boundary layer dynamics, ground-level aerosol concentration, aerosol composition, and related meteorological parameters were illustrated for the whole experiment period. In

this section, two cases are discussed in detail to better understand the boundary layer dynamics, ground-level aerosol, and air quality in downtown Stuttgart in winter. Figure 3.16 demonstrates an overview of one case (called case 1). Figure 3.16a shows the time series of lidar retrieved backscatter coefficients, the BLH (white line), the RLH (white dash line), and the boundary layer from an ERA5 dataset (grey dash line) as well as the BLH retrieved from radiosonde (yellow triangles). Please note that the altitude used here is the height above sea level. The reason for using this altitude is that the altitude of these three observation stations is different as shown in the left of Figure 2.10 and the usage of the same altitudes make these observations comparable. The vertical dis-

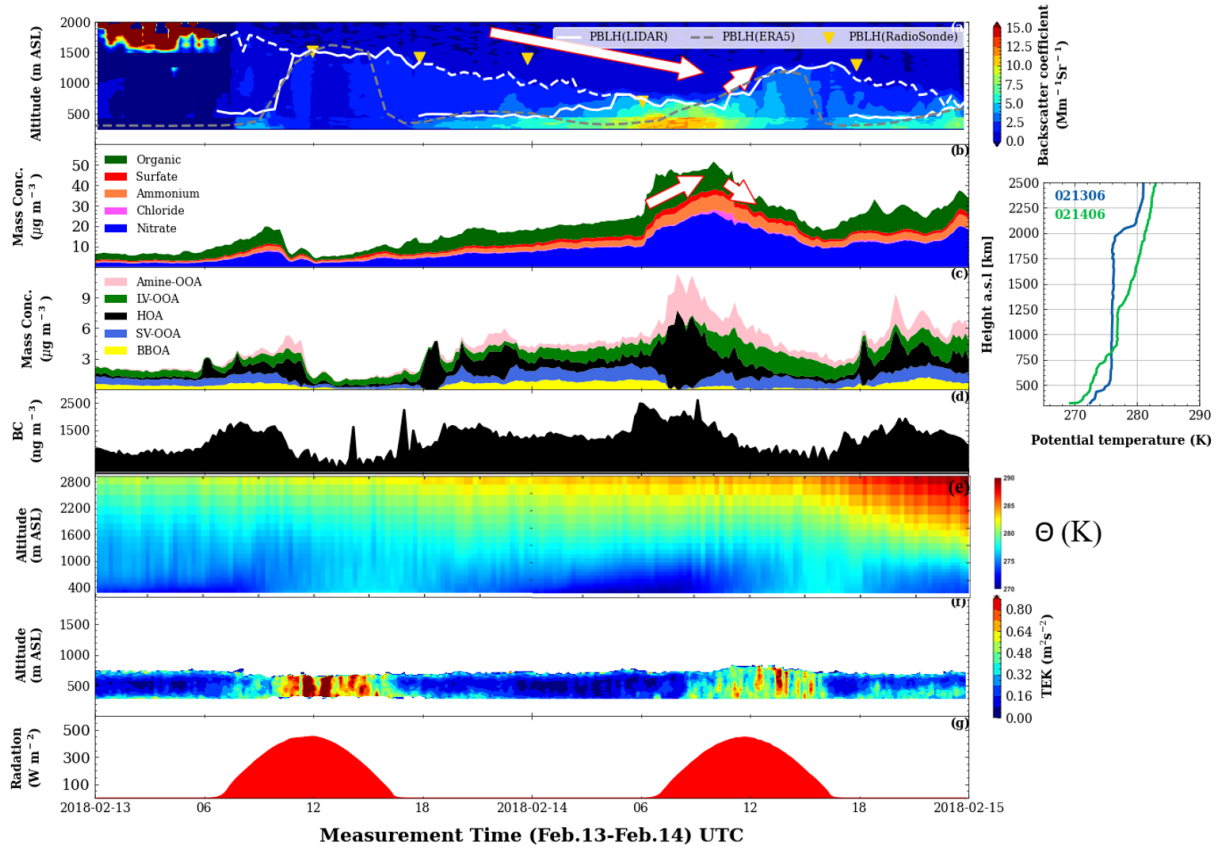

Figure 3.16: Time series of backscatter coefficients from lidar measurements (contour plot), the boundary layer height retrieved from lidar data (white line) and DWD radiosonde (yellow triangle) (a), the aerosol mass concentrations measured by Aerosol Mass Spectrometry (AMS) (b), five-factor Positive Matrix Factorization (PMF) solution of organic aerosol source factors (c), black carbon (BC) concentration (d), potential temperature measured by Microwave Radiometer (MWR) (e), Turbulent Kinetic Energy (TKE) retrieved from Doppler lidar (f) as well as the global radiation measured by a meteorological sensor (WS700) (g) for case 1 from February 13^{rd} to February 14^{th}, 2018. The inserted plot on the right side shows the potential temperature measured by radiosonde at 06:00 of 13^{rd} (blue) and 14^{th} (red), February 2018.

tribution of backscatter coefficients are shown from ground level to free troposphere. They were calculated from zenith and near horizontal (5° above the horizon) measurements and allow thus also determination of data close to the ground level. Despite an overlap range of about 200 m for the scanning lidar, the analysis of measurement a 5° elevation angle allows retrieval of backscatter and extinction coefficients down to about 10 m above ground level. The time series of aerosol chemical composition measured by AMS is shown in Figure 3.16b. A PMF analysis of the OA resulting in 5 major source factors is shown in Figure 3.16c. In addition, the potential temperature from MWR and Turbulent Kinetic Energy (TKE) from wind lidar are shown in Figures 3.16e and Figure 3.16f, respectively. Finally, BC concentration and solar radiation are shown in Figure 3.16d and Figure 3.16g, respectively. The backscatter coefficients in this figure show that aerosol particles can only reach a maximum height of 1800 m (below BLH) for the whole period, which indicates that most aerosol stayed within the boundary layer or residual layer and could not reach to free troposphere as stated in previous literature (Su et al. 2018, Quan et al. 2013, Yuval et al. 2020, Li et al. 2017*b*, Guo et al. 2009). I also found that the mixing layer heights measured by lidar and radiosondes show a good agreement for this case. A decreasing trend of the residual layer and a rather constant, maybe slowly increasing stable boundary layer at around 550 $\pm$ 93 m above sea level can be seen during the night time. The shallow and stable boundary layer and increased emission during morning rush hours (05:00 a.m. - 10:00 a.m.) caused accumulation of aerosol near the surface as can be seen from low-attitude backscatter coefficients and *in-situ* measurements at ground level. Then, an expanding boundary layer driven by solar radiation after 10:00 on February 14^{th} diluted the aerosol in the boundary layer, thus causing a decrease of aerosol concentrations at ground level. Furthermore, I found that the aerosol concentrations increased more in morning rush hours (05:00 - 10:00) than in evening rush hours (17:00 - 20:00) due to the shallow boundary layer in the morning hours. Increasing aerosol concentrations during morning and evening rush hours is related to the emissions of traffic (HOA) and industry (Amine-OOA) as can be seen from a PMF analysis shown in panel (c). At night time, a potential temperatureinversion shown in panel (e) and small values TKE shown in panel (f) indicate a stable and shallow boundary layer.

A more interesting phenomenon in this case is that the boundary layer increased faster on the first day (February 13^{th}) than that on the second day (February 14^{th}), which means that there is a time delay of boundary layer rising on the second day. But the solar radiation is the same for these two days as shown in Figure 3.16g. The reason for these different boundary layer behaviours is due

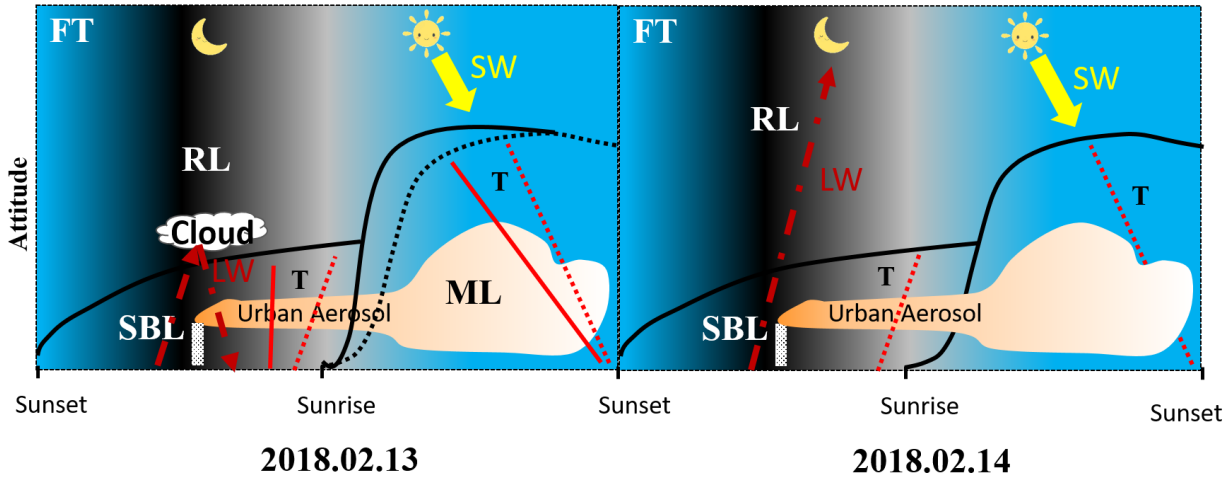

Figure 3.17: A schematic figure showing the boundary layer and the feedback of a cloud on the boundary layer evolution. The red lines labled with "T" illustrate the air temperature profile (solid and dotted lines show scenario for cases with a cloud and without a cloud during the previous night). The yellow arrow lines with "SW" denote the solar short wave radiation and the dashed red line with "LW" denote the terrestrial long wavelength emission. (SBL: Stable Boundary Layer RL: Residual Layer ML: Mixing Layer LW: Long wavelength Radiation FT: Free Troposphere)

.

to different vertical thermal structures as can be seen in the vertical temperature profiles shown in Figure 3.16d as well as the vertical profiles of temperature measured by radiosonde at 06:00 of 13^{rd} and 14^{th}, February 2018 as shown in the right side of Figure 3.16. On the first day, the temperature inversion is weaker and the TKE is larger than on the second day as can be seen from Figure 3.16d and Figure 3.16e, which means that it takes a shorter time to transform the stable boundary layer (SBL) into a CBL. Hence, the boundary layer increases faster on the first day than on the second day. One explanation of this thermal structure difference is because of the existence of clouds on the night of the first day. This cloud hindered the long wave emission during the nighttime, hence causing a higher temperature at the surface and a weaker temperature inversion on the first day. In conclusion, the existence of clouds on the first day prevented long wave emission and weaken the temperature inversion, which would cause a neutral layer during the night time and the boundary layer would increase faster after sunrise. The conceptual schematic for this phenomenon is illustrated in 3.17. In addition, the slower increase of the boundary layer on the second day presented diffusion of aerosol during morning rush hour (5:00 - 10:00, February 14 th), thus causing accumulation of aerosol at ground level as shown in Figure 3.16a-c.

Figure 3.18 shows an overview of another case (called case 2), in which I used the same methods as case 1 but the data were collected from 24^{th} to 25^{th}, February 2018. The most obvious obser-

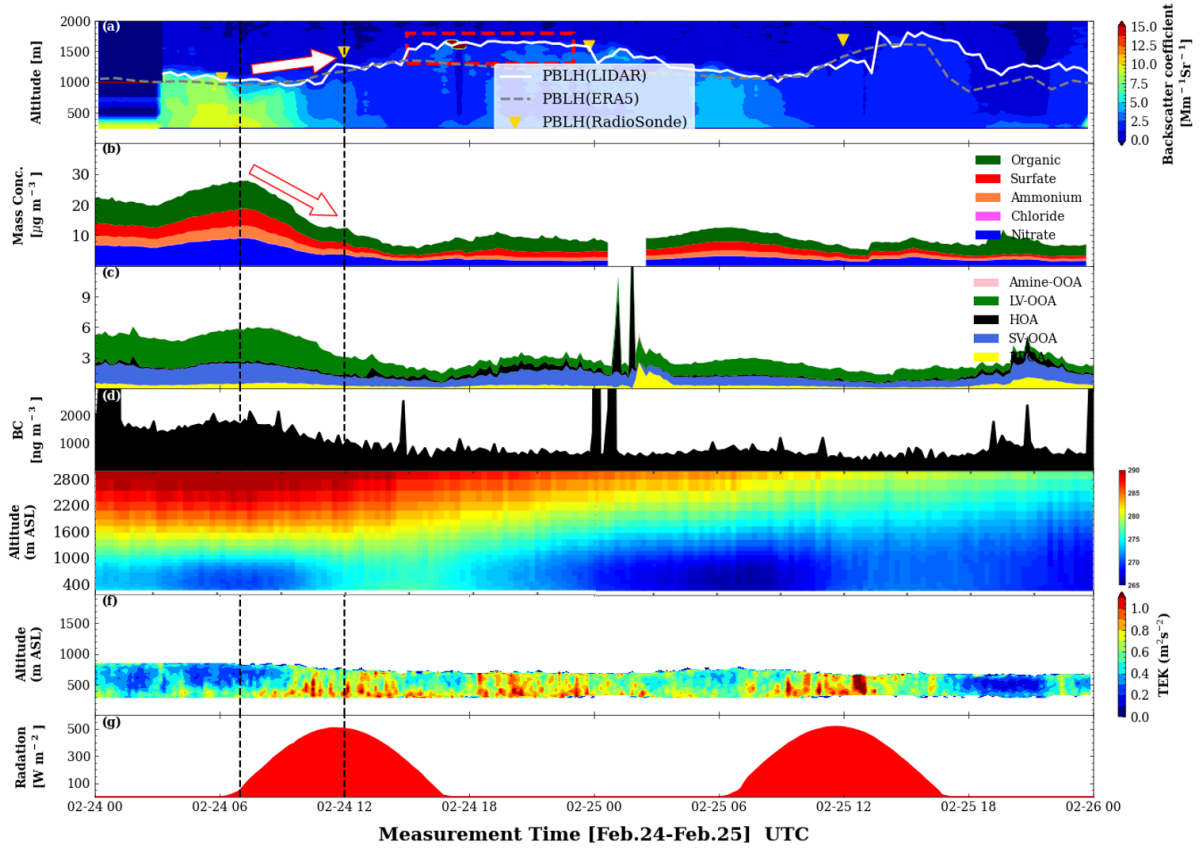

Figure 3.18: Time series of backscatter coefficients from lidar measurements (contour plot), the boundary layer height retrieved fron lidar data (white line) and the DWD radiosonde (yellow triangle) (a), the aerosol mass concentrations measured by Aerosol Mass Spectrometry (AMS) (b), five-factor Positive Matrix Factorization (PMF) solution of organic aerosols(c), black carbon concentration (d), potential temperature measured by Microwave Radiometer (MWR) (e), Turbulent Kinetic Energy (TKE) retrieved from Doppler lidar (f) as well as the global radiation measured by meteorological sensors (WS700) (g) for case 1 from February 24^{th} to February 25^{th}, 2018.

vation or difference for case 2 is a sharp decrease of aerosol particles from 07:00 to 12:00, 24^{th}, February 2018. Even though the BLH only increased from 1042 m to 1280 m. In addition, the BLH did not decrease after the sunset of February 24^{th} as shown in the red rectangle in Figure 3.18a. Furthermore, the boundary layer measured by radiosonde is higher than that derived from lidar measurements. I also found that the aerosol at ground level was much lower on 25^{th}, February 2018 than that on 24^{th}, February 2018 corresponding to a higher boundary layer on February 25^{th}. Finally, the PMF analysis result shown in panel (c) reveal a large fraction of the organic aerosol particles comprises of LV-OOA which is related more to long-range transport.

Figure 3.16 and Figure 3.18 showed the different boundary layer behaviors and different patterns of aerosol concentration at ground level even with the similar evolution of solar radiation as shown

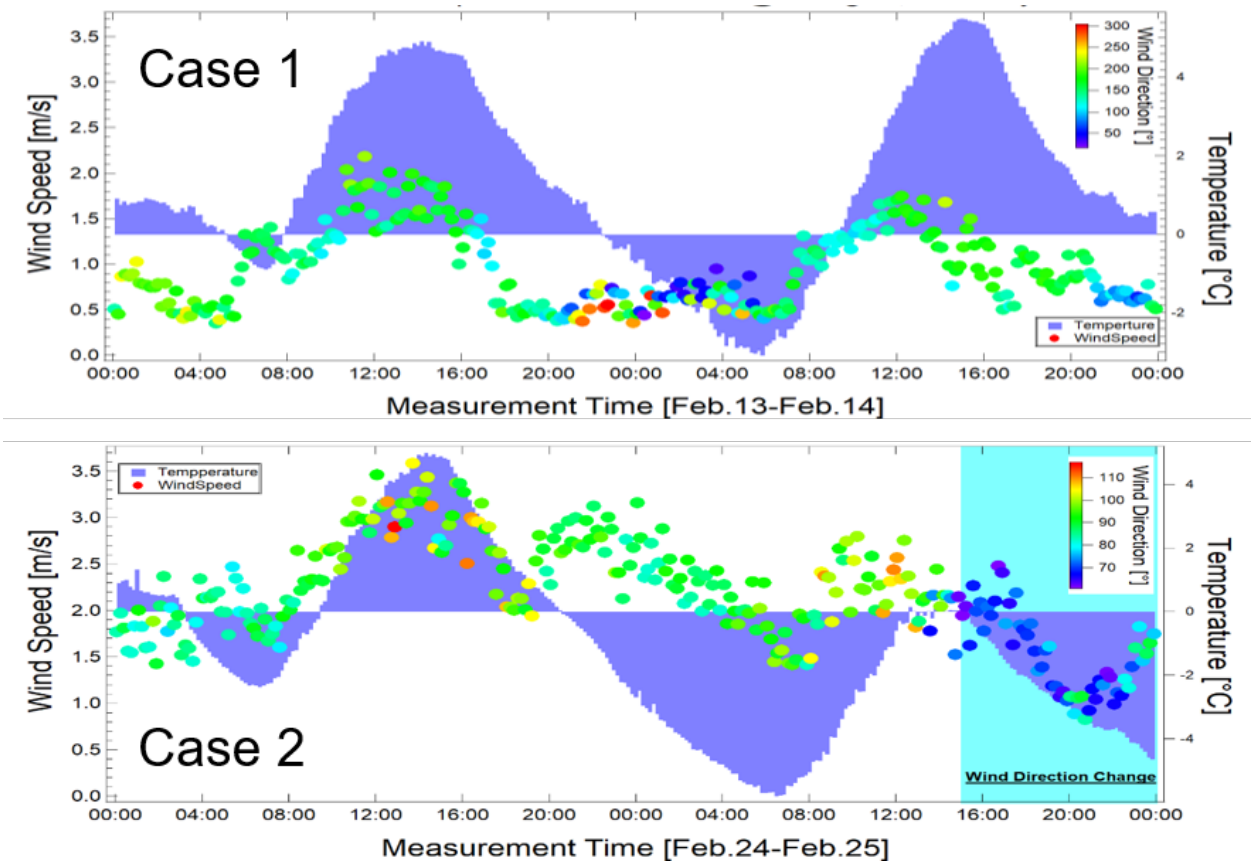

Figure 3.19: Time series of temperature and wind for case 1 (upper panel) and case 2 (bottom panel).

in the panel (e) of both figures. However, the evolution of temperature and wind are different as shown in Figure 3.19. Comparing the meteorological background in these two cases, we can find that the temperature decreased more sharply in case 2 than that in case 1. This decrease caused a low temperature on 25^{th}, February 2018 as indicated that the temperature was below 0° C even during daytime on 25^{th}, February 2018. In addition, a higher wind speed can be found from 00:00 on 24^{th}, February to 16:00 on 25^{th}, February 2018 for case 2. Then, the wind speed began to decrease, and the wind direction also changed from east to north since 16:00, 25^{th}, February 2018. All this meteorological information indicate that a cold front passed by the observation station from 24^{th}, February to 25^{th}, February 2018 affected local temperature and wind, thus having an impact on the boundary layer behavior and aerosol distribution in the boundary layer. The high wind speed during this cold front causes stronger turbulences in the boundary layer as shown in Figure 3.18f, thus increasing the BLH, especially at nighttime. In addition, this high wind speed also blew the local aerosol away and caused a low aerosol concentration on 25^{th}, February 2018.

From the above two cases, I conclude that the evolution of the boundary layer was affected by

related meteorological parameters such as solar radiation, wind speed, and wind direction, thus affecting the aerosol dilution and transport in the boundary layer. The general relationship is that the ground-level aerosol concentration is anti-correlated with BLH, which means that a low boundary layer will lead to accumulation of aerosol near ground level, thus causing high aerosol concentrations near the surface layer as stated in previous literature. (Su et al. 2018, Quan et al. 2013, Spracklen et al. 2006).

3.2.3 Potential comparison of LES simulation (PALM-4U) with experimental observations

In this work, I wanted to compare my observational results with those of the high-resolution (10 m) LES model, PALM-4U. Although modellers (Dr. Christopher Holst and Dr. Basit Ali Khan, IMK-IFU) have made substantial progress to run the model including the transport of aerosol particles, still no reliable data are available for comparison. However, this should be the case in the near future and become part of my first author publication on the boundary layer and air pollution evolution in the city of Stuttgart.

In this section, I show which observational results (cf. Figure 3.20) I plan to compare with the model results and what scientific questions I expect to answer based on comparison with the model simulation. Firstly, I will do this comparison for the time series of particulate matter concentrations ($PM_{2.5}$ & PM_{10}) as shown in Figure 3.20b. Secondly, I will compare the vertical profiles of backscatter coefficients from lidar measurements as shown in Figure 3.20a with vertical profiles of aerosol particle concentrations from the model predictions to better understand the mechanism of aerosol boundary layer interaction. Thirdly, I intend to compare the plane of the measured backscatter coefficients with three-dimensional model-predicted aerosol distributions to investigate the horizontal and vertical distributions in the basin-like topography of Stuttgart. In the plane of the measured backscatter coefficient, I chose two time periods (one in the morning rush hour as shown in Figure 3.20c and one in the later afternoon as shown in Figure 3.20d) to study the evolution of the boundary layer and the corresponding aerosol distributions.

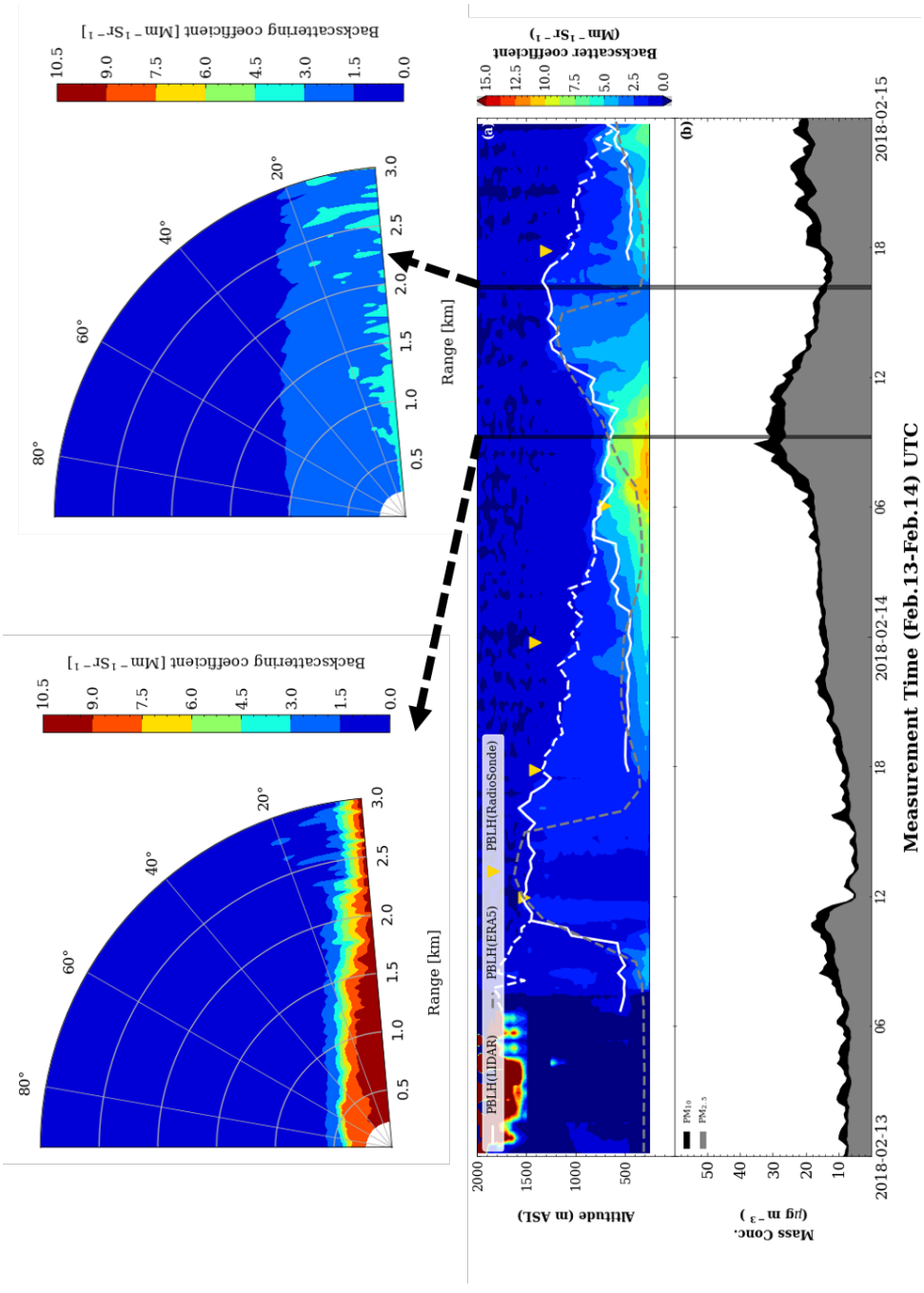

Figure 3.20: Time series of backscatter coefficients from lidar measurements (middle contour plot), the boundary layer height retrieved from lidar data (white line) and DWD radiosonde (yellow triangles) (a), particulate matter concentrations ($PM_{2.5}$ & PM_{10}) from OPC (b), and planes of the backscatter coefficients for two selected time periods (c: 09:12-09:19; d: 16:07-16:15) for case 1 from February 13^{rd} to February 14^{th}, 2018.

3.2.4 Summary

In this section I investigated boundary layer dynamics and its correlation with ground-level aerosol particle concentrations by combining remote sensing methods, ground-level *in-situ* measurements, radiosonde data, and the PALM-4U high resolution LES model for downtown Stuttgart in winter. A major advantage of the scanning lidar, KASCAL is, that it can measure the boundary layer structure with high spatial resolution and vertical profiles of aerosol particles down to about 10 m above ground level despite an overlap range of 200 m employing low elevation angles. This attitude range is usually in the overlap region which is not accessible for traditional vertically pointing lidars. This allows direct comparison of lidar data with ground-level *in-situ* measurements to achieve a better understanding of the interaction between the boundary layer dynamics and aerosol concentrations. I could show that the BLH retrieved from lidar has a good agreement with that from radiosonde retrievals with a slope of 1.102 ± 0.135 and a Pearson correlation coefficient of 0.86, respectively. This agreement reflects also a good quality of our measurements and retrieval algorithms. Stagnant meteorological pattern with strong temperature inversion and low wind speeds can cause an accumulation of aerosol particles near ground level, thus causing air pollution especially in cities with topographic wind barriers. Ground-level aerosol concentrations are anti-correlated with the MLH as stated in previous literature but are correlated with the SBL height due to strong emissions during morning rush hours. For two selected cases, I could show that the diurnal evolution of the boundary layer was strongly affected by solar radiation, temperature, as well as wind, and can substantially differ for different meteorological conditions. Even clouds present only during night time can already weaken a temperature inversion causing a faster increase of the BLH after sunrise than in without a cloud. In addition, these observational data can be used to validate the large eddy simulation model, PALM-4U, simulating the evolution of the boundary layer and the spatial-temporal distribution of aerosols in Stuttgart with a spatial resolution of 10 m. In conclusion, I could show how the boundary layer dynamics impacted air pollution in a city with a basin like topography and this should allow a quantification of aerosol emissions, transport, and dilution with a validated PALM-4U model in the near future.

3.3 Urban and rural boundary layer dynamics in summer

This chapter presents results of boundary layer dynamics, aerosol concentrations, and chemical compositions during summer heat wave periods by combining scanning aerosol lidar, *in-situ* measurements at ground level and on the UAV flights. The aim of this chapter is to illustrate the boundary layer dynamics and aerosol distributions in summer to compare these results with the results in winter time as presented in chapter 3.2. These two chapters discuss the seasonal variation of boundary layer dynamics and its relationship with aerosols. In this chapter, the data collected in three field campaigns (Jülich MOSES, Swabian MOSES, and Karlsruhe Mülldeponie West) will be presented. During the Jülich MOSES campaign, the scanning aerosol lidar and airborne *in-situ* instruments were deployed. During the other two field campaigns, the same scanning aerosol lidar and ground-level *in-situ* instruments were used. Detailed information on methods used in these field campaigns can be found in "Jülich MOSES", "Swabian MOSES", and "Karlsruhe" sections.

3.3.1 Boundary layer dynamics during the summer heat wave in Jülich

During the Jülich MOSES field campaign, the KASCAL did zenith scanning measurement from 90° to 5° with steps of 5° as stated in chapter 2 together with UAV flights. The UAV conducted two-day fights on 9^{th} and 12^{th}, July 2018 as shown in table 3.1. In this experiment, the PBL heights were retrieved from both KASCAL and the *in-situ* meteorological sensor on the UAV. The boundary layer heights retrieved from lidar measurements can be compared with that from UAV measurements and from an ERA5 dataset provided by the European Centre for Medium-Range Weather Forecasts (ECWMF). Figure 3.21 shows the time series of backscatter coefficients and boundary layer retrieved from lidar measurement (pink solid line) as well as BLH obtained from the ERA5 dataset (white dashed line) and potential temperature obtained from UAV measurements (white solid line) on 9^{th}, July 2018 in Jülich. This figure shows that the boundary layer heights retrieved from the lidar measurements is consistent with the BLH from the UAV measurements (the maximum gradient of potential temperature) which both show an increasing trend of the BLH during the morning of this day. In addition, the boundary layer data from ERA5 also shows a similar trend as the above observations but overestimate BLH especially with increasing time of the day. A possible reason for this overestimation is the appearance of clouds during daytime preventing solar radiation reaching the surface and reducing convective mixing and hence leading to a lower

boundary layer. This figure also shows the stable nocturnal boundary layer and the residual layer (red squares) during nighttime measured by KASCAL. The low and stable boundary at night time can suppress the dispersion of aerosol near the surface level. Hence, the backscatter coefficients within the boundary layer are maximum (highest aerosol concentration) during the morning rush hour due to the combined effect of the shallow boundary layer and local anthropogenic emission. After sunrise, the convection became stronger, which caused an increase in the boundary layer and dilution of aerosol within the boundary layer, so the aerosol concentration within the boundary layer decreased.

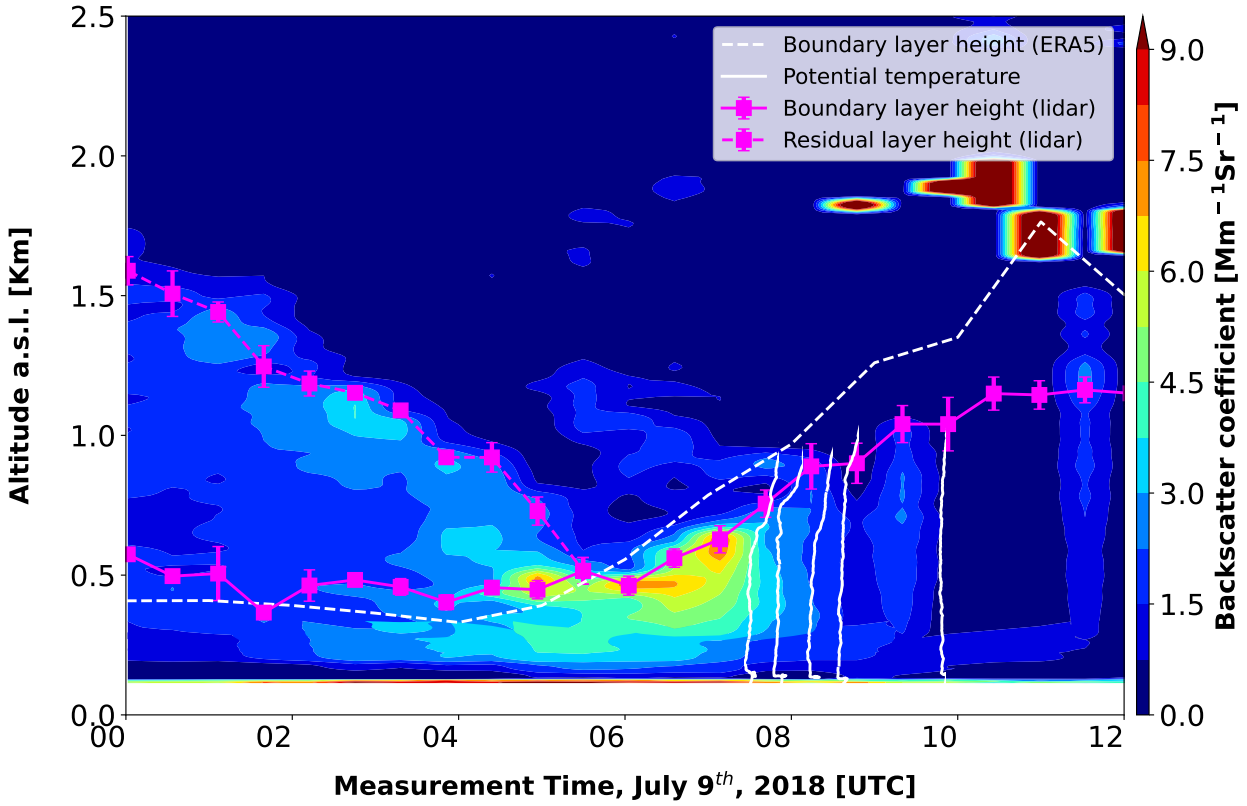

Figure 3.21: Time series of backscatter coefficients (contour) and boundary layer heights (pink; residual layer in red) retrieved from KASCAL as well as boundary layer heights obtained from an ERA5 dataset (dashed white line) and potential temperature measured by UAV flights (white lines) on 9^{th}, July 2018.

Figure 3.22 shows a time series of RCS and boundary layer heights retrieved from lidar as well as boundary layer heights obtained from an ERA5 dataset (white dash line) and potential temperature obtained from UAV measurements (white solid line) on 12^{th}, July 2018. On this day, 7 flights of the UAV were launched from the early morning to the later afternoon to study the boundary layer evolution. This figure also shows consistency in boundary layer heights among data from lidar,

UAV, and ERA5. From this figure, we can also see that clouds played a role. More interestingly, the clouds were located at the top of the boundary layer from 05:00 to 13:00 and the cloud base increased with BLH as captured by the lidar measurements. The reason for the cloud formation at the top of the boundary layer is that the relative humidity has a maximum value at the top of the boundary layer in the well-mixing boundary layer. This high humidity environment with a relatively high number of potential cloud condensation nuclei provided a good opportunity for cloud formation.

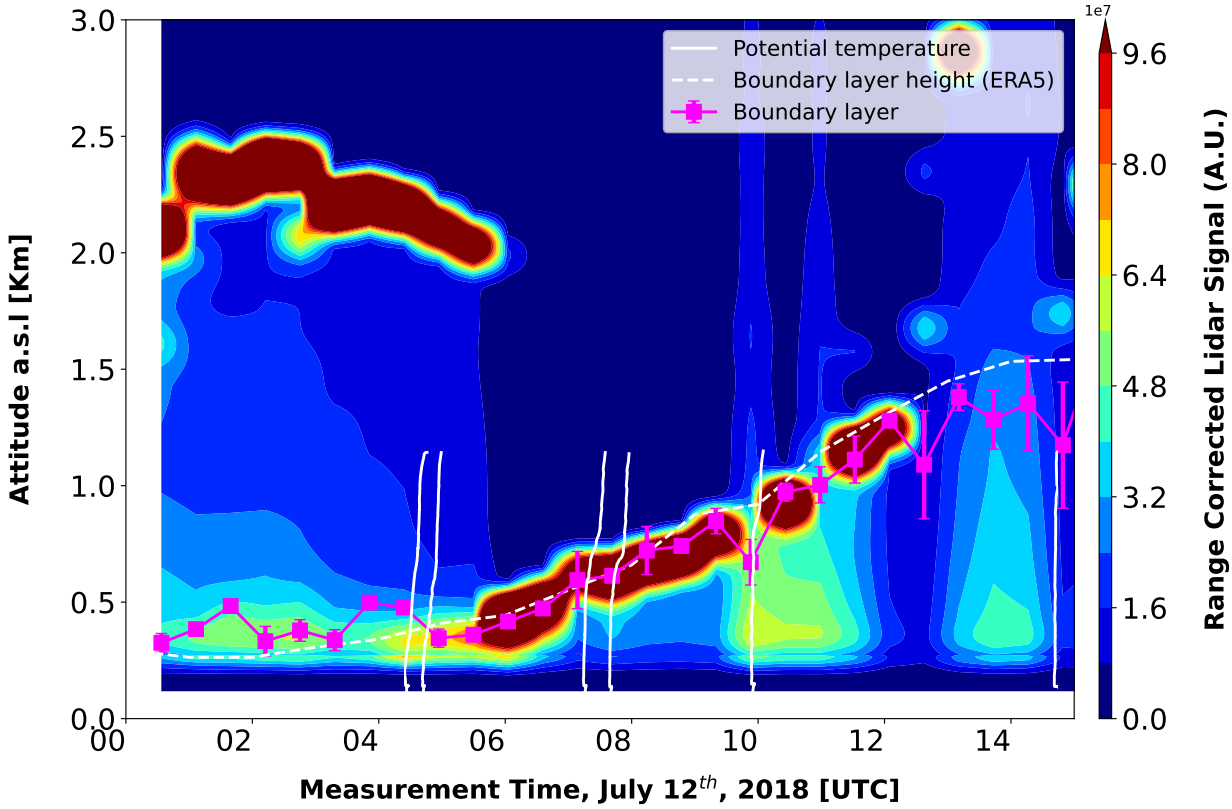

Figure 3.22: Time series of range corrected lidar signals (contour)and boundary layer heights (pink squares) retrieved from KASCAL as well as boundary layer heights obtained from ERA5 dataset (dashed white line) and potential temperature measured by UAV flights (white lines) on 12^{th}, July 2018 in Jülich.

In addition to the zenith scanning measurement shown above, the KASCAL also did azimuth scanning measurement with an elevation angle of 5°. This near-horizontal scanning measured the aerosol spatial distribution of aerosol near the surface. Figure 3.23 shows maps of the horizontal distribution of backscatter coefficients retrieved from the scanning aerosol lidar at three different periods on 11^{th}, July 2018. The maps show the evolution of aerosol particles' horizontal distributions and the dissipation of aerosol particles near the observation station. The evolution of aerosol

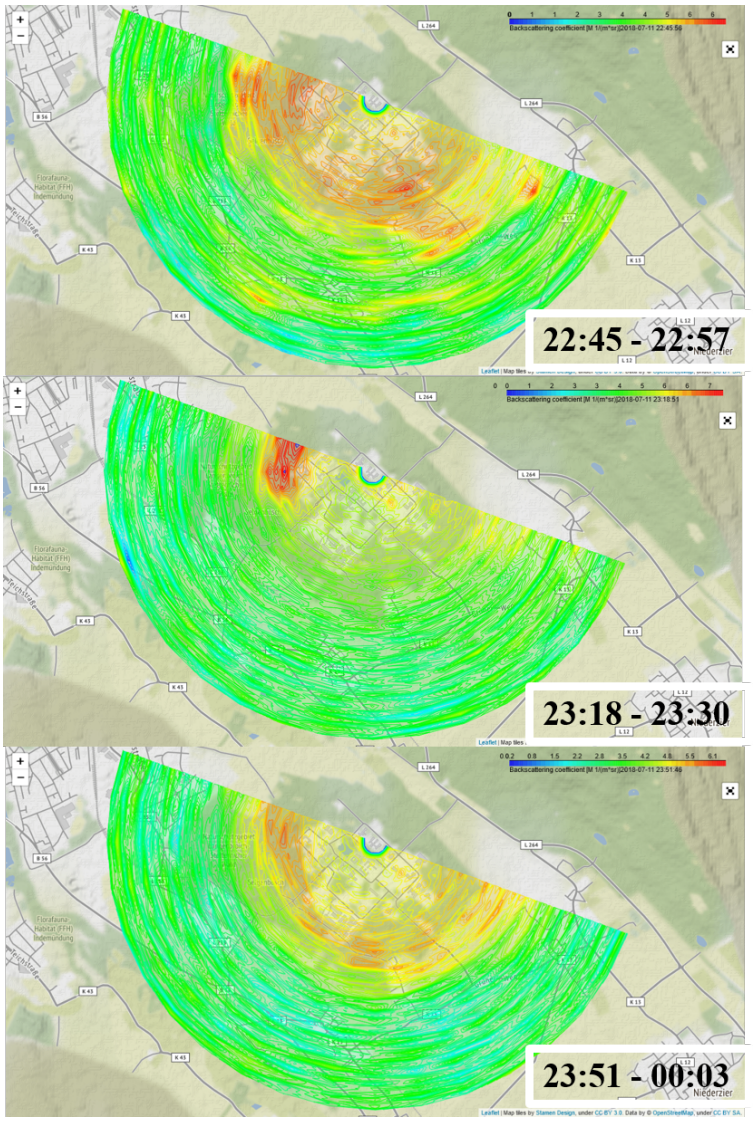

Figure 3.23: Maps of horizontal distribution of backscatter coefficients retrieved from the scanning aerosol lidar at three different periods on 11^{th}, July 2018. The radius of the sector shown on the map is 3.0 km.

horizontal distribution shown in these maps can be used to validate the high-resolution LES result.

3.3.2 Boundary layer dynamics during a summer heat wave in Rottenburg

During the Swabian MOSES campaign, the KASCAL did zenith scans from 90° to 5° with the steps of 5° at two perpendicular azimuth angles. One mobile container carrying different aerosol characterization instruments was deployed with the KASCAL on the roof of the container. Figure 3.24 shows the time series of backscatter coefficient and boundary layer retrieved from KASCAL as well as boundary layer heights from an ERA5 dataset, particle matter concentrations measured by OPC, and solar radiation measured by the meteorological sensor from 22^{nd} to 24^{th}, July 2021

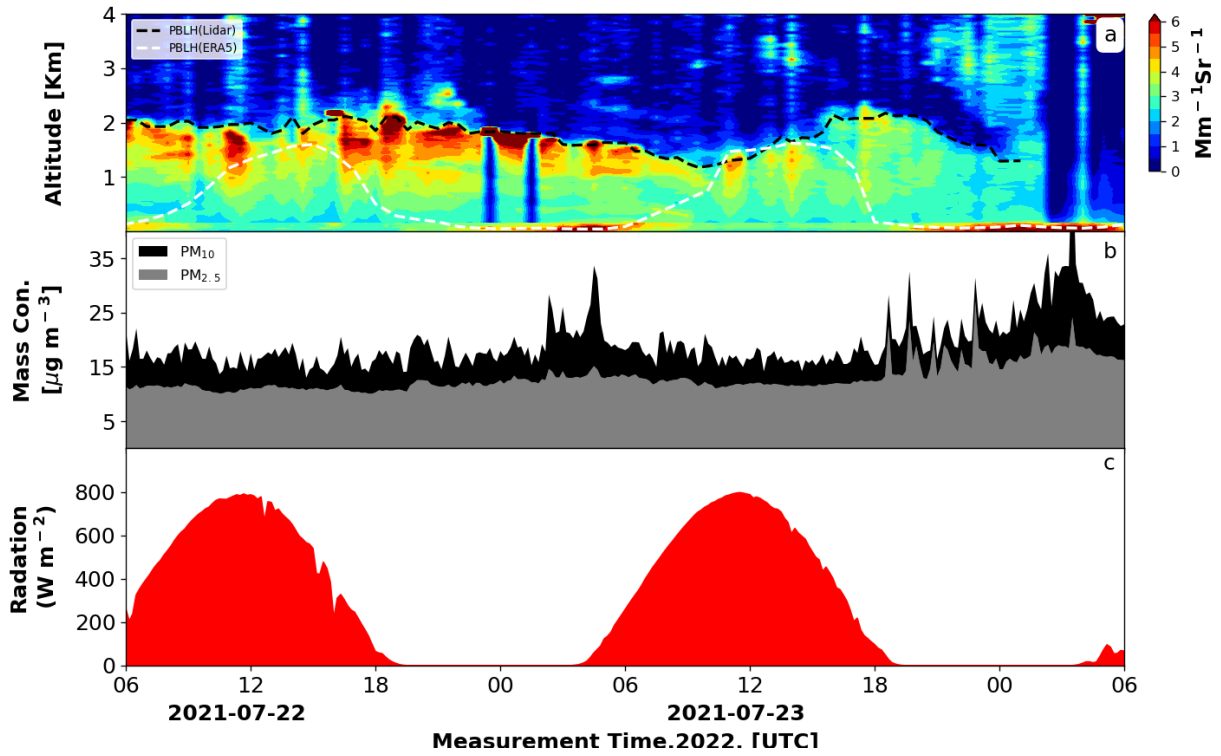

Figure 3.24: Time series of backscatter coefficients (contour) and boundary layer heights (dashed black line) retrieved from KASCAL as well as boundary layer heights obtained from an ERA5 dataset (dashed white line) (a), particulate matter concentration measured by Fidas200 (b), and solar radiation measured by a meteorological sensor (c) from 22^{nd} to 24^{th}, July 2021 in Rottenburg am Neckar.

in Rottenburg am Neckar. This figure shows that the BLH retrieved from KASCAL seems to be at an altitude of around 2.0 km with relatively small diurnal variations. However, during night time and especially in the early morning a shallow stable boundary layer becomes visible associated by strong temperature inversion. The vertical backscatter coefficients have their maximum value at the top of the boundary layer. One explanation for this phenomenon is that the aerosol and water vapor were well-mixed due to strong convection during summer time and this well-mixed boundary has the maximum value of relative humidity at the top of the boundary layer. This high relative humidity caused a large backscatter coefficient value at the top of the boundary layer due to hygroscopic growths of the aerosol particles. Compared to the observations in Jülich the aerosol didn't fully activate to cloud droplets. In addition, the boundary layer from ERA5 dataset is consistent with that retrieved from KASCAL at noon (MLH) and also shows a shallow SBL during the night and morning hours. In addition, the particle matter concentrations in Figure 3.24b shows relative constant values due to relative constant boundary layer heights but still are anti-correlated with BLH with peaks during the night and early morning hours.

3.3.3 Boundary layer dynamics and horizontal aerosol distributions during a summer heat wave in Karlsruhe

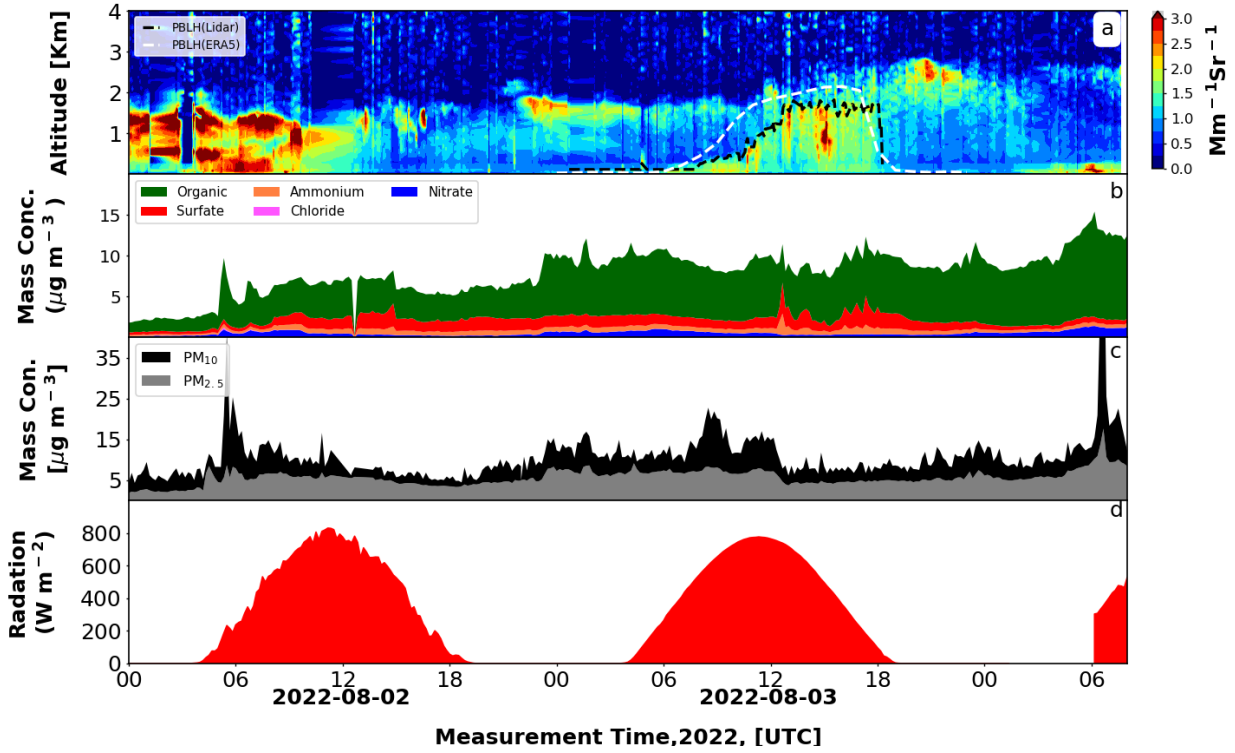

Figure 3.25: Time series of backscatter coefficients (contour) and boundary layer heights (dashed black line) retrieved from KASCAL as well as boundary layer heights obtained from an ERA5 dataset (dashed white line) (a), aerosol chemical composition measured by Aerosol Mass Spectrometry (AMS) (b), particulate matter concentrations measured by Fidas200 (c), and solar radiation measured by a meteorological sensor (d) from 2^{nd} to 4^{th}, August 2022 in Karlsruhe on top of a hill 50 m above ground level.

During the Karlsruhe Mülldeponie West field campaign, the KASCAL was deployed on the roof of a mobile 16-feet container which contained various instruments to characterize aerosol particles and trace gases. The KASCAL did zenith scans from 90° to 0° with the steps of 15° at four azimuth angles (north, east, south, and west). In addition, the KASCAL also did horizontal scans (from 90°to 243° with step of 17°) with a time resolution of 30 minutes to measure the horizontal aerosol particle distribution over downtown Karlsruhe. This scanning mode aims to investigate the boundary layer dynamics for different underlying surfaces and the spatial-temporal distribution of aerosol particles over Karlsruhe during a heatwave period in summer 2022. A detailed description of this field campaign can be found in section 2.4.

Figure 3.25 shows the time series of backscatter coefficients (contour) and BLH (dashed black line)

retrieved from KASCAL as well as boundary layer heights obtained from ERA5 dataset (dashed white line), aerosol chemical composition measured by the AMS, particulate matter concentration measured by an OPC, and solar radiation measured by a meteorological sensor from 2^{nd} to 4^{th}, August 2022 in Karlsruhe near the Rhein habour. Evolution of the boundary layer including the residual layer is clearly visible in the lidar data. This figure also shows smoke plumes (a layer with a large value of backscatter coefficient (> 2 Mm^{-1}) but a low value of particle depolarization ratio (< 0.05)) over the observation station and this smoke plume touched to ground level before 10:00 on 2^{nd} to 4^{th}, August 2022 as indicated by peak values of PM10. These smoke plumes may originate from forest fires in south of Europe (Spain, Portugal, Italy) or even France according to back-trajectories calculated by HYSPLIT model. This figure also shows the transition of the SBL to a CBL after sunrise on 3^{rd}, August 2022, with an increase of BLH from 200 m to 2000 m and dilution of local aerosols during daytime. The BLHs from an ERA5 dataset shows a similar trend but systematically higher values than that retrieved from KASCAL for this case. This may be due to the limited resolution of the ERA5 data. The aerosol chemical composition shows that organic aerosol is dominant during the summer period which is in agreement with previous studies (Huang et al. 2019, Song et al. 2022, Jiang et al. 2022). In addition, the peak value of particulate matter concentrations is consistent with the peak value of the backscatter coefficient at low attitudes at 06:00 of 2^{nd} and 4^{th}, August 2022 and this consistency reflects good data quality of our measurements in both remote sensing and *in-situ* methods.

Figure 3.26 shows a time series of particulate matter concentrations ($PM_{2.5}$ & PM_{10}) (d) measured by a Fidas200 as well as horizontal distributions of backscatter coefficients retrieved from scanning aerosol lidar data for three different periods during July 26^{th}, 2022. These map plots show the horizontal distribution of aerosol nearby the observation station. Please note that the radius of the sector shown on the map is 2.0 km, which corresponds to the maximum detection range in these cases. In addition, there is no lidar data within 200 m from the lidar position due to the overlap limit of this lidar system. The lidar measurements show a good agreement with *in-situ* measurement. The strong intensities of the backscatter coefficients near or at the observation station as shown in Figure 3.26a and Figure 3.26c correspond to peak values of particulate matter concentrations as shown in 3.26d. The unexpected increase of aerosol particles shown in these two periods is caused by dust emission from a nearby construction site and this construction site is in about 200 m distance south of our observation station. In Figure 3.26b, smoke was detected by the scanning

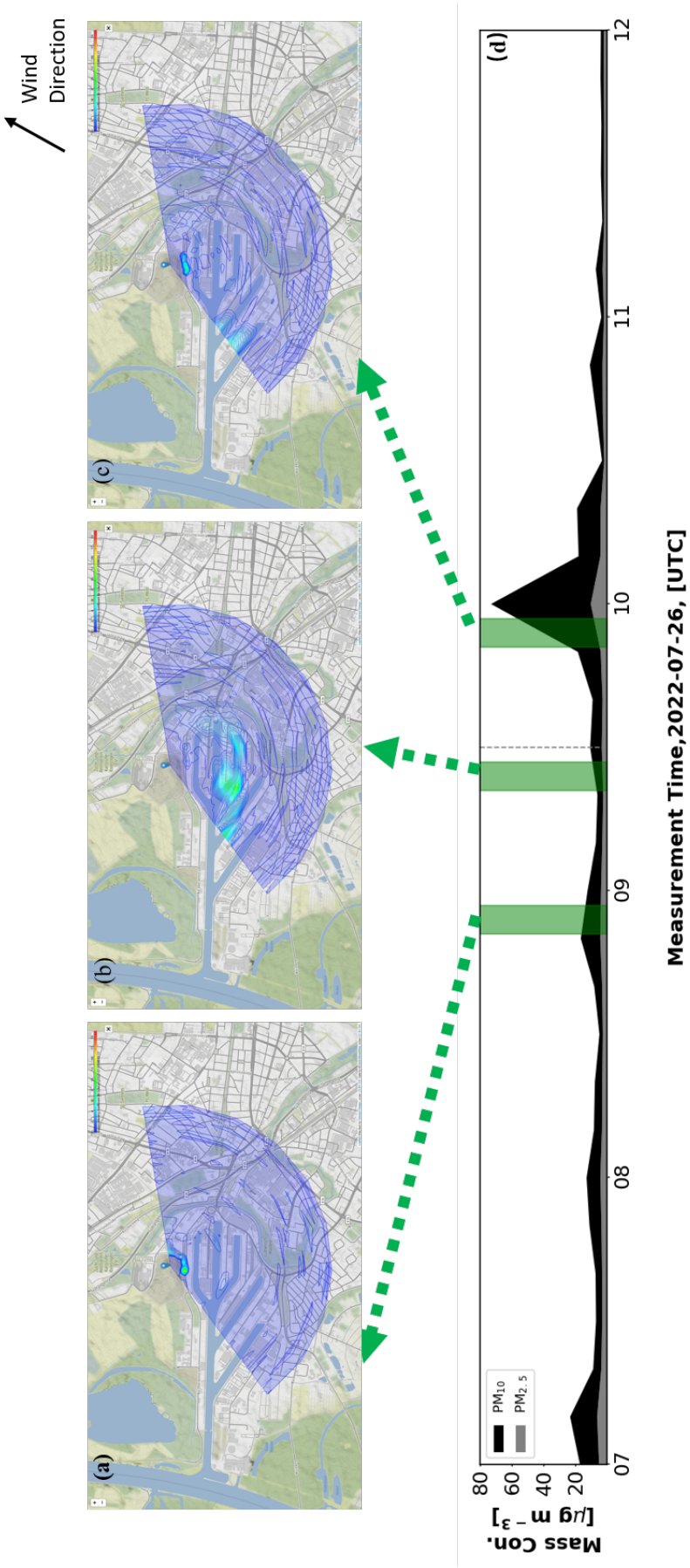

Figure 3.26: Map of horizontal distribution of backscatter coefficients retrieved from the scanning aerosol lidar (a, b, c) at three different periods as well as time series of particle matter (PM) concentrations measured by Fidas200 (d) on July 26^{th}, 2022. The radius of the sector shown on the map is 2.0 km. The mean wind direction from 8:00 to 10:00 is shown in the upper right corner of this plot.

aerosol lidar at a distance of around 1 km away from the observation station. About 3 minutes later, a small aerosol peak concentration was measured by the Fidas200 as shown in the grey dashed line in Figure 3.26d. The wind speed was measured to 5 m/s with the direction as indicated in the right upper corner of this figure from 08:00 to 10:00, which matched very well with the aerosol transport speed. This good agreement between lidar retrievals and *in-situ* measurement reflects the good quality of our observation data. However, the lidar horizontal scans did not resolve the movement of aerosol particles due to the coarse temporal resolution of scanning lidar measurement (30 min per scanning plane). Further field experiments can increase this temporal resolution of lidar scans to better resolve the transport of local aerosol in the urban and industrial area. This kind of high-resolution observational data can then be used to validate high-resolution LES models.

3.3.4 Summary

In this chapter, I presented an overview of boundary layer evolution and corresponding ground-level aerosol concentrations during summer heat waves by combining a scanning aerosol lidar, *in-situ* measurements at ground level and on an UAV. The boundary layer evolution at the three different locations for typical summer heat waves are quite similar showing shallow stable boundary layers with high aerosol concentrations during the night and early morning hours with intensive residual aerosol structures. All cases showed a dynamic increase of BLH in the morning and substantial aerosol particle mixing and dilution until noon. The summer boundary layer increased faster after sunrise than that in winter due to stronger solar radiation during summer, resulting in effective dilution and lower aerosol concentrations than in winter. In addition, the comparison of horizontal lidar scans with *in-situ* measurements show a good agreement and potential understanding of the horizontal transport of aerosol particles in the urban area and the consistency of this comparison reflects the good quality of our observational data. The data analysis of this observation data and the comparison with other data (e.g. source fingerprint from mass spectrometry) is still ongoing.

3.4 Characterization of Saharan dust plumes in Western Europe

During my Ph.D. studies, I analyzed four Saharan dust cases as labeled from case 1 to case 4 in Table 2.6 by combining remote sensing, *in-situ* measurements, and ICON-ART model calculations. I demonstrate the advantages of multi-angle lidar measurements in characterizing Saharan dust plumes and compared lidar with sun photometer measurements to better understand the dust opti-

cal properties in western Europe. Furthermore, I validated transport model predictions for these 4 dust events in terms of dust arrival time, dust layer height, and dust backscatter intensity. Finally, I used different aerosol sizers (e.g. OPC, SMPS, APS) to investigate the dust size distributions and compared these size distributions with ICON-ART model results. It was my aim to investigate the Saharan dust plume properties in western Europe and to validate the ICON-ART predictions of the Saharan dust plumes.

The transport of Saharan dust plumes was first investigated by the HYSPLIT model. The hourly seven-day backward trajectories were calculated during Saharan dust periods for altitudes from 500 to 7500 m with an interval of 1000 m based on the HYSPLIT model. The frequency of these trajectories at two altitudes levels (Low altitude: 500 m & High altitude: 1500 m - 7500 m) is shown in Figure 3.27. The reasons for classifying these trajectories into two groups is that the trajectories at an altitude of 500 m are related to the transport of aerosol within the boundary layer while the high-altitude (1500 - 7500 m) ones are related to the long-distance transport in the free troposphere. From the frequency map of high altitude trajectories shown at the bottom of Figure 3.27, most of the trajectories originated from north Africa (Sahara Desert) as expected. However, the places of origin are different at low-altitude for these 4 Saharan dust cases. For case one, most of the trajectories originated from the Atlantic Ocean, which is related to long-distance sea salt transport. During case 2 period, most of the low-altitude trajectories also originated from north Africa (Sahara Desert), which is the reason why the Saharan dust particles could be measured by ground *in-situ* instruments during this case. Detailed results of ground-level dust measurement are discussed in section 3.4.2 for case 2. During case 3 and case 4, the low-altitude trajectories are local originated, which is related to the transport of local aerosol.

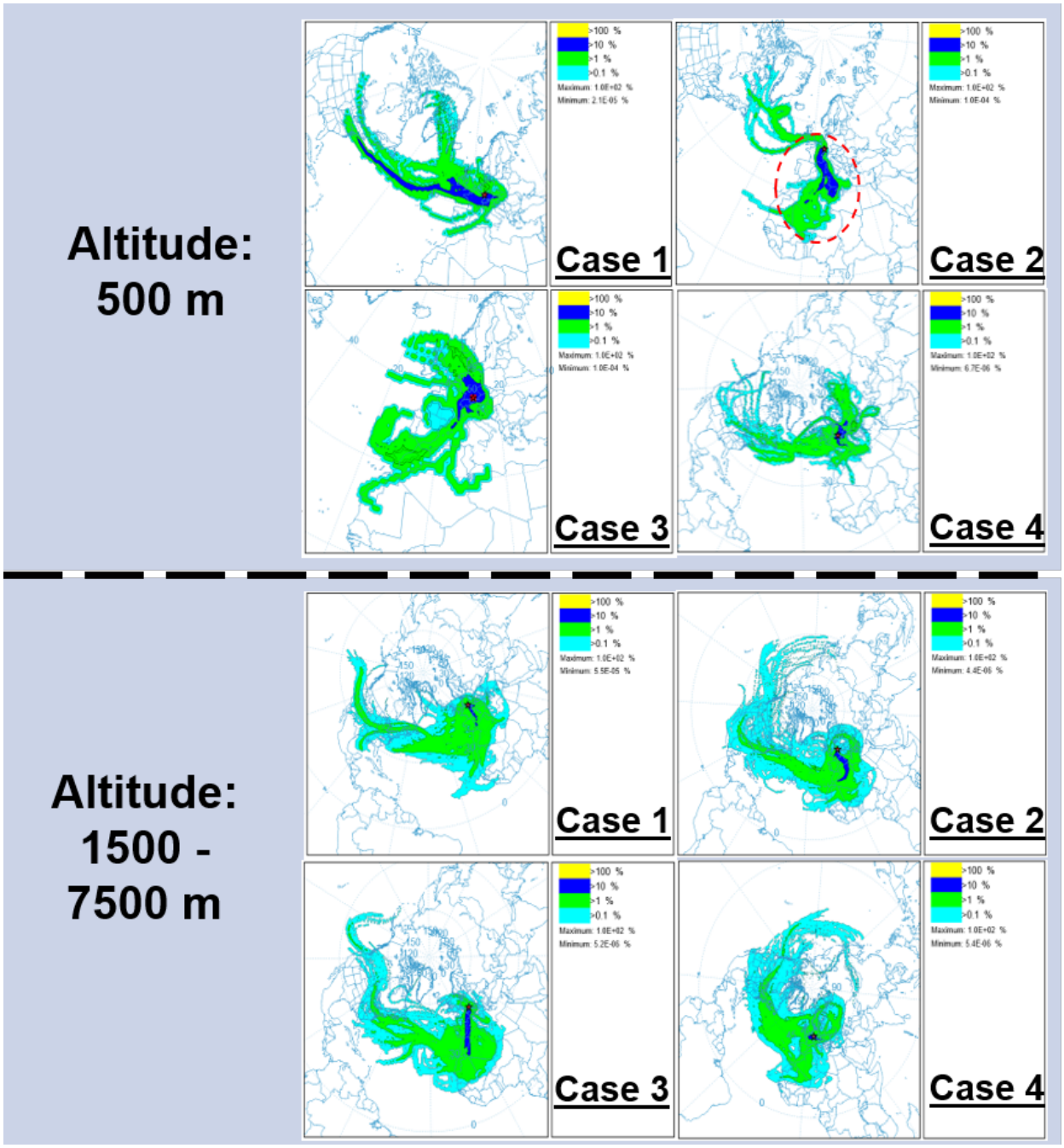

Figure 3.27: Frequency of trajectories at two altitude levels (500 m and 1500 - 7500 m) during four Saharan dust case periods based on back trajectories calculated by the HYbrid Single-Particle Lagrangian Integrated Trajectory (HYSPLIT) model. (The case IDs are labeled in Table 2.6)

In this section, the advantages of multi-angle lidar measurements in characterizing Saharan dust plumes introduced in section 3.1.1 will be applied and be discussed in section 3.4.1. Detailed information on observation results is discussed in section 3.4.2 and the comparison of model results with observational data is presented in section 3.4.3.

3.4.1 Application of two-angle lidar measurements for a Saharan dust case

The method to retrieve lidar ratios discussed in the section 3.1.1 was applied for the Saharan dust case 1 from 19:21 to 22:54 (UTC) on 8^{th}, April 2018 with the dust layer at altitudes between 2.5 - 6.0 km. I choose this time period since I had a well-stratified dust layer and also Raman data available. Figure 3.28 shows backscatter coefficients from vertical and slant lidar measurements for different values of assumed lidar ratios ranging from 20 sr to 80 sr. Consistent backscatter values for vertical and slant profiles in the dust layer are only available for a lidar ratio being 50 sr. This means that a lidar ratio of around 50 sr at the Saharan dust layer can be derived from this case, which is also a typical value for Saharan dust over Europe (Groß et al. 2013).

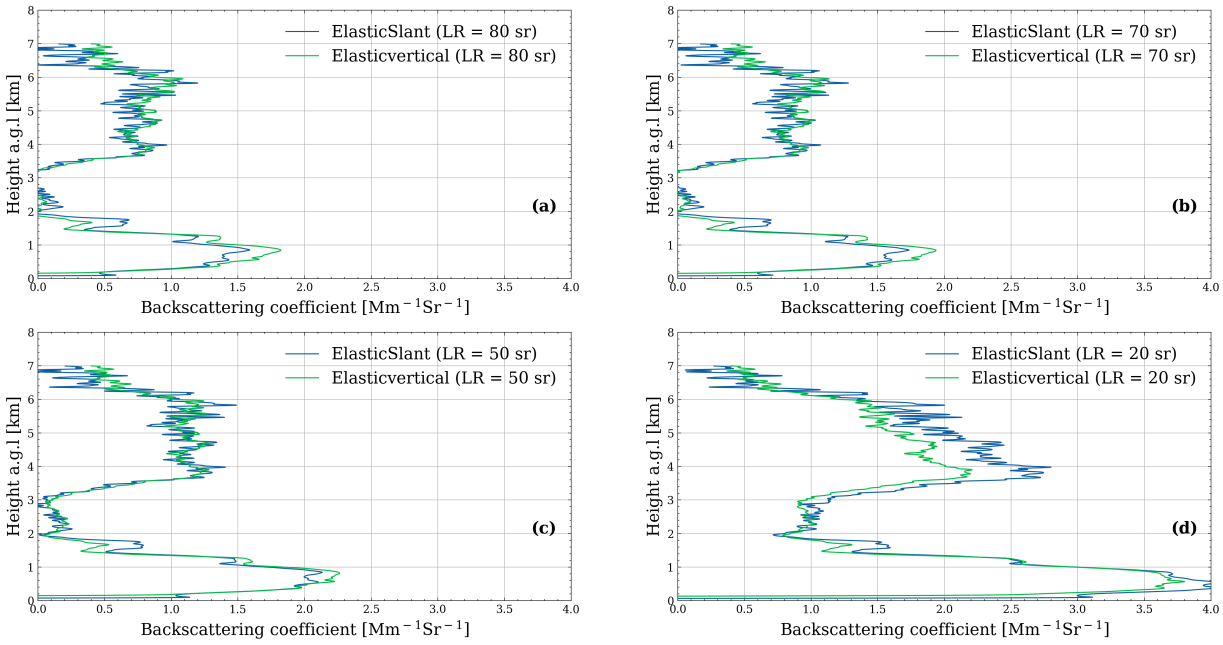

Figure 3.28: Vertical and slant backscatter coefficients from lidar measurements from 19:21 to 22:54 (UTC) on 8^{th}, April 2018 for lidar ratios ranging from 20 to 55 sr.

Figure 3.29a shows that the backscatter coefficients for vertical and slant measurements are consistent for Saharan dust particles (2.5 - 6.0 km) but inconsistent for boundary layer aerosol particles (below 1 km) when the lidar ratio is assumed to be 50 sr. This is because a lidar ratio of 50 sr is not suitable for boundary layer aerosol particles at this location (Groß et al. 2011). Therefore, I calculated lidar ratios based on our Raman signals for boundary layer aerosol particles and the Saharan dust particles. The results are shown in the right panel of Figure 3.29. The lidar ratio is

46 ± 5 sr for the dust particles and 31 ± 3 sr for the boundary layer aerosol particles as the average of both vertical and slant measurements. I parameterized these lidar ratios being 46 sr and 31 sr, respectively, as a function of altitude with a single step at 2 km and then used it as a lidar ratio for the elastic lidar signal retrieval. The results are shown in the left of Figure 3.29. These backscatter coefficients are consistent for vertical and slant measurements for both dust and boundary layer aerosol. A lidar ratio of 31 sr below 2 km altitude leads to much better agreement of backscatter coefficient profiles from the elastic channel and Raman channel compared to Figure 3.28c. However, there remain small differences at low altitudes for backscatter coefficients from elastic data for two elevation angles. This inconsistency may be related to an inhomogeneous atmosphere in the boundary layer as can also be seen in the backscatter coefficients calculated from Raman data.

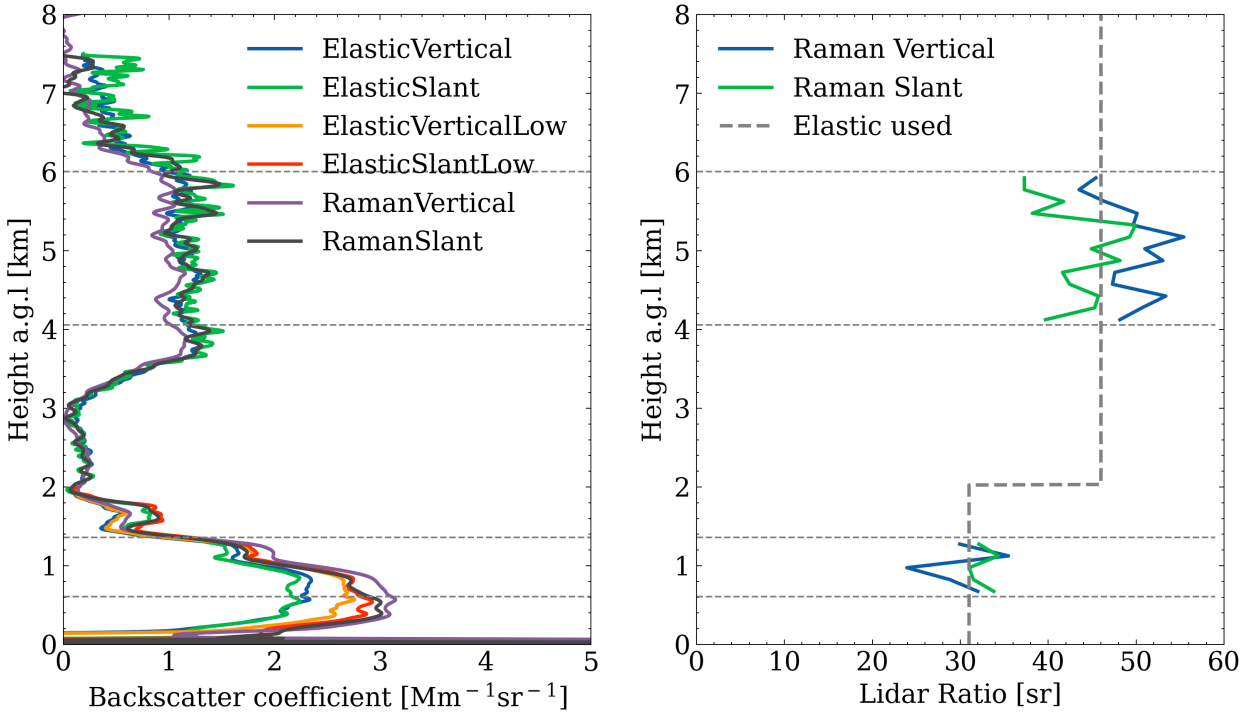

Figure 3.29: Backscatter coefficients from elastic and Raman methods for different optical paths (left) and lidar ratios retrieved (right) from 19:21 to 22:54 (UTC) on 8^{th}, April, 2018. The retrieval for the elastic channel data uses two different lidar ratios at different altitudes. (Elastic and Raman represent the channels of lidar data used in retrieval; Vertical and slant represent the laser beam direction; and low represents data retrieval for low altitude (below 2 km). E.g. ElasticVerticalLow means the backscatter coefficient is retrived from the elastic channel in vertical direction for altitudes below 2 km.

The application of this multi-angle method for this Saharan dust case has proven that this method is useful to retrieve lidar ratios from scanning elastic lidar measurements. Compared with other

methods like Raman or HSRL, the multi-angle method provides an applicable solution for both day and night as the elastic lidar can get reliable measurements for both periods. Furthermore, this method can also be used in multi-wavelength scanning lidar systems to determine wavelength-dependent lidar ratios.

3.4.2 Properties of the Saharan dust determined for four different cases

Dust case 1 in April, 2018:

In early April 2018, a far southward reaching upper-level trough associated with a large low-pressure complex in the western North Atlantic led to a cold front with strong surface winds and dust emission in the northern Sahara in Morocco and Algeria. The dust was transported northward into the western Mediterranean where it entered a warm conveyor belt that effectively lifted the dust and transported it towards central Europe. This Saharan dust plume was characterized by remote sensing and model simulations for nearly three days in April 2018 near the city of Karlsruhe in southwest Germany. The ICON-ART model has predicted the arrival of the dust plume and its spatial-temporal evolution which I characterized by lidar and sun photometer measurements. Figure 3.30 shows the corresponding backscatter coefficients from the KASCAL (a) and the Deutscher Wetterdienst- Depolarizarion Raman lidar (DWD-DELiRA) (b) measurements, predicted backscatter coefficients by ICON-ART for spherical (SPH) particles (c) and non-spherical (NSP) particles (d) as well as the LVDR (e) and the Linear Particle Depolarization Ratio (LPDR) (f) from of the KASCAL measurement from April 7^{th} to April 9^{th}, 2018. The KASCAL was operated by doing vertical and slant measurements at 90° and 30° elevation angle alternatively with integration times for each observation angle of 300 s. The data shown for KASCAL is averaged over two of these measurement periods. The data shown for the DWD-DELiRA is averaged for 30 minutes. As can be seen in these figures, the plume arrived in Karlsruhe at 11:00 on April 7^{th} (dashed line T1) and lasted about 3 days. Initially, this dust layer showed a maximum backscatter at an altitude of 2.5 km which subsequently also reached lower altitudes. At 12:00 UTC, April 8^{th}, another dust layer between 5.0 -11.0 km arrived at the observation station (dashed line T2). Then the dust layer started sinking and overlapped with the lower dust layer at around 03:00 am on April 9^{th} (dashed line T3). A cloud with a base at 4.5 km appearing at 11:00 (UTC) of April 9^{th} made it difficult to retrieve the backscatter coefficients for the aerosol particles below. Hence, the backscatter coefficients of the lidar measurements are not shown for this period. In addition, two periods (C1 and C2) are

highlighted for which I have done a more detailed analysis.

All six panels in Figure 3.30 show a good agreement among dust layer height, dust plume arrival time, and dust plume structures. In particular, ICON-ART predicts the arrival time of the dust plume precisely (± 20 minutes difference with the observations). This indicates that the model reproduces the synoptic scale processes very well which leads to precise prediction of dust transport. Thus, the generally good agreement between lidar measurements and ICON-ART partially validates the model's capabilities to predict dust transport. The dust NSP particles backscatter coefficients predicted by the model are on average larger by a factor of 1.01 ± 0.56 than those from the lidar measurements. Please note that this special model run did only include desert dust aerosols. Hence, differences due to boundary layer aerosol particles are expected in this case. Furthermore, there are dust layers predicted by the model for higher altitudes (e.g. a dust plume at around 8 km on April 7^{th} and April 8^{th}) which were not detected by lidar measurements. Potential reasons for the agreement and differences between lidar observations and model predictions are discussed in detail in section 3.4.3.

During this dust event, the lidars used three optical measurement paths (two vertical measurements and one slant measurement with an elevation angle of 30°). The comparison of these three profiles can be used to test different lidar retrieval methods and to characterize the properties of the dust plume (e.g. horizontal homogeneity of the dust plume). Figure 3.31 shows the extinction and backscatter coefficients obtained for different retrieval methods and different optical paths for the measurement time from 19:21 to 22:54 (UTC) of April 8^{th} (period C2 in Figure 3.30) and averaged over 66 minutes for scanning lidar measurements and 213 minutes for vertical lidar measurements. Please note that the scanning lidar measured alternating at the two angles (90° and 30°). A lidar ratio of 50 sr, which is a typical value observed for Saharan dust (Groß et al. 2013), was used in the Klett-Fernald method to retrieve the elastic backscatter coefficients and extinction coefficients. The extinction coefficients and backscatter coefficients calculated using the above methods as shown in Figure 3.31a and Figure 3.31c are consistent but the extinction coefficients calculated from the Raman measurements have larger variations. In addition to the classical methods to retrieve extinction coefficients, I also calculated the extinction coefficients from the elastic channels with a multi-angle method, which also agrees with the other methods. The denoising methods can have a substantial impact on the remaining variability of the extinction coefficients retrieved from Raman data. In Figure S8, I provide extinction coefficients retrieved from Raman data for different

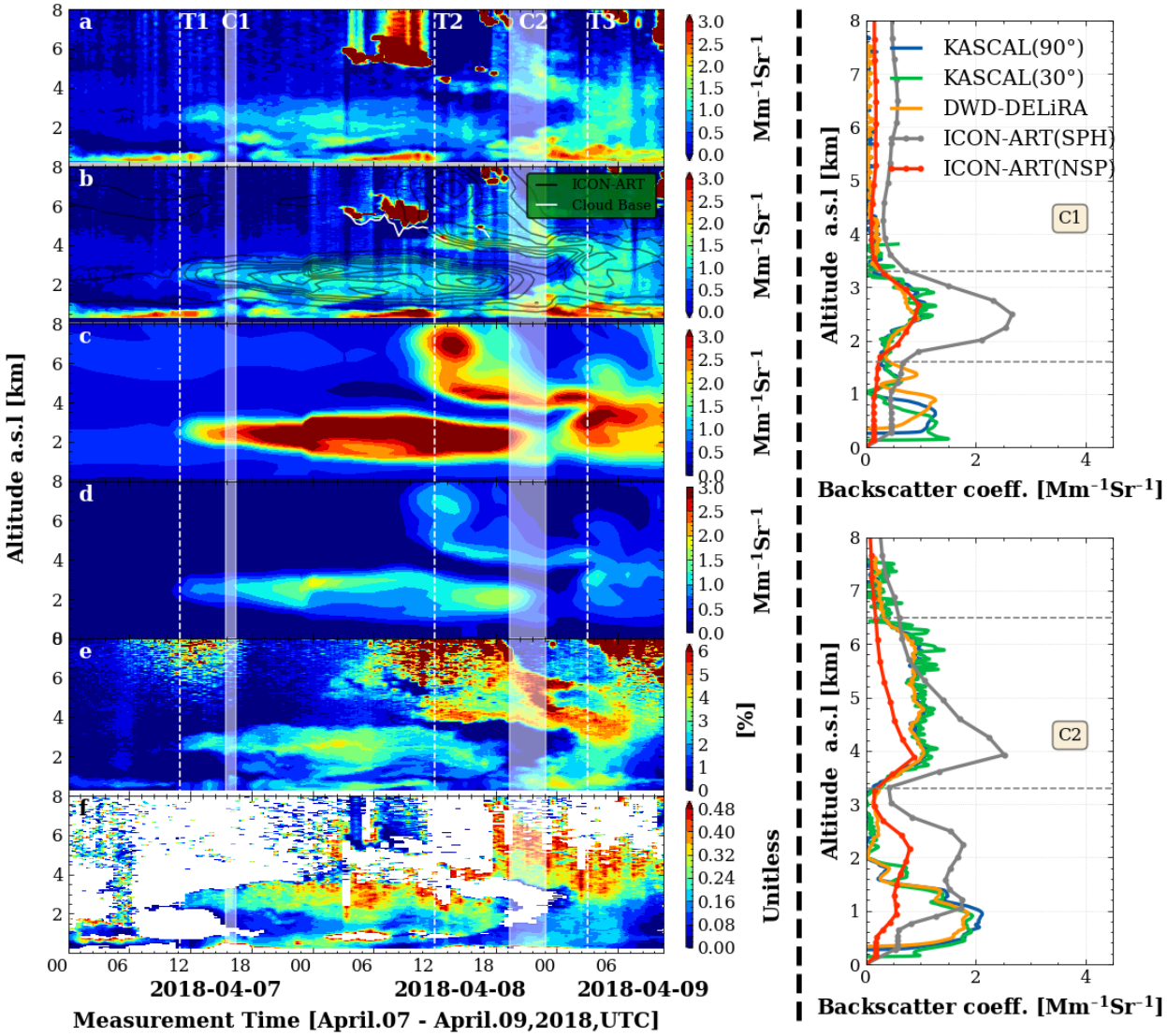

Figure 3.30: Time series of backscatter coefficients from KASCAL measurements (a) and from DWD-DELiRA measurements (b), predicted backscatter coefficients by ICON-ART for spherical (SPH) particles (c) and for non-spherical (NSP) particles (d), linear volume depolarization ratios (e), and particle depolarization ratios (f) from KASCAL measurements from April 7^{th} to 9^{th}, 2018. Please note that the model data shown only includes the Saharan dust while the lidar data shows also other aerosol particles and clouds. The profiles of backscatter coefficients measured by the two lidars and predicted by ICON-ART model for C1 case (Averaged profiles from 15:30 to 16:30 for lidar measurement and profile at 16:00 for ICON-ART prediction on April 7^{th}, 2018) and for C2 case (Averaged profiles from 20:21 to 22:54 for lidar measurement and averaged profile from 21:00 to 23:00 for ICON-ART prediction on April 8^{th}, 2018) are shown on the right side of this figure. The vertical dashed lines in the contour plots indicate dust arrival (T1), second dust layer appeared (T2), and the two dust layers merged (T3). C1 and C2 represent time periods used for a more detailed data analysis as shown in the right size of this figure.

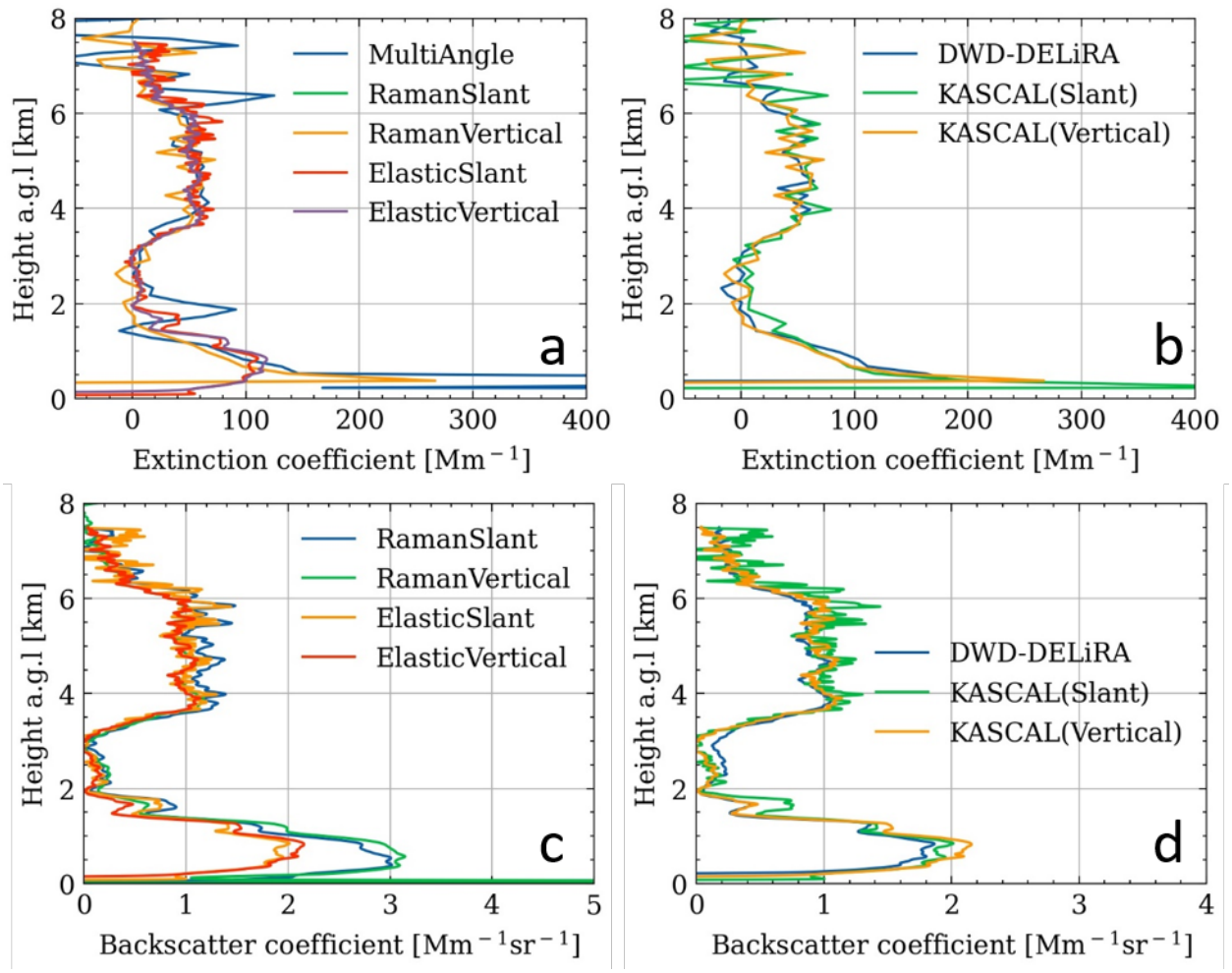

Figure 3.31: Extinction coefficients (a) and backscatter coefficients (c) from elastic and Raman retrieval methods are shown on the left. On the right Raman extinction coefficients (b) and elastic backscatter coefficients (d) are given for different optical paths for measurements in the time from 19:21 to 22:54 (UTC) on April, 8^{th}, 2018. (Two vertical paths are from DWD-DELiRA and KASCAL and one slant path is from KASCAL).

filters and different filter lengths. In addition, the average extinction coefficients and their standard deviations averaging from 4.0 km to 6.0 km altitude are listed in Table S1. These data show that the mean values of extinction coefficients for different filter types and filter lengths remain almost constant. In contrast, their uncertainties vary from around 35 to 5 Mm^{-1} with window lengths from 82.5 m to 1207.5 m for different types of filters. Hence, the Raman extinction coefficients are affected more by the filter window lengths than the filter type, which is in agreement with observations by Shen & Cao (2019). The backscatter coefficients and extinction coefficients for different optical paths are shown in Figure 3.31b and Figure 3.31d, respectively. The consistency of these profiles reflects the high quality of measurements and retrieval algorithms.

Figure 3.30e and Figure 3.30f shows the LVDR and LPDR respectively, which show the same dust

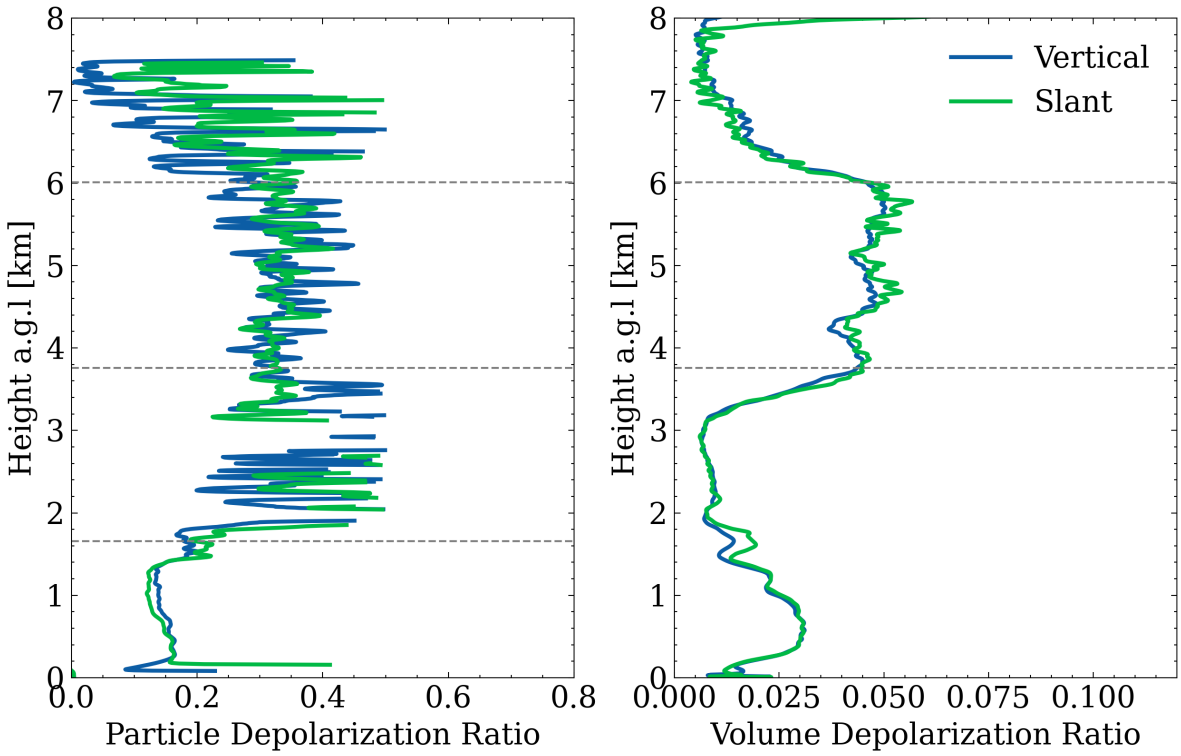

Figure 3.32: Volume and particle depolarization ratio in vertical and slant observation direction from the scanning lidar (KASCAL) from 19:21 to 22:54 (UTC) on 8^{th}, April 2018.

structure as the backscatter coefficients. The average value of LPDR for this Saharan dust plume is 0.29 ± 0.04, which agrees well with literature data (Freudenthaler et al. 2009, Haarig et al. 2017). LVDR and LPDRs were measured by KASCAL for different elevation angles, and the values of them for the C1 case at these two elevation angles are shown in Figure 3.32. No obvious difference between vertical and slant measurements was found for LVDR and LPDR. This may mean that the dust particles had no specific orientation (Asano 1983, Geier & Arienti 2014). The LPDR of this dust plume in this case was 0.33 ± 0.07 which is very similar to depolarisation ratios determined at 532 nm for Saharan dust particles (Freudenthaler et al. 2009) but about 20% larger than typical values reported for aged Saharan dust at 355 nm (Freudenthaler et al. 2009, Haarig et al. 2017). However, this is still within the combined uncertainty limits. Furthermore, the day-to-day variability of values given by Freudenthaler et al. (2009) is ranging from about 0.22 to 0.31.

Comparison between the active lidars and the passive sun photometer can help to understand the properties of the dust aerosol particles employing dust aerosol scattering information from different scattering angles to retrieve dust particles' microphysical properties. During this dust event, I compared the AOD from DWD-DELiRA measurements and a sun photometer for two continuous days

(April 7^{th}-8^{th}). The AOD from the sun photometer is the AERONET version 3 level 2.0 product (Sinyuk et al. 2020) while that of lidar measurement was corrected in the following ways. First, as discussed above, two aerosol layers existed with different lidar ratios. Hence, I used two different lidar ratios at different altitudes to retrieve the backscatter coefficients, which are shown in Figure S9. I have used a lidar ratio of 50 sr for the upper layer (above 2 km, red line) and 30 sr for the lower layer (below 2 km, green line), typical values for Saharan dust and boundary layer aerosol (Groß et al. 2013). Secondly, constant backscatter coefficients are used in the lidar overlap region and these constant values are set to be the backscatter coefficient at 255 m (the overlap region of DWD-DELiRA). Finally, the AOD in the far range (e.g. stratosphere) is assumed to be zero. The hourly AODs from the sun photometer, the vertical lidar (DWD-DELiRA) and the ICON-ART model are shown in Figure 3.33. As the signal-to-noise ratio of lidar data is low for KASCAL during daytime, the AODs were not calculated by this lidar. All these three methods show a similar trend with AODs increasing from around 0.13 to 0.45 during these two days. However, the average AOD retrieved from the lidar data for two days is systematically lower by 0.053 ± 0.031 than that from the sun photometer after wavelength conversion to 340 nm. The AE used for this wavelength conversion is 0.471, which is calculated from the sun photometer data at wavelengths of 340 nm and 380 nm. The average stratospheric AOD in the Northern Hemisphere for the years 2018-2019 was 0.01 at 340 nm (Kloss et al. 2020). Hence, the averaged AOD measured by the sun photometer is still larger by 0.043 ± 0.031 than the AOD from the lidar measurement even considering stratospheric AOD. This bias may be due to an inappropriate assumption of constant backscatter coefficients in the overlap region of the lidar. Such an uncertainty of AOD corresponds to an uncertainty in backscatter coefficients of 5.6 ± 4.1 Mm^{-1} sr^{-1} in the overlap region, which is reasonable for typical boundary layer aerosol variations (Ansmann et al. 1992, Matthias et al. 2004, Navas-Guzman et al. 2013). On April 8^{th}, clouds lead to increased uncertainties in AOD retrievals from the lidar measurements and also to some gaps in the sun photometer data. Hence, the AOD from lidar measurements can be given only for some selected clear sky periods while the sun photometer has still enough valid data points to calculate hourly averages. Figure 3.34 shows the SSA, AE, and ASD calculated based on the sun photometer measurements on April 7^{th} and 8^{th}. The AE at wavelengths of 440/880 nm decreased from 1.38 to 0.08 during these two days as shown in Figure 3.34a and Figure 3.34b. This may be related to a smaller wavelength dependence of the AOD, which may be caused by larger particles. Particle size distributions provided by

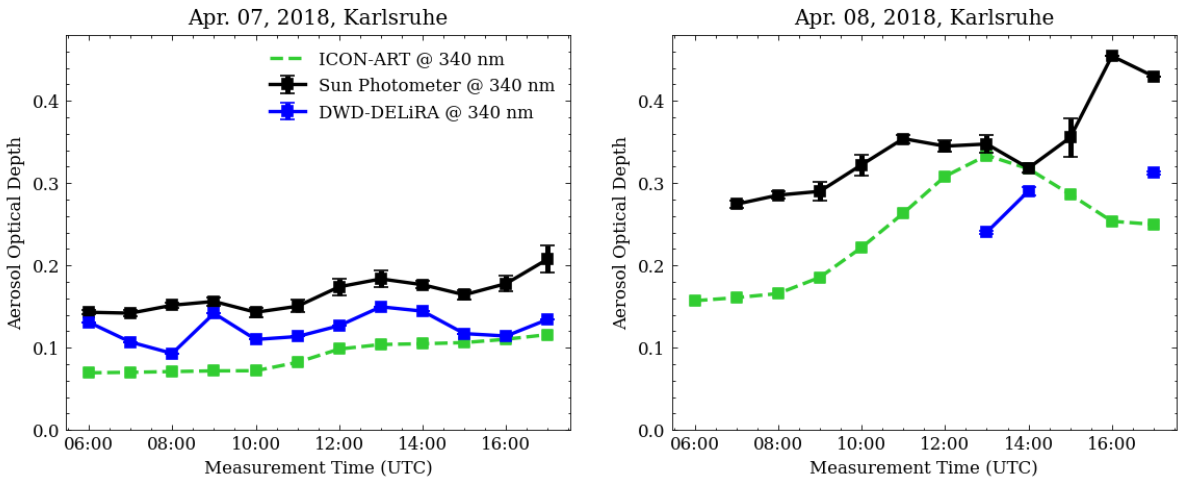

Figure 3.33: AOD from lidars (blue circles) and sun photometer (black squares) on 7^{th} and 8^{th} of April for 1 hour temporal resolution. ICON-ART results are shown for comparison (dashed green line) and will be discussed in section 3.3.

sun photometer retrievals are shown in Figure 3.34c and Figure 3.34d. They indeed show increasing amounts of larger particles. The maximum column-integrated volume concentration of coarse mode particles increased from around 0.007 $\mu m^3/\ \mu m^2$ in the early morning of April 7^{th} (before Saharan dust arrival) to 0.093 $\mu m^3/\ \mu m^2$ in the afternoon of April 8^{th}. The SSA determined for the wavelengths between 439 and 1018 nm range between 0.88 and 0.96 and agree quite well with data from previous observations (cf. table 3.2).

Table 3.2: Overview of Single Scattering Albedos (SSAs) measured for Saharan dust during case 1 in comparions with literature values.

SSA	Wavelength [nm]	Reference
0.88 – 0.92	439	This work
0.91	450	Müller et al., 2011
0.96 – 0.99	530	Petzold et al., 2011
0.96	537	Schladitz et al., 2009
0.96	550	Müller et al., 2011
0.98	637	Schladitz et al., 2009
0.87-0.96	675	This work
0.86-0.94	870	This work
0.98	950	Müller et al., 2011
0.85-0.94	1018	This work

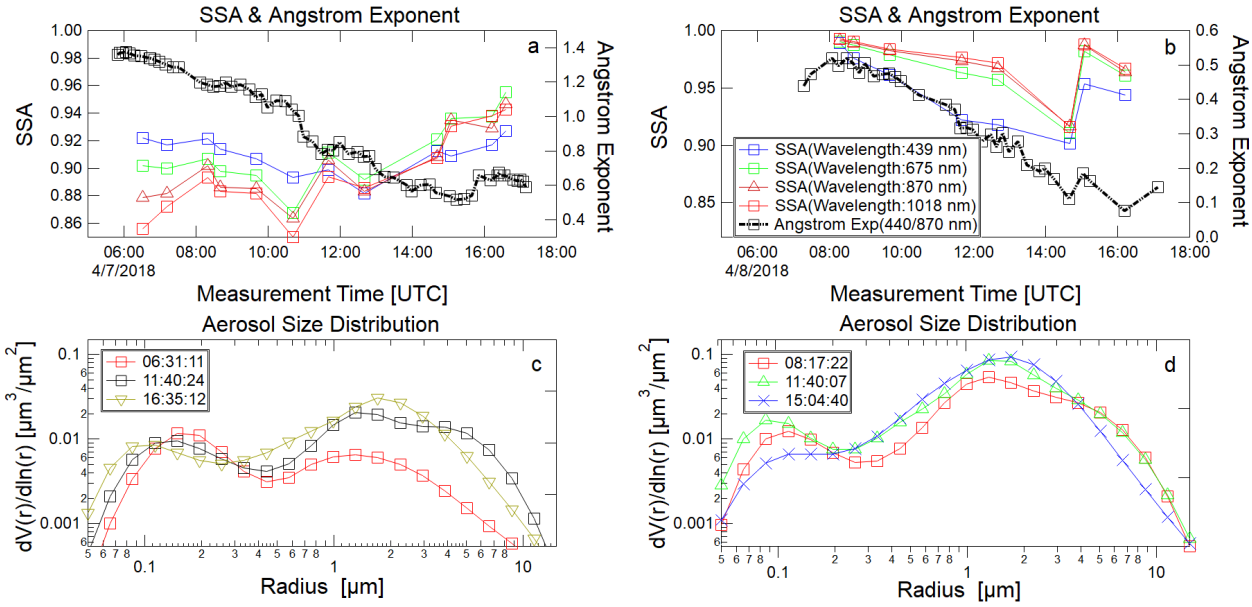

Figure 3.34: Single scattering albedo (SSA), Angström exponents (AE) (a, b), and aerosol size distribution (c, d) from sun photometer measurements for April 7^{th} (left) and 8^{th}(right), 2018.

Dust case 2 in February, 2021:

Another dust plume, case 2, was characterized in February 2021 at the KIT campus north near the city of Karlsruhe by combining remote sensing, ground *in-situ* aerosol characterization instrument, and ICON-ART simulations. During February 2021 actually three different dust periods were observed. In this section, I will focus on the period with the longest duration of nearly 5 days from 22^{nd} to 26^{th}, of February 2021. This period was almost free of clouds. Figure 3.35 shows the time series of backscatter coefficients from KASCAL measurements, ICON-ART predicted backscatter coefficients for NSP and SPH particles, LVDR and LPDR from KASCAL measurements, and particle mass size distributions and particle matter concentrations from OPC (Fidas200) measurements from 22^{nd} to 26^{th}, February 2021. The KASCAL was operated at two observation angles similar as for case 1 but the lidar data shown in this figure is averaged for each observation angle with an integration time of 300 s. The missing lidar data from 22:15 on 22^{nd}, February to 10:25 on 23^{rd}, February 2021 was due to a technical problems (loss of laser cooling). As can be seen from this figure, the dust arrived at the observation site at 04:00 on 22^{nd}, February 2021 (dashed line T1) and lasted for about 5 days. Initially, the dust plume had a maximum backscatter at around 2.0 km altitude, and then the Saharan dust plume started sinking and reached ground level at 10:00 on 23^{rd}, February 2021 (dashed line T2), and these ground level particles were characterized by an *in-situ* aerosol sizer (Fidas200). Subsequently, the ground level aerosol concentration increased

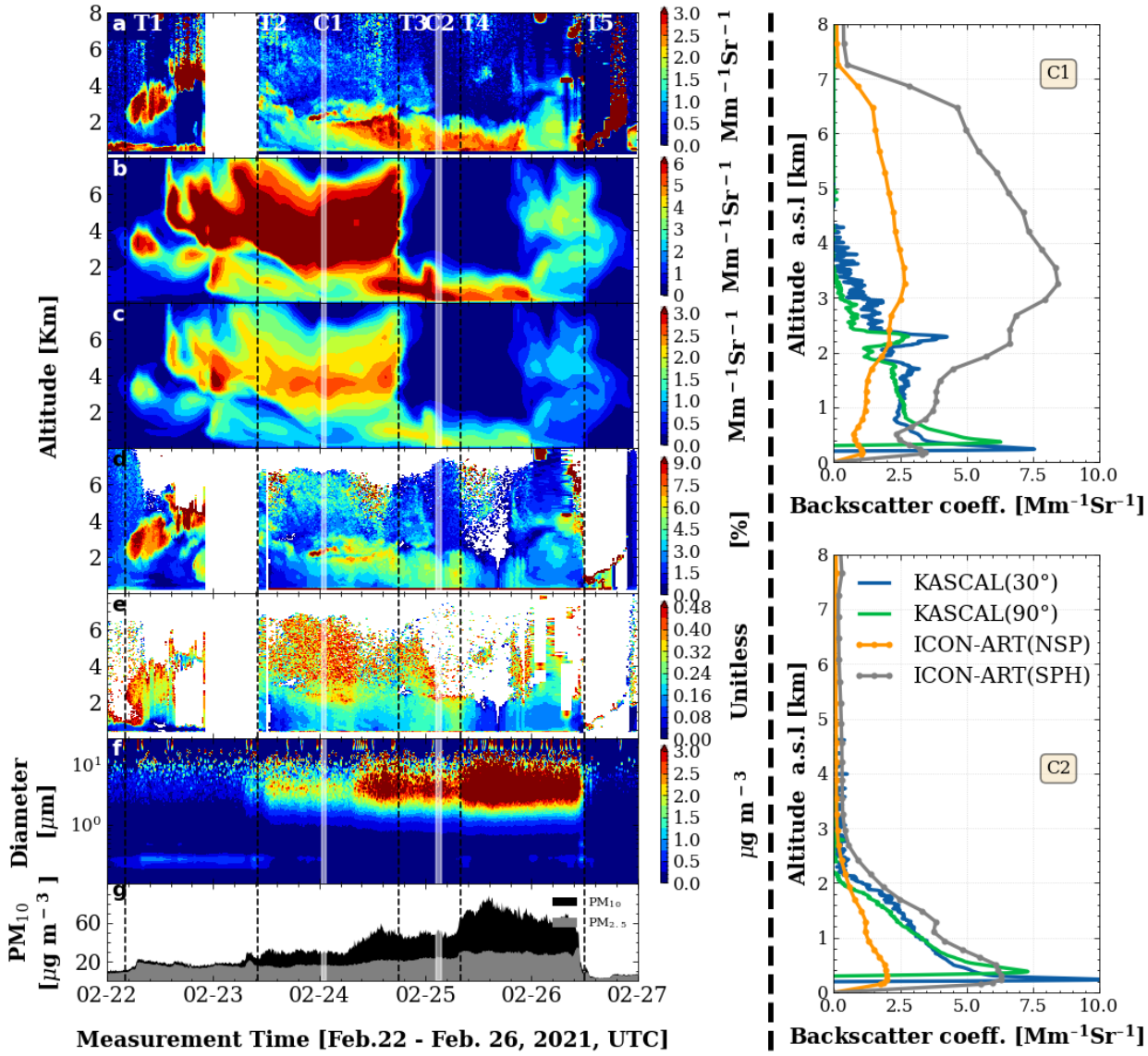

Figure 3.35: Time series of backscatter coefficients from KASCAL measurements (a), predicted backscatter coefficients by ICON-ART for spherical (SPH) particles (b) and for non-spherical (NSP) particles (c), Linear Volume Depolarization Ratio (LVDR) (d) Linear Particle Depolarization Ratio (LPDR) (e) from KASCAL measurements, particle mass size distribution (f) and particle matter concentration (g) from Fidas 200 from February 22^{th} to 26^{th}, 2021. Please note that the model data shown only includes the Saharan dust while the lidar data shows also other aerosol particles and clouds. The profiles of backscatter coefficients measured by the two lidars and predicted by ICON-ART model for C1 case (Averaged profiles from 00:30 to 1:30 for lidar measurement and profile at 01:00 for ICON-ART prediction on 24^{th}, February 2021) and for C2 case (Averaged profiles from 02:30 to 03:30 for lidar measurement and profile at 03:00 for ICON-ART prediction on 25^{th}, February 2021) are shown on the right side of this figure. The vertical dashed lines in the contour plots indicate dust arrival (T1), dust touched to the ground (T2), an increase of PM concentration at ground level (T3 & T4) and a low-level cloud appeared (T5). C1 and C2 represent time periods used for a more detailed data analysis as shown in the right side of this figure.

stepwise as can be seen from the mass size distributions (Figure 3.35f) and particle mass concentrations (Figure 3.35g) from 12:00 of 24^{th}, February 2021 to 12:00 of 26^{th}, February 2021. The size distributions measured by Fidas200 during these periods shows that large particles ($d_p > 1$ µm) dominated the particle mass concentration. Finally, a sharp decrease of ground level aerosol dust particles and vertical dust concentration can be seen both from both, ground level *in-situ* and lidar measurements at 12:00 on 26^{th}, February 2021 (dashed line T5) due to increasing wind speeds which blew the aerosol particles away.

The backscatters measured by lidar and predicted by the ICON-ART model show good agreement in dust arrival time but show some disagreement in dust height and dust structure, especially the time periods from 06:00 on 22^{nd}, February, (dashed line T1) to 18:00 on 24^{th}, February 2021, (dashed time T3). After 18:00 on 24^{th}, February 2021 (dashed time T3), the predicted Saharan dust plume was within 2.0 km altitude, in agreement with lidar measurements in terms of dust layer height and structure. In this figure, two periods (C1 and C2) are highlighted to further investigate this dust plume and vertical profiles of backscatter coefficients measured by lidar and predicted by the ICON-ART model. The right side of this figure shows a comparison of the vertical profiles for C1 and C2. A detailled comparison of lidar measurements and ICON-ART predictions is presented in section 3.4.3.

The LPDR shown in the panel (e) of figure 3.35 indicates that the value of LPDR is 0.25 $\pm$ 0.09 before 08:00 on 24^{th}, February 2018 (former period) while the value of LPDR is 0.119 $\pm$ 0.06 after that time (latter period). The LPDR measured in the latter period is smaller than measured in the former period and both these two periods have a lower value of LPDR than that measured in the dust case 1 and previous literature (Freudenthaler et al. 2009). The reason for this phenomenon is that the dust particles sunk to lower altitudes and mixed with boundary layer aerosol, which results in a lower value of LPDR as expected (Tesche et al. 2009). Figure 3.36 shows the vertical and slant profiles of LPDR measured by scanning lidar for two selected cases (C1 and C2) and both two cases show that an increasing trend of LPDR with altitude. The value of LPDR measured in these two cases is 0.19 $\pm$ 0.09, which is smaller than previous results for pure dust particles Freudenthaler et al. (2009). The reason for these two phenomena is also related to the mixture of Saharan dust particles and boundary layer aerosol during transport. The LPDR values increasing with altitude indicate that the contribution of dust particles to backscatter increased with altitude and this is the reason why the C1 has a larger value of LPDR as the dust layer height is higher in C1 case.

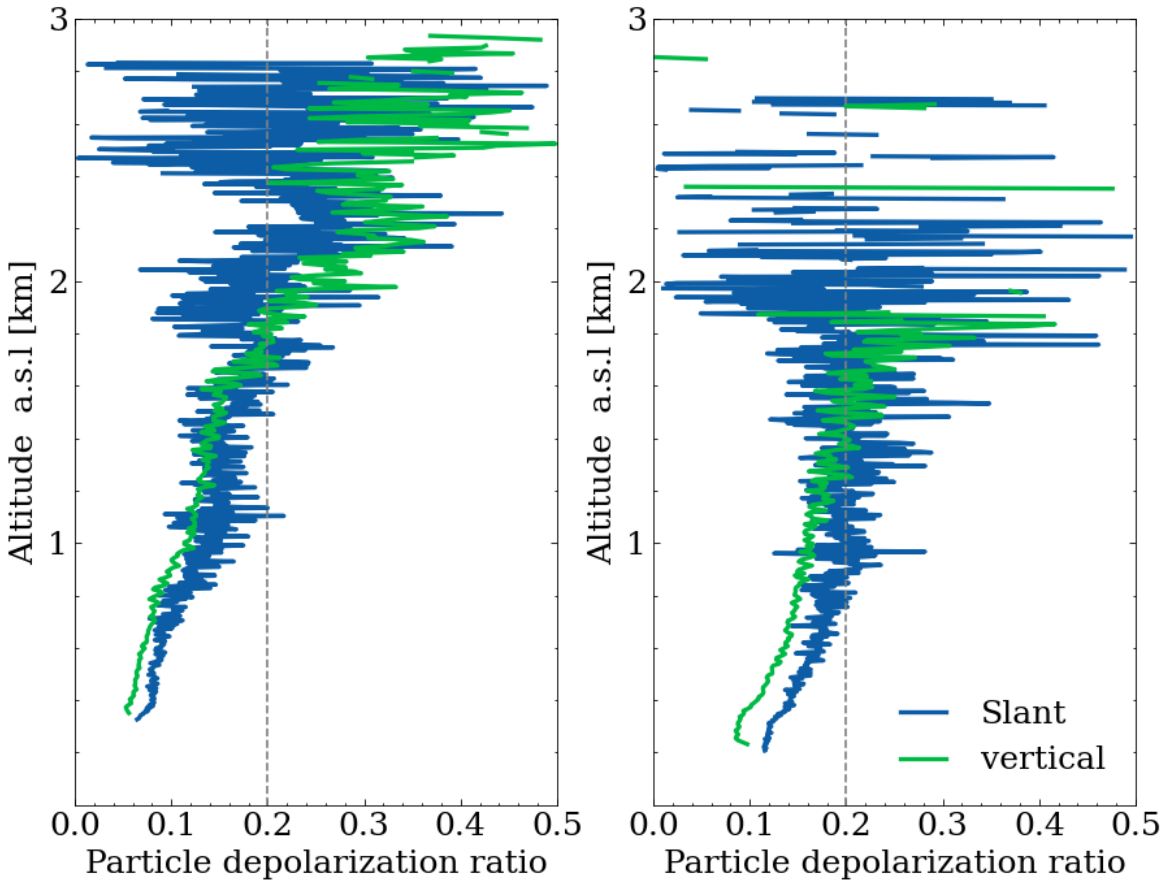

Figure 3.36: Profiles of vertical and slant linear particle depolarization ratio (LPDR) measured by KASCAL for case C1 (left) and case C2 (right) (The time periods selected for C1 and C2 case are indicated in Figure 3.35).

The measured LPDR demonstrates the mixing of boundary layer aerosol with Saharan dust during Saharan its transport and also indicates the contribution of this mixing on the average particle depolarization. Furthermore, the inconsistent values of LPDR for the two observation angles are due to spatial variation of aerosol within the boundary layer as can be seen from both backscatter and volume depolarization as shown in the right side of Figure 3.35.

In addition to the measurements with two fixed elevation angles (90° & 30°), scanning measurements from 90° to 30° with steps of 5° were conducted by KASCAL on 22^{nd}, February 2021 to measure the spatial-temporal distribution of the Saharan dust plume. Figure 3.37 shows the scanning plane of LVDR measured by the scanning aerosol lidar, which demonstrates the spatial-temporal distribution of the Saharan dust plume over Karlsruhe and scenes of dust plume arrival for this Saharan dust case. This figure shows that the dust layers arrive in Karlsruhe around at 04:00 on 22^{nd}, February 2021, and mainly occurred between 1.5 - 3.5 km above ground level. In

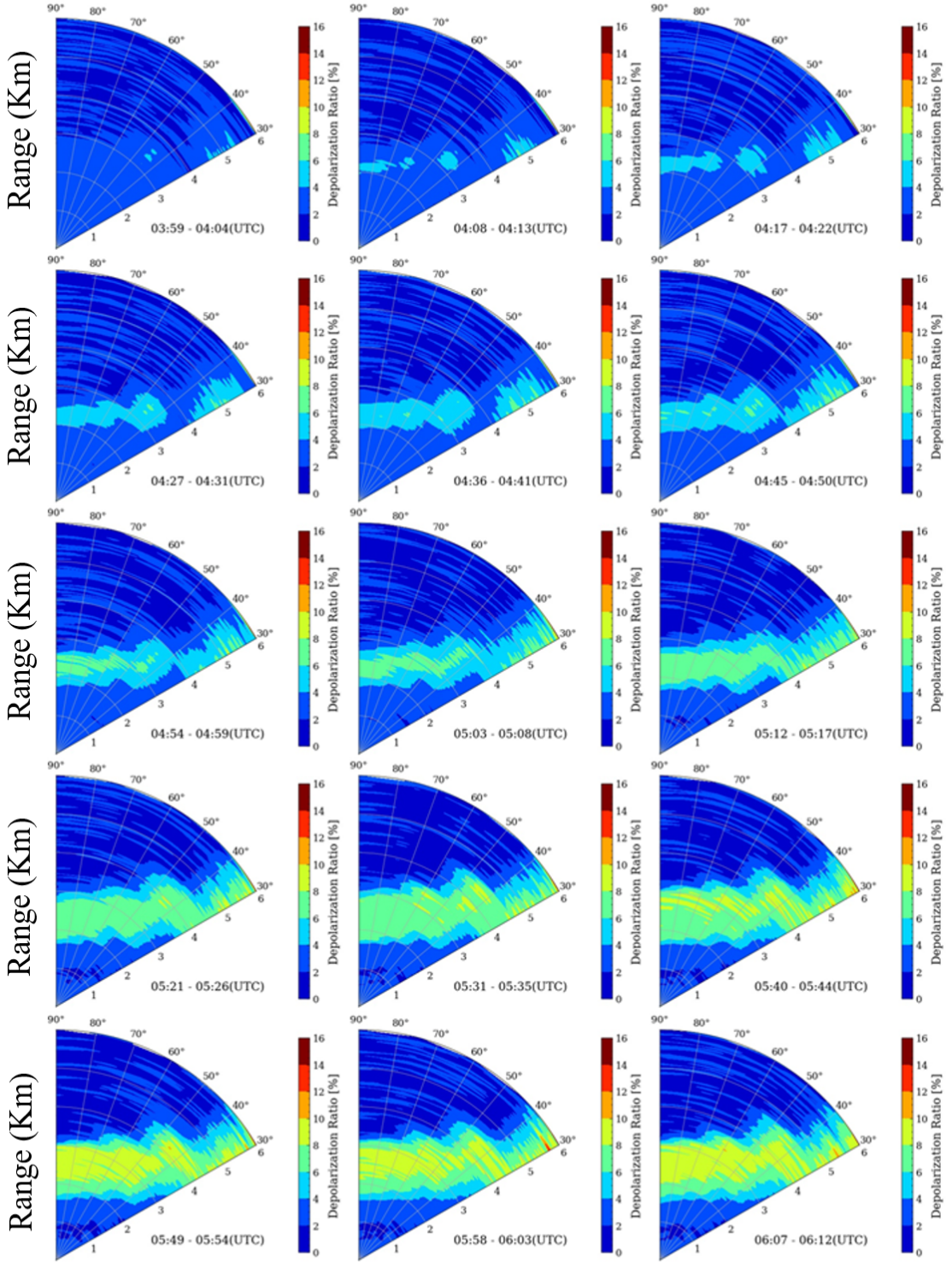

Figure 3.37: Spatial-temporal evolution of volume depolarization ratio measured by KASCAL over a range of 6 km from 3:39 to 06:12, UTC, on 22nd, February, 2021.

addition, this figure shows a partially homogeneous dust layer in horizontal direction. This high spatial-temporal resolution dataset can be used to validate ICON-ART simulations in predicting high spatial resolution aerosol particle distributions.

Sun photometer data from the Karlsruhe AERONET station were also used to investigate this Saharan dust case. Figure 3.38 shows the time series of AOD (a), AE (b), SSA (c) measured by the sun photometer for different wavelengths as well as aerosol volume size distributions retrieved from the sun photometer (d) and aerosol mass size distributions measured by Fidas200 at ground level (e). From this figure, we can see a relatively small trend of AOD for different wavelengths caused by large Saharan dust particles over Karlsruhe. These large particles have only very little wavelength dependence in light scattering, thus causing a low value of AE which is below 0.3 most of the time. In addition, the AOD at the wavelength of 340 nm increased from 0.41 at 07:22 of 23^{nd}, February to 0.66 at 15:57 on 24^{th}, February 2021 and then decreased to 0.42 at 16:00 on 25^{th}, February 2021. The SSA shown in panel (c) of this figure indicates that the SSA is wavelength dependent and has the lowest value at a wavelength of 439 nm. This phenomenon is due to the strong absorption of Saharan dust at short wavelengths and this strong absorption caused a low value of SSA. The aerosol volume size distribution retrieved from sun photometer and mass size distributions measured by Fidas200 shown in panel (d) and panel (e) show relatively large particle ($d_p > 1$ µm) dominating during this Saharan dust period as expected. In addition, the volume size distribution retrieved from sun photometer and the mass size distributions from Fidas200 do not show a similar trend. The volume size distribution retrieved from sun photometer has the highest concentration on 24^{th}, February 2021 while the mass size distribution measured by Fidas200 has the highest concentration on 25^{th}, February 2021. The reason for this inconsistency can be explained as follow: (1) The sun photometer measures the column integral aerosol from ground level to the tropopause while the Fidas200 measured ground level aerosols. (2) the Saharan dust has the strongest intensity on 24^{th}, February 2021 (as can be seen from AOD value at panel(a)) but most dust particles are aloft (can be seen from lidar measurement shown in the 3.35a) which cannot be measured by Fidas200 but can be measured by sun photometer. However, on 25^{th}, February, most of the dust particles were sunken to the ground level (as can also be seen from lidar measurement shown in the 3.35a) which can be measured by Fidas200. In addition, as the dust plume intensity on 25^{th}, February 2021 is weaker than that on 24^{th}, February 2021, the volume size distribution retrieved by sun photometer is lower on 25^{th}, February 2021.

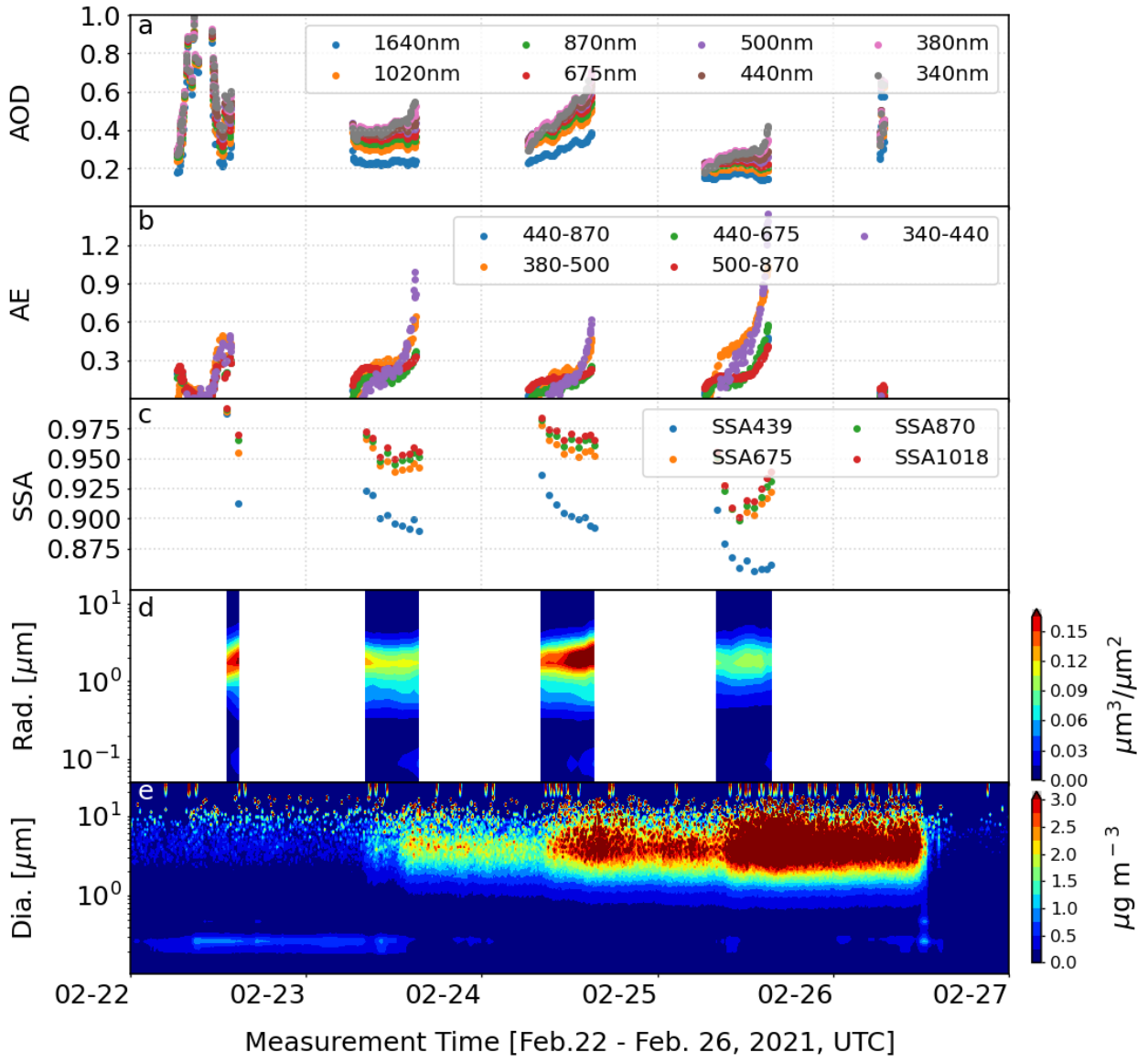

Figure 3.38: Time series of Aeosol Optical Depth (AOD) (a), Ångström Exponent (AE) (b), Single Scattering Albedo (SSA) (c) at different wavelengths, and aerosol size distributions (d) measured or retrieved from sun photometer (AERONET, Karlsruhe station) as well as particle mass size distributions (e) measured by Fidas 200 from February 22^{th} to 26^{th}, 2021.

Dust case 3 during June, 2021:

The Saharan dust case 3 was captured during the Swabian MOSES campaign from June to August 2021 near the city of Rottenburg in western Germany. During this field campaign, several intensive observation periods (IOPs) were conducted and this Saharan dust case was measured during IOP4. Durning this IOP, nearly two days of Saharan dust plume were characterized by combining KASCAL, sun photometer, ground *in-situ* measurements, and ICON-ART simulations. Figure

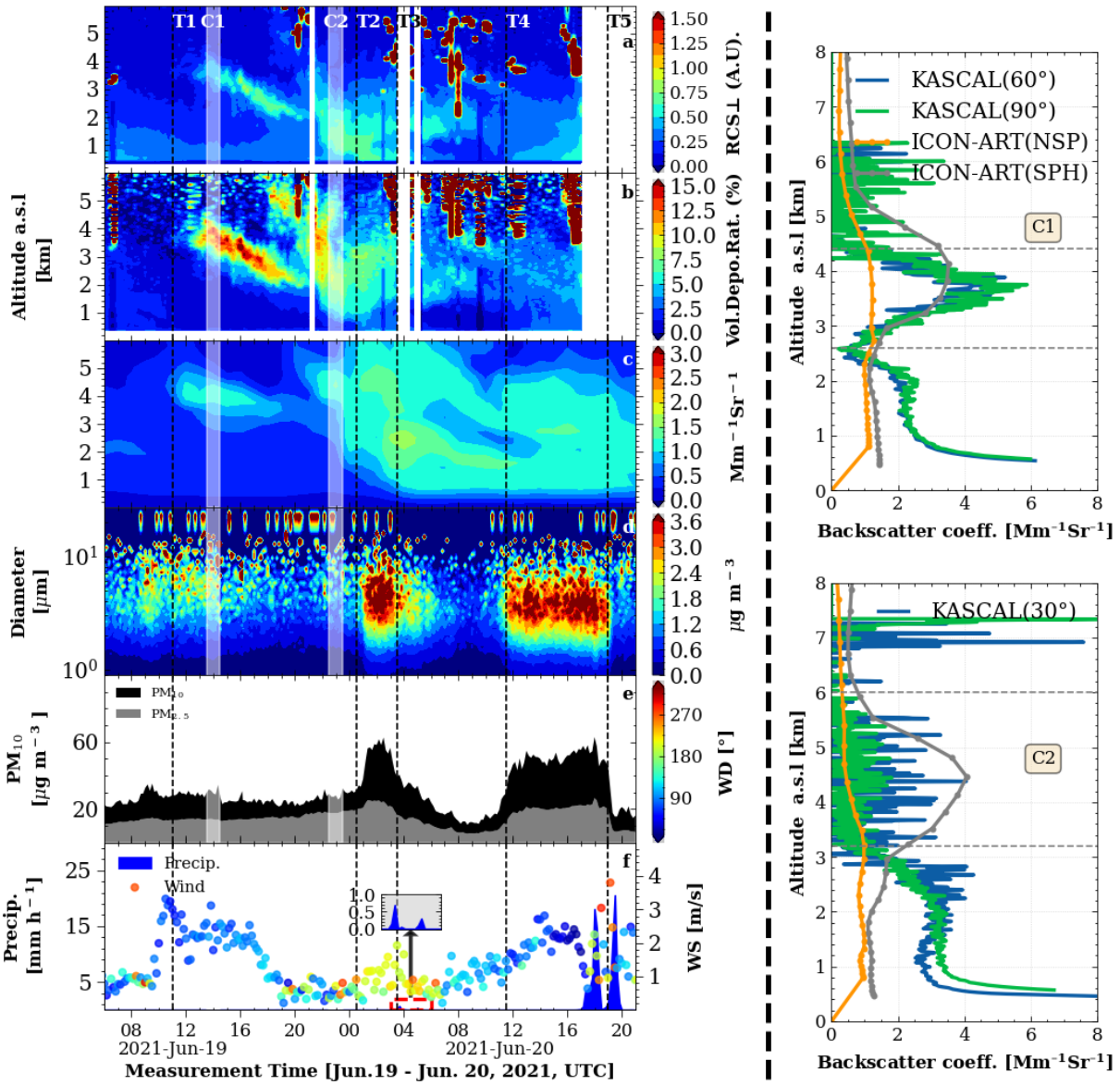

Figure 3.39: Time series of range corrected lidar signal for the cross-polarized channel (a), and Linear Volume Depolarization Ratio (LVDR) from KASCAL measurements (b), backscatter coefficients predicted by ICON-ART for non-spherical (NSP) particles (c), particle mass size distributions (d) and particulate matter concentrations (e) from Fidas200, and ground meteorological parameters (e.g. wind, precipitation, WS700) (f) from February 22^{th} to 26^{th}, 2021. Please note that the model data shown only includes the Saharan dust while the lidar data shows also other aerosol particles and clouds. The profiles of backscatter coefficients measured by the lidar and predicted by the ICON-ART model for case C1 (averaged profiles from 13:30 to 14:30 for lidar measurements and profile at 14:00 for ICON-ART prediction on 19^{th}, June 2021) and for case C2 (averaged profiles from 22:30 to 23:30 for lidar measurements and profile at 21:00 for ICON-ART prediction on 19^{th}, June 2021) are shown on the right side of this figure. The vertical dashed lines in the contour plots indicate dust arrival (T1), dust touched to the ground (T2 & T4), and dust particle removal due to precipitation (T3 & T5). C1 and C2 represent time periods used for a more detailed data analysis as shown in the right side of this figure.

3.39 shows the time series of RCS for the cross-polarized channel and LVDR from KASCAL measurements. The backscatter coefficient and particle depolarizations are not shown in this figure as the retrievals of the backscatter coefficients by the Klett-Fernald method were largely affected by the existence of clouds and this effect would bring large uncertainties in calculating the backscatter coefficients and LPDR. Figure 3.39 also shows the time series of ICON-ART predicted backscatter coefficients for NSP particles (c), the particle mass size distribution (d) and particulate matter concentrations (e) from Fidas200, and meteorological parameters from WS700 from 19^{nd} to 20^{th}, June 2021. The KASCAL conducted zenith scans from 90° to 5° elevation angle with the step of 5° at two azimuth angles as described in section 2.4. The lidar measurements shown in this figure are based only on the vertical profiles extracted from for each scanning plane. As can be seen from this figure, this dust plume arrived in Rottenburg at 11:00 on 19^{th}, June 2021 (dashed line T1) and lasted for nearly 2 days. Initially, the dust layer showed a maximum in volume depolarization ratio at an altitude of 4.0 km which subsequently sunk to an altitude of 2.0 km. At 22:00 on 19^{th}, June 2021, another dust layer with an initial altitude between 2.0 km to 4.0 km arrived at the observation station then subsequently touched ground level at 00:30 on 20^{th}, June 2021 (dashed line T2). Those particles reaching ground level were characterized by Fidas200 showing an increase of aerosol concentrations between 00:30 and 03:30 dashed line T3) on 20^{th}, June 2021. At 03:00 on 20^{th}, June 2021, drizzle occurred as shown in panel (f) of this figure and washed the particles out. This caused a decrease of aerosol concentrations at ground level. At 11:30 on 20^{th}, June 2021 (dashed line T4), the aerosol particles reached ground level again and caused an increase of aerosol concentrations at ground level from 11:30 on 20^{th}, June 2021 to 19:00 on 20^{th}, June 2021 (dashed line T5). Finally, a moderate rain occurred at around 17:00 on 20^{th}, June 2021 causing a sharp decrease of aerosol particles (T5) due to wet removal.

The measurements by lidar and the ICON-ART model predictions show a good agreement for dust arrival time, dust height, and dust structure but still show some discrepancies for some time periods. Two time periods (C1 and C2) are used to further characterize the dust plume and to compare vertical profiles of backscatter coefficients measured by lidar and predicted by the ICON-ART model. A more detailed discussion of the comparison of lidar measurements and ICON-ART predictions is presented in section 3.4.3.

The time series of LPDR are not shown in Figure 3.39 due to the presence of clouds impeding their retrieval for longer periods. However, two time periods free of clouds as indicated in Figure 3.39

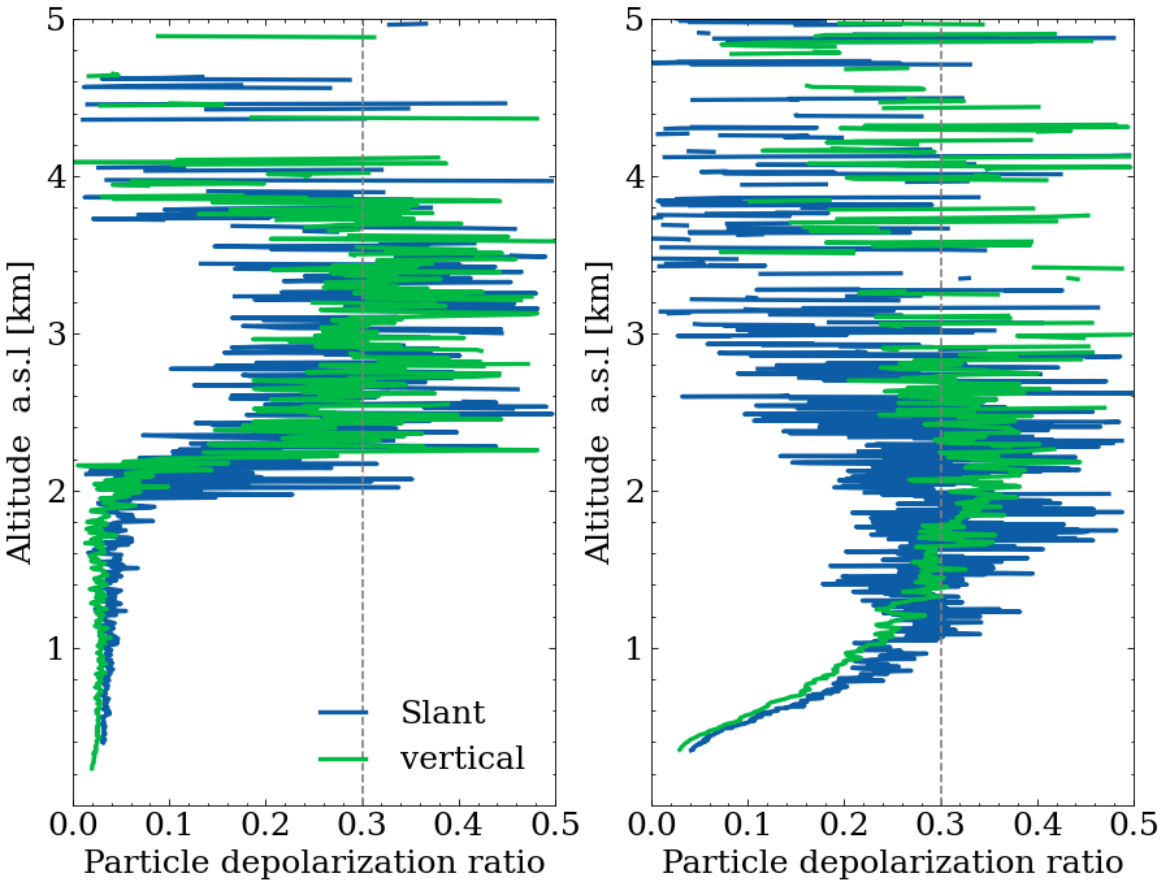

Figure 3.40: Profiles of vertical and slant linear particle depolarization ratios (LPDR) measured by KASCAL for case C1 (left) and case C2 (right). (The time periods selected for the cases C1 and C2 are indicated in Figure 3.39.)

are selected to calculate the LPDR. For case C1 , the profiles measured at an elevation angle of 90° and 60° were analyzed. The reason for not using profiles measured at the elevation angle of 30° is due to the low signal-noise ratio during this time period. The retrieved LPDR for these two cases are shown in Figure 3.40, which shows agreement in LPDR for vertical and slant measurements with a LPDR value of 0.32 ± 0.06. For case C2, an increase of LPDR can also be seen below 2.0 km altitude indicating a lower dust plume mixing with the local aerosol in the boundary layer, similar as discussed for the Saharan dust case 2.

Dust case 4 during March, 2022:

The Saharan dust case 4 was measured at the KIT campus north near the city of Karlsruhe from 16^{th}, March 2022 to 12^{th}, March 2022 combining remote sensing, *in-situ* measurements, and ICON-ART model calculations. This Saharan dust plume is the most intensive dust outbreak among all 4 cases with an AOD reaching values of 1.8 ± 0.07 at a wavelength of 550 nm in Karlsruhe. In addition to

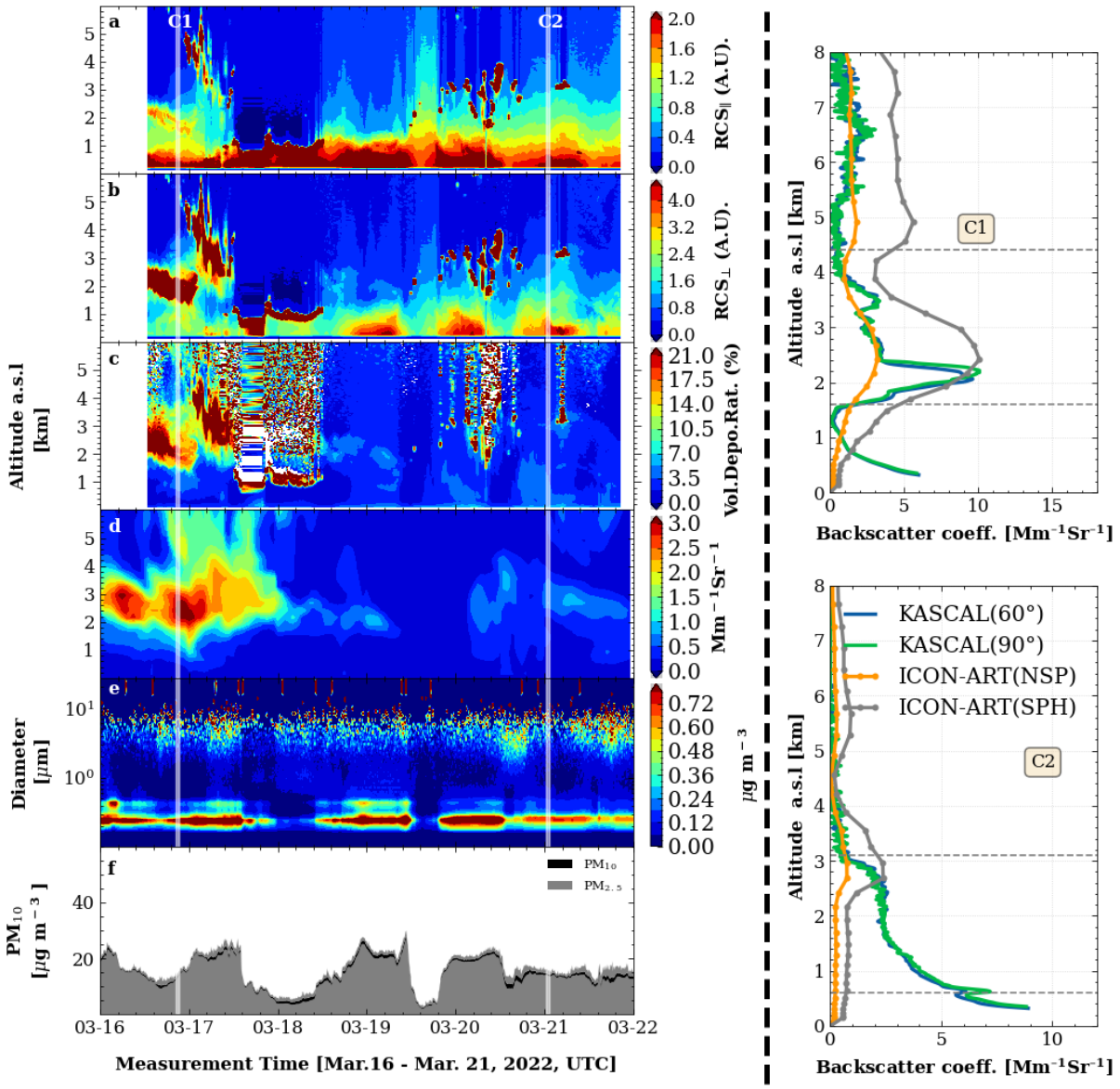

Figure 3.41: Time series of range corrected lidar signal for the parallel polarized channel (a), cross-polarized channel (b), and Linear Volume Depolarization Ratio (LVDR) (c) from KASCAL measurements, backscatter coefficients predicted by ICON-ART for non-spherical (NSP) particles (d), particle mass size distribution (e) and particulate matter concentrations (f) from Fidas200 from February 22^{th} to 26^{th}, 2021. Please note that the model data shown only includes the Saharan dust while the lidar data shows also other aerosol particles and clouds. The profiles of backscatter coefficients measured by the two lidars and predicted by ICON-ART model for C1 case (Averaged profiles from 20:30 to 21:30 for lidar measurement and profile at 21:00 for ICON-ART prediction on 16^{th}, March 2022) and for C2 case (Averaged profiles from 00:30 to 01:30 for lidar measurement and profile at 01:00 for ICON-ART prediction on 21 th, March 2022) are shown on the right side of this figure. C1 and C2 represent time periods used for a more detailed data analysis as shown in the right side of this figure.

the measurements in Karlsruhe, I also participated in joint measurements with the DWD combining remote sensing measurements (e.g. at Hohenpeissenberg) and aircraft *in-situ* measurements, and with colleagues from the University of Granada performing measurements in Granada, Spain. In this section, I will mainly focus on the measurements conducted in Karlsruhe. Figure 3.41 shows the time series of RCS for the polarized channel (a), cross-polarized channel (b), and LVDR (c) from KASCAL measurements. The backscatter coefficients and particle depolarizations are not shown in this figure since their retrieval was impeded due to the presence of clouds from time to time. Figure 3.41 also shows the time series of ICON-ART predicted backscatter coefficents for NSP particles, particle size distributions, and particulate matter concentrations from 16^{th} to 22^{th}, March 2022. The KASCAL conducted two-angle fixed pointed measurements during this field campaign in a similar way as for Saharan dust cases 1 and 2. As can be seen from this figure, the Saharan dust arrived in Karlsruhe at 12:00 on 16^{th}, March 2022 at an altitude between 2.0-3.5 km, and a cloud began to appear at 00:00 on 17^{th}, March 2022 at an altitude above 2.0 km. From 12:00 of 17^{th}, March to 12:00 of 18^{th}, March 2018, the presence of low level clouds and intermittent drizzle prevented the observation of the dust plume by KASCAL. On midday of 18^{th}, March, another dust plume arrived in Karlsruhe at an altitude of 2.0 - 3.0 km and subsequently sunk to lower altitudes. This latter dust plume was less intensive than that observed on 16^{th}, March as can be seen from the lower LVDR shown in panel (c) of this figure. The dust particles in the Saharan dust event did not reach the ground as can be seen from aerosol mass size distributions and particulate matter concentrations shown in panel (e) and panel (f) of Figure 3.41. In addition, two special periods (C1 and C2) are highlighted in this figure. These periods were used to further investigate dust properties measured by lidar and predicted by the ICON-ART model for different dust mass loadings.

Figure 3.42 shows the profiles of vertical and slant LPDR of two selected time periods. From this figure, I deduced that the dust particles have no special orientation and have a LPDR value of 0.32 $\pm$ 0.06 for case C1 and 0.13 $\pm$ 0.02 for case C2 . The LPDR for case C1 is significantly larger than that for case C2 due to mixing of the dust plume with local aerosol for case C2 as discussed already before.

Figure 3.43 shows LPDR versus lidar ratios retrieved from KASCAL for aerosol layers present during different days. This figure shows that the Saharan dust plume, biomass burning aerosol, and a mixture of both were all detected during this period. On 16^{th}, March 2022, a dense dust

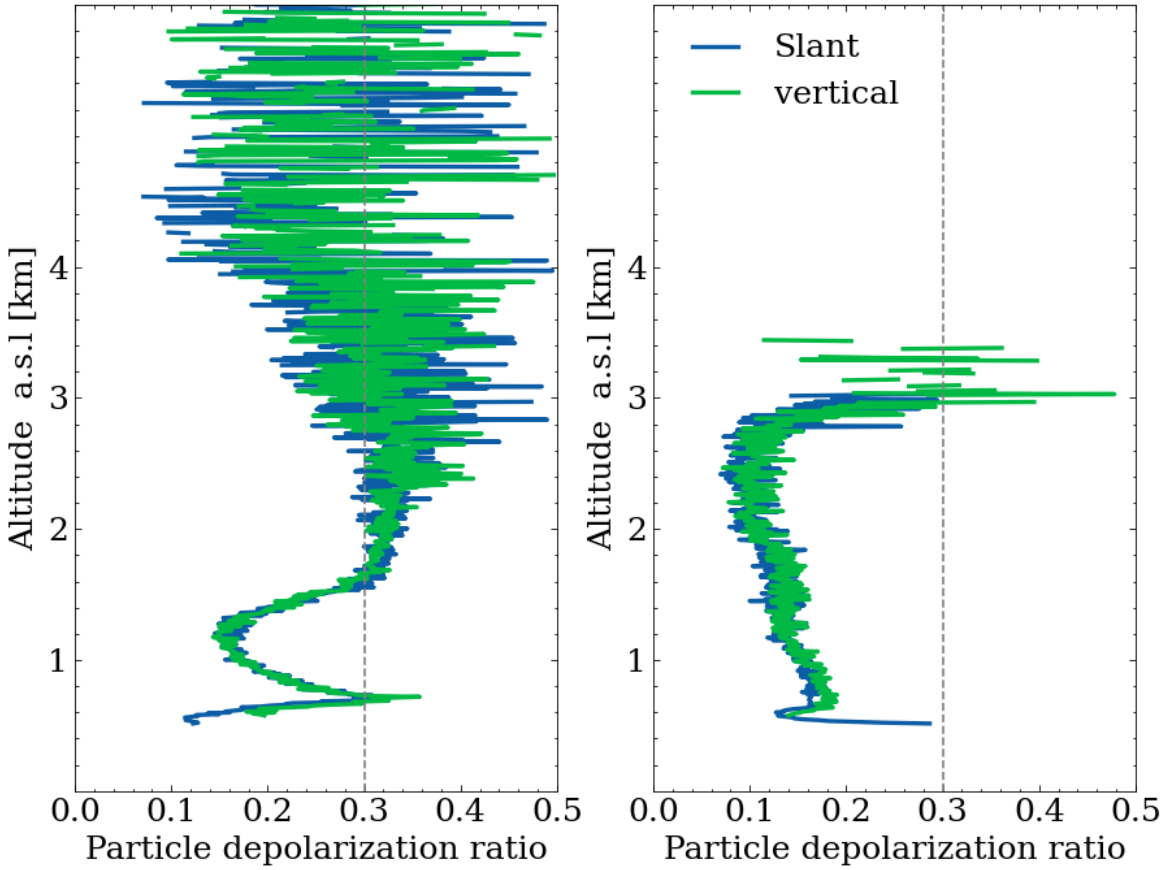

Figure 3.42: Profiles of vertical and slant linear particle depolarization ratios (LPDR) measured by KASCAL for case C1 (left) and case C2 (right). (The time periods selected for cases C1 and C2 are indicated in Figure 3.41.)

layer was detected with a large value of depolarization (0.32 ± 0.06) and a large value of the lidar ratio (56 ± 11) and on 18^{th}, March 2022, two layers were detected with the dust layer above (LPDR: 0.32 ± 0.04, lidar ratio: 38 ± 8) and a biomass burning aerosol layer below (LPDR: 0.02 ± 0.003, lidar ratio: 36 ± 7). On 19^{th}, March 2022, a layer of Saharan dust mixed with biomass burning aerosol (LPDR: 0.11 ± 0.019, lidar ratio: 27 ± 7) and the pure biomass burning aerosol layer(LPDR: 0.05 ± 0.004, lidar ratio: 49 ± 3) were detected with the biomass burning aerosol layer above. On the 19^{th}, March, the dust layer and the biomass burning aerosol layer were mixed homogeneously (LPDR: 0.1 ± 0.02, lidar ratio: 33 ± 13). The temporal evolution of those LPDR and lidar ratios illustrate the mixing process between Saharan dust and biomass burning particles.

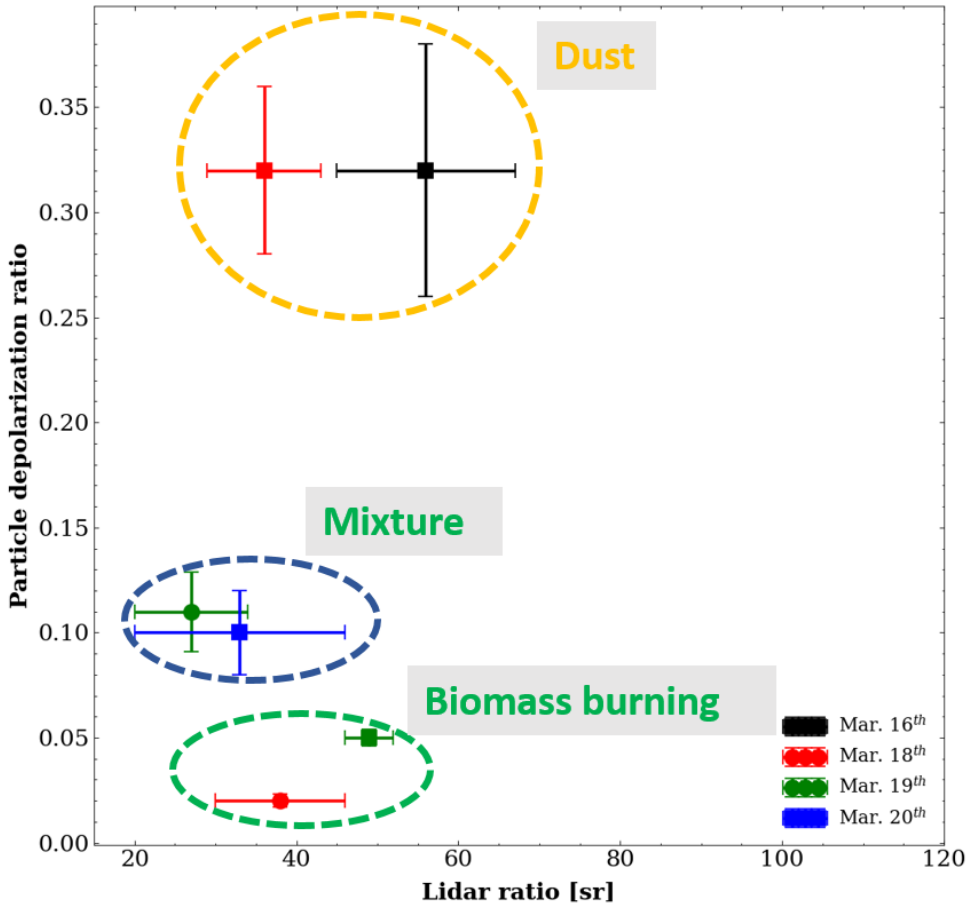

Figure 3.43: Linear Particle Depolarization Ratio (LPDR) versus lidar ratio retrieved from KASCAL for aerosol layers present on different days for Saharan dust case 4. (A square and a circle indicate different aerosol layers and a square point indicates that the aerosol layer is the upper layer. Only a square is used when just one aerosol layer was detected.)

3.4.3 Comparison of Saharan dust predictions by ICON-ART with observations

Model simulations and remote sensing observations were used to study the spatial and temporal evolution of these four dust cases. The comparison between the model results and observations can be used to evaluate the performance of model predictions including dust layer height, dust arrival time, dust layer structure, and dust optical parameters. In this section, I will discuss the comparison between remote sensing observations and ICON-ART simulations for the 4 dust cases mentioned before.

Dust case 1 during April, 2018:

The evolution of the dust plume over Karlsruhe for dust case 1 predicted by the ICON-ART model is shown in panel (c) and panel (d) of Figure 3.30. According to the model simulation, the dust layer arrived in Karlsruhe at 11:00 of April 7^{th}, and this plume passed over that location for nearly two and a half days. Two dust layers were observed from 12:00 (UTC) of April 8^{th} until the morning of April 9^{th} when they merged. A comparison between model prediction and lidar measurement is shown in panel (b) of Figure 3.30, where the black contour line is the modeled backscatter coefficient and the contour fill is the lidar (DWD - DELiRA) observation. The white line in panel (b) is the cloud base height from the lidar measurements. The dust layer heights (vertical extend) and their peak heights (the heights for the maximum backscatter coefficients) for both lidar measurements and ICON-ART prediction for this Saharan dust case are shown in Figure 3.49a. The criteria for an aloft dust layer are as follows: (i) the value of LVDR is larger than 0.1 throughout the layer and the value of LPDR is between 0.2 and 0.4; (ii) the layer thickness exceeds 0.3 km; (iii) the layer base is above the PBL (He et al. 2021). Figure 3.49a shows a very good agreement in dust layer heights for these two measurements and the ICON-ART prediction. The comparison shows that dust plume arrival time, layer height, structure, and backscatter coefficients are consistent between lidar measurements and model simulations for this event. Although the lidar data shows more details of the dust plume structures, the agreement with the model is quite good considering the relatively coarse spatial resolution used in this model run (20 km). On the other hand, in the presence of clouds, aerosol properties cannot be retrieved well from lidar data. Therefore, a comparison of thin dust layers is not always meaningful. The dust layer height range is based on the dust layer heights shown in Figure 3.49a which doesn't include the boundary layer aerosol for lidar measurements. All comparisons between lidar measurements and ICON-ART model results

follow these criteria. The vertical profiles of the backscatter coefficients from two lidar measurements and two ICON-ART modes are shown in the right of Figure 3.30 for two selected periods indicated as C1 and C2 in Figure 3.30. For case C1, the backscatter coefficients are given for lidar measurements from 15:30 to 16:30 and ICON-ART calculations for 16:00 on 7^{th}, April, and for case C2, the backscatter coefficients are given for lidar measurements 20:21 to 22:54 (UTC) and ICON-ART calculations for the average profile from 21:00 - 23:00 on 8^{th}, April 2018. The case C1 shows a good agreement in dust layer vertical backscatter coefficients from the model calculation for this time period. Comparing cases C1 and C2, I found that ICON-ART can predict dust layer structures quite well for most of the time of this event but also shows substantial differences with lidar measurements e.g. for the time period C2. The substantial difference between lidar and model simulation may be caused by the coarse spatial resolution used in this model run (20 km) and inhomogeneous dust horizontal distribution. The comparison between lidar and ICON-ART model shows that the ICON-ART predictions agree very well with the measurements, although some variability can be observed as well.

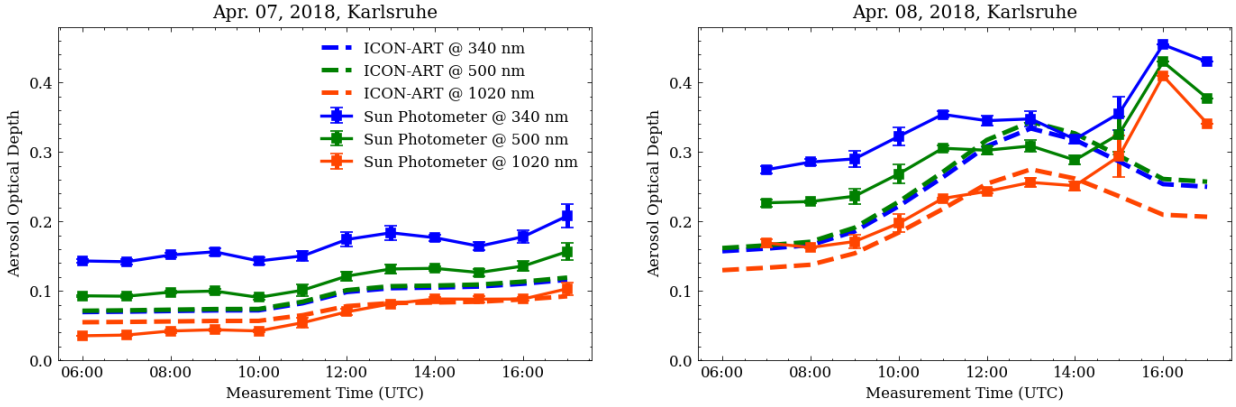

Figure 3.44: Time series of AODs at three wavelengths from the sun photometer and ICON-ART model simulation on 7^{th} and 8^{th} of April for 1 hour temporal resolution.

Besides, the AODs for three wavelengths from sun photometer and model calculation are shown in Figure 3.44. This figure shows that the AODs from sun photometer and model show a similar trend. However, the modeled AODs are systematically lower than those from the sun photometer. Figure S10 shows the time series of coarse particle mode AOD for sun photometer and modeled AOD, which shows that the modeled AOD values agree well with coarse mode AOD of the sun photometer at a wavelength of 550 nm. Hence, the reason for underestimating the AOD by the model shown in Figure 3.44 is partially due to the fact that the modeled AOD only includes the

Saharan dust plume and the sun photometer also the boundary layer aerosol. After the arrival of the dust plume, the AOD from the model calculation is systematically lower than the sun photometer measurement and the bias between the model and sun photometer increases with decreasing wavelength towards the ultraviolet (UV) spectral region. In other words, the discrepancy is wavelength dependent with a bigger difference in the UV. This wavelength-dependent discrepancy may be related to the overestimation of small particles in the model simulation.

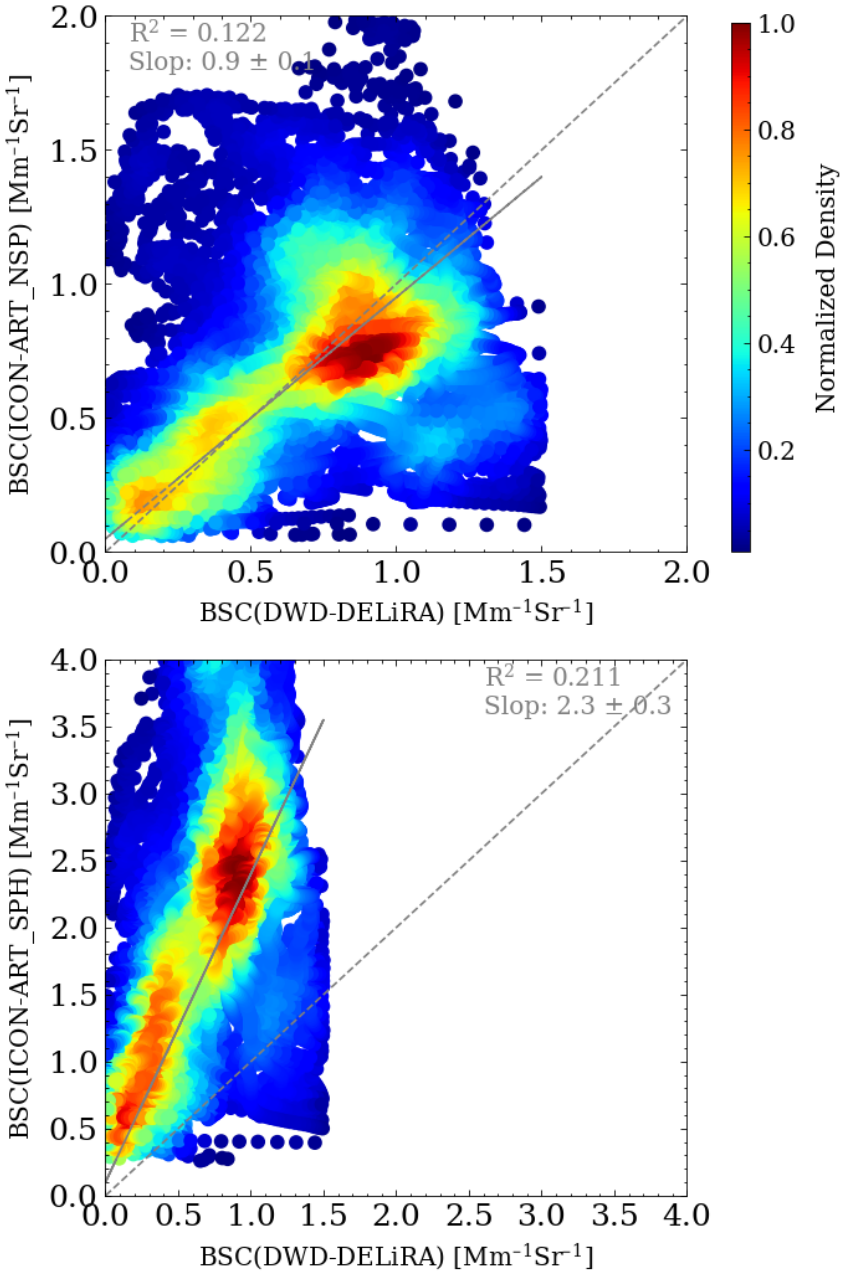

Figure 3.45: Correlation of Saharan dust backscatter coefficients measured by lidar and simulated by ICON-ART assuming non-spherical (top) and spherical particles (bottom). SPH = spherical; NSP = non-spherical.

Figure 3.45 shows the correlation of backscatter coefficients from lidar measurements and ICON-ART simulations for the dust plume, assuming both NSP (left panel) and SPH (right panel) particles. The color of the scatter points in this figure indicates the normalized density of backscatter coefficients, which indicates the frequency of occurrence of these values. These data points are selected according to the dust layers shown in Figure 3.49 which doesn't include the boundary layer aerosol for lidar measurements. The parameterizations for NSP and SPH are given in Hoshyaripour et al. (2019) and are based on work by Meng et al. (2010). For the whole dust episode, there is a remarkable agreement between model simulation and observations although individual profiles might differ significantly. The regression fitting was done for both NSP and SPH data points which have a normalized density larger than 0.4. The corresponding results of a regression analysis for NSP show a slope of 0.9 ± 0.1 and an R^2 of 0.68. This is an excellent result taking into account all uncertainties and assumptions for measurements and model simulations. However, the regression fitting for the SPH has a slope of 2.3 ± 0.3 and an R^2 of 0.68. This means that assuming spherical particles leads to overestimated backscatter coefficients. This is confirmed in Figure 3.30 which shows the backscatter coefficients of two lidar measurements and two model simulations using SPH and NSP particle parameterizations, respectively. This figure shows that the ICON-ART model overestimates backscatter coefficients at a wavelength of 355 nm by assuming spherical particles to calculate backscatter coefficients. The reason for the overestimation is that the spherical particles have larger backscatter coefficients (at 180°) than non-spherical particles Mishchenko (2014), Hoshyaripour et al. (2019). The physical meaning behind this phenomenon is that for spherical particles surface waves can contribute to the backscatter, hence causing larger backscatter coefficients for spherical particles (Hovenac & Lock 1992). The coarse mode AOD of the sun photometer and ICON-ART results for spherical and non-spherical particle models are shown in Figure S10. All AOD values follow a similar trend but the model results are higher by a factor of 1.25 ± 0.21 for NSP particles and 1.14 ± 0.18 for SPH particles, both at a wavelength of 550 nm.

Dust case 2 during February, 2021:

The evolution of the dust plume over Karlsruhe for dust case 2 predicted by the ICON-ART model is shown in panel (b) and panel (c) of Figure 3.35. According to the model simulation, the dust plume arrived in Karlsruhe at 04:00 on 22^{nd}, February 2021, and lasted for about five days. Initially, the ICON-ART predicted vertical backscatter between 1.0 to 8.0 km. Subsequently, the high-altitude

dust plume disappeared at 18:00 on 24^{th}, February 2021 and the main dust layer began to reach ground level. The vertical backscatter coefficients from lidar measurements and ICON-ART simulation are shown in Figure 3.35a and 3.35b&c. The dust layer height predicted by ICON-ART did not agree well with lidar measurements before 18:00 on 24^{th}, February 2021 while it shows consistency after this time. The dust layer heights and their peak heights for both lidar measurement and ICON-ART prediction are shown in figure 3.49b. The dust peak heights are not shown after 18:00 on 24^{th}, February 2021 for lidar measurement due to the influence of boundary layer aerosol loading during this time and boundary layer aerosol tends to have maximum values near ground level. The vertical profiles of backscatter coefficients from lidar measurements and two ICON-ART modes are shown in the right of Figure 3.35 for two selected periods indicated as C1 and C2 in Figure 3.35. For case C1, the backscatter coefficients are given for lidar measurements from 00:30 to 01:30 and ICON-ART calculations for 01:00 on 24^{th}, February and for case C2, the backscatter coefficients are given for lidar measurements between 02:30 to 03:30 and ICON-ART calculations for the average profile from 03:00 on 25^{th}, February 2021. As can be seen in the vertical profiles for the C2 period, the boundary layer aerosol and dust particles are mixed below 2.0 km and this mixing causes problems to determine dust peak heights from lidar measurements. In addition, the vertical profiles of the backscatter coefficients for case C1 show inconsistencies for dust layer heights and backscatter coefficients while profiles in case C2 show consistency in dust layer height but inconsistency in backscatter coefficients. As discussed for Saharan dust case 1, the predicted backscatter coefficients can agree well with values retrieved from lidar measurements if non-spherical particles are assumed while overestimating a factor of 2.3 ± 0.3 when spherical particles are assumed. However, during period C2 of Saharan dust case 2, the ICON-ART predicted backscatter coefficients for non-spherical particles were systematically lower than those from lidar retrievals. The main reason for this underestimation of the backscatter coefficient retrieved from lidar measurements is the contribution of non-dust particles to the total backscatter coefficient in this mixing layer.

Tesche et al. (2009) proposed a method to separate the total backscatter coefficient into a dust part and a non-dust part using the following equation:

$$\beta_{\lambda,d} = \beta_{\lambda,p} \frac{(\delta_{\lambda,p} - \delta_{\lambda,nd})(1 + \delta_{\lambda,d})}{(\delta_{\lambda,d} - \delta_{\lambda,nd})(1 + \delta_{\lambda,p})} \tag{3.1}$$

Where $\beta_{\lambda,d}$ is the pure dust backscatter coefficient, $\beta_{\lambda,p}$ is the total particle backscatter coefficient, $\delta_{\lambda,p}$ is the total particle depolarization ratio, $\delta_{\lambda,nd}$ is the particle depolarization ratio of non-dust particles, $\delta_{\lambda,d}$ is the particle depolarization ratio of pure dust plume. In this equation, $\beta_{\lambda,p}$ and $\delta_{\lambda,p}$ can be retrieved from lidar measurement. The particle depolarization ratio of pure dust plume, $\delta_{\lambda,d}$, is estimated from the high-altitude dust layer which is not mixed with non-dust particles and the particle depolarization ratio of non-dust particles, $\delta_{\lambda,nd}$, is the average value of particle depolarization measured on $1st$, March 2021 when there was no dust layer over Karlsruhe. For this Saharan dust case, a value of 0.3 for $\delta_{\lambda,d}$ and a value of 0.046 for $\delta_{\lambda,nd}$ were used.

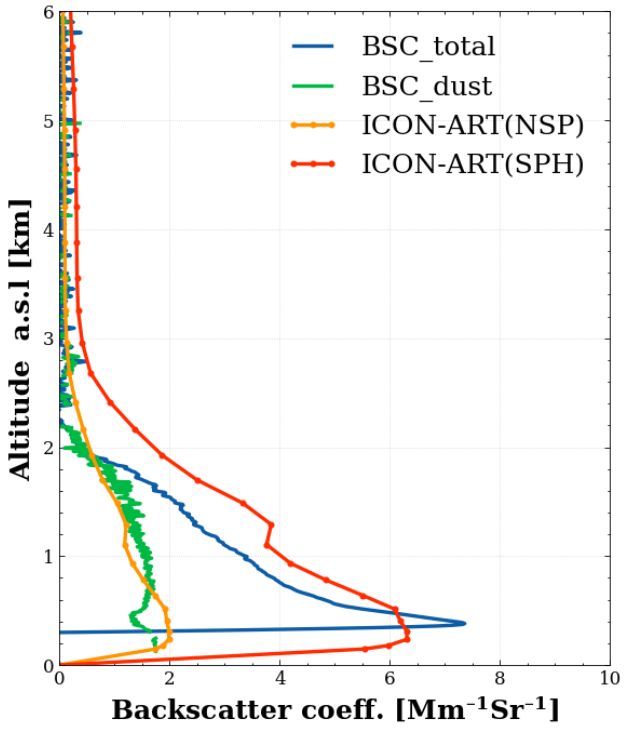

Figure 3.46: Vertical profile of total backscatter coefficients and dust backscatter coefficients from KASCAL and the predicted backscatter coefficient for non-spherical (NSP) and spherical (SPH) particles from ICON-ART for case C2 as indicated in Figure 3.35.

Figure 3.46 shows vertical profiles of total backscatter coefficients and pure dust backscatter coefficients from KASCAL measurement and ICON-ART predicted backscatter coefficients for NSP and SPH particles. This figure shows that backscatter coefficients predicted by ICON-ART for NSP particles are smaller than the total backscatter coefficients measured by KASCAL by a factor of 2.12 $\pm$ 0.66 while it agrees well with the pure dust backscatter coefficient by a factor of 1.06 $\pm$ 0.22. Figure 3.47 shows the correlation of the backscatter coefficient predicted by ICON-ART for NSP particles and retrieved from KASCAL measurement for both total aerosol particles (top)

and dust particles only (bottom). This correlation only shows the data after 20:00, 24^{th}, February 2021 as the dust layer heights are inconsistent between lidar and ICON-ART model before this time. The backscatter coefficients predicted by ICON-ART is systematically lower than the total backscatter coefficient retrieved from lidar data by a factor of 1.94 $\pm$ 0.65. However, the pure dust backscatter coefficients retrieved from KASCAL agrees well with the backscatter coefficients predicted by ICON-ART for NSP particles with the a slop of 0.976 $\pm$ 0.01 and a Pearsonr cor-

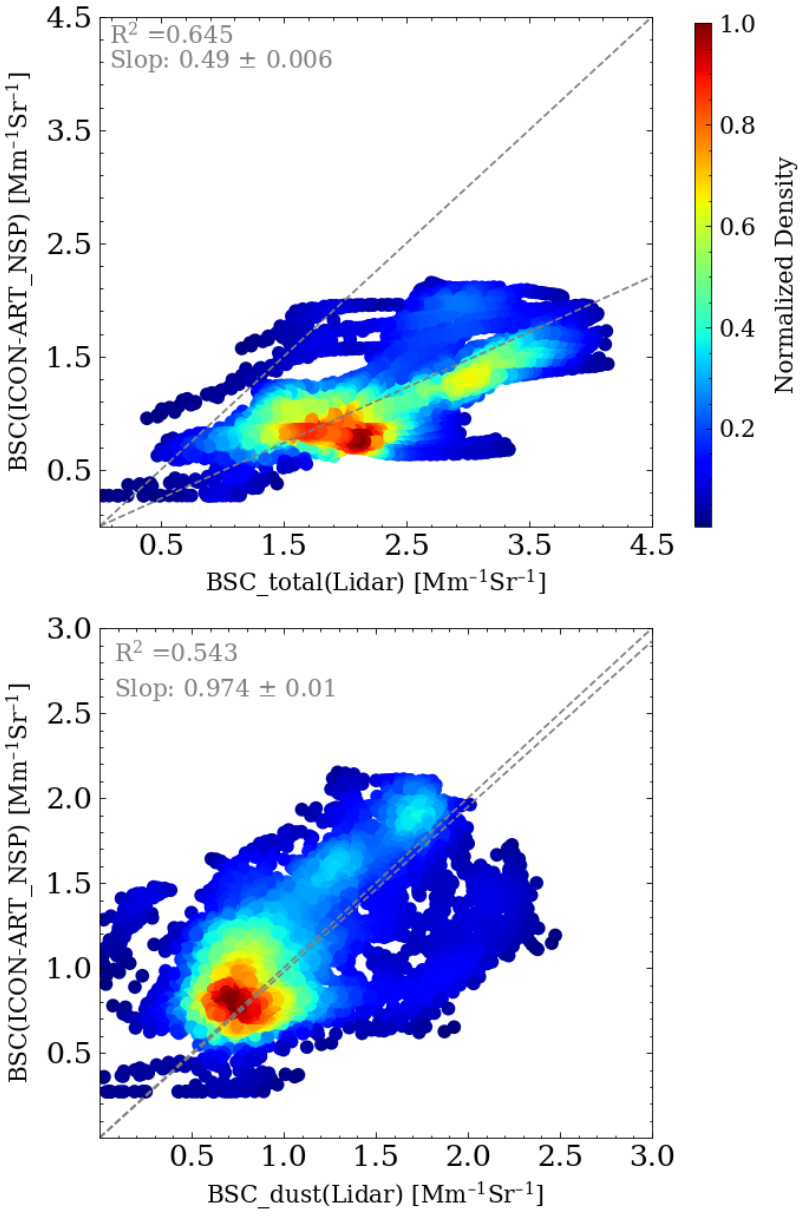

Figure 3.47: Correlation of backscatter coefficients predicted by ICON-ART for non-spherical (NSP) particles and retrieved from KASCAL for both total aerosol particles (top) and dust particles only (bottom).

relation coefficient of 0.96 0.543 as shown in Figure 3.47. From these comparisons, we can see that the non-dust aerosol particles can contribute to total backscatter coefficients, thus causing an apparent inconsistency between lidar measurement and ICON-ART simulation. The contribution of non-dust aerosol particles can also be seen from comparisonof AOD values between ICON-ART results and sun photometer data.

The time series of AODs at three wavelengths from sun photometer measurements and ICON-ART model simulations from 22^{nd}, February 2022 to 26^{th}, February 2021 is shown in Figure 3.48. This time series was divided into three periods (A, B, C) as shown in the figure based on the relationship of AOD from model simulations and sun photometer data. This figure shows that the AOD measured by the sun photometer is systematically larger than that predicted from ICON-ART by a factor of 2.78 ± 1.60 due to the contribution of non-dust particles as shown for the periods A and C . However, during period B, the AOD from ICON-ART prediction is larger than that measured by sun photometer by a factor of 1.41 ± 0.18 due to overestimating the dust loading during this period, which can also be seen from the comparison between model simulation and lidar measurements as shown in 3.35.

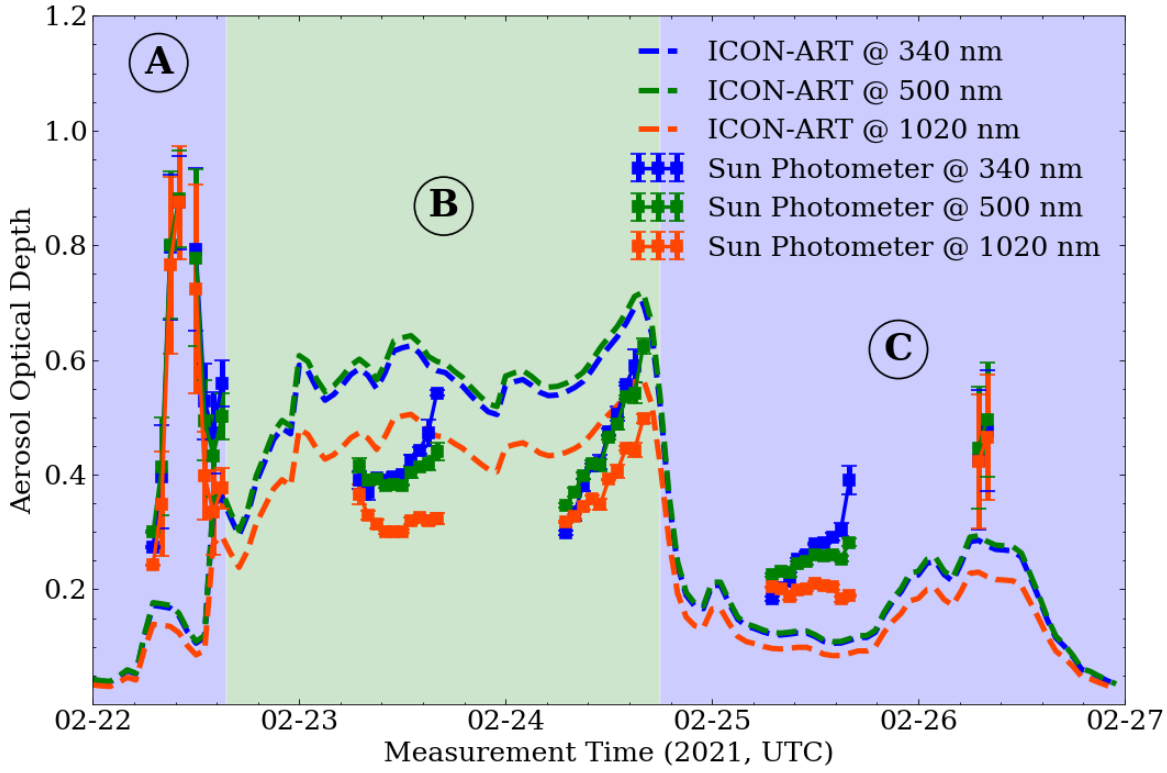

Figure 3.48: Time series of AODs at three wavelengths from the sun photometer and ICON-ART model simulations from 22^{nd}, February 2022 to 26^{th}, February 2021 for 1-hour temporal resolution.

Dust case 3 during June, 2021:

The evolution of the dust plume over Rottenburg for dust case 3 predicted by the ICON-ART model is shown in panel (c) of Figure 3.39. This panel shows that the dust plume arrived at Rottenburg at 11:00 on 19^{th}, June 2021 with an initial dust layer height between 4.0 - 5.0 km and lasted for nearly two days. Since 23:30 on 19^{th}, June 2021, a thick dust layer between ground level and up to 6.0 km was over Rottenburg. The dust layer heights and their peak heights for both lidar measurements and ICON-ART predictions for this Saharan dust case are shown in Figure 3.49c. The dust peak heights from KASCAL after 02:00, 20^{th}, June 2021 are not shown in this panel as low clouds and precipitation impeded the retrieval of dust peak heights from lidar measurement. This figure shows that the dust layer heights from ICON-ART predictions and lidar measurements show similar trends but still show some discrepancy. The ICON-ART predicted dust layer heights are 899 $\pm$ 693 m higher than those retrieved from lidar measurements. The vertical profiles of the backscatter coefficients from lidar retrievals and ICON-ART predictions for two selected periods indicated as C1 and C2 in Figure 3.39 are shown on the right side of Figure 3.39. For case C1, the backscatter coefficients predicted by ICON-ART for NSP particles is systematically lower than those retrieved from lidar measurements by a factor of 3.91 $\pm$ 1.66 between 2.6 - 4.4 km. There are two possible reasons for this underestimation of the backscatter coefficients. One is that ICON-ART underestimated the dust loading in this case and the second one is that the Saharan dust particles increased in size by condensation of water vapor at this altitude, which enhances the backscatter measured by lidar. For case C2, the backscatter coefficients predicted by ICON-ART were lower by a factor of 7.48 $\pm$ 1.9 below 3.2 km. The first reason for this underestimation of the backscatter coefficients is because of the mixture of dust particles with non-dust particles. So I separated the backscatter coefficients into the dust part and non-dust part as I have done it also for Saharan dust case 2. The results are shown in Figure S11, which shows that the mixing effect cannot explain all this underestimation as the pure dust backscatter coefficient is still higher than ICON-ART predicted backscatter coefficient. The second possible reason for this underestimation is that ICON-ART underestimates dust loading in this case. Although the ICON-ART results did not agree well with lidar measurements in this case, some consistency between model simulations and lidar measurement can also be seen. For example, the dust layer between 3.2 - 6.0 km for case C2 as shown in the right side of Figure 3.39 shows a good agreement between model simulation and lidar measurement.

Dust case 4 during March, 2022:

The evolution of the dust plume over Karlsruhe for dust case 4 predicted by the ICON-ART model is shown in panel (d) of Figure 3.41. This panel shows that two dust plumes arrived at Karlsruhe during these six days. The first dust plume arrived at Karlsruhe at 00:00 on 16^{th}, March 2022 with an initial dust layer height between 2.0 - 4.0 km and lasted nearly 3 days. This dust plume was dense until 00:00 on 18^{th}, March 2022 and was washed out by precipitation on 18^{th}, March 2022. Then another dust plume arrived at Karlsruhe at 06:00 on 21^{th}, March 2022 at an altitude of 2.0-3.0 km but was less dense. The dust layer heights and their peak heights for both lidar measurement and ICON-ART prediction for this Saharan dust case are shown in Figure 3.49d, which shows that the dust layer heights from ICON-ART prediction and lidar measurement show good agreement with each other. The vertical profiles of the backscatter coefficient from lidar retrieval and ICON-ART prediction for two selected periods indicated as C1 and C2 in Figure 3.41 are shown on the right side of Figure 3.41. For case C1, the vertical profile of backscatter coefficients predicted by ICON-ART for NSP particles agrees well with those retrieved from lidar measurements except for abrupt change of backscatter coefficients at altitudes between 1.6 km and 2.4 km. One possible reason for this phenomenon is that the ICON-ART model cannot resolve this high-resolution vertical aerosol distributions. For case C2, the backscatter coefficients predicted by ICON-ART underestimated the backscatter coefficients below 3.2 km. The one main possible reason for this underestimation of the backscatter coefficient is because of a mixing of dust particles with non-dust particles. Another possible reason is that ICON-ART overestimate the washout effect of precipitation in this case, thus calculating low concentration of dust particles.

So far, I have discussed mainly the properties (backscatter & depolarization) of the Saharan dust plumes and compared these observational data with ICON-ART results. In the following part, I will discuss average values of Saharan dust parameters in a systematic comparison between observational data and model results.

Table 3.3 shows the optical parameters of Saharan dust as measured by lidar and sun photometers for all four cases. The lidar ratio for case 3 is not shown in this table as there is no reliable lidar data during cloud free periods at nighttime and the SSA values for case 3 are not provided due to the presence of clouds. The optical parameters of Saharan dust summarized in this table shows good agreement with data provided by previous publications (Freudenthaler et al. 2009, Schuster et al. 2012, Cao et al. 2014).

Table 3.3: Overview of optical parameters of Saharan dust determined from lidar data, sun photometer measurements, and ICON-ART simulations for all four Saharan dust cases. (The light green shaded rows indicate the values of the ICON-ART model predictions.)

Parameter	λ [nm]	Case 1	Case 2	Case 3	Case 4	Average	Reference
BSC. ($Mm^{-1}sr^{-1}$)	355	0.95 ± 0.23	0.91 ± 0.43	1.52 ± 0.31	3.17 ± 2.48	1.64 ± 0.70	
BSC. ($Mm^{-1}sr^{-1}$)	355	0.71 ± 0.37	1.15 ± 0.41	0.73 ± 0.30	0.77 ± 0.73	0.84 ± 0.47	
LPDR	355	0.28 ± 0.03	0.27 ± 0.02	0.31 ± 0.04	0.30 ± 0.03	0.29 ± 0.03	0.252 ± 0.03 (Haarig et al. 2017)
LR (sr)	355	46 ± 10	57 ± 13		55 ± 10	53 ± 11	48 ± 8 (Haarig et al. 2022)
AOD	340	0.21 ± 0.12	0.33 ± 0.12	0.52 ± 0.14	0.80 ± 0.42	0.47 ± 0.20	
AOD	500	0.25 ± 0.11	0.39 ± 0.12	0.57 ± 0.12	0.91 ± 0.42	0.53 ± 0.19	
AOD	500	0.17 ± 0.09	0.36 ± 0.22		0.18 ± 0.06	0.24 ± 0.12	
AOD	1020	0.30 ± 0.11	0.41 ± 0.14	0.69 ± 0.12	1.01 ± 0.43	0.60 ± 0.20	
SSA	439	0.92 ± 0.03	0.90 ± 0.27		0.93 ± 0.01	0.91 ± 0.10	0.91 (Müller et al., 2011)
SSA	870	0.93 ± 0.04	0.95 ± 0.23		0.95 ± 0.01	0.94 ± 0.09	0.86 - 0.98 (Cachorro et.al., 2018)

BSC: backscatter coefficient; Exc: extinction coefficient; LR: lidar ratio

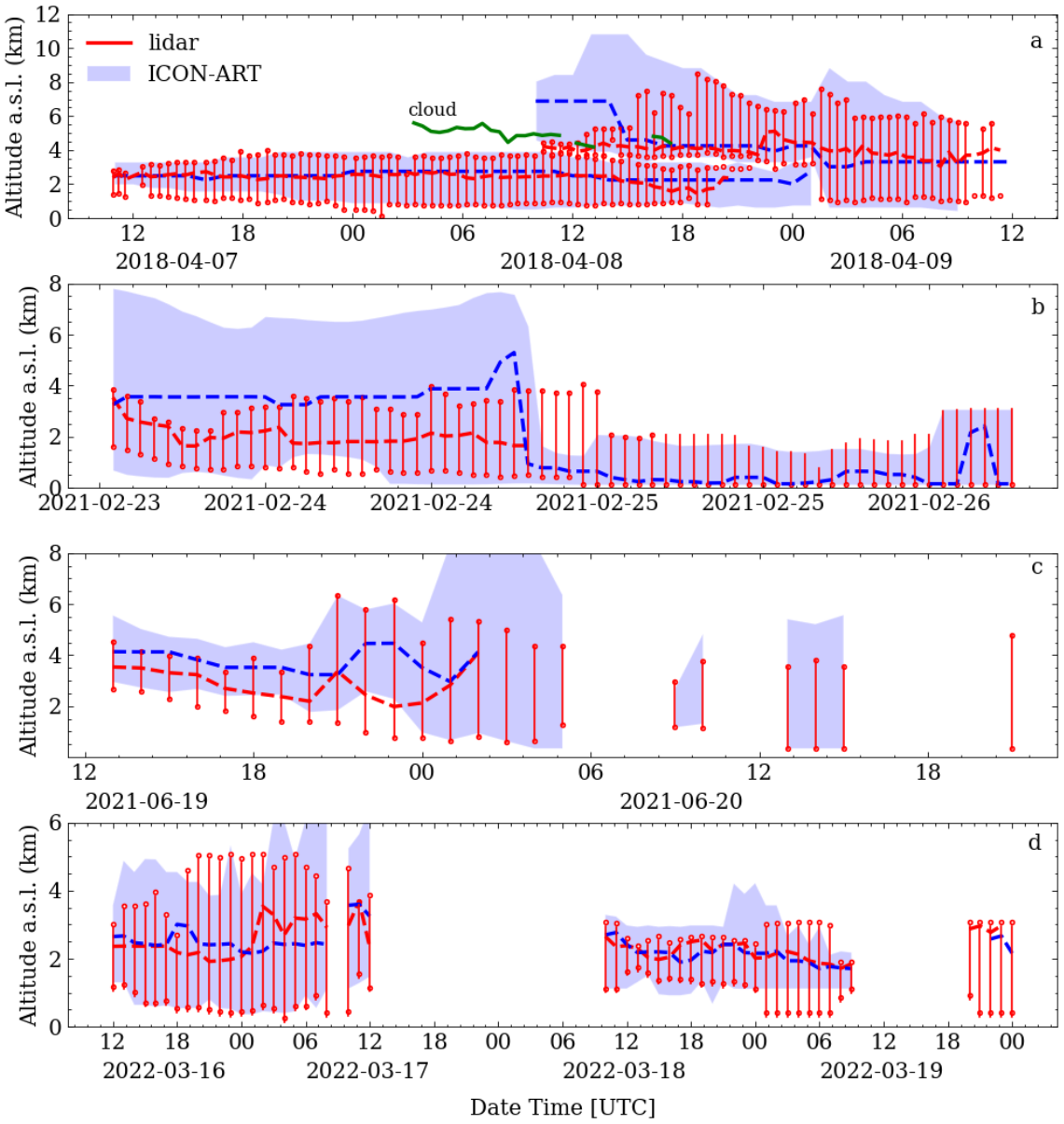

Figure 3.49: Time series of dust layer heights (vertical extend) and their peak heights (heights of maximum backscatter coefficients, indicated as red (lidar) and blue (ICON-ART) solid line) from both lidar measurements (red bars) and ICON-ART predictions (light blue area) for cases 1 - 4 (a-d).

The comparison of ICON-ART predictions with lidar measurements presented in this section is focused on the dust arrival time and dust layer height. The comparison of dust backscatter intensity was discussed for different cases. Figure 3.49 shows the time series of dust base height, dust top height, and dust peak height for both lidar measurements and ICON-ART simulations. This figure shows that the dust arrival times predicted by the ICON-ART model agrees well with lidar mea-

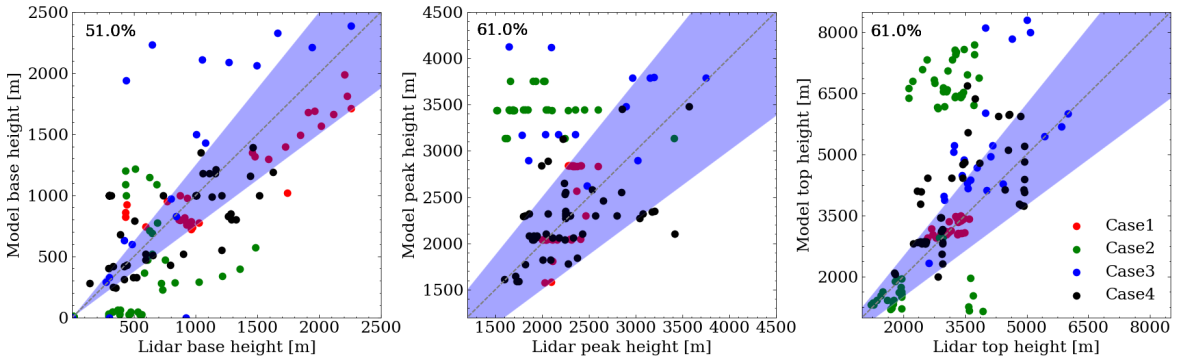

Figure 3.50: Correlation of dust base heights (left), dust peak heights (middle), and dust top heights (right) from lidar measurements and ICON-ART simulations for all 4 Saharan dust cases.The blue-shaded area indicates slopes between 0.75 and 1.25 and the number shown in the left upper corner is the percentage of data points within this blue-shaded area.

surements (± 20 minutes) for all 4 cases. This plot also shows that the dust layer heights predicted by ICON-ART model and measured by lidar show consistency most of the time but still show some inconsistencies for certain time periods (e.g. the first half experiment for case 2 as shown in Figure 3.49b). The remaining discrepancies between observations and ICON-ART predictions may be related to the following reasons: 1) The ICON-ART model simulation used a relatively coarse horizontal resolution (20 km), which means that ICON-ART simulation results can't reflect structural details of Saharan dust plumes in such detail as possible e.g. by lidar measurements. Therefore, larger differences are to be expected especially for inhomogenously structured dust plumes. In the future, this may be improved with a high-resolution ICON-ART model e.g. coupled with the LES model PALM. 2) Depending on different meteorological conditions during transport of the dust plumes from Africa to Germany especially the washout of dust particles may need different parameterizations. This may be improved also using my scanning lidar data before and after heavy and light precipitation as will be discussed in the following section on aerosol cloud interaction. 3) The inappropriate meteorological background information used in ICON-ART may also cause the discrepancy between model simulation and observation data. Figure 3.50 shows the correlation of dust base heights, dust peak heights, and dust top heights from lidar measurement and ICON-ART prediction for 4 Saharan dust cases. The blue-shaded area in these plots indicates slopes between 0.75 and 1.25 and the number shown in the left upper corner of each plot is the percentage of data points within this blue-shaded area. These plots show that there are 51%, 61%, and 61% of data points within this blue-shaded area for dust base heights, dust peak heights, and dust top heights. To be detailed, good agreement in dust layer heights can be seen for case 1, case 3, and case 4 but

not for case 2 as discussed for Figure 3.49. In general, the ICON-ART model predicts dust arrival times and dust layer heights very well if considering the spatial resolution of ICON-ART model (20.0 km horizontally).

Figure 3.51 shows theAOD values at a wavelength of 500 nm both from sun photometer measurements and ICON-ART predictions as well as the AE values retrieved from sun photometer measurements for all 4 Saharan dust cases. The AOD values given in the left side of this figure show that Saharan dust case 4 had the largest AOD with a value of 0.91 ± 0.42, which indicates that the Saharan dust case 4 was the strongest dust events among these 4 cases. In addition, the AOD predicted by ICON-ART model is systematically lower than that measured by the sun photometer even though the ICON-ART model overestimates the dust concentration for part of the Saharan dust case 2. The reason for this phenomenon is that the sun photometer measured the total AOD while only the dust particles are considered in ICON-ART model prediction. The biggest difference in AOD values between sun photometer measurements and ICON-ART simulations can be seen for case 4. This was caused by the strong haze over Karlsruhe during that time as discussed in section 3.4.2 and this strong haze was not considered in the ICON-ART model simulation. The AE values shown on the right side of this figure illustrate relatively lower value of AE for Saharan dust cases 2 and 4 compared to cases 1 and 3. These smaller values of AE refer to larger Saharan dust particles over the observational stations for these two cases.

3.4.4 Saharan dust cloud interaction

Aerosol-cloud-interaction was investigated during the Swabian MOSES field campaign in Rottenburg am Neckar (see section 2.4) by combining remote sensing methods (e.g. lidar, ceilometer, sun photometer, radar), *in-situ* measurements (e.g PINE,OPC, CPC, and APS), as well as radiosondes. Several intensive observation periods (IOPs) were conducted during this Swabian MOSES field campaign as indicated in Table 2.4. During IOP4 also Saharan dust was present at that location and therefore I will discuss potential aerosol-cloud-interactions for this case. A Saharan dust plume arrived in Rottenburg during this IOP as discussed in section 3.4.2 and dust particles are known to be effective INPs (Brunner et al. 2021*a*, Ansmann et al. 2019). Furthermore, the precipitation observed during IOP4 was less than predicted by most weather forecast models (Kunz et al. 2022). The objective of the aerosol measurements in this experiment was to study potential INP concentrations in relation to other aerosol particle characteristics. Various meteorological parameters were

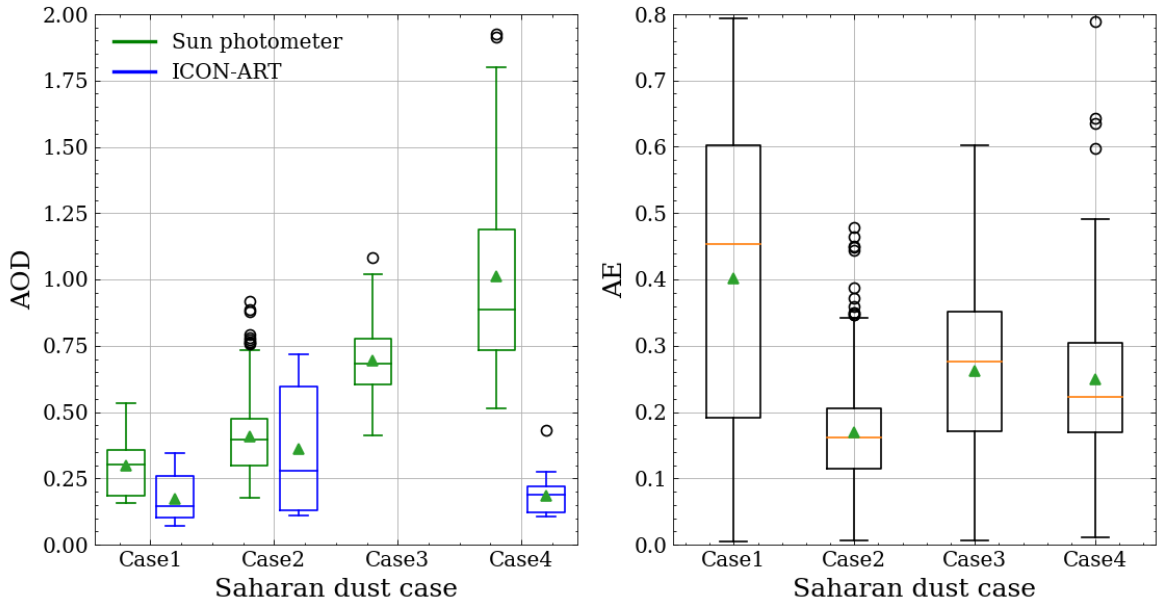

Figure 3.51: Mean value and standard deviation of Aerosol Optical Depths (AODs) both from sun photometer measurement for total aerosol and ICON-ART predictions for Saharan dust only (left) as well as Ångström exponen (AE) (right) measured by sun photometer for all four Saharan dust cases.

measured to investigate the role of aerosol particles and INPs for the formation of strong convective clouds. Therefore, aerosol particles were characterized with respect to their number and mass concentration, size distribution, ice nucleation ability, and their spatial distribution. In addition to the measurements at the Swabian MOSES main site in Rottenburg, mobile INP measurements were performed for special events in conjunction with the mobile operation of the swarmsondes. The INP concentrations were measured by my colleaguesDr. Franziska Vogel and Alexander Böhmländer.

An especially interesting period during IOP4 is shown in Figure 3.52, during which a Saharan dust plume was reaching ground level (indicated by the grey shaded areas). These periods show higher PM10/PM2.5 ratios (particulate matter with maximum diameter of 10/2.5 µm) and significantly more particles with sizes larger than 2 µm. Please note, that the particle number concentrations are dominated by smaller particles, as opposed to the mass concentration, which is dominated by the larger ones. The fraction of ice active aerosol particles at 251 K (Figure 3.52D), calculated by dividing the ice crystal number concentration by the total aerosol number concentration, shows similar patterns as the PM10 concentrations (Figure 3.52B).

The volume depolarization ratios and range corrected backscatter signals of the lidar (Figure 3.52E and F) illustrate the spatial distribution of the aerosol particles in and above the PBL. The Saha-

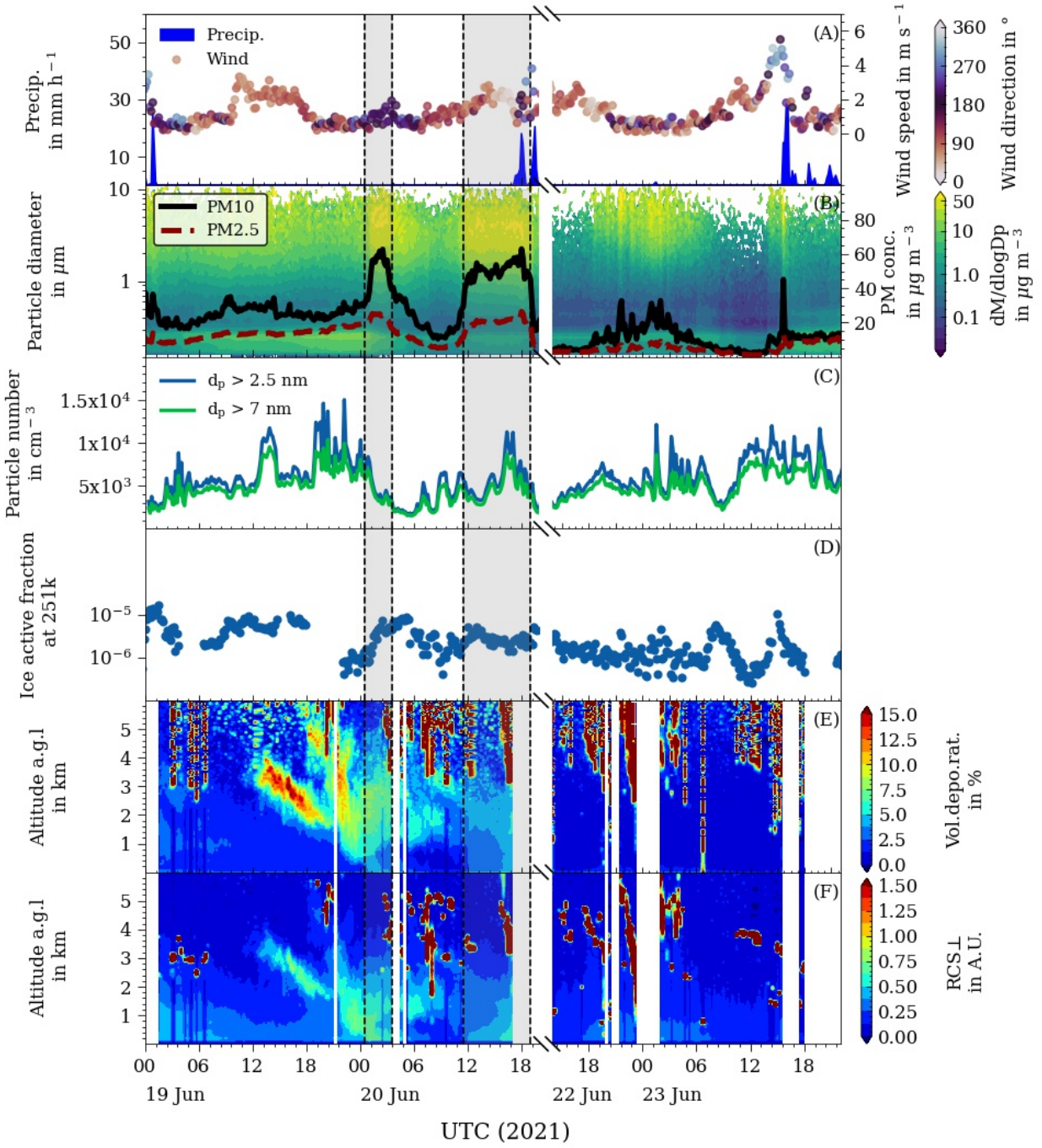

Figure 3.52: Overview of aerosol measurements at the Swabian MOSES main site Rottenburg during IOP4 with higher concentrations of Saharan dust. (A) Wind speed, wind direction, and precipitation, (B) particle mass (PM10 and PM2.5; lines) and particle mass size distributions (contour), (C) particle number concentrations for particles larger than 2.5 and 7 nm, (D) ice active fraction at 251 K, (E) lidar volume depolarization ratio (contour), (F) lidar range corrected backscatter signal perpendicular to the emitted laser polarization (contour). Grey shaded areas indicate Saharan dust reaching ground level. I generated this figure for (Kunz et al. 2022).

ran dust plume arrived at noon (19^{th}, June) above the measurement site at an altitude between 3 and 4 km and reached ground level about 12 hours later. Please note that aerosol lidar data are not available during precipitation events (cf. Figure 3.52A). Both the PM10 and PM2.5 concentrations were highly affected by thunderstorms. On 20^{th}, June around 18:00 UTC, for example, an mesoscale convective systeme (MCS) that passed the measurement site led to an abrupt decrease in

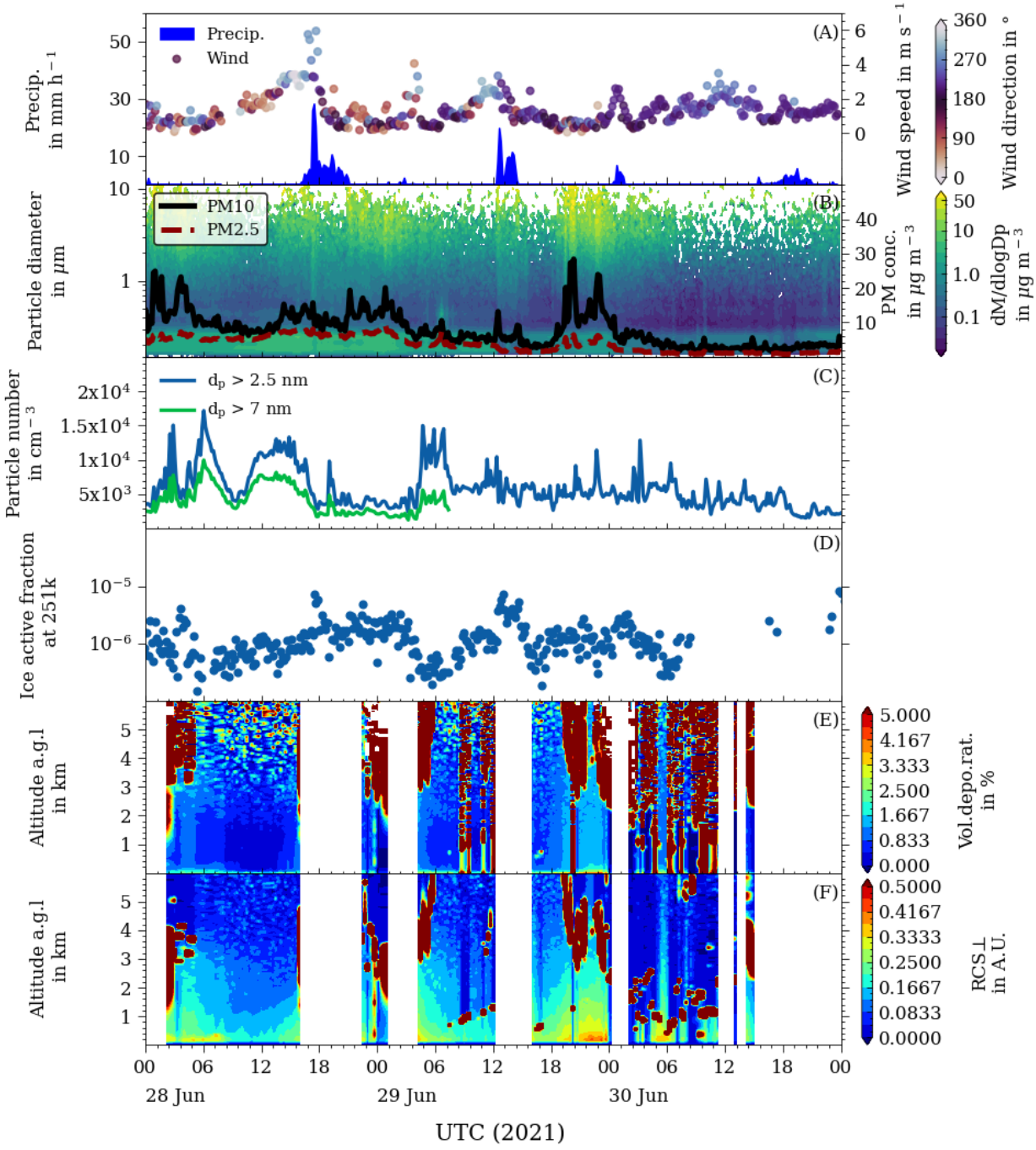

Figure 3.53: Same as Figure 3.52, but for IOP5.

the particle mass concentrations due to wet deposition of the aerosol particles. On 23^{th} June around 15:45 UTC, the concentration of larger particles presumably from the surface (PM10) substantially increased prior the passage of a supercell over the measurement site. Directly with the onset of heavy precipitation (rain and small hail), the PM10 concentration abruptly dropped to low values that remained almost constant until midnight. A direct relation between thunderstorms and the ice active fraction (Figure 3.52D), however, is not evident based on this data.

Figure 3.53 shows the evolution of aerosol particles during IOP5. During this period, no substantial Saharan dust influence was detected. Therefore, aerosol particles in the boundary layer dominated. On 28 July, as a supercell passed the measurement site, no substantial changes in aerosol properties were detected. As can be seen by comparing both IOPs, there was no significant precipitation in presence of Saharan dust over Rottenburg from 12:00 of 19^{th} June, 2021 to the 15:00 of 20^{th} June, 2021. In contrast several precipitation event occurred in absence of Saharan dust as shown in Figure 3.52A and Figure 3.53A. One possible explanation for this phenomenon is that the presence of Saharan dust suppressed precipitation in this case (Rosenfeld et al. 2001). In presence of Saharan dust more cloud droplets or ice crystals may have formed in the cloud leading to smaller droplets and less ice and rain formation. However, also the mixing with air of Saharan origin may have altered the humidity profiles of the air masses reaching Rottenburg leading to a supression of precipitation. These and other protential reasons are currently studied by different colleagues using the large set of observational data and the cloud resolving version the the ICON-ART model.

In addition my aerosol measurements, I could also use a comprehensive set of data from a cloud radar, a ceilometer, a sun photometer, and several radiosonde measurements all operated and analyzed by my colleagues from the KITcube. These data help to better understand the vertical profiles of clouds and the meteorological background (e.g. wind shear, CAPE), thus helping us to study the potential role of aerosol particles in formation of clouds and precipitation. I have analyzed these data together with Dr. Yuxuan Bian. Figure 3.54 shows the time series of wind profiles from radiosonde, RCS and LVDR from scanning aerosol lidar, RCS from ceilometer, AOD and aerosol coarse-mode fraction from sun photometer, temperature and relative humidity from weather sensor (WS 700), aerosol volume size distribution and particulate matter concentration from OPC measurements, Radar reflectivity, Doppler velocity, and spectral width from Doppler cloud lidar during a Saharan dust outbreak from 19^{th} to 20^{th}, June 2021 during IOP4 at Rottenburg am Neckar. This figure shows a comprehensive dataset we obtained during this Swabian MOSES campaign. This

dataset can help to understand the the aerosol and cloud properties as well as the mechanism of aerosol cloud interaction. However, to achieve a scientific understanding of the relevant different and complex processes a dedicated comparison of the also complex observations with a cloud resolving model is required. The data analysis on this scientific topic is still ongoing together with Dr. Yuxuan Bian (IMK-AAF, now at Chinese Academy of Meteorological Sciences) and other colleagues at IMK-TRO (Dr. Heike Vogel, Dr. Gholamali Hoshyaripour, Dr. Lena Anna Frey and Dr. Christian Barthlott).

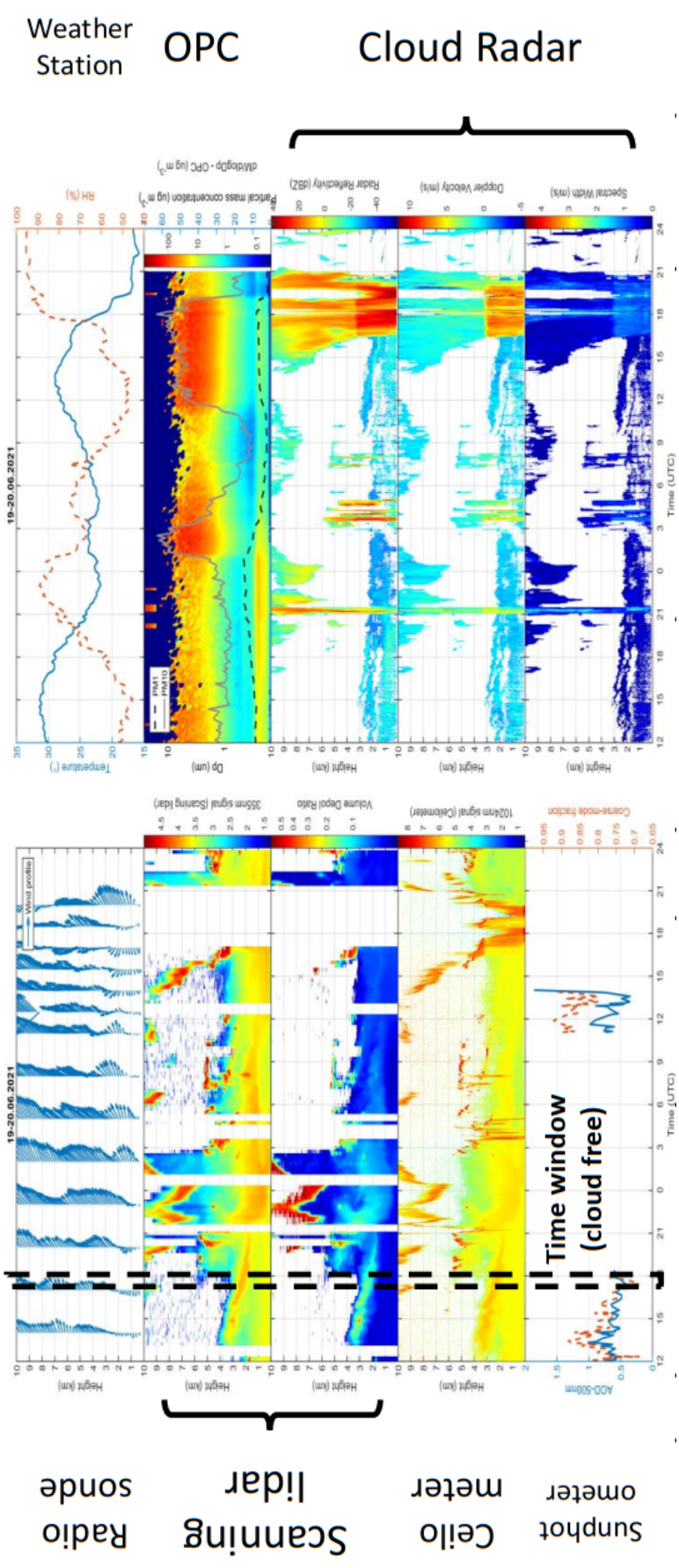

Figure 3.54: Time series of wind profiles from radiosonde, Range Corrected lidar Signal (RCS) and Linear Volume Depolarization Ratio (LVDR) from scanning aerosol lidar, RCS from ceilometer, Aerosol OPtical Depth (AOD) and aerosol coarse-mode fraction from sun photometer, temperature and relative humidity from a weather sensor (WS 700), aerosol volume size distribution and particulate matter concentrations from OPC measurements, Radar reflectivity, Doppler velocity, and spectral width from Doppler cloud lidar from 19^{th} to 20^{th}, June 2021 during IOP4 at Rottenburg am Neckar.

3.4.5 Summary

The objectives of the work presented in this section were to compare different measurements and retrieval methods including remote sensing and *in-situ* measurements and to demonstrate which aerosol properties can be determined by combining the different measurement techniques. Furthermore, I wanted to understand the quality of the dust plume predictions with the ICON-ART model by comparison with the observations. The evolution and the properties of Saharan dust were characterized for 4 Saharan dust plume cases combining data from lidars, a sun photometer, and ground level *in-situ* measurements. The comprehensive dataset from different methods could characterize the dust plume in different ways, thus providing additional information for further analysis. The scanning angle lidar measurements enabled us retrieving lidar ratios and extinction coefficients independently and during day and night, which were comparable to Raman based retrievals. The comparison of extinction and backscatter coefficients for different retrieval methods was used to quantify uncertainties of the different methods and the impact of different denoise filters on extinction coefficients from Raman scattering lidar signals. The consistency among three different lidar laser beam paths reflects the high quality of the measurements as well as the retrieval algorithms. Vertical and slant volume and particle depolarization ratio measurements contain information on shape and partially orientation of dust particles. Comparison between lidar and sun photometer measurements has proven useful to study the dust optical properties like aerosol optical depth and to obtain information about lidar parameters like the lidar ratio. Comparison among lidar measurements, sun photometer, and ICON-ART predictions shows a quite good agreement for dust arrival time, dust layer height and structure, backscatter coefficients, and AODs. The modeled backscatter coefficients for dust show a good agreement with lidar retrievals at a wavelength of 355 nm if assuming non-spherical particle but the model would overestimate the backscatter coefficients if assuming spherical particle. This demonstrates how crucial it is to use an appropriate parameterisation for the dust particle properties. This has also implications for a potential particle assimilation scheme. Despite the good agreement between model predictions and observations for these four Saharan dust plumes still some deviation can be seen for certain periods. The discrepancies between ICON-ART predictions and observational data still needs to be studied further in order to identify potential model improvements. The systematic comparisons for different meteorological conditions and at different locations are discussed here to substantiate the model validation and to

facilitate a potential improvement of the dust processes (emission, transport, removal and microphysics) and properties (size distribution and optics) in models like ICON-ART. Finally, the role of Saharan dust particles on cloud formation and precipitation was discussed combining a broad set of remote sensing, *in-situ*, and radiosonde measurements. These measurements are currently compared with ICON-ART model results to study potential mechanisms of aerosol-cloud-precipitation interaction.

4 Conclusion and outlook

4.1 Conclusions and atmospheric implications

The impact of atmospheric aerosols on the Earth's climate system is significant and remains highly uncertain, which is attributed to the large spatial-temporal variability of aerosol particles and their complex interaction with other atmospheric constituents as well as radiation and clouds (Zhao et al. 2011, Alam et al. 2011). Hence, to assess their environmental and climatic impacts it is crucial to characterize aerosol distributions and especially three dimensional aerosol distributions on a global and regional scale, as well as their transport, and their characteristic properties (e.g. optical, CCN, INP). Based on the advanced capabilities of the scanning aerosol lidar (Zhang et al. 2022, Ji et al. 2022), I investigated the boundary layer dynamics and air quality in urban and rural background areas as well as Saharan dust transport over Western Europe in detail.

In this dissertation, I compared different lidar retrieval methods including software from the lidar manufacture Raymetrics Inc., the reference software (SCC) from the European lidar network EARLINET, software developed by the university of Granada, as well as the software code developed by myself. The good agreement between the retrievals using different software validates my development which is especially suitable for scanning lidar retrievals. I also proposed a new method to retrieve lidar ratios based on scanning aerosol lidar measurement with at least two different elevation angles. Compared to only vertical lidar measurements this method allows determination of lidar ratios or extinction even without a Raman channel and thus helps to significantly reduce uncertainties in lidar retrievals (Zhang et al. 2022, Wandinger 2005). Also, the retrieved lidar ratio from scanning aerosol lidar will be helpful in aerosol classification (Haarig et al. 2022). In addition, I validated my lidar retrievals by different *in-situ* measurements including aerosol sizers at ground level, an optical particle counter on an UAV, as well as an *in-situ* backscatter detector (COBALD) on a balloon radiosonde. The extinction coefficients retrieved from the scanning lidar KASCAL is well correlated with that calculated from Mie calculations based on the aerosol size distributions measured at ground level OPC with a slop and Pearson correlation coefficient of 1.037 ± 0.015 and 0.878, respectively. The comparison between my lidar retrievals with OPC data from drone flights up to 1200 m above ground shows a very similar vertical aerosol distribution and boundary layer evolution. The comparison of my lidar retrievals with COBALD also shows a good agreement in

backscatter measurements up to the stratosphere with a slop of 1.063 ± 0.016 and a Pearson correlation coefficient of 0.925. The good agreement between the lidar data and these *in-situ* methods reflects the good data quality of my datasets and also validates the scanning lidar retrievals (Xiafukaiti et al. 2020, Brunamonti et al. 2021*a*). This is a good basis also for further comparison of the scanning lidar data with other remote sensing data like EARLINET, AERONET or satellite data (Deng et al. 2010, McGill et al. 2007, Abril-Gago et al. 2022).

Based on the dataset collected in downtown Stuttgart in winter, I investigated the boundary layer dynamics and air quality in the urban background of downtown Stuttgart in a basin-like topography. The comparison of the boundary layer heights and detailed structures from lidar retrieval and radiosonde measurement shows a very good agreement with a slop and a Pearson correlation coefficient of 1.102 ± 0.135 and 0.860, respectively. Also and the boundary layer from the ERA5 dataset shows a similar trend but systematically lower heights than those retrieved from lidar measurements. This comparison shows the advantage of scanning aerosol lidar measurements in determining the structural details of the boundary layer including the residual layer in greater detail and accuracy than the other methods. Furthermore, I could show that the ground-level aerosol concentrations were anti-correlated with mixing layer heights but were correlated with the nocturnal boundary layer height (Yuval et al. 2020). Stagnant weather conditions with strong temperature inversions and low wind speeds cause accumulation of aerosol particles in the shallow boundary layers especially during nighttime and early morning hours. These stagnant weather conditions with shallow boundary layers suppress the dispersion of local aerosol, potentially causing strong air pollution especially in bigger cities in winter. This case study allows to distinguish how the dispersion of local aerosol is affected by the boundary layer dynamics versus horizontal transport and varying local emissions. This includes also the potential role of clouds above the city during night as they influence the thermal structure underneath and can lead to accelerated growth of the boundary layer after sunrise. My observational data are thus ideally suited to validate high-resolution models like PALM-4U. The dataset collected in this field campaign and the simulation conducted in this area help us better understand the mechanism of air pollution in bigger urban areas like the Stuttgart basin.

Based on the data collected during Saharan dust events in April 2018, February 2021, June 2021, and March 2022, I determined the proprieties and transport of Saharan dust plumes and validated the dust transport model, ICON-ART, for Saharan dust transport to Western Europe. The newly

proposed method to retrieve lidar ratios from scanning elastic lidar data was applied for Saharan dust and the lidar ratios retrieved by this method agree well with those from the classic Raman retrieval method. The lidar measurement shows the pure dust particles measured during these four cases have a lidar ratio of 53 ± 11 sr and a linear particle depolarisation ratio of 0.29 ± 0.03. These values are in good agreement with those obtained in previous studies of Saharan dust plumes in Western Europe (Freudenthaler et al. 2009). The properties of mixtures of dust particles with other aerosol particles were also characterized by scanning aerosol lidar in this dissertation. Saharan dust particles also mixed with other aerosol particles (e.g. sea salt and biomass burning emissions) during dust transport and this mixing substantially changed the proprieties (e.g. lidar ratio, extinction, and particle depolarization ratio) of the mixed aerosol. Also the condensation of organic and inorganic gaseous compounds contribute to the aging of the dust particles and corresponding modified properties e.g. to act as condensation or ice nuclei. The comparison of ICON-ART model simulations with sun photometer data shows that the predicted AOD is systematically lower than observed values. This was expected since the ICON-ART model version only accounted for the Saharan dust while the sun photometer sums up the contributions of all aerosol particles. Compared to the lidar measurements, the ICON-ART model predicted the plume arrival time, its layer height, and its structure very well. The comparison of dust plume backscatter values from the ICON-ART model and lidar observations show that ICON-ART model can predict dust backscatter intensities quantitatively when a non-spherical particles parameterization is used but would overestimate the backscatter by a factor of 2-3 when assuming spherical particles. This demonstrates how crucial it is to use an appropriate parameterization for dust particle optics. This has implications for the particle assimilation scheme of the models. This systematic comparison between the transport model and observational shows typically reasonable to very good Saharan dust predictions by the ICON-ART model. However, for some cases or periods I observed some discrepancies that still need to be discussed for different meteorological conditions and at different locations. Generally, my observational data could be used in the context of the dust transport model comparison (Weimer et al. 2017, Zängl et al. 2015). Finally, I discussed the potential role of Saharan dust particles on cloud formation and precipitation combining different observational data including remote sensing (e.g. lidar, cloud radar, and sun photometer), *in-situ*, and radiosonde measurements. These measurements are currently compared with the cloud resolving ICON-ART model to study the mechanisms of aerosol-cloud-precipitation interaction. So far, it seems that there was less precipi-

tation than predicted in presence of Saharan dust plumes. However, a causal relationship is not yet proven.

To conclude, this dissertation contributes new insights regarding the application of scanning elastic lidar to boundary layer dynamics, aerosol transport, and transport model validation, which improves our understanding of their impacts on air quality. Figure 4.1 summarizes the major findings of this dissertation in a simplified schematic.

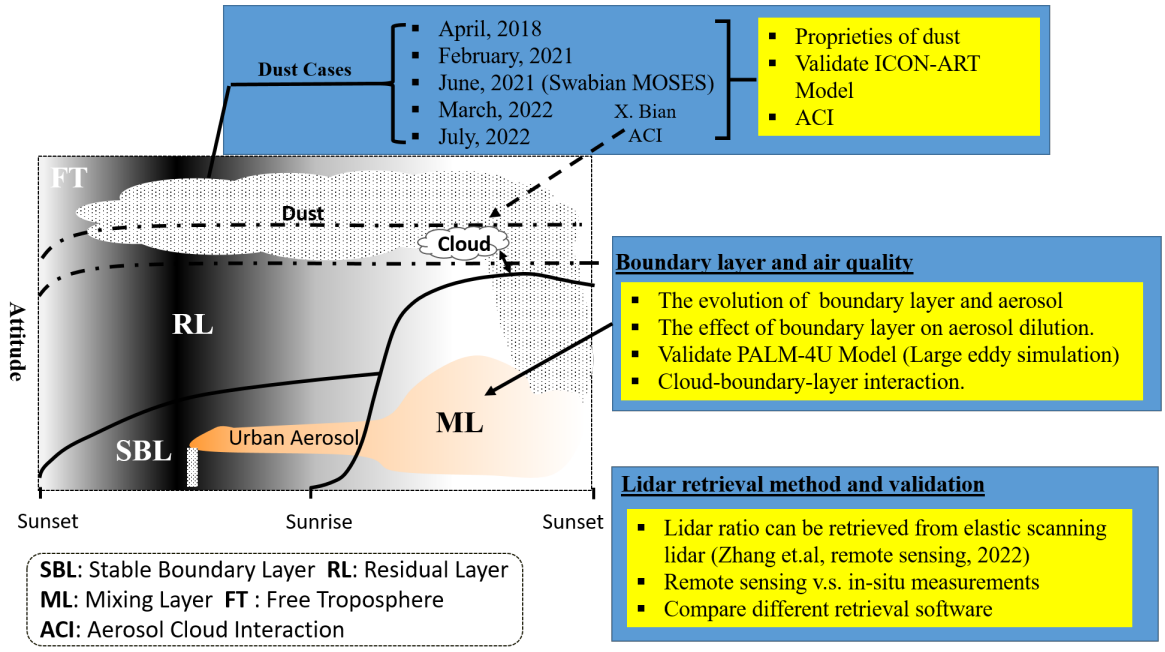

Figure 4.1: Schematic of boundary layer evolution modified based on Stull (1988) and the scientific topics related to my thesis. My major results are related to scanning lidar validation, boundary layer dynamics and air pollution, and Saharan dust properties and transport.

4.2 Outlook

This dissertation studies planetary boundary layer dynamics and aerosol spatial-temporal distributions combining remote sensing and *in-situ* methods as well as numerical simulations. The diurnal evolution of the boundary layer and the proprieties of aerosol particles were investigated in detail benefiting from additional information from scanning aerosol lidar data. In addition, this dissertation also raises several new technical and scientific questions, which could be the research topics for future studies:

1. In this dissertation, I proposed a new method to retrieve lidar ratio based on scanning aerosol lidar. However, this method was only applied in our KASCAL system that has only one

emission wavelength at 355 nm. In principle, this method can be applied in scanning multi-wavelength lidar systems as well to determine the wavelength-dependent lidar ratios, which can help to better distinguish different aerosol types by remote sensing.

2. Mie theory was used in this dissertation to calculate extinction and backscatter coefficients from aerosol particle size distributions. The assumption of the spherical particle is needed when using Mie theory. Further studies can be focused on using T-matrix or Discrete Dipole Approximation (DDA) to calculate optical parameters by considering the shape of particles.

3. In this dissertation, mainly the vertical boundary layer height was considered. Employing scanning lidar measurements, it is also possible to determine the horizontal boundary layer heights to investigate boundary layer dynamics for different underlying surfaces or topographies.

4. The impact of pre-existing clouds during the previous night on the evolution of the boundary layer during the following day was discussed in this dissertation for one case. More data including from satellites or reanalysis should be used to validate my finding.

5. The validation of Saharan dust predictions by the ICON-ART model was only conducted for western Germany. It would be valuable to validate this model in other regions as well e.g. by satellite data or data collected in observation networks (e.g. AERONET, EARLINET). More importantly, it would be valuable to discuss the potential reasons for the discrepancies between model simulations and observations for different meteorological conditions to improve model predictions in the future.

5 Reference

Aarons, S., Aciego, S. & Gleason, J. (2013), 'Variable hfsrnd radiogenic isotopic compositions in a saharan dust storm over the atlantic: Implications for dust flux to oceans, ice sheets and the terrestrial biosphere', *Chemical Geology* **349-350**, 18–26.
URL: *https://www.sciencedirect.com/science/article/pii/S0009254113001745*

Abril-Gago, J., Guerrero-Rascado, J. L., Costa, M. J., Bravo-Aranda, J. A., Sicard, M., Bermejo-Pantaleón, D., Bortoli, D., Granados-Muñoz, M. J., Rodríguez-Gómez, A., Muñoz Porcar, C., Comerón, A., Ortiz-Amezcua, P., Salgueiro, V., Jiménez-Martín, M. M. & Alados-Arboledas, L. (2022), 'Statistical validation of aeolus l2a particle backscatter coefficient retrievals over actris/earlinet stations on the iberian peninsula', *Atmospheric Chemistry and Physics* **22**(2), 1425–1451.
URL: *https://acp.copernicus.org/articles/22/1425/2022/*

Ackerman, A. S., Kirkpatrick, M. P., Stevens, D. E. & Toon, O. B. (2004), 'The impact of humidity above stratiform clouds on indirect aerosol climate forcing', *Nature* **432**(7020), 1014–1017.

Adam, M. (2012), 'Vertical versus scanning lidar measurements in a horizontally homogeneous atmosphere', *Applied optics* **51**(19), 4491–4500.

Äijälä, M., Heikkinen, L., Fröhlich, R., Canonaco, F., Prévôt, A. S., Junninen, H., Petäjä, T., Kulmala, M., Worsnop, D. & Ehn, M. (2017), 'Resolving anthropogenic aerosol pollution types–deconvolution and exploratory classification of pollution events', *Atmospheric Chemistry and Physics* **17**(4), 3165–3197.

Akritidis, D., Katragkou, E., Georgoulias, A. K., Zanis, P., Kartsios, S., Flemming, J., Inness, A., Douros, J. & Eskes, H. (2020), 'A complex aerosol transport event over europe during the 2017 storm ophelia in cams forecast systems: analysis and evaluation', *Atmos. Chem. Phys.* **20**(21), 13557–13578.

Alam, K., Trautmann, T. & Blaschke, T. (2011), 'Aerosol optical properties and radiative forcing over mega-city karachi', *Atmospheric Research* **101**(3), 773–782.

Alas, H. D. C., Müller, T., Weinhold, K., Pfeifer, S., Glojek, K., Gregorič, A., Močnik, G., Drinovec, L., Costabile, F., Ristorini, M. et al. (2020), 'Performance of microaethalometers: real-world field intercomparisons from multiple mobile measurement campaigns in different atmospheric environments', *Aerosol and Air Quality Research* **20**(12), 2640–2653.

Aljawhary, D., Lee, A. K. Y. & Abbatt, J. P. D. (2013), 'High-resolution chemical ionization mass spectrometry (tof-cims): application to study soa composition and processing', *Atmospheric Measurement Techniques* **6**(11), 3211–3224.

Amiridis, V., Balis, D., Kazadzis, S., Bais, A., Giannakaki, E., Papayannis, A. & Zerefos, C. (2005), 'Four-year aerosol observations with a raman lidar at thessaloniki, greece, in the framework of european aerosol research lidar network (earlinet)', *Journal of Geophysical Research: Atmospheres* **110**(D21).

Ansmann, A., Mamouri, R.-E., Bühl, J., Seifert, P., Engelmann, R., Hofer, J., Nisantzi, A., Atkinson, J. D., Kanji, Z. A., Sierau, B., Vrekoussis, M. & Sciare, J. (2019), 'Ice-nucleating particle versus ice crystal number concentration in altocumulus and cirrus layers embedded in saharan dust: a closure study', *Atmospheric Chemistry and Physics* **19**(23), 15087–15115.
URL: *https://acp.copernicus.org/articles/19/15087/2019/*

Ansmann, A., Petzold, A., Kandler, K., Tegen, I., Wendisch, M., Mueller, D., Weinzierl, B., Mueller, T. & Heintzenberg, J. (2011), 'Saharan mineral dust experiments samum–1 and samum–2: what have we learned?', *Tellus B. Chem. Phys. Meteorol.* **63**(4), 403–429.

Ansmann, A., Riebesell, M., Wandinger, U., Weitkamp, C., Voss, E., Lahmann, W. & Michaelis, W. (1992), 'Combined raman elastic-backscatter lidar for vertical profiling of moisture, aerosol extinction, backscatter, and lidar ratio', *Applied Physics B* **55**(1), 18–28.

Ansmann, A., Tesche, M., Althausen, D., Müller, D., Seifert, P., Freudenthaler, V., Heese, B., Wiegner, M., Pisani, G., Knippertz, P. et al. (2008), 'Influence of saharan dust on cloud glaciation in southern morocco during the saharan mineral dust experiment', *J. Geophys. Res. Atmos.* **113**(D4).

Asadi, S., Wexler, A. S., Cappa, C. D., Barreda, S., Bouvier, N. M. & Ristenpart, W. D. (2019),

‘Aerosol emission and superemission during human speech increase with voice loudness’, *Scientific reports* **9**(1), 1–10.

Asano, S. (1983), ‘Light scattering by horizontally oriented spheroidal particles’, *Appl. Opt* **22**(9), 1390–1396.

Avdikos, G. (2015), Powerful raman lidar systems for atmospheric analysis and high-energy physics experiments, *in* ‘EPJ Web of Conferences’, Vol. 89, EDP Sciences, p. 04003.

Barlow, J. F., Dunbar, T., Nemitz, E., Wood, C. R., Gallagher, M., Davies, F., O’Connor, E. & Harrison, R. (2011), ‘Boundary layer dynamics over london, uk, as observed using doppler lidar during repartee-ii’, *Atmospheric Chemistry and Physics* **11**(5), 2111–2125.

Bell, M. L., Ebisu, K., Peng, R. D., Samet, J. M. & Dominici, F. (2009), ‘Hospital admissions and chemical composition of fine particle air pollution’, *American journal of respiratory and critical care medicine* **179**(12), 1115–1120.

Bianco, L., Djalalova, I., King, C. & Wilczak, J. (2011), ‘Diurnal evolution and annual variability of boundary-layer height and its correlation to other meteorological variables in california’s central valley’, *Boundary-layer meteorology* **140**(3), 491–511.

Blay-Carreras, E., Pino, D., Vilà-Guerau de Arellano, J., van de Boer, A., De Coster, O., Darbieu, C., Hartogensis, O., Lohou, F., Lothon, M. & Pietersen, H. (2014), ‘Role of the residual layer and large-scale subsidence on the development and evolution of the convective boundary layer’, *Atmospheric Chemistry and Physics* **14**(9), 4515–4530.

Boselli, A., Armenante, M., D’Avino, L., D’Isidoro, M., Pisani, G., Spinelli, N. & Wang, X. (2009), ‘Atmospheric aerosol characterization over naples during 2000–2003 earlinet project: Planetary boundary-layer evolution and layering’, *Boundary-layer meteorology* **132**(1), 151–165.

Bösenberg, J. & Matthias, V. (2003), ‘Earlinet: A european aerosol research lidar network to establish an aerosol climatology’.

Brabec, M., Wienhold, F. G., Luo, B. P., Vömel, H., Immler, F., Steiner, P., Hausammann, E., Weers, U. & Peter, T. (2012), ‘Particle backscatter and relative humidity measured across cirrus clouds and comparison with microphysical cirrus modelling’, *Atmospheric Chemistry and Physics* **12**(19), 9135–9148.

Brunamonti, S., Jorge, T., Oelsner, P., Hanumanthu, S., Singh, B. B., Kumar, K. R., Sonbawne, S., Meier, S., Singh, D., Wienhold, F. G., Luo, B. P., Boettcher, M., Poltera, Y., Jauhiainen, H., Kayastha, R., Karmacharya, J., Dirksen, R., Naja, M., Rex, M., Fadnavis, S. & Peter, T. (2018), 'Balloon-borne measurements of temperature, water vapor, ozone and aerosol backscatter on the southern slopes of the himalayas during stratoclim 2016–2017', *Atmospheric Chemistry and Physics* **18**(21), 15937–15957.

Brunamonti, S., Martucci, G., Romanens, G., Poltera, Y., Wienhold, F. G., Hervo, M., Haefele, A. & Navas-Guzmán, F. (2021*a*), 'Validation of aerosol backscatter profiles from raman lidar and ceilometer using balloon-borne measurements', *Atmospheric Chemistry and Physics* **21**(3), 2267–2285.

Brunamonti, S., Martucci, G., Romanens, G., Poltera, Y., Wienhold, F. G., Hervo, M., Haefele, A. & Navas-Guzmán, F. (2021*b*), 'Validation of aerosol backscatter profiles from raman lidar and ceilometer using balloon-borne measurements', *Atmospheric Chemistry and Physics* **21**(3), 2267–2285.

Brunner, C., Brem, B. T., Collaud Coen, M., Conen, F., Hervo, M., Henne, S., Steinbacher, M., Gysel-Beer, M. & Kanji, Z. A. (2021*a*), 'The contribution of saharan dust to the ice-nucleating particle concentrations at the high altitude station jungfraujoch (3580 m asl), switzerland', *Atmospheric Chemistry and Physics* **21**(23), 18029–18053.

Brunner, C., Brem, B. T., Collaud Coen, M., Conen, F., Hervo, M., Henne, S., Steinbacher, M., Gysel-Beer, M. & Kanji, Z. A. (2021*b*), 'The contribution of saharan dust to the ice-nucleating particle concentrations at the high altitude station jungfraujoch (3580 m a.s.l.), switzerland', *Atmospheric Chemistry and Physics* **21**(23), 18029–18053.

Cao, C., Zheng, S. & Singh, R. P. (2014), 'Characteristics of aerosol optical properties and meteorological parameters during three major dust events (2005–2010) over beijing, china', *Atmospheric research* **150**, 129–142.

Chan, C. K. & Yao, X. (2008), 'Air pollution in mega cities in china', *Atmospheric Environment* **42**(1), 1–42.

Chapman, E., Gustafson, W., Easter, R., Barnard, J., Ghan, S., Pekour, M. & Fast, J. (2008), 'Coupling aerosol-cloud-radiative processes in the wrf-chem model: Investigating the radiative impact of elevated point sources', *Atmos. Chem. Phys. Discuss* **8**, 14–765.

Charlson, R. J., Schwartz, S., Hales, J., Cess, R. D., Coakley Jr, J., Hansen, J. & Hofmann, D. (1992), 'Climate forcing by anthropogenic aerosols', *Science* **255**(5043), 423–430.

Chen, W.-N., Chen, Y.-W., Chou, C. C., Chang, S.-Y., Lin, P.-H. & Chen, J.-P. (2009), 'Columnar optical properties of tropospheric aerosol by combined lidar and sunphotometer measurements at taipei, taiwan', *Atmos. Environ.* **43**(17), 2700–2708.

Chu, Y., Li, J., Li, C., Tan, W., Su, T. & Li, J. (2019), 'Seasonal and diurnal variability of planetary boundary layer height in beijing: Intercomparison between mpl and wrf results', *Atmospheric research* **227**, 1–13.

Cirisan, A., Luo, B. P., Engel, I., Wienhold, F. G., Sprenger, M., Krieger, U. K., Weers, U., Romanens, G., Levrat, G., Jeannet, P., Ruffieux, D., Philipona, R., Calpini, B., Spichtinger, P. & Peter, T. (2014), 'Balloon-borne match measurements of midlatitude cirrus clouds', *Atmospheric Chemistry and Physics* **14**(14), 7341–7365.

Cook, K. H. & Vizy, E. K. (2015), 'Detection and analysis of an amplified warming of the sahara desert', *Journal of Climate* **28**(16), 6560–6580.

Cooper, D. & Eichinger, W. (1994), 'Structure of the atmosphere in an urban planetary boundary layer from lidar and radiosonde observations', *Journal of Geophysical Research: Atmospheres* **99**(D11), 22937–22948.

Cross, M. (2015), Pysplit: a package for the generation, analysis, and visualizations of hysplit air parcel trajectories, *in* 'Proceedings of 14th Ann. Scientific Computing with Python Conference (SciPy 15)'.

Dang, R., Yang, Y., Hu, X.-M., Wang, Z. & Zhang, S. (2019), 'A review of techniques for diagnosing the atmospheric boundary layer height (ablh) using aerosol lidar data', *Remote Sensing* **11**(13), 1590.

de Arruda Moreira, G., Guerrero-Rascado, J. L., Bravo-Aranda, J. A., Benavent-Oltra, J. A., Ortiz-Amezcua, P., Róman, R., Bedoya-Velásquez, A. E., Landulfo, E. & Alados-Arboledas, L. (2018), 'Study of the planetary boundary layer by microwave radiometer, elastic lidar and doppler lidar estimations in southern iberian peninsula', *Atmospheric Research* **213**, 185–195.

de Arruda Moreira, G., Guerrero-Rascado, J. L., Bravo-Aranda, J. A., Foyo-Moreno, I., Cazorla, A., Alados, I., Lyamani, H., Landulfo, E. & Alados-Arboledas, L. (2020), 'Study of the planetary boundary layer height in an urban environment using a combination of microwave radiometer and ceilometer', *Atmospheric Research* **240**, 104932.

Deardorff, J. W. (1970), 'A numerical study of three-dimensional turbulent channel flow at large reynolds numbers', *Journal of Fluid Mechanics* **41**(2), 453–480.

Deetz, K., Klose, M., Kirchner, I. & Cubasch, U. (2016), 'Numerical simulation of a dust event in northeastern germany with a new dust emission scheme in cosmo-art', *Atmos. Environ.* **126**, 87–97.

DeMott, P. J., Prenni, A. J., McMeeking, G. R., Sullivan, R. C., Petters, M. D., Tobo, Y., Niemand, M., Möhler, O., Snider, J. R., Wang, Z. & Kreidenweis, S. M. (2015), 'Integrating laboratory and field data to quantify the immersion freezing ice nucleation activity of mineral dust particles', *Atmospheric Chemistry and Physics* **15**(1), 393–409.

Deng, M., Mace, G. G., Wang, Z. & Okamoto, H. (2010), 'Tropical composition, cloud and climate coupling experiment validation for cirrus cloud profiling retrieval using cloudsat radar and calipso lidar', *Journal of Geophysical Research: Atmospheres* **115**(D10).

Dias-Júnior, C. Q., Carneiro, R. G., Fisch, G., D'Oliveira, F. A. F., Sörgel, M., Botía, S., Machado, L. A. T., Wolff, S., Santos, R. M. N. d. & Pöhlker, C. (2022), 'Intercomparison of planetary boundary layer heights using remote sensing retrievals and era5 reanalysis over central amazonia', *Remote Sensing* **14**(18).
URL: *https://www.mdpi.com/2072-4292/14/18/4561*

Ding, A., Huang, X., Nie, W., Sun, J., Kerminen, V.-M., Petäjä, T., Su, H., Cheng, Y., Yang, X.-Q., Wang, M. et al. (2016), 'Enhanced haze pollution by black carbon in megacities in china', *Geophysical Research Letters* **43**(6), 2873–2879.

Ding, K., Huang, X., Ding, A., Wang, M., Su, H., Kerminen, V.-M., Petäjä, T., Tan, Z., Wang, Z., Zhou, D. et al. (2021), 'Aerosol-boundary-layer-monsoon interactions amplify semi-direct effect of biomass smoke on low cloud formation in southeast asia', *Nature communications* **12**(1), 1–9.

Dubovik, O. & King, M. D. (2000), 'A flexible inversion algorithm for retrieval of aerosol optical properties from sun and sky radiance measurements', *Journal of Geophysical Research: Atmospheres* **105**(D16), 20673–20696.

Engel, I., Luo, B. P., Khaykin, S. M., Wienhold, F. G., Vömel, H., Kivi, R., Hoyle, C. R., Grooß, J.-U., Pitts, M. C. & Peter, T. (2014), 'Arctic stratospheric dehydration – part 2: Microphysical modeling', *Atmospheric Chemistry and Physics* **14**(7), 3231–3246.

Fernald, F. G. (1984), 'Analysis of atmospheric lidar observations: some comments', *Applied optics* **23**(5), 652–653.

Fernald, F. G., Herman, B. M. & Reagan, J. A. (1972), 'Determination of aerosol height distributions by lidar', *Journal of Applied Meteorology and Climatology* **11**(3), 482–489.

Ferrero, L., Cappelletti, D., Moroni, B., Sangiorgi, G., Perrone, M., Crocchianti, S. & Bolzacchini, E. (2012), 'Wintertime aerosol dynamics and chemical composition across the mixing layer over basin valleys', *Atmospheric environment* **56**, 143–153.

Fiedler, S., Kinne, S., Huang, W. T. K., Räisänen, P., O'Donnell, D., Bellouin, N., Stier, P., Merikanto, J., Van Noije, T., Makkonen, R. et al. (2019), 'Anthropogenic aerosol forcing–insights from multiple estimates from aerosol-climate models with reduced complexity', *Atmospheric Chemistry and Physics* **19**(10), 6821–6841.

Fochesatto, G. J., Drobinski, P., Flamant, C., Guedalia, D., Sarrat, C., Flamant, P. H. & Pelon, J. (2001), 'Evidence of dynamical coupling between the residual layer and the developing convective boundary layer', *Boundary-layer meteorology* **99**(3), 451–464.

for Environmental Protection, O. (2016), 'Office for environmental protection: Luft: Erfolgreiche maßnah-men zur luftreinhaltung in stuttgart: available at:'. (last accessed: 18 February 2022).

Freudenthaler, V. (2016), 'About the effects of polarising optics on lidar signals and the δ90 calibration', *Atmospheric Measurement Techniques* **9**(9), 4181–4255.

Freudenthaler, V., Esselborn, M., Wiegner, M., Heese, B., Tesche, M., Ansmann, A., Müller, D., Althausen, D., Wirth, M., Fix, A. et al. (2009), 'Depolarization ratio profiling at several wavelengths in pure saharan dust during samum 2006', *Tellus B: Chemical and Physical Meteorology* **61**(1), 165–179.

Fuller, R., Landrigan, P. J., Balakrishnan, K., Bathan, G., Bose-O'Reilly, S., Brauer, M., Caravanos, J., Chiles, T., Cohen, A., Corra, L. et al. (2022), 'Pollution and health: a progress update', *The Lancet Planetary Health* .

Garratt, J. (1994), 'Review: the atmospheric boundary layer', *Earth-Science Reviews* **37**(1), 89–134.

Garrison, V., Foreman, W., Genualdi, S., Griffin, D. W., Kellogg, C., Majewski, M., Mohammed, A., Ramsubhag, A., Shinn, E., Simonich, S. et al. (2006), 'Saharan dust-a carrier of persistent organic pollutants, metals and microbes to the caribbean?', *Revista de Biología Tropical* **54**, 9–21.

Gasch, P., Rieger, D., Walter, C., Khain, P., Levi, Y., Knippertz, P. & Vogel, B. (2017), 'Revealing the meteorological drivers of the september 2015 severe dust event in the eastern mediterranean', *Atmos. Chem. Phys.* **17**(22), 13573–13604.

Geier, M. & Arienti, M. (2014), 'Detection of preferential particle orientation in the atmosphere: Development of an alternative polarization lidar system', *J. Quant. Spectrosc. Radiat. Transf.* **149**, 16–32.

Genc, D. D., Yesilyurt, C. & Tuncel, G. (2010), 'Air pollution forecasting in ankara, turkey using air pollution index and its relation to assimilative capacity of the atmosphere', *Environmental monitoring and assessment* **166**(1), 11–27.

Gentine, P., Chhang, A., Rigden, A. & Salvucci, G. (2016), 'Evaporation estimates using weather station data and boundary layer theory', *Geophysical Research Letters* **43**(22), 11–661.

Gläser, G., Kerkweg, A. & Wernli, H. (2012), 'The mineral dust cycle in emac 2.40: sensitivity to the spectral resolution and the dust emission scheme', *Atmos. Chem. Phys.* **12**(3), 1611–1627.

Goudie, A. S. (2014), 'Desert dust and human health disorders', *Environment international* **63**, 101–113.

Greenberg, J., Guenther, A., Zimmerman, P., Baugh, W., Geron, C., Davis, K., Helmig, D. & Klinger, L. (1999), 'Tethered balloon measurements of biogenic vocs in the atmospheric boundary layer', *Atmospheric Environment* **33**(6), 855–867.

Groß, S., Esselborn, M., Weinzierl, B., Wirth, M., Fix, A. & Petzold, A. (2013), 'Aerosol classification by airborne high spectral resolution lidar observations', *Atmospheric chemistry and physics* **13**(5), 2487–2505.

Groß, S., Tesche, M., Freudenthaler, V., Toledano, C., Wiegner, M., Ansmann, A., Althausen, D. & Seefeldner, M. (2011), 'Characterization of saharan dust, marine aerosols and mixtures of biomass-burning aerosols and dust by means of multi-wavelength depolarization and raman lidar measurements during samum 2', *Tellus B: Chemical and Physical Meteorology* **63**(4), 706–724.

Guerzoni, S. & Chester, R. (1996), *The impact of desert dust across the Mediterranean*, Vol. 11, Springer Science & Business Media.

Guerzoni, S. & Rampazzo, G. (1993), 'Contribution of saharan dust to the central mediterranean basin', *Processes Controlling the Composition of Clastic Sediments* **284**, 303.

Guo, J.-P., Zhang, X.-Y., Che, H.-Z., Gong, S.-L., An, X., Cao, C.-X., Guang, J., Zhang, H., Wang, Y.-Q., Zhang, X.-C., Xue, M. & Li, X.-W. (2009), 'Correlation between pm concentrations and aerosol optical depth in eastern china', *Atmospheric Environment* **43**(37), 5876–5886.

Guo, J., Su, T., Li, Z., Miao, Y., Li, J., Liu, H., Xu, H., Cribb, M. & Zhai, P. (2017), 'Declining frequency of summertime local-scale precipitation over eastern china from 1970 to 2010 and its potential link to aerosols', *Geophysical Research Letters* **44**(11), 5700–5708.

Guo, J., Tilgner, A., Yeung, C., Wang, Z., Louie, P. K., Luk, C. W., Xu, Z., Yuan, C., Gao, Y., Poon, S. et al. (2014), 'Atmospheric peroxides in a polluted subtropical environment: seasonal variation, sources and sinks, and importance of heterogeneous processes', *Environmental science & technology* **48**(3), 1443–1450.

Gutkowicz-Krusin, D. (1993), 'Multiangle lidar performance in the presence of horizontal inhomogeneities in atmospheric extinction and scattering', *Applied optics* **32**(18), 3266–3272.

Görsdorf, U., Lehmann, V., Bauer-Pfundstein, M., Peters, G., Vavriv, D., Vinogradov, V. & Volkov, V. (2015), 'A 35-GHz polarimetric Doppler radar for long-term observations of cloud parameters—description of system and data processing', *jaot* **32**(4), 675–690.

Haarig, M., Ansmann, A., Baars, H., Jimenez, C., Veselovskii, I., Engelmann, R. & Althausen, D. (2018), 'Depolarization and lidar ratios at 355, 532, and 1064 nm and microphysical properties of aged tropospheric and stratospheric canadian wildfire smoke', *Atmos. Chem. Phys.* **18**(16), 11847–11861.

Haarig, M., Ansmann, A., Engelmann, R., Baars, H., Toledano, C., Torres, B., Althausen, D., Radenz, M. & Wandinger, U. (2022), 'First triple-wavelength lidar observations of depolarization and extinction-to-backscatter ratios of saharan dust', *Atmos. Chem. Phys.* **22**(1), 355–369.

Haarig, M., Ansmann, A., Gasteiger, J., Kandler, K., Althausen, D., Baars, H., Radenz, M. & Farrell, D. A. (2017), 'Dry versus wet marine particle optical properties: Rh dependence of depolarization ratio, backscatter, and extinction from multiwavelength lidar measurements during saltrace', *Atmos. Chem. Phys.* **17**(23), 14199–14217.

Haarig, M., Walser, A., Ansmann, A., Dollner, M., Althausen, D., Sauer, D., Farrell, D. & Weinzierl, B. (2019), 'Profiles of cloud condensation nuclei, dust mass concentration, and ice-nucleating-particle-relevant aerosol properties in the saharan air layer over barbados from polarization lidar and airborne in situ measurements', *Atmos. Chem. Phys.* **19**(22), 13773–13788.

Hatzianastassiou, N., Matsoukas, C., Drakakis, E., Stackhouse Jr., P. W., Koepke, P., Fotiadi, A., Pavlakis, K. G. & Vardavas, I. (2007), 'The direct effect of aerosols on solar radiation based on satellite observations, reanalysis datasets, and spectral aerosol optical properties from global aerosol data set (gads)', *Atmospheric Chemistry and Physics* **7**(10), 2585–2599.
URL: *https://acp.copernicus.org/articles/7/2585/2007/*

He, Y., Zhang, Y., Liu, F., Yin, Z., Yi, Y., Zhan, Y. & Yi, F. (2021), 'Retrievals of dust-related particle mass and ice-nucleating particle concentration profiles with ground-based polarization lidar and sun photometer over a megacity in central china', *Atmospheric Measurement Techniques* **14**(9), 5939–5954.

Heald, C. L., Jacob, D. J., Park, R. J., Alexander, B., Fairlie, T. D., Yantosca, R. M. & Chu, D. A. (2006), 'Transpacific transport of asian anthropogenic aerosols and its impact on surface air quality in the united states', *Journal of Geophysical Research: Atmospheres* **111**(D14).

Hebbert, M., Webb, B., Gossop, C. & Nan, S. (2012), *Towards a Liveable Urban Climate: Lessons from Stuttgart*, Routledge, United Kingdom, pp. 132–150. ESRC support gratefully acknowledged under project 'Climate Science Urban Design' RES-062-23-2134.

Heintzenberg, J. (2009), 'The samum-1 experiment over southern morocco: overview and introduction', *Tellus B Chem Phys Meteorol* **61**(1), 2–11.

Holben, B. N., Eck, T. F., Slutsker, I. a., Tanre, D., Buis, J., Setzer, A., Vermote, E., Reagan, J. A., Kaufman, Y., Nakajima, T. et al. (1998), 'Aeronet—a federated instrument network and data archive for aerosol characterization', *Remote sensing of environment* **66**(1), 1–16.

Holben, B. N., Tanre, D., Smirnov, A., Eck, T., Slutsker, I., Abuhassan, N., Newcomb, W., Schafer, J., Chatenet, B., Lavenu, F. et al. (2001), 'An emerging ground-based aerosol climatology: Aerosol optical depth from aeronet', *J. Geophys. Res. Atmos.* **106**(D11), 12067–12097.

Hong, C., Zhang, Q., Zhang, Y., Davis, S. J., Zhang, X., Tong, D., Guan, D., Liu, Z. & He, K. (2020), 'Weakening aerosol direct radiative effects mitigate climate penalty on chinese air quality', *Nature Climate Change* **10**(9), 845–850.

Hoshyaripour, G., Bachmann, V., Förstner, J., Steiner, A., Vogel, H., Wagner, F., Walter, C. & Vogel, B. (2019), 'Effects of particle nonsphericity on dust optical properties in a forecast system: Implications for model-observation comparison', *Journal of Geophysical Research: Atmospheres* **124**(13), 7164–7178.

Hovenac, E. A. & Lock, J. A. (1992), 'Assessing the contributions of surface waves and complex rays to far-field mie scattering by use of the debye series', *JOSA A* **9**(5), 781–795.

Huang, Q., Cai, X., Wang, J., Song, Y. & Zhu, T. (2018), 'Climatological study of the boundary-layer air stagnation index for china and its relationship with air pollution', *Atmospheric Chemistry and Physics* **18**(10), 7573–7593.

Huang, W., Saathoff, H., Shen, X., Ramisetty, R., Leisner, T. & Mohr, C. (2019), 'Seasonal characteristics of organic aerosol chemical composition and volatility in stuttgart, germany', *Atmospheric Chemistry and Physics* **19**(18), 11687–11700.

Huang, X., Ding, A., Wang, Z., Ding, K., Gao, J., Chai, F. & Fu, C. (2020), 'Amplified transboundary transport of haze by aerosol–boundary layer interaction in china', *Nature Geoscience* **13**(6), 428–434.

Ji, D., Li, L., Wang, Y., Zhang, J., Cheng, M., Sun, Y., Liu, Z., Wang, L., Tang, G., Hu, B., Chao, N., Wen, T. & Miao, H. (2014), 'The heaviest particulate air-pollution episodes occurred in northern china in january, 2013: Insights gained from observation', *Atmospheric Environment* **92**, 546–556.

Ji, J., Xie, C., Chen, J., Zhao, M., Yang, H., Xing, K. & Wang, B. (2022), 'The application of measuring atmospheric properties in overlap factor region using scanning lidar', *Results in Physics* **43**, 106050.

Jiang, F., Song, J., Bauer, J., Gao, L., Vallon, M., Gebhardt, R., Leisner, T., Norra, S. & Saathoff, H. (2022), 'Chromophores and chemical composition of brown carbon characterized at an urban kerbside by excitation–emission spectroscopy and mass spectrometry', *Atmospheric Chemistry and Physics* **22**(22), 14971–14986.
URL: *https://acp.copernicus.org/articles/22/14971/2022/*

Jöckel, P., Kerkweg, A., Pozzer, A., Sander, R., Tost, H., Riede, H., Baumgaertner, A., Gromov, S. & Kern, B. (2010), 'Development cycle 2 of the modular earth submodel system (messy2)', *Geoscientific Model Development* **3**(2), 717–752.

Jöckel, P., Tost, H., Pozzer, A., Brühl, C., Buchholz, J., Ganzeveld, L., Hoor, P., Kerkweg, A., Lawrence, M., Sander, R. et al. (2006), 'The atmospheric chemistry general circulation model echam5/messy1: consistent simulation of ozone from the surface to the mesosphere', *Atmos. Chem. Phys.* **6**(12), 5067–5104.

Jordan, A., Haidacher, S., Hanel, G., Hartungen, E., Märk, L., Seehauser, H., Schottkowsky, R., Sulzer, P. & Märk, T. (2009), 'A high resolution and high sensitivity proton-transfer-reaction

time-of-flight mass spectrometer (ptr-tof-ms)', *International Journal of Mass Spectrometry* **286**(2), 122–128.

Kaimal, J., Wyngaard, J., Haugen, D., Coté, O., Izumi, Y., Caughey, S. & Readings, C. (1976), 'Turbulence structure in the convective boundary layer', *Journal of Atmospheric Sciences* **33**(11), 2152–2169.

Kandler, K., Benker, N., Bundke, U., Cuevas, E., Ebert, M., Knippertz, P., Rodriguez, S., Schütz, L. & Weinbruch, S. (2007), 'Chemical composition and complex refractive index of saharan mineral dust at izaña, tenerife (spain) derived by electron microscopy', *Atmospheric Environment* **41**(37), 8058–8074.

Kandler, K., Lieke, K., Benker, N., Emmel, C., Küpper, M., Müller-Ebert, D., Ebert, M., Scheuvens, D., Schladitz, A., Schütz, L. et al. (2011), 'Electron microscopy of particles collected at praia, cape verde, during the saharan mineral dust experiment: particle chemistry, shape, mixing state and complex refractive index', *Tellus B Chem Phys Meteorol* **63**(4), 475–496.

Kandler, K., Schütz, L., Deutscher, C., Ebert, M., Hofmann, H., Jäckel, S., Jaenicke, R., Knippertz, P., Lieke, K., Massling, A. et al. (2009), 'Size distribution, mass concentration, chemical and mineralogical composition and derived optical parameters of the boundary layer aerosol at tinfou, morocco, during samum 2006', *Tellus B Chem Phys Meteorol* **61**(1), 32–50.

Kang, J.-Y., Yoon, S.-C., Shao, Y. & Kim, S.-W. (2011), 'Comparison of vertical dust flux by implementing three dust emission schemes in wrf/chem', *J. Geophys. Res. Atmos.* **116**(D9).

Kanitz, T., Engelmann, R., Heinold, B., Baars, H., Skupin, A. & Ansmann, A. (2014), 'Tracking the saharan air layer with shipborne lidar across the tropical atlantic', *Geophys. Res. Lett.* **41**(3), 1044–1050.

Karydis, V. A., Tsimpidi, A. P., Bacer, S., Pozzer, A., Nenes, A. & Lelieveld, J. (2017), 'Global impact of mineral dust on cloud droplet number concentration', *Atmos. Chem. Phys.* **17**(9), 5601–5621.

Katsoulis, B. (1988), 'Some meteorological aspects of air pollution in athens, greece', *Meteorology and Atmospheric Physics* **39**(3), 203–212.

Kiehl, J. T. & Briegleb, B. P. (1993), 'The relative roles of sulfate aerosols and greenhouse gases in climate forcing', *Science* **260**(5106), 311–314.

Kim, J. & Mahrt, L. (1992), 'Simple formulation of turbulent mixing in the stable free atmosphere and nocturnal boundary layer', *Tellus A* **44**(5), 381–394.

Kim, M.-S. & Kwon, B. H. (2019), 'Estimation of sensible heat flux and atmospheric boundary layer height using an unmanned aerial vehicle', *Atmosphere* **10**(7), 363.

Kiseleva, O., Kalthoff, N., Adler, B., Kossmann, M., Wieser, A. & Rinke, R. (2021), 'Nocturnal atmospheric conditions and their impact on air pollutant concentrations in the city of stuttgart', *Meteorological Applications* **28**(6), e2037.

Klett, J. D. (1981), 'Stable analytical inversion solution for processing lidar returns', *Applied optics* **20**(2), 211–220.

Klett, J. D. (1985*a*), 'Lidar inversion with variable backscatter/extinction ratios', *Applied optics* **24**(11), 1638–1643.

Klett, J. D. (1985*b*), 'Lidar inversion with variable backscatter/extinction ratios', *Appl. Opt.* **24**(11), 1638–1643.

Kloss, C., Sellitto, P., Legras, B., Vernier, J.-P., Jegou, F., Venkat Ratnam, M., Suneel Kumar, B., Lakshmi Madhavan, B. & Berthet, G. (2020), 'Impact of the 2018 ambae eruption on the global stratospheric aerosol layer and climate', *Journal of Geophysical Research: Atmospheres* **125**(14), e2020JD032410.

Kong, W. & Yi, F. (2015), 'Convective boundary layer evolution from lidar backscatter and its relationship with surface aerosol concentration at a location of a central china megacity', *Journal of Geophysical Research: Atmospheres* **120**(15), 7928–7940.

Korenyi-Both, A., Korenyi-Both, A., Molnar, A. & Fidelus-Gort, R. (1992), 'A1 eskan disease: desert storm pneumonitis', *Military medicine* **157**(9), 452–462.

Korhonen, K., Giannakaki, E., Mielonen, T., Pfüller, A., Laakso, L., Vakkari, V., Baars, H., Engelmann, R., Beukes, J., Van Zyl, P. et al. (2014), 'Atmospheric boundary layer top height in

south africa: Measurements with lidar and radiosonde compared to three atmospheric models', *Atmospheric Chemistry and Physics* **14**(8), 4263–4278.

Kotthaus, S. & Grimmond, C. S. B. (2018), 'Atmospheric boundary-layer characteristics from ceilometer measurements. part 1: A new method to track mixed layer height and classify clouds', *Quarterly Journal of the Royal Meteorological Society* **144**(714), 1525–1538.

Kovalev, V., Wold, C., Petkov, A. & Hao, W. M. (2011), 'Modified technique for processing multiangle lidar data measured in clear and moderately polluted atmospheres', *Appl. Opt* **50**(25), 4957–4966.

Kovalev, V., Wold, C., Petkov, A. & Hao, W. M. (2012), 'Direct multiangle solution for poorly stratified atmospheres', *Appl. Opt* **51**(25), 6139–6146.

Kovalev, V., Wold, C., Petkov, A. & Hao, W. M. (2015), 'Backscatter near-end solution in processing of scanning lidar data', *Appl. Opt* **54**(24), 7335–7341.

KULMALA, M., HÄMERI, K., Aalto, P., Mäkelä, J., PIRJOLA, L., Nilsson, E. D., Buzorius, G., Rannik, Ü., MASO, M. D., Seidl, W. et al. (2001), 'Overview of the international project on biogenic aerosol formation in the boreal forest (biofor)', *Tellus B* **53**(4), 324–343.

Kunz, A., Pan, L., Konopka, P., Kinnison, D. & Tilmes, S. (2011), 'Chemical and dynamical discontinuity at the extratropical tropopause based on start08 and waccm analyses', *Journal of Geophysical Research: Atmospheres* **116**(D24).

Kunz, M., Abbas, S. S., Bauckholt, M., Böhmländer, A., Feuerle, T., Gasch, P., Glaser, C., Groß, J., Hajnsek, I., Handwerker, J. et al. (2022), 'Swabian moses 2021: An interdisciplinary field campaign for investigating convective storms and their event chains', *Frontiers in Earth Science* p. 1886.

Lachmann, G. V. (2014), *Boundary layer and flow control: its principles and application*, Elsevier.

Lee, J., Hong, J.-W., Lee, K., Hong, J., Velasco, E., Lim, Y. J., Lee, J. B., Nam, K. & Park, J. (2019), 'Ceilometer monitoring of boundary-layer height and its application in evaluating the dilution effect on air pollution', *Boundary-Layer Meteorology* **172**(3), 435–455.

Lei, L., Berkoff, T. A., Gronoff, G. P., Su, J., Nehrir, A. R., Wu, Y., Moshary, F. & Kuang, S. (2021), 'Retrieval of uvb aerosol extinction profiles from the ground-based langley mobile ozone lidar (lmol) system', *Atmos. Meas. Tech. Discuss.* **2021**, 1–22.

Lei, Y., Zhang, Q., He, K. & Streets, D. (2011), 'Primary anthropogenic aerosol emission trends for china, 1990–2005', *Atmospheric Chemistry and Physics* **11**(3), 931–954.

Lenschow, D. H. (1986), Aircraft measurements in the boundary layer, *in* 'Probing the atmospheric boundary layer', Springer, pp. 39–55.

Lenschow, D. H., Lothon, M., Mayor, S. D., Sullivan, P. P. & Canut, G. (2012), 'A comparison of higher-order vertical velocity moments in the convective boundary layer from lidar with in situ measurements and large-eddy simulation', *Boundary-layer meteorology* **143**(1), 107–123.

Leung, N. H. (2021), 'Transmissibility and transmission of respiratory viruses', *Nature Reviews Microbiology* **19**(8), 528–545.

Levy, H., Horowitz, L. W., Schwarzkopf, M. D., Ming, Y., Golaz, J.-C., Naik, V. & Ramaswamy, V. (2013), 'The roles of aerosol direct and indirect effects in past and future climate change', *Journal of Geophysical Research: Atmospheres* **118**(10), 4521–4532.

Li, J., Li, C., Zhao, C. & Su, T. (2016), 'Changes in surface aerosol extinction trends over china during 1980–2013 inferred from quality-controlled visibility data', *Geophysical Research Letters* **43**(16), 8713–8719.

Li, J., Sun, J., Zhou, M., Cheng, Z., Li, Q., Cao, X. & Zhang, J. (2018), 'Observational analyses of dramatic developments of a severe air pollution event in the beijing area', *Atmospheric Chemistry and Physics* **18**(6), 3919–3935.

Li, Z., Guo, J., Ding, A., Liao, H., Liu, J., Sun, Y., Wang, T., Xue, H., Zhang, H. & Zhu, B. (2017*a*), 'Aerosol and boundary-layer interactions and impact on air quality', *National Science Review* **4**(6), 810–833.
URL: *https://doi.org/10.1093/nsr/nwx117*

Li, Z., Guo, J., Ding, A., Liao, H., Liu, J., Sun, Y., Wang, T., Xue, H., Zhang, H. & Zhu, B. (2017*b*), 'Aerosol and boundary-layer interactions and impact on air quality', *National Science Review* **4**(6), 810–833.

Lindberg, J., Wurth, M., Frank, B. P., Tang, S., LaDuke, G., Trojanowski, R., Butcher, T. & Mahajan, D. (2022), 'Realistic operation of two residential cordwood-fired outdoor hydronic heater appliances—part 3: Optical properties of black and brown carbon emissions', *Journal of the Air & Waste Management Association* **72**(7), 777–790.

Liu, F., Yi, F., Yin, Z., Zhang, Y., He, Y. & Yi, Y. (2021), 'Measurement report: characteristics of clear-day convective boundary layer and associated entrainment zone as observed by a ground-based polarization lidar over wuhan (30.5 n, 114.4 e)', *Atmospheric Chemistry and Physics* **21**(4), 2981–2998.
URL: *https://acp.copernicus.org/articles/21/2981/2021/*

Liu, Q., Jia, X., Quan, J., Li, J., Li, X., Wu, Y., Chen, D., Wang, Z. & Liu, Y. (2018), 'New positive feedback mechanism between boundary layer meteorology and secondary aerosol formation during severe haze events', *Scientific reports* **8**(1), 1–8.

Liu, Z., Matsui, I. & Sugimoto, N. (1999), 'High-spectral-resolution lidar using an iodine absorption filter for atmospheric measurements', *Opt. Eng.* **38**(10), 1661–1670.

Lohmann, U. & Feichter, J. (2005), 'Global indirect aerosol effects: a review', *Atmospheric Chemistry and Physics* **5**(3), 715–737.

Löhnert, U. & Maier, O. (2012), 'Operational profiling of temperature using ground-based microwave radiometry at payerne: prospects and challenges', *Atmospheric Measurement Techniques* **5**(5), 1121–1134.
URL: *https://amt.copernicus.org/articles/5/1121/2012/*

Lu, C., Deng, Q.-h., Liu, W.-w., Huang, B.-l. & Shi, L.-z. (2012), 'Characteristics of ventilation coefficient and its impact on urban air pollution', *Journal of Central South University* **19**(3), 615–622.

LUBW (2019), 'Luftreinhaltepläne für baden-württemberg (grundlagen- band 2017), in: Lubw state institute for the environment baden-württemberg, karlsruhe, germany'.

Ma, Y., Xin, J., Wang, Z., Tian, Y., Wu, L., Tang, G., Zhang, W., de Arellano, J. V.-G., Zhao, D., Jia, D. et al. (2022), 'How do aerosols above the residual layer affect the planetary boundary layer height?', *Science of the Total Environment* **814**, 151953.

Mallet, M., Tulet, P., Serça, D., Solmon, F., Dubovik, O., Pelon, J., Pont, V. & Thouron, O. (2009), 'Impact of dust aerosols on the radiative budget, surface heat fluxes, heating rate profiles and convective activity over west africa during march 2006', *Atmospheric Chemistry and Physics* **9**(18), 7143–7160.

Marinou, E., Amiridis, V., Binietoglou, I., Tsikerdekis, A., Solomos, S., Proestakis, E., Konsta, D., Papagiannopoulos, N., Tsekeri, A., Vlastou, G., Zanis, P., Balis, D., Wandinger, U. & Ansmann, A. (2017), 'Three-dimensional evolution of saharan dust transport towards europe based on a 9-year earlinet-optimized calipso dataset', *Atmos. Chem. Phys.* **17**(9), 5893–5919.

Matthias, V., Balis, D., Bösenberg, J., Eixmann, R., Iarlori, M., Komguem, L., Mattis, I., Papayannis, A., Pappalardo, G., Perrone, M. et al. (2004), 'Vertical aerosol distribution over europe: Statistical analysis of raman lidar data from 10 european aerosol research lidar network (earlinet) stations', *Journal of Geophysical Research: Atmospheres* **109**(D18).

Mayer, H. (1999), 'Air pollution in cities', *Atmospheric Environment* **33**(24), 4029–4037.

McGill, M. J., Vaughan, M. A., Trepte, C. R., Hart, W. D., Hlavka, D. L., Winker, D. M. & Kuehn, R. (2007), 'Airborne validation of spatial properties measured by the calipso lidar', *Journal of Geophysical Research: Atmospheres* **112**(D20).

Medeiros, B., Hall, A. & Stevens, B. (2005), 'What controls the mean depth of the pbl?', *Journal of climate* **18**(16), 3157–3172.

Meng, Z., Yang, P., Kattawar, G. W., Bi, L., Liou, K. & Laszlo, I. (2010), 'Single-scattering properties of tri-axial ellipsoidal mineral dust aerosols: A database for application to radiative transfer calculations', *J.Aerosol.Sci.* **41**(5), 501–512.

Miao, Y., Li, J., Miao, S., Che, H., Wang, Y., Zhang, X., Zhu, R. & Liu, S. (2019), 'Interaction between planetary boundary layer and pm2. 5 pollution in megacities in china: a review', *Current Pollution Reports* **5**(4), 261–271.

Middleton, N. & Goudie, A. (2001), 'Saharan dust: sources and trajectories', *Transactions of the Institute of British Geographers* **26**(2), 165–181.

Min, Q.-L., Li, R., Lin, B., Joseph, E., Wang, S., Hu, Y., Morris, V. & Chang, F. (2009), 'Evidence of mineral dust altering cloud microphysics and precipitation', *Atmos. Chem. Phys.* **9**(9), 3223–3231.

Mishchenko, M. I. (2014), *Electromagnetic scattering by particles and particle groups: an introduction*, Cambridge University Press.

Moallemi, A., Modini, R. L., Lapyonok, T., Lopatin, A., Fuertes, D., Dubovik, O., Giaccari, P. & Gysel-Beer, M. (2022), 'Information content and aerosol property retrieval potential for different types of in situ polar nephelometer data', *Atmospheric Measurement Techniques* **15**(19), 5619–5642.

Moeng, C.-H. & Wyngaard, J. C. (1988), 'Spectral analysis of large-eddy simulations of the convective boundary layer', *Journal of Atmospheric Sciences* **45**(23), 3573–3587.

Möhler, O., Adams, M., Lacher, L., Vogel, F., Nadolny, J., Ullrich, R., Boffo, C., Pfeuffer, T., Hobl, A., Weiß, M., Vepuri, H. S. K., Hiranuma, N. & Murray, B. J. (2021), 'The portable ice nucleation experiment (pine): a new online instrument for laboratory studies and automated long-term field observations of ice-nucleating particles', *Atmospheric Measurement Techniques* **14**(2), 1143–1166.

Mona, L., Papagiannopoulos, N., Basart, S., Baldasano, J., Binietoglou, I., Cornacchia, C. & Pappalardo, G. (2014), 'Earlinet dust observations vs. bsc-dream8b modeled profiles: 12-year-long systematic comparison at potenza, italy', *Atmos. Chem. Phys.* **14**(16), 8781–8793.

Müller, D., Weinzierl, B., Petzold, A., Kandler, K., Ansmann, A., Müller, T., Tesche, M., Freudenthaler, V., Esselborn, M., Heese, B. et al. (2010), 'Mineral dust observed with aeronet sun photometer, raman lidar, and in situ instruments during samum 2006: Shape-independent particle properties', *Journal of Geophysical Research: Atmospheres* **115**(D7).

Murphy, W. F. (1977), 'The rayleigh depolarization ratio and rotational raman spectrum of water vapor and the polarizability components for the water molecule', *The Journal of Chemical Physics* **67**(12), 5877–5882.

NASA (2022), 'Aerosol robotic network (aeronet). url: https://aeronet.gsfc.nasa.gov/, last access: 25 march 2022'.

Nash, D. G., Baer, T. & Johnston, M. V. (2006), 'Aerosol mass spectrometry: An introductory review', *International Journal of Mass Spectrometry* **258**(1), 2–12. Aerosols/Microparticles Special Issue.

Navas-Guzman, F., Antonio Bravo-Aranda, J., Luis Guerrero-Rascado, J., Jose Granados-Munoz, M. & Alados-Arboledas, L. (2013), 'Statistical analysis of aerosol optical properties retrieved by raman lidar over southeastern spain', *Tellus B: Chemical and Physical Meteorology* **65**(1), 21234.

Neff, W., Helmig, D., Grachev, A. & Davis, D. (2008), 'A study of boundary layer behavior associated with high no concentrations at the south pole using a minisodar, tethered balloon, and sonic anemometer', *Atmospheric Environment* **42**(12), 2762–2779. Antarctic Tropospheric Chemistry Investigation (ANTCI) 2003.

Niemand, M., Möhler, O., Vogel, B., Vogel, H., Hoose, C., Connolly, P., Klein, H., Bingemer, H., DeMott, P., Skrotzki, J. et al. (2012), 'A particle-surface-area-based parameterization of immersion freezing on desert dust particles', *Journal of the Atmospheric Sciences* **69**(10), 3077–3092.

Nilsson, E., Rannik, Ü., Kumala, M., Buzorius, G. & O'dowd, C. (2001), 'Effects of continental boundary layer evolution, convection, turbulence and entrainment, on aerosol formation', *Tellus B: Chemical and Physical Meteorology* **53**(4), 441–461.

Nishizawa, T., Sugimoto, N., Matsui, I., Shimizu, A., Higurashi, A. & Jin, Y. (2016), The asian dust and aerosol lidar observation network (ad-net): Strategy and progress, *in* 'EPJ Web of Conferences', Vol. 119, EDP Sciences, p. 19001.

Osborne, M., Malavelle, F. F., Adam, M., Buxmann, J., Sugier, J., Marenco, F. & Haywood, J. (2019), 'Saharan dust and biomass burning aerosols during ex-hurricane ophelia: observations from the new uk lidar and sun-photometer network', *Atmos. Chem. Phys.* **19**(6), 3557–3578.

O'Sullivan, D., Marenco, F., Ryder, C. L., Pradhan, Y., Kipling, Z., Johnson, B., Benedetti, A., Brooks, M., McGill, M., Yorks, J. et al. (2020), 'Models transport saharan dust too low in the atmosphere: a comparison of the metum and cams forecasts with observations', *Atmos. Chem. Phys.* **20**(21), 12955–12982.

Pal, S. (2014), 'Monitoring depth of shallow atmospheric boundary layer to complement lidar measurements affected by partial overlap', *Remote Sensing* **6**(9), 8468–8493.
URL: *https://www.mdpi.com/2072-4292/6/9/8468*

Pal, S., Behrendt, A. & Wulfmeyer, V. (2010*a*), Elastic-backscatter-lidar-based characterization of the convective boundary layer and investigation of related statistics, *in* 'Annales Geophysicae', Vol. 28, Copernicus GmbH, pp. 825–847.

Pal, S., Behrendt, A. & Wulfmeyer, V. (2010*b*), 'Elastic-backscatter-lidar-based characterization of the convective boundary layer and investigation of related statistics', *Annales Geophysicae* **28**(3), 825–847.
URL: *https://angeo.copernicus.org/articles/28/825/2010/*

Pal, S., Lee, T., Phelps, S. & De Wekker, S. (2014), 'Impact of atmospheric boundary layer depth variability and wind reversal on the diurnal variability of aerosol concentration at a valley site', *Science of The Total Environment* **496**, 424–434.
URL: *https://www.sciencedirect.com/science/article/pii/S0048969714010973*

Panahifar, H., Moradhaseli, R. & Khalesifard, H. R. (2020), 'Monitoring atmospheric particulate matters using vertically resolved measurements of a polarization lidar, in-situ recordings and satellite data over tehran, iran', *Scientific reports* **10**(1), 1–15.

Papayannis, A., Mamouri, R. E., Amiridis, V., Remoundaki, E., Tsaknakis, G., Kokkalis, P., Veselovskii, I., Kolgotin, A., Nenes, A. & Fountoukis, C. (2012), 'Optical-microphysical properties of saharan dust aerosols and composition relationship using a multi-wavelength raman lidar, in situ sensors and modelling: a case study analysis', *Atmos. Chem. Phys.* **12**(9), 4011–4032.

Pappalardo, G., Amodeo, A., Apituley, A., Comeron, A., Freudenthaler, V., Linné, H., Ansmann, A., Bösenberg, J., D'Amico, G., Mattis, I. et al. (2014), 'Earlinet: towards an advanced sustainable european aerosol lidar network', *Atmospheric Measurement Techniques* **7**(8), 2389–2409.

Peng, R. D., Bell, M. L., Geyh, A. S., McDermott, A., Zeger, S. L., Samet, J. M. & Dominici, F. (2009), 'Emergency admissions for cardiovascular and respiratory diseases and the chemical composition of fine particle air pollution', *Environmental health perspectives* **117**(6), 957–963.

Perrone, M. R., Barnaba, F., De Tomasi, F., Gobbi, G. P. & Tafuro, A. M. (2004), 'Imaginary refractive-index effects on desert-aerosol extinction versus backscatter relationships at 351 nm: numerical computations and comparison with raman lidar measurements', *Appl. Opt* **43**(29), 5531–5541.

Petäjä, T., Järvi, L., Kerminen, V.-M., Ding, A., Sun, J., Nie, W., Kujansuu, J., Virkkula, A., Yang, X., Fu, C. et al. (2016), 'Enhanced air pollution via aerosol-boundary layer feedback in china', *Scientific reports* **6**(1), 1–6.

Petzold, A., Rasp, K., Weinzierl, B., Esselborn, M., Hamburger, T., Doernbrack, A., Kandler, K., SchuüTZ, L., Knippertz, P., Fiebig, M. et al. (2009), 'Saharan dust absorption and refractive index from aircraft-based observations during samum 2006', *Tellus B Chem Phys Meteorol* **61**(1), 118–130.

Pfafferott, J., Rißmann, S., Sühring, M., Kanani-Sühring, F. & Maronga, B. (2021), 'Building indoor model in palm-4u: indoor climate, energy demand, and the interaction between buildings and the urban microclimate', *Geoscientific Model Development* **14**(6), 3511–3519.
URL: *https://gmd.copernicus.org/articles/14/3511/2021/*

Piironen, P. & Eloranta, E. (1994), 'Demonstration of a high-spectral-resolution lidar based on an iodine absorption filter', *Opt. Lett.* **19**(3), 234–236.

Pino, D., Jonker, H. J., Arellano, J. V.-G. d. & Dosio, A. (2006), 'Role of shear and the inversion strength during sunset turbulence over land: characteristic length scales', *Boundary-layer meteorology* **121**(3), 537–556.

Pitsch, H. (2006), 'Large-eddy simulation of turbulent combustion', *Annu. Rev. Fluid Mech.* **38**, 453–482.

Port, J. R., Yinda, C. K., Avanzato, V. A., Schulz, J. E., Holbrook, M. G., van Doremalen, N., Shaia, C., Fischer, R. J. & Munster, V. J. (2022), 'Increased small particle aerosol transmission of b. 1.1. 7 compared with sars-cov-2 lineage a in vivo', *Nature Microbiology* **7**(2), 213–223.

Pörtner, H.-O., Roberts, D. C., Adams, H., Adler, C., Aldunce, P., Ali, E., Begum, R. A., Betts, R., Kerr, R. B., Biesbroek, R. et al. (2022), 'Climate change 2022: impacts, adaptation, and vulner-

ability. contribution of working group ii to the sixth assessment report of the intergovernmental panel on climate change'.

Pozzoli, L., Bey, I., Rast, S., Schultz, M., Stier, P. & Feichter, J. (2008*a*), 'Trace gas and aerosol interactions in the fully coupled model of aerosol-chemistry-climate echam5-hammoz: 1. model description and insights from the spring 2001 trace-p experiment', *J. Geophys. Res. Atmos.* **113**(D7).

Pozzoli, L., Bey, I., Rast, S., Schultz, M., Stier, P. & Feichter, J. (2008*b*), 'Trace gas and aerosol interactions in the fully coupled model of aerosol-chemistry-climate echam5-hammoz: 2. impact of heterogeneous chemistry on the global aerosol distributions', *J. Geophys. Res. Atmos.* **113**(D7).

Prabha, T. V., Venkatesan, R., Mursch-Radlgruber, E., Rengarajan, G. & Jayanthi, N. (2002), 'Thermal internal boundary layer characteristics at a tropical coastal site as observed by a mini-sodar under varying synoptic conditions', *Journal of Earth System Science* **111**(1), 63–77.

Quan, J., Gao, Y., Zhang, Q., Tie, X., Cao, J., Han, S., Meng, J., Chen, P. & Zhao, D. (2013), 'Evolution of planetary boundary layer under different weather conditions, and its impact on aerosol concentrations', *Particuology* **11**(1), 34–40. Recent Advances for Aerosol and Environment Study in Asia.

Ramanathan, V., Crutzen, P. J., Kiehl, J. & Rosenfeld, D. (2001), 'Aerosols, climate, and the hydrological cycle', *science* **294**(5549), 2119–2124.

Rao, I. S., Anandan, V. & Reddy, P. N. (2008), 'Evaluation of dbs wind measurement technique in different beam configurations for a vhf wind profiler', *Journal of Atmospheric and Oceanic Technology* **25**(12), 2304–2312.

Raymatrics (2021), '3d scanning raman depolarization. url: https://www.raymetrics.com/product/3d-scanning-lidar, last access: 8 march 2021', *Raymatrics Inc.* .

Reineman, B. D., Lenain, L. & Melville, W. K. (2016), 'The use of ship-launched fixed-wing uavs for measuring the marine atmospheric boundary layer and ocean surface processes', *Journal of Atmospheric and Oceanic Technology* **33**(9), 2029–2052.

Rieger, D., Bangert, M., Bischoff-Gauss, I., Förstner, J., Lundgren, K., Reinert, D., Schröter, J., Vogel, H., Zängl, G., Ruhnke, R. et al. (2015), 'Icon–art 1.0–a new online-coupled model system from the global to regional scale', *Geoscientific Model Development* **8**(6), 1659–1676.

Rieger, D., Steiner, A., Bachmann, V., Gasch, P., Förstner, J., Deetz, K., Vogel, B. & Vogel, H. (2017*a*), 'Impact of the 4 april 2014 saharan dust outbreak on the photovoltaic power generation in germany', *Atmos. Chem. Phys.* **17**(21), 13391–13415.

Rieger, D., Steiner, A., Bachmann, V., Gasch, P., Förstner, J., Deetz, K., Vogel, B. & Vogel, H. (2017*b*), 'Impact of the 4 april 2014 saharan dust outbreak on the photovoltaic power generation in germany', *Atmospheric Chemistry and Physics* **17**(21), 13391–13415.

Roeckner, E., Brokopf, R., Esch, M., Giorgetta, M., Hagemann, S., Kornblueh, L., Manzini, E., Schlese, U. & Schulzweida, U. (2006), 'Sensitivity of simulated climate to horizontal and vertical resolution in the echam5 atmosphere model', *Journal of Climate* **19**(16), 3771–3791.

Rosen, J. M. & Kjome, N. T. (1991), 'Backscattersonde: a new instrument for atmospheric aerosol research', *Appl. Opt.* **30**(12), 1552–1561.

Rosenfeld, D., Rudich, Y. & Lahav, R. (2001), 'Desert dust suppressing precipitation: A possible desertification feedback loop', *Proceedings of the National Academy of Sciences* **98**(11), 5975–5980.

Rostási, Á., Topa, B. A., Gresina, F., Weiszburg, T. G., Gelencsér, A. & Varga, G. (2022), 'Saharan dust deposition in central europe in 2016—a representative year of the increased north african dust removal over the last decade', *Frontiers in Earth Science* **10**, 869902.

Saidou Chaibou, A. A., Ma, X. & Sha, T. (2020), 'Dust radiative forcing and its impact on surface energy budget over west africa', *Scientific Reports* **10**(1), 1–18.

Salma, I. & Maenhaut, W. (2006), 'Changes in elemental composition and mass of atmospheric aerosol pollution between 1996 and 2002 in a central european city', *Environmental pollution* **143**(3), 479–488.

Samset, B. H., Sand, M., Smith, C. J., Bauer, S. E., Forster, P. M., Fuglestvedt, J. S., Osprey, S. & Schleussner, C.-F. (2018), 'Climate impacts from a removal of anthropogenic aerosol emissions', *Geophysical Research Letters* **45**(2), 1020–1029.

Schillinger, M., Morancais, D., Fabre, F. & Culoma, A. J. (2003), ALADIN: the lidar instrument for the AEOLUS mission, *in* H. Fujisada, J. B. Lurie, M. L. Aten, K. Weber, J. B. Lurie, M. L. Aten & K. Weber, eds, 'Sensors, Systems, and Next-Generation Satellites VI', Vol. 4881, International Society for Optics and Photonics, SPIE, pp. 40 – 51.

Schladitz, A., Müller, T., Nordmann, S., Tesche, M., Gross, S., Freudenthaler, V., Gasteiger, J. & Wiedensohler, A. (2011), 'In situ aerosol characterization at cape verde: Part 2: Parametrization of relative humidity-and wavelength-dependent aerosol optical properties', *Tellus B Chem Phys Meteorol* **63**(4), 549–572.

Schuster, G. L., Vaughan, M., MacDonnell, D., Su, W., Winker, D., Dubovik, O., Lapyonok, T. & Trepte, C. (2012), 'Comparison of calipso aerosol optical depth retrievals to aeronet measurements, and a climatology for the lidar ratio of dust', *Atmospheric Chemistry and Physics* **12**(16), 7431–7452.

Schwartz, J., Spix, C., Wichmann, H. & Malin, E. (1991), 'Air pollution and acute respiratory illness in five german communities', *Environmental Research* **56**(1), 1–14.

Shen, J. & Cao, N. (2019), 'Accurate inversion of tropospheric aerosol extinction coefficient profile by mie-raman lidar', *Optik* **184**, 153–164.

Shen, L., Zhao, T., Wang, H., Liu, J., Bai, Y., Kong, S., Zheng, H., Zhu, Y. & Shu, Z. (2021), 'Importance of meteorology in air pollution events during the city lockdown for covid-19 in hubei province, central china', *Science of the Total Environment* **754**, 142227.

Sinyuk, A., Holben, B. N., Eck, T. F., Giles, D. M., Slutsker, I., Korkin, S., Schafer, J. S., Smirnov, A., Sorokin, M. & Lyapustin, A. (2020), 'The aeronet version 3 aerosol retrieval algorithm, associated uncertainties and comparisons to version 2', *Atmospheric Measurement Techniques* **13**(6), 3375–3411.

Smagorinsky, J. (1963), 'General circulation experiments with the primitive equations: I. the basic experiment', *Monthly weather review* **91**(3), 99–164.

Smith, A. K., Garcia, R. R., Marsh, D. R. & Richter, J. H. (2011), 'Waccm simulations of the mean circulation and trace species transport in the winter mesosphere', *J. Geophys. Res. Atmos.* **116**(D20).

Song, J., Saathoff, H., Gao, L., Gebhardt, R., Jiang, F., Vallon, M., Bauer, J., Norra, S. & Leisner, T. (2022), 'Variations of pm2.5 sources in the context of meteorology and seasonality at an urban street canyon in southwest germany', *Atmospheric Environment* **282**, 119147.
URL: *https://www.sciencedirect.com/science/article/pii/S1352231022002126*

Soupiona, O., Papayannis, A., Kokkalis, P., Foskinis, R., Sánchez Hernández, G., Ortiz-Amezcua, P., Mylonaki, M., Papanikolaou, C.-A., Papagiannopoulos, N., Samaras, S., Groß, S., Mamouri, R.-E., Alados-Arboledas, L., Amodeo, A. & Psiloglou, B. (2020), 'Earlinet observations of saharan dust intrusions over the northern mediterranean region (2014–2017): properties and impact on radiative forcing', *Atmos. Chem. Phys.* **20**(23), 15147–15166.

Spracklen, D. V., Carslaw, K. S., Kulmala, M., Kerminen, V.-M., Mann, G. W. & Sihto, S.-L. (2006), 'The contribution of boundary layer nucleation events to total particle concentrations on regional and global scales', *Atmospheric Chemistry and Physics* **6**(12), 5631–5648.

Stein, A., Draxler, R. R., Rolph, G. D., Stunder, B. J., Cohen, M. & Ngan, F. (2015), 'Noaa's hysplit atmospheric transport and dispersion modeling system', *Bulletin of the American Meteorological Society* **96**(12), 2059–2077.

Stellmach, S., Lischper, M., Julien, K., Vasil, G., Cheng, J. S., Ribeiro, A., King, E. M. & Aurnou, J. M. (2014), 'Approaching the asymptotic regime of rapidly rotating convection: boundary layers versus interior dynamics', *Physical review letters* **113**(25), 254501.

Steuri, B., Bender, S. & Cortekar, J. (2020), 'Successful user-science interaction to co-develop the new urban climate model palm-4u', *Urban Climate* **32**, 100630.
URL: *https://www.sciencedirect.com/science/article/pii/S2212095519301592*

Stocker, T. (2014), *Climate change 2013: the physical science basis: Working Group I contribution to the Fifth assessment report of the Intergovernmental Panel on Climate Change*, Cambridge university press.

Stoll, R., Gibbs, J. A., Salesky, S. T., Anderson, W. & Calaf, M. (2020), 'Large-eddy simulation of the atmospheric boundary layer', *Boundary-Layer Meteorology* **177**, 541–581.

Strawbridge, K. & Snyder, B. (2004), 'Planetary boundary layer height determination during

pacific 2001 using the advantage of a scanning lidar instrument', *Atmospheric Environment* **38**(34), 5861–5871.

Stull, R. B. (1988), *An introduction to boundary layer meteorology*, Vol. 13, Springer Science & Business Media.

Stull, R. B. & Eloranta, E. W. (1984), 'Boundary layer experiment—1983', *Bulletin of the American Meteorological Society* **65**(5), 450–456.

Su, J., Huang, J., Fu, Q., Minnis, P., Ge, J. & Bi, J. (2008), 'Estimation of asian dust aerosol effect on cloud radiation forcing using fu-liou radiative model and ceres measurements', *Atmos. Chem. Phys.* **8**(10), 2763–2771.

Su, T., Li, J., Li, C., Xiang, P., Lau, A. K.-H., Guo, J., Yang, D. & Miao, Y. (2017), 'An inter-comparison of long-term planetary boundary layer heights retrieved from calipso, ground-based lidar, and radiosonde measurements over hong kong', *Journal of Geophysical Research: Atmospheres* **122**(7), 3929–3943.

Su, T., Li, Z. & Kahn, R. (2018), 'Relationships between the planetary boundary layer height and surface pollutants derived from lidar observations over china: regional pattern and influencing factors', *Atmospheric Chemistry and Physics* **18**(21), 15921–15935.

Sugimoto, N., Nishizawa, T., Shimizu, A., Matsui, I. & Jin, Y. (2014), Characterization of aerosols in east asia with the asian dust and aerosol lidar observation network (ad-net), *in* 'Lidar Remote Sensing for Environmental Monitoring XIV', Vol. 9262, SPIE, pp. 74–82.

Sullivan, P. P., McWilliams, J. C. & Moeng, C.-H. (1994), 'A subgrid-scale model for large-eddy simulation of planetary boundary-layer flows', *Boundary-Layer Meteorology* **71**(3), 247–276.

Sullivan, P. P. & Patton, E. G. (2011), 'The effect of mesh resolution on convective boundary layer statistics and structures generated by large-eddy simulation', *Journal of the Atmospheric Sciences* **68**(10), 2395–2415.

Takemura, T., Nozawa, T., Emori, S., Nakajima, T. Y. & Nakajima, T. (2005), 'Simulation of climate response to aerosol direct and indirect effects with aerosol transport-radiation model', *Journal of Geophysical Research: Atmospheres* **110**(D2).

Tanaka, T. Y., Kurosaki, Y., Chiba, M., Matsumura, T., Nagai, T., Yamazaki, A., Uchiyama, A., Tsunematsu, N. & Kai, K. (2005), 'Possible transcontinental dust transport from north africa and the middle east to east asia', *Atmospheric Environment* **39**(21), 3901–3909.

Taylor, R., Coulombe, S., Otanicar, T., Phelan, P., Gunawan, A., Lv, W., Rosengarten, G., Prasher, R. & Tyagi, H. (2013), 'Small particles, big impacts: A review of the diverse applications of nanofluids', *Journal of applied physics* **113**(1), 1.

Tegen, I. & Fung, I. (1994), 'Modeling of mineral dust in the atmosphere: Sources, transport, and optical thickness', *J. Geophys. Res. Atmos.* **99**(D11), 22897–22914.

Tesche, M., Ansmann, A., Müller, D., Althausen, D., Engelmann, R., Freudenthaler, V. & Groß, S. (2009), 'Vertically resolved separation of dust and smoke over cape verde using multiwavelength raman and polarization lidars during saharan mineral dust experiment 2008', *Journal of Geophysical Research: Atmospheres* **114**(D13).

Tjernström, M., Balsley, B. B., Svensson, G. & Nappo, C. J. (2009), 'The effects of critical layers on residual layer turbulence', *Journal of the atmospheric sciences* **66**(2), 468–480.

Tkachenko, E., Debolskiy, A. & Mortikov, E. (2021), 'Intercomparison of subgrid scale models in large-eddy simulation of sunset atmospheric boundary layer turbulence: Computational aspects', *Lobachevskii Journal of Mathematics* **42**(7), 1580–1595.

Vaisal (2021), 'Description of wind cube lidar. url: https://www.vaisala.com/en/wind-lidars/wind-energy/windcube, last access: 1 september 2022', *Vaisal Inc.* .

Vermeulen, A., Devaux, C. & Herman, M. (2000), 'Retrieval of the scattering and microphysical properties of aerosols from ground-based optical measurements including polarization. i. method', *Applied optics* **39**(33), 6207–6220.

Vernier, J.-P., Fairlie, T. D., Natarajan, M., Wienhold, F. G., Bian, J., Martinsson, B. G., Crumeyrolle, S., Thomason, L. W. & Bedka, K. M. (2015), 'Increase in upper tropospheric and lower stratospheric aerosol levels and its potential connection with asian pollution', *Journal of Geophysical Research: Atmospheres* **120**(4), 1608–1619.

Vernier, J.-P., Fairlie, T., Deshler, T., Ratnam, M. V., Gadhavi, H., Kumar, B., Natarajan, M., Pandit, A., Raj, S. A., Kumar, A. H. et al. (2018), 'Batal: The balloon measurement campaigns of the asian tropopause aerosol layer', *Bulletin of the American Meteorological Society* **99**(5), 955–973.

Vogel, B., Hoose, C., Vogel, H. & Kottmeier, C. (2006), 'A model of dust transport applied to the dead sea area', *Meteorologische Zeitschrift* pp. 611–624.

Vogel, H., Förstner, J., Vogel, B., Hanisch, T., Mühr, B., Schättler, U. & Schad, T. (2014), 'Time-lagged ensemble simulations of the dispersion of the eyjafjallajökull plume over europe with cosmo-art', *Atmos. Chem. Phys.* **14**(15), 7837–7845.

Vraciu, C. V. (2021), 'On the analytical solution for two-dimensional convective plume and analytical modeling of the entrainment zone thickness', *Dynamics of Atmospheres and Oceans* **93**, 101191.

Wagner, C., Hüttl, T. & Sagaut, P. (2007), *Large-eddy simulation for acoustics*, Vol. 20, Cambridge University Press.

Wandinger, U. (2005), Raman lidar, *in* 'Lidar', Springer, pp. 241–271.

Wang, Z., Cao, X., Zhang, L., Notholt, J., Zhou, B., Liu, R. & Zhang, B. (2012), 'Lidar measurement of planetary boundary layer height and comparison with microwave profiling radiometer observation', *Atmospheric Measurement Techniques* **5**(8), 1965–1972.

Wei, J., Peng, Y., Mahmood, R., Sun, L. & Guo, J. (2019), 'Intercomparison in spatial distributions and temporal trends derived from multi-source satellite aerosol products', *Atmospheric Chemistry and Physics* **19**(10), 7183–7207.

Weimer, M., Schröter, J., Eckstein, J., Deetz, K., Neumaier, M., Fischbeck, G., Hu, L., Millet, D. B., Rieger, D., Vogel, H. et al. (2017), 'An emission module for icon-art 2.0: implementation and simulations of acetone', *Geosci. Model Dev.* **10**(6), 2471–2494.

Weinzierl, B., Petzold, A., Esselborn, M., Wirth, M., Rasp, K., Kandler, K., Schuetz, L., Koepke, P. & Fiebig, M. (2009), 'Airborne measurements of dust layer properties, particle size distribution and mixing state of saharan dust during samum 2006', *Tellus B Chem Phys Meteorol* **61**(1), 96–117.

Weinzierl, B., Sauer, D., Esselborn, M., Petzold, A., Veira, A., Rose, M., Mund, S., Wirth, M., Ansmann, A., Tesche, M. et al. (2011), 'Microphysical and optical properties of dust and tropical biomass burning aerosol layers in the cape verde region—an overview of the airborne in situ and lidar measurements during samum-2', *Tellus B Chem Phys Meteorol* **63**(4), 589–618.

Welton, E. J., Campbell, J. R., Berkoff, T. A., Valencia, S., Spinhirne, J. D., Holben, B., Tsay, S.-C. & Schmid, B. (2006), 'The nasa micro-pulse lidar network (mplnet): an overview and recent results', *Opt. Pur. Apl* **39**, 67–74.

Welton, E. J., Stewart, S. A., Lewis, J. R., Belcher, L. R., Campbell, J. R. & Lolli, S. (2018), Status of the nasa micro pulse lidar network (mplnet): overview of the network and future plans, new version 3 data products, and the polarized mpl, *in* 'EPJ Web of Conferences', Vol. 176, EDP Sciences, p. 09003.

WHO (2014), '7 million premature deaths annually linked to air pollution, last access: 14 october 2022'.

WHO (2021), 'Forecast comparison — wmo sds-was. url: https://sds-was.aemet.es/forecast-products/dust-forecasts/forecast-comparison,last access: on 22 september 2021', *WHO Inc.* .

Wiegner, M., Emeis, S., Freudenthaler, V., Heese, B., Junkermann, W., Münkel, C., Schäfer, K., Seefeldner, M. & Vogt, S. (2006), 'Mixing layer height over munich, germany: Variability and comparisons of different methodologies', *Journal of Geophysical Research: Atmospheres* **111**(D13).

Williams, B. J., Jayne, J. T., Lambe, A. T., Hohaus, T., Kimmel, J. R., Sueper, D., Brooks, W., Williams, L. R., Trimborn, A. M., Martinez, R. E., Hayes, P. L., Jimenez, J. L., Kreisberg, N. M., Hering, S. V., Worton, D. R., Goldstein, A. H. & Worsnop, D. R. (2014), 'The first combined thermal desorption aerosol gas chromatograph—aerosol mass spectrometer (tag-ams)', *Aerosol Science and Technology* **48**(4), 358–370.

Xiafukaiti, A., Lagrosas, N., Ong, P. M., Saitoh, N., Shiina, T. & Kuze, H. (2020), 'Comparison of aerosol properties derived from sampling and near-horizontal lidar measurements using mie scattering theory', *Applied Optics* **59**(26), 8014–8022.

Yuval, Levi, Y., Dayan, U., Levy, I. & Broday, D. M. (2020), 'On the association between characteristics of the atmospheric boundary layer and air pollution concentrations', *Atmospheric Research* **231**, 104675.

Zängl, G., Reinert, D., Rípodas, P. & Baldauf, M. (2015), 'The icon (icosahedral non-hydrostatic) modelling framework of dwd and mpi-m: Description of the non-hydrostatic dynamical core', *Quarterly Journal of the Royal Meteorological Society* **141**(687), 563–579.

Zardini, A. A., Sjogren, S., Marcolli, C., Krieger, U. K., Gysel, M., Weingartner, E., Baltensperger, U. & Peter, T. (2008), 'A combined particle trap/htdma hygroscopicity study of mixed inorganic/organic aerosol particles', *Atmospheric Chemistry and Physics* **8**(18), 5589–5601.
URL: *https://acp.copernicus.org/articles/8/5589/2008/*

Zeitung, S. (2016), 'Süddeutsche zeitung: Stuttgart löst als erste stadt in deutschland den feinstaubalarm aus: available at:'. (last accessed: 18 February 2022).

Zhang, H., Wagner, F., Saathoff, H., Vogel, H., Hoshyaripour, G., Bachmann, V., Förstner, J. & Leisner, T. (2022), 'Comparison of scanning lidar with other remote sensing measurements and transport model predictions for a saharan dust case', *Remote Sensing* **14**(7).
URL: *https://www.mdpi.com/2072-4292/14/7/1693*

Zhang, J. A., Atlas, R., Emmitt, G. D., Bucci, L. & Ryan, K. (2018), 'Airborne doppler wind lidar observations of the tropical cyclone boundary layer', *Remote Sensing* **10**(6), 825.

Zhang, Y., Wang, L., Santanello, J. A., Pan, Z., Gao, Z. & Li, D. (2020), 'Aircraft observed diurnal variations of the planetary boundary layer under heat waves', *Atmospheric Research* **235**, 104801.

Zhao, C., Liu, X., Leung, L., Johnson, B., McFarlane, S. A., Gustafson Jr, W., Fast, J. D. & Easter, R. (2010), 'The spatial distribution of mineral dust and its shortwave radiative forcing over north africa: modeling sensitivities to dust emissions and aerosol size treatments', *Atmospheric Chemistry and Physics* **10**(18), 8821–8838.

Zhao, C., Liu, X., Ruby Leung, L. & Hagos, S. (2011), 'Radiative impact of mineral dust on monsoon precipitation variability over west africa', *Atmospheric Chemistry and Physics* **11**(5), 1879–1893.

Publication during PhD study

[1] **Zhang, H.**, Wagner, F., Saathoff, H., Vogel, H., Hoshyaripour, G., Bachmann, V.,Förstner, J., Leisner, T., Comparison of Scanning LiDAR with Other Remote Sensing Measurements and Transport Model Predictions for a Saharan Dust Case, Remote Sensing, 14(7), 1693, 2022.

[2] Michael Kunz et al., Swabian MOSES 2021: An interdisciplinary field campaign for investigating convective storms and their event chains, Frontiers in Earth Science, 1886, 2022.

Close to submission:

[3] **Zhang, H.**, Rolf, C., Tillmann, C., Wienhold, F., Leisner, T., Saathoff, H., Comparison of aerosol physical properties, and boundary layer heights measured *in-situ* and by a scanning aerosol LIDAR, in preparation for AMT.

[4] **Zhang, H.**, Leisner, T., Saathoff, H., et al., Aerosol composition, air quality, and boundary layer dynamics in the urban background of Stuttgart in winter, in preparation for ACP or Romote sensing of Environment.

Appendix A: Supplement for result and discussion

Table S1: Averaged extinction coefficients and its their stand deviations for different window types and lengths.

Ext. coeff. (Mm^{-1})	H=82.5 m	H=157.5 m	H=307.5 m	H=457.5 m	H=607.5 m	H=1207.5 m
Rect. window	48 ± 32	49 ± 19	48 ± 11	49 ± 8	51 ± 5	53 ± 5
Hamming window	49 ± 36	48 ± 27	49 ± 14	49 ± 9	50 ± 6	51 ± 4
Hanning window	49 ± 37	48 ± 29	49 ± 16	49 ± 10	49 ± 7	51 ± 4
Kalman filter	46 ± 39	47 ± 14	46 ± 8	48 ± 8	48 ± 6	48 ± 5

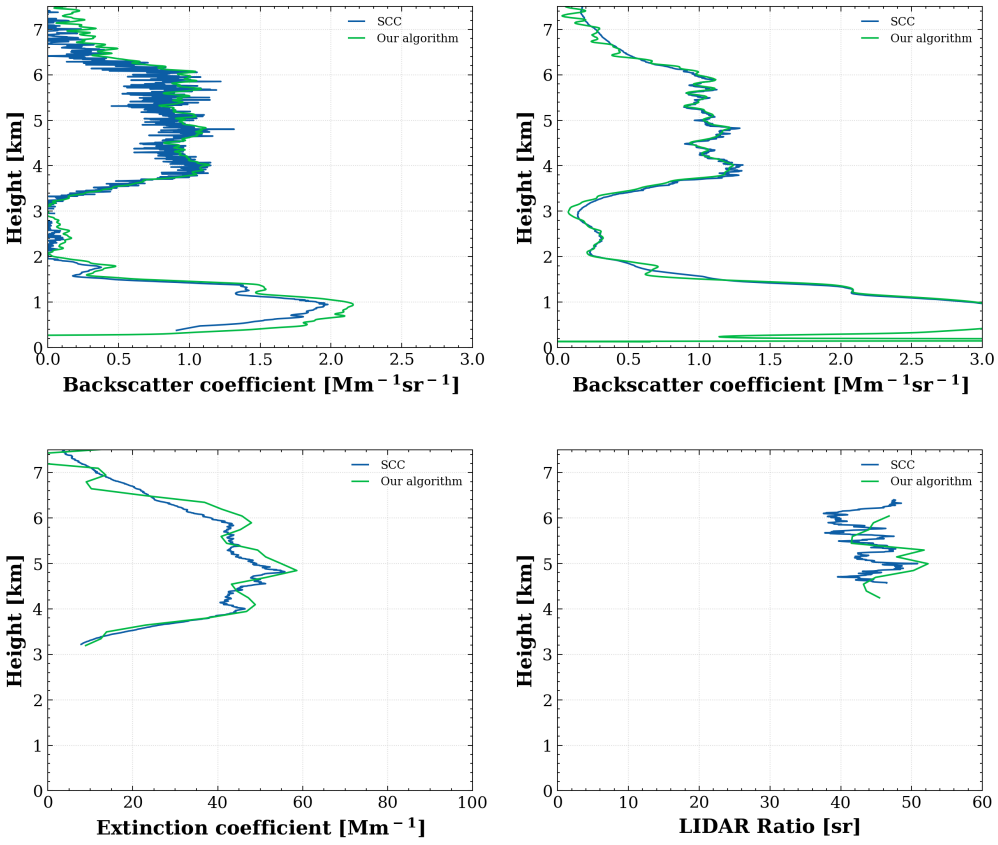

Figure S1: Elastic backscatter coefficient (a), Raman backscatter coefficient (b), Raman extinction coefficient (c) and lidar ratio (d) retrieved using the Single Calculus Chain (SCC) and our data algorithm (Klett – Fernald).

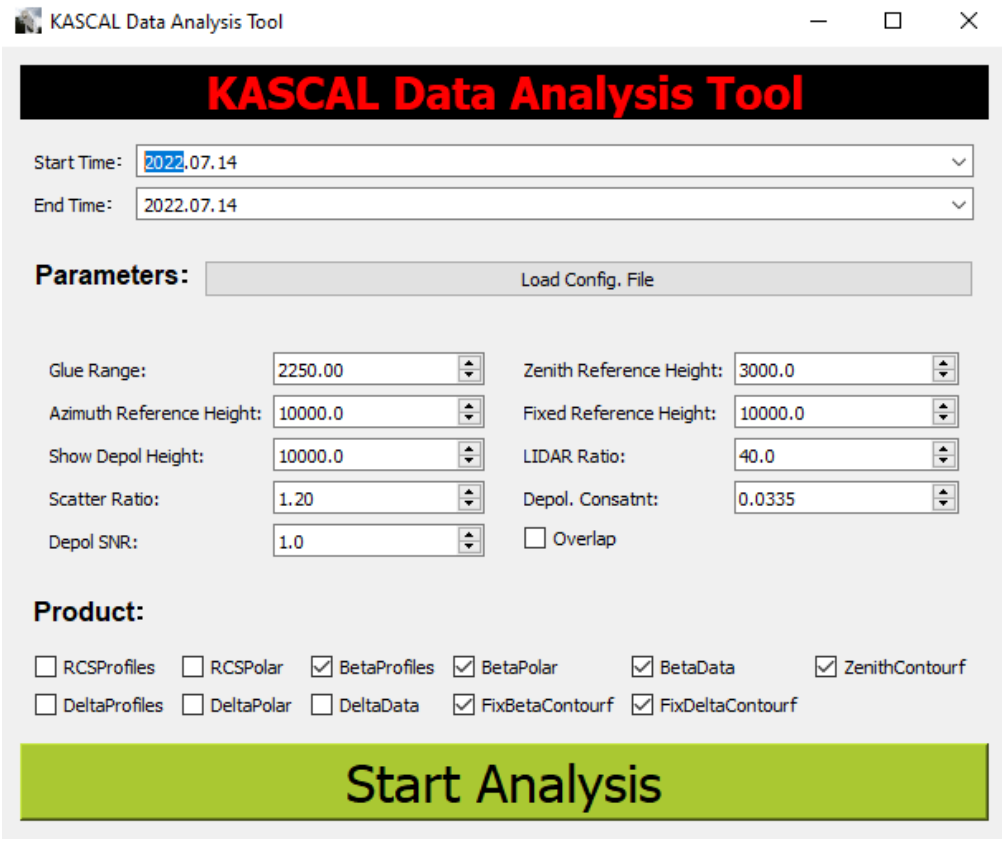

Figure S2: GUI of KASCAL data analysis software developed by me

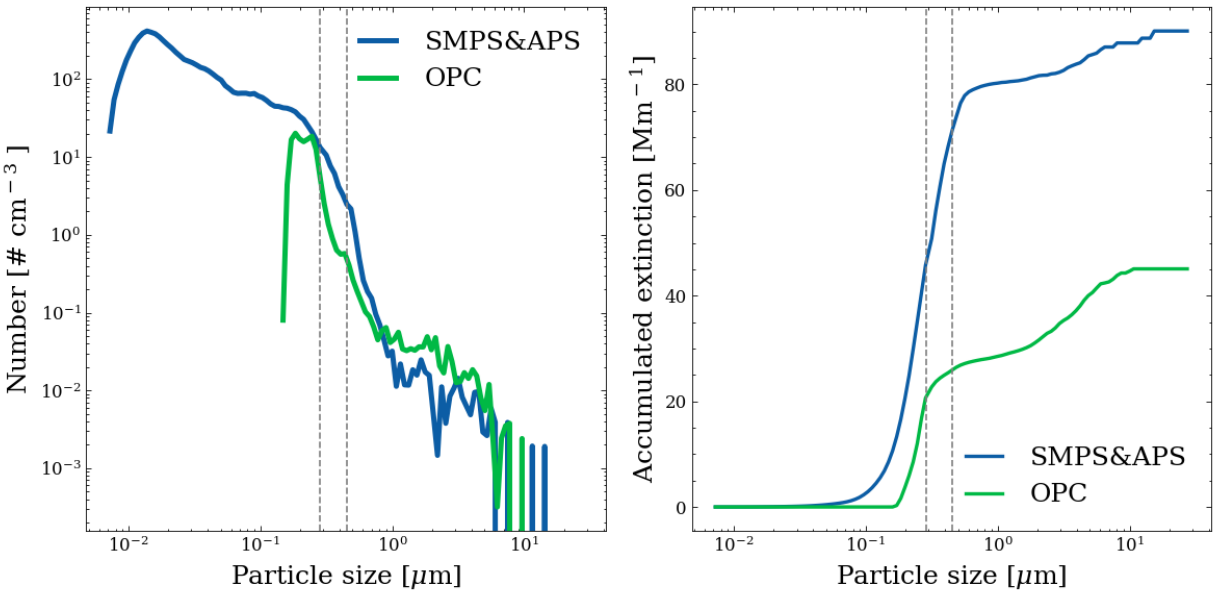

Figure S3: Particle size distribution measured by OPC and merged size distribution measured by SMPS and APS (left) as well as accumulated extinction coefficients calculated from model calculation based on these two size distributions.

Figure S4: The particle counting effective curve calculated from merged aerosol number size distribution by SMPS and APS data and measured by OPC.

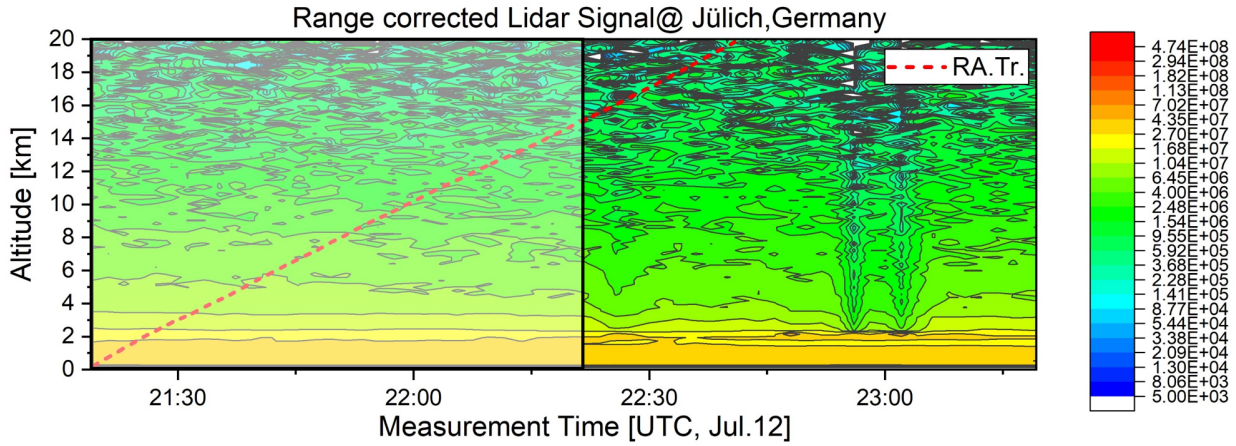

Figure S5: Time series of Range corrected lidar signal and radiosonde vertical trajectory indicated as red dash line on July 9^{th} July 12^{th}, 2018.

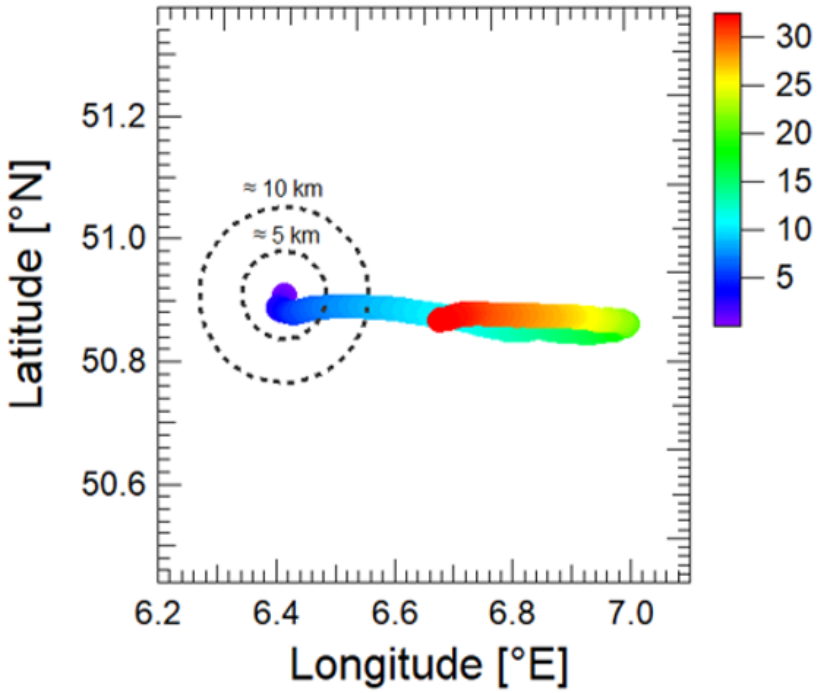

Figure S6: Horizontal trajectory of radiosonde on 9^{th} July 12^{th}, 2018. The color of this plot indicates the altitude of radiosonde and the circle indicates the distance from the lidar observation station.

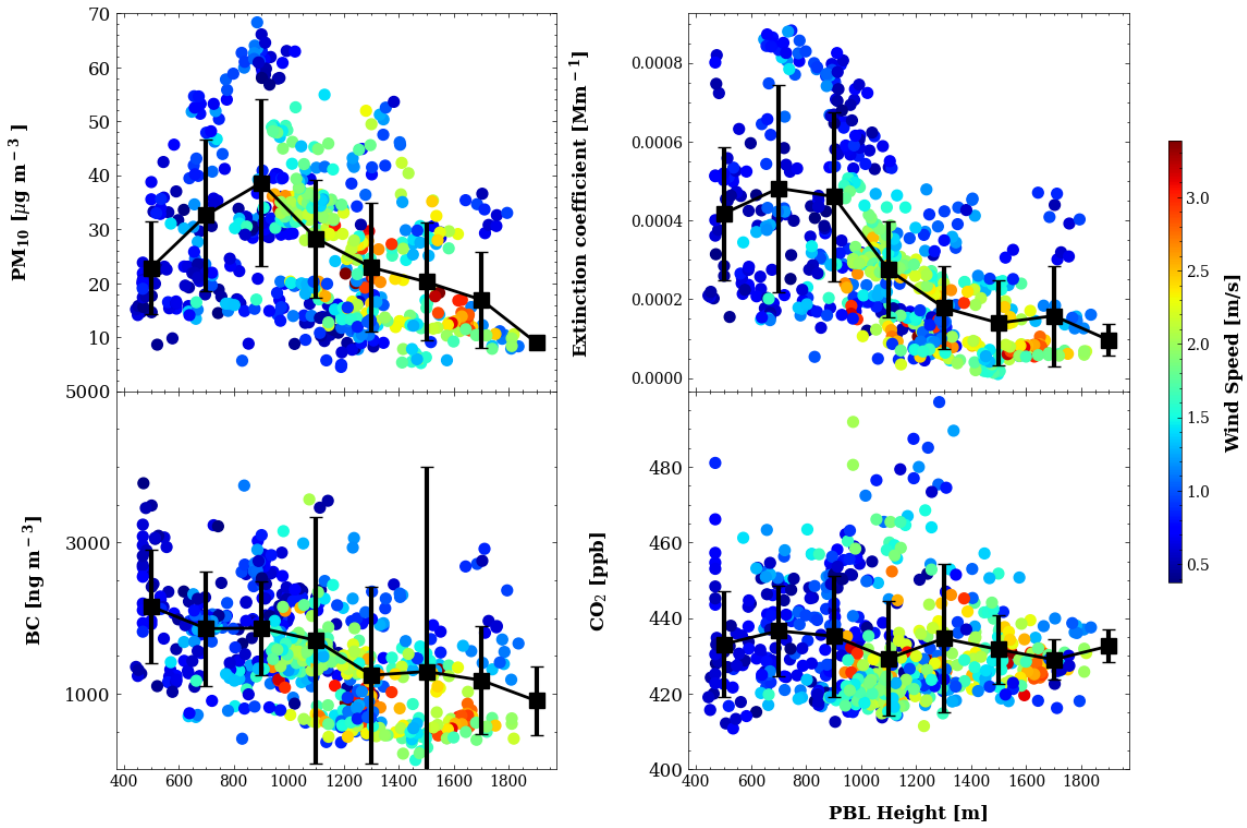

Figure S7: The correlation between boundary layer height and PM_{10}, extinction coefficient, black carbon, and carbon dioxide from February 5^{th} to March 5^{th}, 2018 in Stuttgart.(The color of scatter point indicated wind speed.)

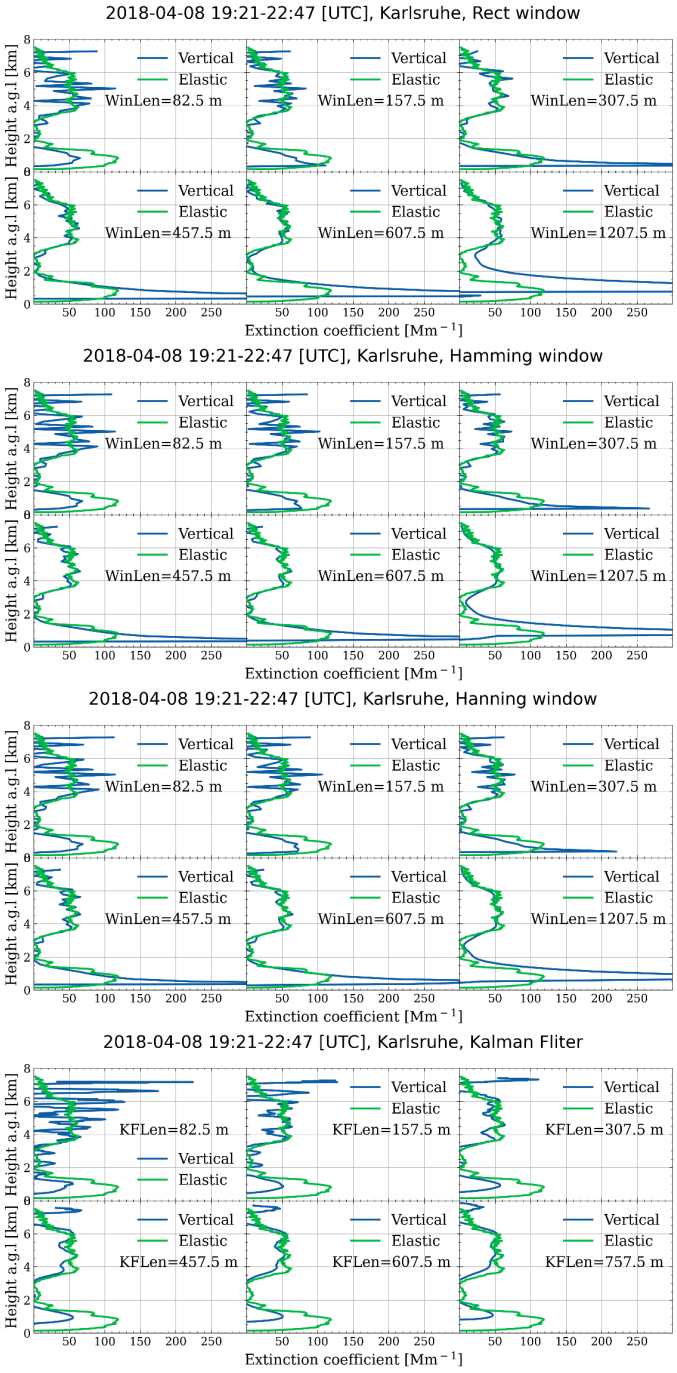

Figure S8: Extinction coefficients from Raman signal from vertical and slant measurements with different types of filters and different filter lengths.

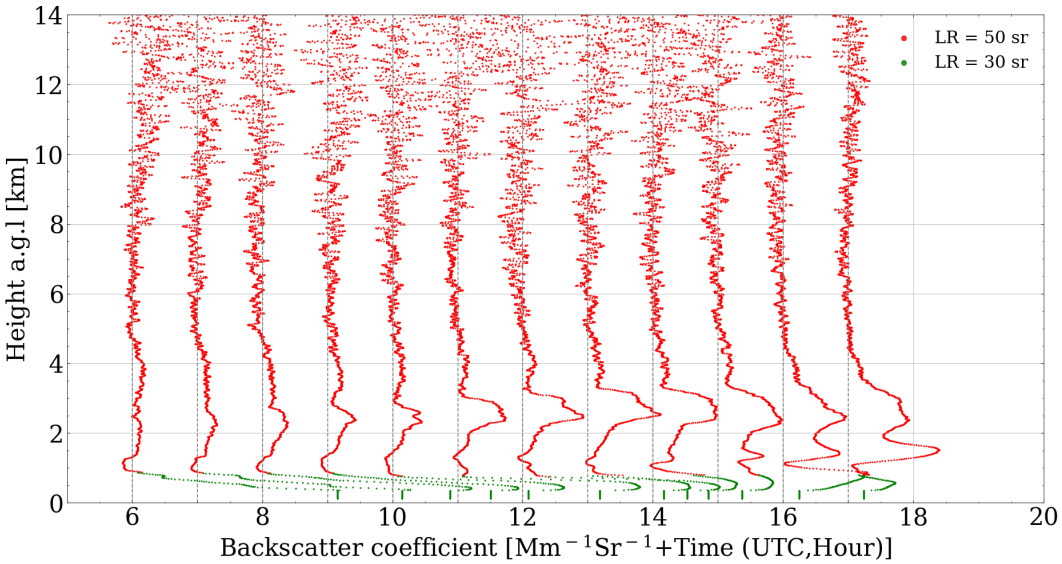

Figure S9: Elastic backscatter coefficients from vertical lidar measurement for different values of altitude -dependent lidar ratios with interval time being 1 hour on 7^{th}, April 2018.

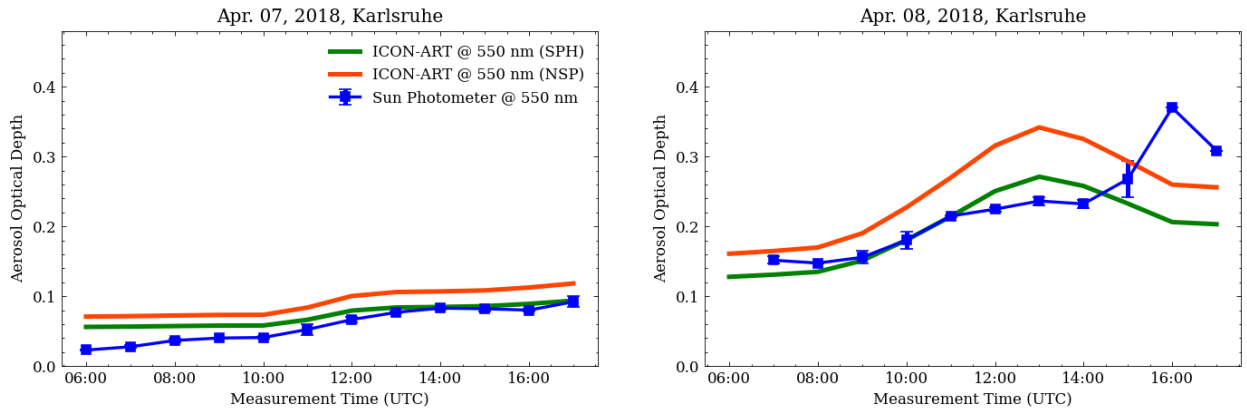

Figure S10: AOD from the sun photometer (coarse mode) and ICON-ART for both SPH and NSP particles model simulation on 7^{th} and 8^{th} of April for 1hour temporal resolution. SPH = spherical; NSP = non-spherical.

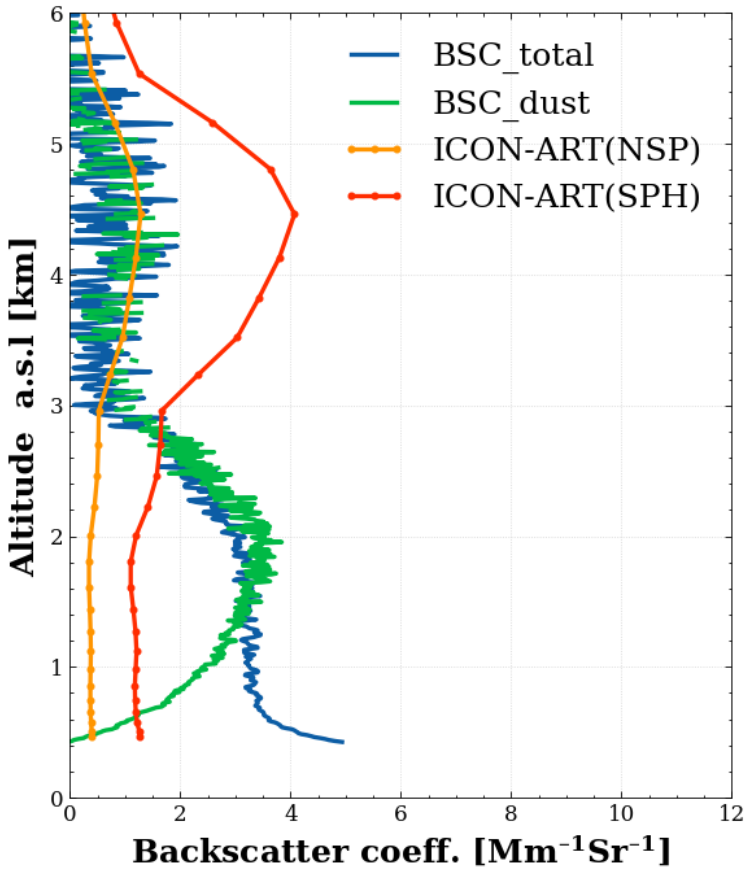

Figure S11: The same plot as 3.46 but for C2 case during Saharan dust case 2.

Appendix B: Mathematical derivation

B.1 Mathematical derivation lidar retrieval method

This supplement reviewed the elastic lidar retrival methods mainly based on the previous literature (Fernald et al. 1972, Fernald 1984, Klett 1981, 1985*b*). The aim of work to be clarify these methods and summary these methods. In addition, some mistake in previous literature was corrected in this supplement.

Let begin with lidar equation:

$$P(r) = C_0 \frac{\beta_{aer}(r) + \beta_{mol}(r)}{r^2} \exp\left(-2\int_0^r \left[\alpha_{aer}(r) + \alpha_{mol}(r)\right] dr\right) \tag{B.1}$$

Then

$$P(r) * r^2 = C_0 * (\beta_{aer}(r) + \beta_{mol}(r)) \exp\left(-2\int_0^r \left[\alpha_{aer}(r) + \alpha_{mol}(r)\right] dr\right) \tag{B.2}$$

Assume in very polluted conditions, $\beta_{aer}(r) >> \beta_{mol}(r))$ and $\alpha_{aer}(r) >> \alpha_{mol}(r))$, so $\beta(r) \approx \beta_{aer}(r)$ and $\alpha(r) \approx \alpha_{aer}(r)$. Let $\alpha(r) = K\beta(r)$. we get

$$P(r) * r^2 = C_0 * \frac{\alpha(r)}{K} \exp(-2\int_0^r \alpha(r)dr) \tag{B.3}$$

Take logarithm on both size and let $S(r) = ln(P(r) * r^2)$, we can get

$$S(r) = ln(C_0) + ln(\alpha(r)) - ln(K) - 2\int_0^r \alpha(r)dr \tag{B.4}$$

Take the derivative of r,

$$\frac{dS(r)}{dr} = \frac{1}{\alpha(r)}\frac{d\alpha(r)}{dr} - 2\alpha(r) \tag{B.5}$$

Equation B.5 is Bernoulli differential equation. Then we can get the solution of lidar equation.

$$\alpha(r) = \frac{RCS(r)}{\frac{RCS(r_c)}{\alpha(r_c)} + 2\int_r^{r_c} RCS(r)dr} \tag{B.6}$$

If condition: $\beta_{aer}(r) >> \beta_{mol}(r))$ and $\alpha_{aer}(r) >> \alpha_{mol}(r))$, cannot be satisfied. We can separate the extinction and backscatter into particle part and molecule part. Then we can get the follow:

$$P(r) * r^2 = C_0 * (\beta_{aer}(r) + \beta_{mol}(r)) \exp\left(-2 \int_0^r [\alpha_{aer}(r) + \alpha_{mol}(r)]\, dr\right) \tag{B.7}$$

let $S(r) = ln(P(r) * r^2)$, $\beta(r) = \beta_{aer}(r) + \beta_{mol}(r))$ and take logarithm on both size, we can get

$$S(r) = ln(C_0) + ln(\beta(r)) - 2 \int_0^r [\alpha_{aer}(r) + \alpha_{mol}(r)]\, dr \tag{B.8}$$

Take the derivative of r

$$\frac{dS(r)}{dr} = \frac{1}{\beta(r)} \frac{\beta(r)}{dr} - 2[\alpha_{aer}(r) + \alpha_{mol}(r)] \tag{B.9}$$

we have $\alpha_{aer}(r) = S_a(r) * \beta_{aer}(r)$ and $\alpha_{mol}(r) = S_m * \beta_{mol}$, Then

$$\begin{aligned}
&\frac{dS(r)}{dr} = \frac{1}{\beta(r)} \frac{\beta(r)}{dr} - 2[S_a(r) * \beta_{aer}(r) + S_m \beta_{mol}(r)] \\
&= \frac{1}{\beta(r)} \frac{\beta(r)}{dr} - 2[S_a(r) * \beta_{aer}(r) + S_m * \beta_{mol}(r) + S_a(r) * \beta_{mol}(r) - S_a(r) * \beta_{mol}(r)] \\
&= \frac{1}{\beta(r)} \frac{\beta(r)}{dr} - 2[S_a(r) * \beta_(r) + S_m * \beta_{mol}(r) - S_a(r) * \beta_{mol}(r)] \\
&= \frac{1}{\beta(r)} \frac{\beta(r)}{dr} - 2S_a(r) * \beta_(r) + 2\beta_{mol}(r) * (S_a(r) - S_m)
\end{aligned} \tag{B.10}$$

let $S^{'}(r) = S(r) - S(r_m) - 2 \int_r^{r_m} (S_m - S_a(r)) * \beta_{mol}(r^{'}) dr^{'}$. Here is sign correction for Klett (1985*b*)). r_m is the reference height for lidar retrieval. Then

$$\begin{aligned}
&\frac{dS^{'}(r)}{dr} = \frac{dS(r)}{dr} + 2S_a(r) * \frac{d}{dr} \int_r^{r_m} \beta_{mol}(r^{'}) dr^{'} - 2S_m * \frac{d}{dr} \int_r^{r_m} \beta_{mol}(r^{'}) dr^{'} \\
&= \frac{dS(r)}{dr} - 2S_a(r) * \beta_{mol}(r) + 2S_m * \beta_{mol}(r)
\end{aligned} \tag{B.11}$$

Put equation B.10 into equation B.11, we get

$$\begin{aligned}\frac{dS^{'}(r)}{dr} &= \frac{dS(r)}{dr} - 2S_a(r) * \beta_{mol}(r) + 2S_m * \beta_{mol}(r) \\ &= \frac{1}{\beta(r)}\frac{\beta(r)}{dr} - 2S_a(r) * \beta_(r) + 2\beta_{mol}(r) * (S_a(r) - S_m) - 2S_a(r) * \beta_{mol}(r) + 2S_m * \beta_{mol}(r) \\ &= \frac{1}{\beta(r)}\frac{d\beta(r)}{dr} - 2S_a(r) * \beta_(r)\end{aligned} \tag{B.12}$$

Then

$$\frac{1}{\beta^2(r)}\frac{d\beta(r)}{dr} - \frac{1}{\beta(r)}\frac{dS^{'}(r)}{dr} = 2S_a(r) \tag{B.13}$$

Hence,

$$\beta(r) = \frac{e^{[S^{'}(r) - S^{'}(r_m)]}}{C + \int_{r_m}^{r} -2S_a(r) * e^{[S^{'}(r^{'}) - S^{'}(r_m)]}dr^{'}} \tag{B.14}$$

Then we arrive at,

$$\beta(r) = \frac{P(r)r^2 e^{\int_{r_m}^{r} -2(S_a(r) - S_m) * \beta_{mol}(r^{'})dr^{'}}}{C * P(r_m) * r_m^2 - \int_{r_m}^{r} 2S_a(r) * P(r)r^2 e^{\int_{r_m}^{r} -2(S_a(r) - S_m) * \beta_{mol}(r^{'})dr^{'}} dr^{'}} \tag{B.15}$$

AS $r = r_m$, $\beta(r) = \beta(r_m)$, Hence, $C = \frac{1}{\beta(r_m)}$, let $RCS(r) = P(r) * r^2$,

$$\beta(r) = \frac{RCS(r)e^{\int_{r_m}^{r} -2(S_a(r) - S_m) * \beta_{mol}(r^{'})dr^{'}}}{\frac{RCS(z_m)}{\beta(r_m)} - \int_{r_m}^{r} 2S_a(r) * RCS(z)e^{\int_{r_m}^{r} -2(S_a(r) - S_m) * \beta_{mol}(r^{''})dr^{''}} dr^{'}} \tag{B.16}$$

For the Forward integral,r_m can be set to zero (from ground integral)

$$\beta(r) = \frac{RCS(r)e^{\int_{0}^{r} -2(S_a(r) - S_m) * \beta_{mol}(r^{'})dr^{'}}}{\frac{RCS(r_0)}{\beta(r_0)} - \int_{0}^{r} 2S_a(r) * RCS(z)e^{\int_{0}^{r} -2(S_a(r) - S_m) * \beta_{mol}(r^{''})dr^{''}} dr^{'}} \tag{B.17}$$

As $C_0 = \frac{RCS(0)}{\beta(r_0)}$, Then,

$$\beta(r) = \frac{RCS(z)e^{\int_{0}^{r} -2(S_a(r) - S_m) * \beta_{mol}(r^{'})dr^{'}}}{C_0 - \int_{0}^{r} 2S_a(r) * RCS(z)e^{\int_{0}^{r} -2(S_a(r) - S_m) * \beta_{mol}(r^{''})dr^{''}} dr^{'}} \tag{B.18}$$

From B.18, we know that for a well calibration lidar system (C_0 is know), the reference value is unnecessary.) Here test the application of this forward method using lidar constant. The simulation result is shown in Figure 2.4. As shown in this figure, the stability of forward method is wavelength

dependent (more stable at longer wavelength). So this method is common used in ceilometer with wavelength at 1064 nm.

B.2 Mathematical derivation of multi-angle method

This supplement gives the mathematical derivation of innovation lidar retrieval method based on scanning elastic lidar.

The lidar equation and klett-Fernald method can be expressed as following:

$$P(r) = C_0 \frac{\beta_{aer}(r) + \beta_{mol}(r)}{r^2} \exp\left(-2\int_0^r \left[\alpha_{aer}(r) + \alpha_{mol}(r)\right] dr\right) \tag{B.19}$$

$$\beta(r) = \frac{\text{RCS}(r) * \exp\left\{2 * (S_a - S_m) * \int_r^{R_{ref}} \beta_{mol}(r')\, dr'\right\}}{\frac{RCS(r)}{C * \beta_{\text{mol}}(r_{ref})} + 2 * S_a * \int_r^{R_{ref}} \left[\text{RCS}(r') * \exp\left\{2 * (S_a - S_m) * \int_r^{R_{ref}} \beta_{mol}(r'')\, dr''\right\}\right] dr'} \tag{B.20}$$

In term of the numerator, S_a is for the retrieval method and S_{a0} is for the input lidar ratio. Let elevation angle be θ_1 and θ_2, and $\theta_1 > \theta_2$, $\mu_1 = \frac{1}{sin\theta_1}$, $\mu_2 = \frac{1}{sin\theta_2}$, $\mu = \mu_2 - \mu_1$. For θ_1 direction:

$$P(\mu_1 r) = C_0 \frac{\beta_{aer}(\mu_1 r) + \beta_{mol}(\mu_1 r)}{(\mu_1 r)^2} \exp\left(-2\int_0^{\mu_1 r} \left[\alpha_{aer}(\mu_1 r) + \alpha_{mol}(\mu_1 r)\right] dr\right) \tag{B.21}$$

$$\beta(\mu_1 r) = \frac{\text{RCS}(\mu_1 \text{r}) * \exp\left\{2 * (S_a - S_m) * \int_{\mu_1 r}^{\mu_1 r_{ref}} \beta_{mol}(\mu_1 r')\, dr'\right\}}{\frac{RCS(\mu_1 r)}{C * \beta_{mol}(\mu_1 r_{ref})} + 2 * S_a * \int_{\mu_1 r}^{\mu_1 R_{ref}} \left[\text{RCS}(\mu_1 r') * \exp\left\{2 * (S_a - S_m) * \int_{\mu_1 r'}^{\mu_1 R'_{ref}} \beta_{mol}(\mu_1 r'')\, dr''\right\}\right] dr'} \tag{B.22}$$

For θ_2 direction:

$$P(\mu_2 r) = C_0 \frac{\beta_{aer}(\mu_2 r) + \beta_{mol}(\mu_2 r)}{(\mu_2 r)^2} \exp\left(-2\int_0^{\mu_2 r} \left[\alpha_{aer}(\mu_2 r) + \alpha_{mol}(\mu_2 r)\right] dr\right) \tag{B.23}$$

$$\beta(\mu_2 r) = \frac{\text{RCS}(\mu_2 \text{r}) * \exp\left\{2 * (S_a - S_m) * \int_{\mu_2 r}^{\mu_2 r_{ref}} \beta_{mol}(\mu_2 r')\, dr'\right\}}{\frac{RCS(\mu_2 r)}{C * \beta_{\text{mol}}(\mu_2 r_{\text{ref}})} + 2 * S_a * \int_{\mu_2 r}^{\mu_2 R_{ref}} \left[\text{RCS}(\mu_2 r') * \exp\left\{2 * (S_a - S_m) * \int_{\mu_2 r'}^{\mu_2 R'_{ref}} \beta_{mol}(\mu_2 r'')\, dr''\right\}\right] dr'} \tag{B.24}$$

Replace the RCS in Equation B.22 and Equation B.24 by Equation B.21 and Equation B.23, respectively. Please note that RCS = P(r)*r2. Equation (4) divided by Equation (6). For numerator:

$$\begin{aligned}
&\frac{\mathrm{RCS}\left(\mu_1 \mathrm{r}\right)_1 * \exp\left\{2 * \left(S_a - S_m\right) * \int_{\mu_1 r}^{\mu_1 r_{ref}} \beta_{mol}\left(\mu_1 r'\right)_1 dr'\right\}}{\mathrm{RCS}\left(\mu_2 \mathrm{r}\right)_2 * \exp\left\{2 * \left(S_a - S_m\right) * \int_{\mu_2 r}^{\mu_2 r_{ref}} \beta_{mol}\left(\mu_2 r'\right)_2 dr'\right\}} \\
&= \frac{\exp\left\{-2\int_0^{\mu_1 r_{ref}} \alpha_{mol}\left(\mu_1 r'\right)_1 dr' - 2\int_0^{\mu_1 r} \alpha_{aer}\left(\mu_1 r'\right)_1 dr' + 2 * S_a * \int_{\mu_1 r}^{\mu_1 r_{ref}} \beta_{mol}\left(\mu_1 r'\right)_1 dr'\right\}}{\exp\left\{-2\int_0^{\mu_2 r_{ref}} \alpha_{mol}\left(\mu_2 r'\right)_2 dr' - 2\int_0^{\mu_2 r} \alpha_{\mathrm{aer}}\ \left(\mu_2 r'\right)_2 dr' + 2 * S_a * \int_{\mu_2 r}^{\mu_2 r_{ref}} \beta_{mol}\left(\mu_2 r'\right)_2 dr'\right\}} \\
&= \frac{1}{\exp\left\{-2\int_0^{\mu r_{ref}} \alpha_{mol}\left(r'\right) dr' - 2\int_0^{\mu r} \alpha_{aer}\left(r'\right) dr' + 2 * S_a * \int_{\mu r}^{\mu r_{ref}} \beta_{mol}\left(r'\right) dr'\right\}} \\
&= \frac{1}{\exp\left\{-2\int_0^{\mu r_{ref}} \alpha_{mol}\left(r'\right) dr' - 2\int_0^{\mu r} \alpha_{aer}\left(r'\right) dr' + 2 * S_a * \int_0^{\mu r_{ref}} \beta_{mol}\left(r'\right) dr' - 2 * S_a * \int_0^{\mu r} \beta_{mol}\left(r'\right) dr'\right\}}
\end{aligned} \tag{B.25}$$

And for the denominator:

$$\frac{\frac{\mathrm{RCS}\left(\mu_1 r_{ref}\right)_1}{C*\beta_{\mathrm{mol}}\left(\mu_1 r_{ref}\right)_1}+2*\mathrm{Sa}*\int_{\mu_1 r}^{\mu_1 ref} RCS\left(\mu_1 r'\right)_1*\exp\left\{2*\left(S_a-S_m\right)*\int_{\mu_1 r}^{\mu_1 r_{ref}}\beta_{mol}\left(\mu_1 r''\right)_1 dr''\right\}dr'}{\frac{RCS\left(\mu_2 r_{ref}\right)_2}{C*\beta_{\mathrm{mol}}\left(\mu_2 r_{ref}\right)_2}+2*\mathrm{Sa}*\int_{\mu_2 r}^{\mu_2 ref} RCS\left(\mu_2 r'\right)_2*\exp\left\{2*\left(S_a-S_m\right)*\int_{\mu_2 r}^{\mu_2 r_{ref}}\beta_{mol}\left(\mu_2 r''\right)_2 dr''\right\}dr'}$$

$$=\frac{k*\exp\left(-2\int_0^{\mu_1 r_{ref}}\left[\alpha_{aer}\left(\mu_1 r\right)_1+\alpha_{\mathrm{mol}}\left(\mu_1 r\right)_1\right]dr\right)+2*S_a*\int_{\mu_1 r}^{\mu_1 ref} k*\left(\beta_{aer}\left(\mu_1 r'\right)_1+\beta_{mol}\left(\mu_1 r'\right)_1\right)*\exp\left(-2\int_0^{\mu_1 r_{ref}}\alpha_{mol}\left(\mu_1 r''\right)_1 dr''-2\int_0^{\mu_1 r}\alpha_{aer}\left(\mu_1 r''\right)_1 dr''+2*S_a\int_{\mu_1 r}^{\mu_1 r_{ref}}\beta_{mol}\left(\mu_1 r''\right)_1\right.}{k*\exp\left(-2\int_0^{\mu_2 r_{ref}}\left[\alpha_{aer}\left(\mu_2 r\right)_2+\alpha_{mol}\left(\mu_2 r\right)_2\right]dr\right)+2*S_a*\int_{\mu_2 r}^{\mu_2 ref} k**\left(\beta_{aer}\left(\mu_2 r'\right)_2+\beta_{mol}\left(\mu_2 r'\right)_2\right)*\exp\left(-2\int_0^{\mu_2 r_{ref}}\alpha_{mol}\left(\mu_2 r''\right)_2 dr''-2\int_0^{\mu_2 r}\alpha_{aer}\left(\mu_2 r''\right)_2 dr''+2*S_a\int_{\mu_2 r}^{\mu_2 r_{ref}}\beta_{mol}\left(\mu_2 r''\right)_2\right.}$$

$$=\frac{\exp\left(-2\int_0^{\mu_1 r_{ref}}\left[\alpha_{aer}\left(\mu_1 r\right)_1+\alpha_{mol}\left(\mu_1 r\right)_1\right]dr\right)+2*S_a*\int_{\mu_1 r}^{\mu_1 ref}\left[\beta_{aer}\left(\mu_1 r'\right)_1+\beta_{mol}\left(\mu_1 r'\right)_2\right]*\exp\left\{-2\int_0^{\mu_1 r_{ref}}\left[\alpha_{mol}\left(\mu_1 r''\right)_1-S_a*\beta_{mol}\left(\mu_1 r''\right)_1\right]dr''-2\int_0^{\mu_1 r}\left[\alpha_{aer}\left(\mu_1 r''\right)_1+S_a*\beta_{mol}\left(\mu_1 r''\right)\right.\right.}{\exp\left(-2\int_0^{\mu_2 r_{ref}}\left[\alpha_{aer}\left(\mu_2 r\right)_2+\alpha_{mol}\left(\mu_2 r\right)_2\right]dr\right)+2*S_a*\int_{\mu_2 r}^{\mu_2 ref}\left[\beta_{aer}\left(\mu_2 r'\right)_2+\beta_{mol}\left(\mu_2 r'\right)_2\right]*\exp\left\{-2\int_0^{\mu_2 r_{ref}}\left[\alpha_{mol}\left(\mu_2 r''\right)_2-S_a*\beta_{mol}\left(\mu_2 r''\right)_2\right]dr''-2\int_0^{\mu_2 r}\left[\alpha_{aer}\left(\mu_2 r''\right)_2+S_a*\beta_{mol}\left(\mu_2 r''\right)\right.\right.}$$

$$=\frac{\exp\left(-2\int_0^{\mu_1 r_{ref}}\left[\alpha_{aer}\left(\mu_1 r\right)_1+\alpha_{mol}\left(\mu_1 r\right)_1\right]dr\right)+2*S_a*e^{-2\int_0^{\mu_1 r_{ref}}\left[\alpha_{mol}\left(\mu_1 r''\right)_1-S_a*\beta_{mol}\left(\mu_1 r''\right)_1\right]dr''}*\int_{\mu_1 r}^{\mu_1 ref}\left[\beta_{aer}\left(\mu_1 r'\right)_1+\beta_{mol}\left(\mu_1 r'\right)_1\right]*\mathrm{e}^{f(\mu_1 r)}dr}{\exp\left(-2\int_0^{\mu_2 r_{ref}}\left[\alpha_{aer}\left(\mu_2 r\right)_2+\alpha_{mol}\left(\mu_2 r\right)_2\right]dr\right)+2*S_a*e^{-2\int_0^{\mu_2 r_{ref}}\left[\alpha_{mol}\left(\mu_1 r''\right)_1-S_a*\beta_{mol}\left(\mu_2 r''\right)_1\right]dr''}*\int_{\mu_2 r}^{\mu_2 ref}\left[\beta_{aer}\left(\mu_2 r'\right)_2+\beta_{mol}\left(\mu_2 r'\right)_2\right]*\mathrm{e}^{f(\mu_2 r)}\mathrm{dr}} \tag{B.26}$$

As $\mathrm{f}'(r)=-2\left[S_{a_{\mathrm{in}}}*\beta_{\mathrm{aer}}\left(r\right)+S_a*\beta_{\mathrm{mol}}\left(r\right)\right]$. let $\mathrm{S_{ain}}=\mathrm{S_a}$, then $\mathrm{f}'^{(r)}=-2*S_a*\left[\beta_{aer}(r)+\beta_{mol}(r)\right]$

$$\int_r^{ref} B\left(r'\right)*\mathrm{e}^{f(r')}dr'=\int_r^{ref}\frac{f'\left(r'\right)}{-2*S_a}*\mathrm{e}^{f(r')}dr'=\int_{f(r)}^{f(ref)}\frac{1}{-2*S_a}*\mathrm{e}^{f(r')}df\left(r'\right)=\left.\frac{1}{-2*S_a}*\mathrm{e}^{f(r')}\right|_{f(r)}^{f\left(r_{reff}\right)} \tag{B.27}$$

$$\int_{\mu_1 r}^{\mu_1 ref} B\left(\mu_1 r'\right)*\mathrm{e}^{f(\mu_1 r')}dr'=\frac{1}{-2*S_a}*\left[\mathrm{e}^{-2*S_a*\int_0^{\mu_1 r_{ref}}\left[\beta_{aer}(\mu_1 r')+\beta_{\mathrm{mol}}(\mu_1 r')\right]dr'}-\mathrm{e}^{-2*S_a*\int_0^{\mu_1 r}\left[\beta_{aer}(\mu_1 r')+\beta_{\mathrm{mol}}(\mu_1 r')\right]dr'}\right] \tag{B.28}$$

$$\int_{\mu\mu_2 r}^{\mu_2 ref} B\left(\mu_2 r'\right)*\mathrm{e}^{f(\mu_2 r')}dr'=\frac{1}{-2*S_a}*\left[\mathrm{e}^{-2*S_a*\int_0^{\mu_2 r_{ref}}\left[\beta_{aer}(\mu_2 r')+\beta_{\mathrm{mol}}(\mu_2 r')\right]dr'}-\mathrm{e}^{-2*S_a*\int_0^{\mu_2 r}\left[\beta_{aer}(\mu_2 r')+\beta_{\mathrm{mol}}(\mu_2 r')\right]dr'}\right] \tag{B.29}$$

$$\frac{\exp\left(-2\int_0^{\mu_1 r_{ref}}\left[\alpha_{aer}\left(\mu_1 r\right)_1+\alpha_{mol}\left(\mu_1 r\right)_1\right]dr\right)+2*Sa*e^{-2\int_0^{\mu_1' 1 ref}\left[\alpha_{mol}\left(\mu_1 r''\right)_2-S_a*\beta_{mol}\left(\mu_1 r''\right)_1\right]dr''}*\int_{\mu_1 r}^{\mu_1 ref}\left[\beta_{aer}\left(\mu_1 r'\right)_1+\beta_{mol}\left(\mu_1 r'\right)_1\right]*\mathrm{e}^{f(\mu_1 r)}dr}{\exp\left(-2\int_0^{\mu_2 r_{ref}}\left[\alpha_{aer}\left(\mu_2 r\right)_2+\alpha_{mol}\left(\mu_2 r\right)_2\right]dr\right)+2*Sa*e^{-2\int_0^{\mu_2 ref} f_{\left[\alpha_{mol}\left(\mu_1 r''\right)_1-S_a*\beta_{mot}\left(\mu_2 r''\right)_2\right]}dr''}*\int_{\mu_2 r}^{\mu_2 ref}\left[\beta_{aer}\left(\mu_2 r'\right)_2+\beta_{mol}\left(\mu_2 r'\right)_2\right]*e^{f(\mu_2 r)}dr}$$

$$=\frac{1}{\exp\left\{-2\int_0^{\mu r_{ref}}\left[S_m*\beta_{mol}\left(r'\right)-S_a*\beta_{mol}\left(r'\right)\right]dr'\right\}\exp\left\{-2*S_a*\int_0^{\mu r}\left[\beta_{aer}\left(r'\right)+\beta_{mol}\left(r'\right)\right]dr'\right\}} \tag{B.30}$$

If $S_{ain} = S_a$, the Ratio R = 1, which means that the backscatter coefficient profiles of two elevation angle are consistent. We can also see that $S_{ain} = S_a$ is also the only solution for R = 1, which also means that we can indeed get the lidar ratio from this method.